Few-photon Non-linearities in Nanophotonic Devices for Quantum Information Technology

Nysteen, Anders; Mørk, Jesper; Kristensen, Philip Trøst; McCutcheon, Dara; Nielsen, Per Kær

Publication date:
2015

Document Version
Publisher's PDF, also known as Version of record

Few-photon Non-linearities in Nanophotonic Devices for Quantum Information Technology

A dissertation
submitted to the Department of Photonics Engineering
at the Technical University of Denmark
in partial fulfillment of the requirements
for the degree of
philosophiae doctor

Anders Nysteen
March 14, 2015

DTU Fotonik
Department of Photonics Engineering
Technical University of Denmark

Few-photon Non-linearities in Nanophotonic Devices for Quantum Information Technology

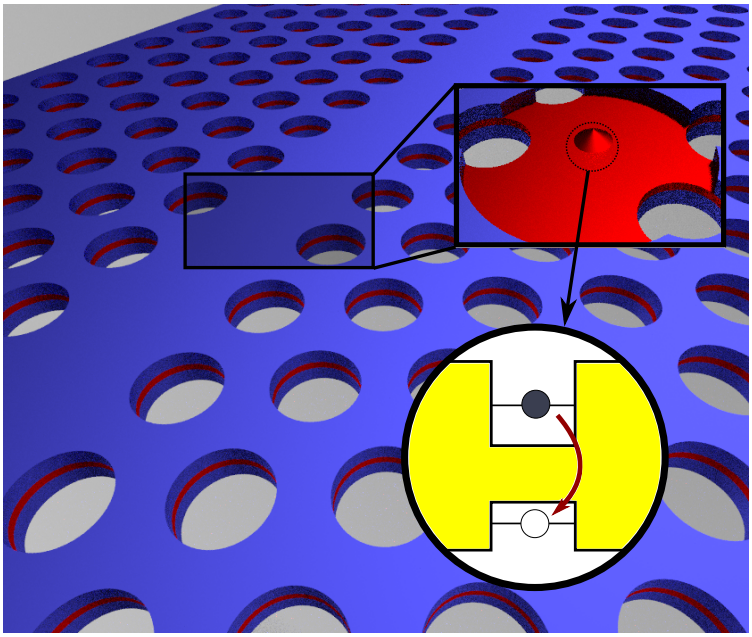

Preface

This thesis is submitted in candidacy for the PhD degree from the Technical University of Denmark. The research has been carried out in the Nanophotonics Theory and Signal Processing Group at DTU Fotonik - Department of Photonics Engineering from 2012-2015, under the supervision of Jesper Mørk, Philip T. Kristensen, Dara P. S. McCutcheon, and Per Kær Nielsen. In July-October 2014 I visited the Quantum Photonics Group at Massachusetts Institute of Technology lead by Prof. Dirk Englund. The main purpose of the visit was to add an experimental point of view to the structures considered in this thesis and to discuss possible implementations of few-photon non-linearities.

Acknowledgements

First and foremost I would like to thank my great team of supervisors: Jesper Mørk, Dara P. S. McCutcheon, Philip Trøst Kristensen, and Per Kær Nielsen. Jesper has been following my studies since 2009, and as my main supervisor during my PhD studies and in several smaller projects, Jesper has provided valuable supervision and encouraging input to the projects with his enormous physical insight. Philip, Per, and Dara have all contributed to different stages of the PhD studies with their solid knowledge of both theoretical and numerical methods, and I valued every discussion we had during the project.

I would like to thank Dirk Englund and Mikkel Heuck for making it possible for me to spend three months in the Quantum Photonics Group at MIT, allowing me to get an great experimental point of view to my research. I also wish to express my gratitude towards the Quantum Photonics Group at the Niels Bohr Institute, especially Peter Lodahl, Kristian H. Madsen and Asger Kreiner-Møller for fruitful discussions about electron-phonon interaction and for carrying out the experimental measurements of phonon-effects in a coupled quantum dot–optical cavity system. Additionally I would like to thank Immo Söllner, Sahand Mahmoodian and Marta Arcari for sharing their insight on the implementation of quantum dot non-linearities in photonic crystal systems.

Furthermore, I would like to thank the entire Nanophotonics Theory and Signal Processing Group, especially my old office mate Anders Lund, and of course also to my two study-buddies Lasse Andersen and Mikkel Settnes, whom I have worked with throughout all of my years of study. Finally, I would like to give special thanks to my family, friends and my girlfriend for supporting me throughout this project.

Abstract

In this thesis we investigate few-photon non-linearities in all-optical, on-chip circuits, and we discuss their possible applications in devices of interest for quantum information technology, such as conditional two-photon gates and single-photon sources.

In order to propose efficient devices, it is crucial to fully understand the non-equilibrium dynamics of strongly interacting photons. Employing both numerical and analytical approaches we map out the full scattering dynamics for two photons scattering on a two-level emitter in a one-dimensional waveguide. The strongest non-linear interaction arise when the emitter is excited the most, which occurs for incoming photon pulses with a spectral bandwidth comparable to the emitter linewidth. For two identical, counter-propagating photons, the emitter works as a non-linear beam splitter, as the emitter induces strong directional correlations between the scattered photons. Even though the non-linearity also alters the pulse spectrum due to a four-wave mixing process, we demonstrate that input pulses with a Gaussian spectrum can be mapped to the output with up to 80 % fidelity.

Using two identical two-level emitters, we propose a setup for a deterministic controlled-phase gate, which preserves the properties of the two incoming photons with almost 80 %, limited by spectral changes induced by the non-linearity and phase modulations upon scattering. Another setup for a controlled-phase operation is suggested with two coupled ring resonators exploiting a strong second-order material non-linearity. By dynamically trapping the first of two temporally separated photons in the non-linear resonator, the scattering of the second photon is altered. Due to the trapping, the undesired aforementioned non-linear effects are avoided, but the gate performance is now limited by the capturing process.

Semiconductor quantum dots (QDs) are promising for realizing few-photon non-linearities in solid-state implementations, although coupling to phonon modes in the surrounding lattice have significant influence on the dynamics. By accounting for the commonly neglected asymmetry between the electron and hole wavefunction in the QD, we show how the phonon-assisted transition rate to a slightly detuned optical mode may be suppressed. This is achieved by properly matching the electrical carrier confinement with the deformation potential interaction, where the suppression only occurs in materials where the deformation potential interaction shifts the electron and hole bands in the same direction. We demonstrate also how the phonon-induced effects may be altered by placing the QD inside an infinite slab, where the confinement of the phonons is modified instead. For a slab thickness below ~ 70 nm, the bulk description

of the phonon modes may be insufficient. The QD decay rate may be strongly increased or decreased, depending on how the detuning between the QD and the optical mode matches the phonon modes in the slab.

Anders Nysteen February 14th, 2015

Resumé

I denne afhandling undersøges få-foton ikke-lineariteter i integrerede optiske kredsløb, og vi diskuterer muligheder for at anvende ikke-lineariteterne i komponenter til kvanteinformatik, såsom betingede to-foton–porte og enkeltfotonkilder.

For at kunne foreslå effektive komponenter er det vigtigt at forstå ikkeligevægtsdynamikken for stærkt vekselvirkende fotoner fuldt ud. Ved at benytte både numeriske og analytiske tilgange beskriver vi den fulde spredningsdynamik for to fotoner, der spreder på en to-niveau-emitter i en en-dimensionel bølgeleder. Den største interaktion opnås, når emitteren er mest eksiteret, hvilket sker når de indkomne foton-pulser har en spektral linjebredde i samme størrelsesorden som emitterens. For to identiske, mod-propagerende fotoner fungerer emitteren som en ikke-lineær beam-splitter, idet emitteren inducerer stærke korrelationer imellem de to fotoners spredningsretning. Selvom ikkelineariteten også ændrer fotonernes spektrum på grund af fire-bølge-blanding, da vil indkomne pulse med et Gaussisk spektrum blive mappet til output-porten med helt op til næsten 80 % fidelity.

Ved at benytte to identiske to-niveau emittere foreslår vi et setup for en deterministisk kontrolleret fase-port, som bevarer egenskaberne af de to indkomne fotoner med næsten 80 %, begrænset af spektrale ændringer induceret af ikkelineariteten og fasemodulationer ved spredningen. Vi foreslår også et andet setup til en kontrolleret fase-port, som består af to koblede ring-resonatorer som har en kraftig anden-ordens materiale-ikke-linearitet. Ved dynamisk at fange den første af de to tidsligt adskildte fotoner i den ikke-lineære resonator, vil spredningen af den anden foton påvirkes. Ved denne dynamiske indfangsmetode undgås de omtalte uønskede effekter fra ikke-lineariteterne, men i stedet vil effektiviteten af porten være begrænset af usikkerhederne ved den dynamiske indfangningsproces.

Halvleder kvantepunkter er lovende kandidater i realiseringen af enkeltfoton ikke-lineariteter i faststof-implementationer, selvom kobling til fonontilstande i det omkringliggende gitter kan have stor indflydelse på dynamikken. Ved at tage højde for den typisk ignorerede asymmetri imellem elektron- og hulbølgefunktionen i kvantepunktet viser vi, hvordan den fonon-assisterede overgangsrate til en nær-resonant optisk tilstand kan blive undertrykt. Dette opnås ved at tilpasse begrænsningen af de elektroniske ladningsbærere med deformationspotentiale-interaktionen, og denne undertrykkelse finder kun sted i materialer hvor deformationspotentiale-interaktionen rykker elektron og hulbånd i samme retning. Vi demonstrerer også, hvordan fonon-inducerede effekter kan ændres ved at placere kvantepunktet inden i en uendelig plade,

hvor begrænsningen af fononerne i stedet er ændret. For pladetykkelser under ~ 70 nm vil beskrivelsen af fononerne som rumligt ubegrænsede ikke være tilstrækkelig længere. I det tilfælde vil henfaldsraten af kvantepunktet kunne være både stærkt øget eller formindsket, afhængig af hvordan energiforskellen imellem kvantedotten og den optiske tilstand matcher med fonon-tilstandene i den uendelige plade.

List of Publications

Journal publications

1. A. Nysteen, P. T. Kristensen, D. P. S. McCutcheon, P. Kaer, and J. Mørk. *Scattering of two photons on a quantum emitter in a one-dimensional waveguide: exact dynamics and induced correlations.* New Jour. Phys. **17**, 023030 (2015)

2. K. H. Madsen, P. K. Nielsen, A. Kreiner-Møller, S. Stobbe, A. Nysteen, J. Mørk, and P. Lodahl. *Measuring the effective phonon density of states of a quantum dot in cavity quantum electrodynamics.* Phys. Rev. B **88**, 045316 (2013).

3. A. Nysteen, P. K. Nielsen, and J. Mørk. *Proposed Quenching of Phonon-Induced Processes in Photoexcited Quantum Dots due to Electron-Hole Asymmetries.* Phys. Rev. Lett. **110**, 087401 (2013).

4. A. Nysteen, P. K. Nielsen, and J. Mørk. *Reducing dephasing in coupled quantum dot-cavity systems by engineering the carrier wavefunctions.* Proceedings of SPIE, the International Society for Optical Engineering **8271**, 82710E (2012)

Submitted manuscripts

1. A. Nysteen, D. P. S. McCutcheon, and J. Mørk. *Strong non-linearity-induced correlations for counter-propagating photons scattering on a two-level emitter.* arXiv:1502.04729 (2015).

Conference contributions

1. K. H. Madsen, P. K. Nielsen, A. Kreiner-Møller, S. Stobbe, A. Nysteen, J. Mørk, and P. Lodahl. *Measuring the effective phonon density of states of a quantum dot.* International Conference on Optics of Excitons in Confined Systems (OECS13) Rome, Italy (2013).

2. K. H. Madsen, P. K. Nielsen, A. Kreiner-Møller, S. Stobbe, A. Nysteen, J. Mørk, and P. Lodahl. *Non-Markovian phonon dephasing of a quantum dot in a photonic-crystal nanocavity.* 11th International Workshop on Nonlinear Optics and Excitation Kinetics in Semiconductors, p. 82 (2012).

3. A. Nysteen, P. K. Nielsen, and J. Mørk. *Suppressing electron-phonon interactions in semiconductor quantum dot systems by engineering the electronic wavefunctions.* 11th International Workshop on Nonlinear Optics and Excitation Kinetics in Semiconductors, p. 64 (2012).

Contents

Chapter 1

Introduction

The fundamentals of quantum mechanics were developed in the beginning of the 20th century in an attempt to explain the spectral properties of thermal radiation, as none of the current theories were sufficient. The first model that was able to explain experimental results was proposed by Max Planck, by assuming that the thermal radiation was in equilibrium with a set of harmonic oscillators with discrete energy levels [1]. Albert Einstein followed up by claiming that a beam of light actually consists of individual packets, which were later to be called photons [2]. This quantization of the light lead to major discussions of the particle-wave duality of light, but it were also able to explain a yet unresolved problem regarding interaction between light and matter, namely the photoelectric effect. These early achievements form the basis of a quantum mechanical description of the world with a fundamentally probabilistic nature, where a single particle has a probability of being in one of multiple states at a given time, in a *quantum superposition*. And where multiple particles may be in a quantum state where each particle cannot be described independently as they are *quantum mechanically entangled*.

This quantum mechanical understanding of the fundamental interaction between light and matter has been of crucial importance in the development of several important components in our daily life such as lasers, diodes, and magnetic resonance imaging. Quantum mechanics also paves the way for a new era in computational schemes, which has been a hot topic in the last couple of decades [3]. New functionalities have been made possible by encoding information into quantum mechanical superpositions called quantum bits (qubits). In contrast to classical bits are is in one of two states at a specific time, the quantum mechanical nature of qubits may be in a superposition of each bit state at the same time until the state of the qubit is measured.

This relatively new field of quantum information technology promises secure communication by quantum cryptography [4, 5, 6]. The quantum encoding also allows new computational algorithms in the field of quantum computation [3], which promise exponentially faster operation times for specific tasks such as searching databases and factorizing, with the latter having been demonstrated experimentally by an implementation of Shor's algorithm [7].

In order to realize quantum circuits and quantum networks [8, 9, 10], photons are promising candidates as carriers of the quantum-encoded information [11]. As flying qubits, the information carried in the photons is not easily affected by the surrounding environment due to the non-interacting nature of the photons. The qubit states may be encoded in various degrees of freedom, for example polarisation states, temporal displacements, and spatial modes (such as the dual-rail representation) etc. [12, 13].

Realizations of the quantum computation schemes rely on the possibility of initializing, processing/interacting and measuring qubits efficiently, but as photons do not mutually interact due to their bosonic nature, advanced approaches must be employed. Using only linear optical elements such as beam splitters, phase shifters and mirrors, Knill, Laflamme, and Milburn demonstrated in 2001 that it was possible to do quantum computation using single-photon sources and photo-detectors [14]. This so-called KLM scheme exploits feedback from the detectors and use several ancilla photons. Suggestions for efficient non-linear gates are proposed, but they are all probabilistic as they only work successfully when a specific combination of detection events is obtained in ancillary arms. This results in scalability-issues when employing multiple gates, although this may be dealt with using quantum teleportation [15]. Experimental implementations of these probabilistic gates have been carried out with high success rates [16].

1.1 Few-photon non-linearities

In contrast to the probabilistic KLM-scheme, which uses several ancillary photons and detectors, few-photon non-linearities [17] open up for possibilites of creating deterministic gate structures without additional ancillary photons and detectors. Material non-linearities such as the Kerr effect is one example, where the photon interaction stems from induced changes in the refractive material. It is, however, an ongoing challenge to find materials with a sufficient non-linear coefficient in order to work in the single-photon regime. For this, single atoms prove viable candidates as few-photon non-linearities due to their discrete energy levels. These few-photon non-linearities are also existing in so-called "artificial atoms" such as semiconductor quantum dots (QDs) [18, 19, 20], nitrogen vacancy (NV) centres in diamonds [21, 22], or superconducting circuits [23], which are all physical objects with bound, discrete electronic states.

The atom–light interaction in these systems may be enhanced by placing the emitter inside an optical cavity, such that the light passes through the atom repediatly. If the rate at which energy oscillates between the atom and the cavity modes exceeds loss of excitation in the system to external reservoirs, the atom–cavity system is said to be in the *strong coupling regime* [24]. In this regime, the atom dresses the energy levels of the optical cavity to an an-harmonic energy ladder. Thus, for an incoming beam of photons matching the lowest energy level of the dressed state, the strong atom–cavity coupling only allows a single electron to couple through the cavity at a time – an effect known as the photon blockade. Experimental demonstrations of this possibility of controlling the reflectivity of a cavity with a single atom have been carried

out e.g. by trapping Caesium atoms in a Fabry–Perot cavity [25]. The continuous improvement of micro- and nanofabrication allows precise control of the electronic and electromagnetic confinement, and has made it possible to observe strong coupling even in solid-state system, with a QD coupling to a photonic crystal cavity [26, 27].

1.2 All-optical integrated circuits

There is currently a great deal of interest on schemes that integrate photonic gates and non-linearities together with photon sources and detectors, on a single on-chip platform in an all-optical circuit [28, 29, 30]. As the quantum schemes rely on minimal decoherence and losses of the information, it is of high importance to minimize the losses caused by coupling the different functionalities together. Coupling losses may be minimized by integrating photon creation, processing and detection on-chip [31]. Promising single-photon sources have been demonstrated using QDs in nanowires and photonic crystal cavities [32, 33], and several designs for efficient few-photon detection exist, e.g. using superconducting nanowires [34, 35, 36, 37]

For processing, both single- and two-photon gates are required to make a quantum computer [3, 38], and finding efficient conditional two-photon gates is still a pressing challenge. Here few-photon non-linearities are promising candidates, and demonstrations of several gate functionalities have been developed. By externally changing the state of an atom trapped in the proximity of an optical cavity, the scattering direction/phase of a signal beam through the cavity may be controlled solely by whether the single atom is able to couple the the cavity or not [39, 40]. Alternatively, by trapping single photons or using multi-level emitters, it is possible to switch a multi-photon beam with only a single control excitation [41, 42, 43]. The dressed cavity–QD system may also be employed in conditional gates for two impinging single-photons of different color, due to the anharmonic energy ladder of the dressed cavity [44]. The structures mentioned above are all viable candidates for conditional phase gates, but they all rely on external manipulations to trap atoms or photons or to manipulate the state of the atom.

Solid-state implementations of the non-linearities such as QDs have been demonstrated to couple with very high efficiency to confined propagating photon modes [45], and they are promising candidates for on-chip integrated non-linearities. However, the solid state implementation also introduce decoherence due to coupling between the electrical carriers and the vibrational modes in the solid-state environment, with the latter being quantized as phonons. When exciting a QD optically, acoustic phonons may assist in the coupling and enhance the coupling rate [46, 47, 48]. The phonons do, however, also introduce dephasing, which e.g. in a single-photon source would decrease the indistinguishability of the emitter photons [49].

The main purpose of this thesis is to investigate the possibility of integrating the non-linearities and functionalities in an all-optical, deterministic on-chip configuration, with a specific focus on the few-photon non-linear processes. In

order to propose efficient structures, it is crucial to understand the non-trivial dynamics of strongly interacting photons fully. Using both numerical and analytical approaches we map out the non-linearity-induced correlations in detail, and we discuss how the non-linearity may be exploited in deterministic quantum gates. By treating the electron-phonon interaction as a non-Markovian coupling to a large phonon bath, we examine in detail how both the electronic and phononic confinement affect the dynamics related to the QD. We describe how the confinement of both the electrical carriers and the phonons may be engineered in order to optimize the performance of the quantum systems.

1.3 Thesis outline

In Chapter 2 the governing Hamiltonians are introduced by specifically considering the individual contributions from the different particles present in a quantum system and their mutual interaction.

Chapter 3 treats scattering of a single-photon wavepacket on a two-level emitter in a one-dimensional waveguide. We describe the fundamental theory of single-photon scattering, with focus on the emitter dynamics and the properties of the scattered state. Additionally we introduce a numerical approach to determine the dynamics of photon scattering in waveguide systems interacting with localized scatterers in general.

We perform a full numerical calculation of the scattering of two-photon pulses on a two-level emitter in Chapter 4. From the numerics we are able map out the full scattering dynamics. Specifically we demonstrate that for two initially counter-propagating photons, the emitter acts like a non-linear beam splitter by imposing strong directional correlations in the scattered state. This only occurs when the bandwidths of the incoming pulses are identical to the emitter linewidth, as the emitter is excited the most in this pulse regime.

In Chapter 5 we exploit the scattering matrix formalism to determine analytical expressions for the post-scattering state in Chapter 4. The analytical approach allows us to investigate the correlations in the scattered state that are specifically caused by the emitter non-linearity. Fidelity measurements are introduced to describe the scattering-induced correlations, which may take both the photon spectrum, phase and propagating direction into account. For the case of two counter-propagating photons, the fidelity of the non-linear beam splitter is almost 80 %, even when taking all scattering-induced changes in the spectrum and phase of the photons into account.

We discuss direct exploitation of few-photon non-linearities in two theoretical proposals of a deterministic controlled-phase gate in Chapter 6 and 7. We specifically focus on the possibility of integrating the gate in a larger optical circuit by imposing requirements on the temporal and spectral properties of the scattered state compared to the input state, as it may be undesirable if the photon properties are altered by the gate. For a passive gate consisting of phase shifters, beam splitters and two emitters, we demonstrate a gate fidelity of almost 80 %. The theoretical fidelity may be increased using a gate scheme which employs dynamical capture of the control photon in the gate, although this scheme relies on very precise experimental manipulations.

In Chapter 8–10 we investigate the influence of phonon coupling in semiconductor QD systems. A description of the phonon modes and interaction mechanisms with the electronic carriers is provided in Chapter 8. By including the phonons as a non-Markovian reservoir, we introduce the reduced density matrix formalism in order to describe the system dynamics.

The possibility of engineering the electronic confinement in order to affect the phonon-induced effects is examined in Chapter 9. We show how the electronic confinement may affect the decay rate of an emitter inside a slightly detuned optical cavity by balancing the deformation potential coupling between the electrons and the phonons. Furthermore we discuss perspective to improve the indistinguishability of the emitted photons by engineering the electronic confinement. Lastly, we apply our theory to map out the existing phonon density from an experimental setup with a QD inside a photonic crystal cavity.

Chapter 10 considers how confinement of the phonons affect the dynamics. We specifically consider a QD placed inside an optical cavity in an infinite slab, and we show how the phonon-assisted coupling may be either suppressed or enhanced, depending on the phonon modes in the slab. Furthermore, we estimate the bulk description to be sufficient when the slab thickness is more than ~ 70 nm.

Finally, we highlight the important results from the thesis in Chapter 11.

Chapter 2

Governing Hamiltonians

To fully understand the dynamics in a many-body quantum system, the interaction mechanisms between the different quantum particles must be understood in detail. In this chapter sketch the derivation of the governing Hamiltonians needed to describe the interaction between light and matter in few-photon optical structures. The interaction between the electromagnetic field and the electrical carriers will be treated in the dipole approximation, valid when the spatial extent of the carrier wavefunction is much smaller than the wavelength of the light. For the phonon-related terms in the Hamiltonian, we specifically consider atoms placed in a rigid periodic lattice, and assume that the external perturbations, which displaces the ions, are small. The assumptions are explained in detail below, where we derive the Hamiltonians expressed in second quantization.

2.1 Many-body Hamiltonian

A system consisting of electrons in a rigid periodic lattice coupled to a electromagnetic field is described by the many-body Hamiltonian [50, 51, 52, 53],

$$H = \sum_j \frac{1}{2m_l} \left[\mathbf{p}_l - q_l \mathbf{A}(\mathbf{r}_l)\right]^2 + \frac{1}{2} \int \mathrm{d}\mathbf{r} \left[\epsilon_0 |\mathbf{E}(\mathbf{r},t)|^2 + \frac{1}{\mu_0} |\mathbf{B}(\mathbf{r},t)|^2\right]. \quad (2.1)$$

The sum describes the kinetic energy of particle l (being either an electron or ion) with momentum operator $\mathbf{p}_l$ and a term $-q_l\mathbf{A}(\mathbf{r}_l)$ which is the change of energy due to the presence of an electromagnetic field, introduced by the Coulomb gauge [52]. The integral represents the energy of the total electromagnetic field, containing operators for the electrical field, $\mathbf{E}$, and the magnetic field, $\mathbf{B}$, and lastly the vacuum permittivity is ϵ_0, and the vacuum permeability is μ_0.

The sum in Eq. (2.1) may be split up into separate contributions from the electrons and the ions [52],

$$\sum_{i,\mathrm{ions}} \frac{p_i^2}{2m_i} + \sum_{j,\mathrm{elec}} \left[\frac{p_j^2}{2m_j} + \frac{e}{m_j}\mathbf{A}(\mathbf{r}_j,t)\cdot\mathbf{p}_j\right], \quad (2.2)$$

where the spin index of the electron for simplicity has been absorbed into the summation index, j, and with $-e$ denoting the charge of an electron. Furthermore, in deriving Eq. (2.2), low field intensities were assumed by which the $\mathbf{A}^2$-term may be neglected. Due to the high mass of the ions compared to the electron, the response to the electromagnetic field is low and the ion-field interaction terms may be neglected. Lastly, we exploit that $\mathbf{p}\cdot\mathbf{A} = \mathbf{A}\cdot\mathbf{p}$ in the Coulomb gauge.

According to Maxwell's equations, $\mathbf{B}$ is purely transverse. The integral in Eq. (2.1) may be divided into a transverse and a longitudinal contribution,

$$H_{\text{trans}} = \frac{1}{2}\int \mathrm{d}\mathbf{r}\,\left[\epsilon_0|\mathbf{E}_\perp(\mathbf{r},t)|^2 + \frac{1}{\mu_0}|\mathbf{B}(\mathbf{r},t)|^2\right], \tag{2.3a}$$

$$H_{\text{long}} = \frac{1}{2}\int \mathrm{d}\mathbf{r}\,\epsilon_0|\mathbf{E}_\parallel(\mathbf{r},t)|^2, \tag{2.3b}$$

In the Coulomb gauge, H_{long} simplifies to the electrostatic Coulomb energy plus a Coulomb self-energy of each particle [51, 52], whereas the latter shift does not affect the dynamics and thus is omitted in the following. In a system of point charges, the Coulomb interaction may be split into contributions from interaction between the individual particle types[1]

$$\begin{aligned} V_{\text{Coulomb}} &= \frac{1}{2}\sum_{\substack{i\neq i'\\ \text{ion-ion}}} \frac{q_i q_{i'}}{4\pi\epsilon_0}\frac{1}{|\mathbf{R}_i-\mathbf{R}_{i'}|} + \frac{1}{2}\sum_{\substack{j\neq j'\\ \text{elec-elec}}} \frac{e^2}{4\pi\epsilon_0}\frac{1}{|\mathbf{r}_j-\mathbf{r}_{j'}|} \\ &\quad + \sum_{\substack{j\neq i\\ \text{elec-ion}}} \frac{(-e)q_i}{4\pi\epsilon_0}\frac{1}{|\mathbf{r}_j-\mathbf{R}_i|}, \end{aligned} \tag{2.4}$$

with $\mathbf{R}_i$ and $\mathbf{r}_j$ being the position of the i'th ion and the j'th electron, respectively.

If the ions are in a static latterice, the last term in Eq. (2.4) may be simplified by introducing displacements of the ions, $\mathbf{u}_i$, relative to their equilibrium position, $\mathbf{R}_i^{(0)}$, giving $\mathbf{R}_i = \mathbf{R}_i^{(0)} + \mathbf{u}_i$. Assuming small relative displacements, a Taylor expansion around $\mathbf{u}_i \approx 0$ gives

$$\sum_{j\neq i}\frac{(-e)q_i}{4\pi\epsilon_0}\frac{1}{|\mathbf{r}_j-\mathbf{R}_i|} \approx \sum_{j\neq i}\frac{(-e)q_i}{4\pi\epsilon_0}\left[\frac{1}{|\mathbf{r}_j-\mathbf{R}_i^{(0)}|} - \mathbf{u}_i\cdot\boldsymbol{\nabla}_{\mathbf{r}_j}\left(\frac{1}{|\mathbf{r}_j-\mathbf{R}_i^{(0)}|}\right)\right],$$

where terms of second or higher order in the displacement are neglected. The first term describes the potential of electrons in a static lattice, which usually is described by a potential for the electrons, $\mathcal{V}(\mathbf{r}_j)$.

Summing up, the Hamiltonian in Eq. (2.1) consists of the following contri-

[1] No factor of 1/2 appears in the electron–ion sum, as no double-counting occurs.

butions

$$H_{0,\text{elec}}\{\mathbf{r}_j\} = \sum_{j,\text{elec}} \left[\frac{p_j^2}{2m_j} + \mathcal{V}(\mathbf{r}_j)\right], \tag{2.5a}$$

$$H_{0,\text{rad}} = \frac{1}{2}\int \mathrm{d}\mathbf{r}\left[\epsilon_0|\mathbf{E}_\perp(\mathbf{r},t)|^2 + \frac{1}{\mu_0}|\mathbf{B}(\mathbf{r},t)|^2\right], \tag{2.5b}$$

$$H_{0,\text{ion}}\{\mathbf{r}_i\} = \sum_{i,\text{ion}} \left[\frac{p_i^2}{2m_i}\right], \tag{2.5c}$$

$$H_{\text{elec-rad}}\{\mathbf{r}_j\} = \sum_{j,\text{elec}} \frac{e}{m_j}\mathbf{A}(\mathbf{r}_j,t)\cdot\mathbf{p}_j, \tag{2.5d}$$

$$H_{\text{elec-ion}}\{\mathbf{r}_j\} = \sum_{j\neq i} \mathbf{u}_i\cdot\boldsymbol{\nabla}_{\mathbf{r}_j}\left(\frac{eq_i}{4\pi\epsilon_0}\frac{1}{|\mathbf{r}_j - \mathbf{R}_i^{(0)}|}\right), \tag{2.5e}$$

$$H_{\text{elec-elec}}\{\mathbf{r}_j\} = \frac{1}{2}\sum_{j'\neq j,\text{elec-elec}} \frac{e^2}{4\pi\epsilon_0}\frac{1}{|\mathbf{r}_j - \mathbf{r}_{j'}|}, \tag{2.5f}$$

$$H_{\text{ion-ion}}\{\mathbf{R}_i\} = \frac{1}{2}\sum_{i'\neq i,\text{ion-ion}} \frac{q_i q_{i'}}{4\pi\epsilon_0}\frac{1}{|\mathbf{R}_i - \mathbf{R}_{i'}|}. \tag{2.5g}$$

In the following we write the different term of the total Hamiltonian, Eqs. (2.5a)-(2.5g), in second quantization, following Refs. [53, 54]. This is carried out by determining the matrix elements of the operators in a basis spanned by a complete orthonormal set of single-particle states, see e.g. Refs. [55, 52, 56] for further details. We denote the bosonic creation and annihilation operators for photons by $a^\dagger$ and a, the bosonic operators for the phonons by $b^\dagger$ and b, and the fermionic operators describing the electron by $c^\dagger$ and c.

Non-interacting parts of the Hamiltonian

By non-interacting parts of the Hamiltonian we refer to the terms containing products of two bosonic or fermionic operators, and these terms have to be time-independent in the Schrödinger picture. The non-interacting part of H consists of an electronic, a photonic, and a phononic part:

Electrons The non-interacting electron part of the Hamiltonian from Eq. (2.5a) may be written as $H_{0,\text{elec}}(\{\mathbf{r}_j\}) = \sum_j H_{0,\text{elec}}(\mathbf{r}_j)$. In second quantization a preferred basis for electrons is the eigenstates of $H_{0,\text{elec}}$, where each electron wavefunction obeys the Schrödinger equation $H_{0,\text{elec}}(\mathbf{r})\psi_\nu(\mathbf{r}) = \hbar\omega_\nu\psi_\nu(\mathbf{r})$, with $\psi_\nu(\mathbf{r})$ being the single-particle wavefunction of an electron. In this basis the Hamiltonian Eq. (2.5a) is diagonal,

$$H_{0,\text{elec}} = \sum_\nu \hbar\omega_\nu c_\nu^\dagger c_\nu. \tag{2.6}$$

where the number operator $c_\nu^\dagger c_\nu$ counts the number of electrons in the state ν, being either 0 or 1 due to Pauli's exclusion principle.

Photons The non-interacting photonic Hamiltonian stems from the energy of the transverse electromagnetic field, Eq. (2.5b). The electric field may be expanded as a weighted sum of orthonormal mode functions $\{\mathbf{w}_n(\mathbf{r})\}$ which are determined by the boundary conditions of the specific problem [52, 56]. The quantum number n is combined of both the spatial and polarization quantum numbers. The total quantized, transverse electric field is obtained by treating each mode of the electric field as a harmonic oscillator, and by summing over all modes

$$\mathbf{E}_t(\mathbf{r},t) = \mathrm{i}\sum_n \mathcal{E}_n[a_n^\dagger(t) - a_n(t)]\mathbf{w}_n(\mathbf{r}), \tag{2.7}$$

where the time-dependence of the photonic annihilation and creation operators $a_n^\dagger(t)$ and $a_n(t)$ are described in the Heisenberg picture. The weight factor $\mathcal{E}_n = \sqrt{\hbar\omega_n/(2\epsilon_0 V_P)}$ describes the electric field „per photon" of energy $\hbar\omega_n$, with V_P being the quantization volume of the photon mode.

By the quantized electric field from Eq. (2.7) in Eq. (2.5b), and relating the **B**-field to the quantized **E**-field through Maxwell's equations,

$$H_{0,\mathrm{rad}} = \sum_n \hbar\omega_n \left(a_n^\dagger a_n + \frac{1}{2}\right), \tag{2.8}$$

where $\sum_n \hbar\omega_n/2$ constitutes the zero-point energy [56].

Phonons The non-interacting part describing the phonons stems from the kinetic energy of the ions in Eq. (2.5c) and the Coulomb-interaction between the ions in Eq. (2.5g). Due to the heavy masses of the ions compared to the electron, the ions react slower to external perturbations. Furthermore, the ions sit in a static lattice, and under the *harmonic approximation*, as we will introduce below, the ion-ion interaction may be approximately described by a quadratic term in the bosonic operators, which is why it treated as a "non-interaction" term here [53, 55].

We consider the displacement of an ion, $\mathbf{Q}_i$, from its equilibrium position in the static lattice, $\mathbf{R}_i^{(0)}$, such that $\mathbf{R}_i = \mathbf{R}_i^{(0)} + \mathbf{Q}_i$. In the same way as done for the electron-ion interaction in Eq. (2.5) a Taylor-expansion of $H_{\text{ion-ion}}$ is carried out around $\mathbf{Q}_i = \mathbf{0}$. The zeroth order term becomes a constant which does not affect the dynamics, and this is neglected. Furthermore the equilibrium position may be defined such that the first order term is zero [55]. The first actual contribution comes from the second order term. The harmonic approximation states that due to the heavy ion masses and the static lattice, it is reasonable only to include the second order term in the Hamiltonian, in which case the quantized Hamiltonian describing the non-interacting part of the phonon Hamiltonian becomes[2] [53, 58]

$$H_{0,\mathrm{ph}} = \sum_\mu \hbar\omega_\mu \left(b_\mu^\dagger b_\mu + \frac{1}{2}\right). \tag{2.10}$$

[2]What is excluded in the harmonic approximation are terms of third or higher order in the displacement. These are the so-called anharmonic effects, where the first term has the

The quantum number μ is a combination of the wavevector $\mathbf{k}$, restricted to the first Brillouin zone, and the phonon branch λ dictating the polarization of the phonon. The term corresponding to $\mathbf{q} = \mathbf{0}$ corresponds to a uniform translation of the crystal and should formally not be included in the sum [55].

Interaction parts of the Hamiltonian

Electron-photon The interaction of the electrons with the electromagnetic field Eq. (2.5d) is in the literature denoted the $\mathbf{A}\cdot\mathbf{p}$-interaction. It is well-known that in the dipole approximation the $\mathbf{A}\cdot\mathbf{p}$-interaction may be replaced by a $\mathbf{d}\cdot\mathbf{E}_\perp$-interaction, where $\mathbf{d}_j = -e\mathbf{r}_j$ is the electric dipole operator describing the interaction of light with an electron at $\mathbf{r}_j$, [59]. The dipole approximation is valid when the wavelength of the radiation field is much larger than the characteristic size of the atoms in the solid. For optical wavelengths $\sim 400-700$ nm are used, and the size of the atoms are on the order of a few ångströms, and the requirement is fulfilled[3], and the vector field may be considered spatially uniform across the atom. In this case, the interaction Hamiltonian becomes [56],

$$H_{\text{elec-rad}} = -\sum_j \mathbf{d}_j \cdot \mathbf{E}_\perp(t). \tag{2.11}$$

The electric field may consist both of a quantized field as in Eq. (2.7) and an external driving field, $\mathbf{E}_{\text{clas}}$. The contribution from the quantized field becomes in second quantization

$$H_{\text{elec-rad}} = \sum_{\nu_a\nu_b n} \hbar g^n_{\nu_a\nu_b} c^\dagger_{\nu_a} c_{\nu_b} (a^\dagger_n + a_n), \tag{2.12}$$

where $\hbar g^n_{\nu_a\nu_b}$ describes the electron-photon coupling strength,

$$\hbar g^n_{\nu_a\nu_b} = \mathcal{E}_n \int \mathrm{d}\mathbf{r}\, \psi^*_{\nu_a}(\mathbf{r}) e\mathbf{r}\cdot\mathbf{w}_n \psi_{\nu_b}(\mathbf{r}) \delta_{\nu_a\nu_b}. \tag{2.13}$$

The contribution from the external (time-dependent) driving field, $W(t)$, is evaluated in the same manner by expanding the operators onto the single-particle basis states, giving

$$W(t) \quad = \quad E_{\text{clas}}(t) \sum_{\nu_a\nu_b} d_{\nu_a\nu_b} c^\dagger_{\nu_a} c_{\nu_b}, \tag{2.14}$$

---

form

$$\sum_{\substack{\mathbf{kq}\\ \lambda_1\lambda_2\lambda_3}} Q_{\mathbf{k},\lambda_1} Q_{\mathbf{q},\lambda_2} Q_{-\mathbf{k}-\mathbf{q},\lambda_3} M_{\mathbf{kq},\lambda_1\lambda_2\lambda_3}, \tag{2.9}$$

with $Q_i = |\mathbf{Q}_i|$ and where $M_{\mathbf{kq},\lambda_1\lambda_2\lambda_3}$ describes the interaction strength. The anharmonic effects include the possibility of one phonon decaying into two or more phonons vice versa. It is reasonable to neglect the anharmonic terms when considering the phonon dispersion relation, but they has to be included when looking at decay of phonon modes [57].

[3] If "artificial atoms" such as quantum dots are used, the dipole approximation may break down, if the quantum dots are too large compared to the wavelength [60]. As an example, InGaAs/GaAs QDs typically have dimensions of 5-70 nm [61].

where the projected dipole matrix element is defined,

$$d_{\nu_a\nu_b} = \int \mathrm{d}\mathbf{r}\, \psi^*_{\nu_a}(\mathbf{r}) e\mathbf{r}\cdot\boldsymbol{\xi}_{\mathbf{E}_{\text{clas}}} \psi_{\nu_b}(\mathbf{r}) \delta_{\nu_a,\nu_b}. \tag{2.15}$$

The polarization vector of $\mathbf{E}_{\text{clas}}$ is denoted $\boldsymbol{\xi}_{\mathbf{E}_{\text{clas}}}$, and again the spin dependence has been absorbed into the summation index.

Electron-phonon The electron-phonon interaction is described by the interaction of the electrons with the ion displacements in the lattice and is given by Eq. (2.5e), which may be written as $H_{\text{elec-ph}}(\{\mathbf{r}_i\}) = \sum_i H_{\text{elec-ph}}(\mathbf{r}_i)$, where $H_{\text{elec-ph}}(\mathbf{r}_i)$ contains the quantized ionic displacement operator $\mathbf{u}$. Following a standard derivation [53, 55], the form of the quantized displacement vector is

$$\mathbf{u}(\mathbf{r}) = \mathrm{i}\sum_{\mu}\sqrt{\frac{\hbar}{2\rho V\omega_\mu(\mathbf{k})}}\boldsymbol{\xi}_\mu\left(b^\dagger_{\overline{\mu}} + b_\mu\right)\mathrm{e}^{\mathrm{i}\mathbf{k}\cdot\mathbf{r}}, \tag{2.16}$$

where $\overline{\mu} = (-\mathbf{k}, \lambda)$ with λ being the polarization quantum number. Here $\mathbf{u}(\mathbf{r})$ has to be evaluated from the equilibrium points of the ions, $\mathbf{r} = \mathbf{R}^{(0)}_j$. Furthermore ρ is the crystal density, V is the normalization volume of the phonon modes, $\boldsymbol{\xi}_\mu$ is the polarization vector[4], and $\omega_\mu(\mathbf{k})$ is the phonon frequency.

Using Eq. (2.5e) we may express the interaction using the second quantization formalism,

$$H_{\text{elec-ph}} = \sum_{\nu_a\nu_b,\mu} M^\mu_{\nu_a\nu_b} c^\dagger_{\nu_a} c_{\nu_b}\left(b_\mu + b^\dagger_{\overline{\mu}}\right), \tag{2.17}$$

where the coupling strength is given by

$$\begin{aligned} M^\mu_{\nu_a\nu_b} &= \mathrm{i}\sqrt{\frac{\hbar}{2\rho V\omega_\mu(\mathbf{k})}}\sum_j \mathrm{e}^{\mathrm{i}\mathbf{k}\cdot\mathbf{R}^{(0)}_j} \\ &\quad\times\int \mathrm{d}\mathbf{r}\,\psi^*_{\nu_a}(\mathbf{r})\boldsymbol{\xi}_\mu\cdot\boldsymbol{\nabla}_{\mathbf{r}}\left[\frac{eq_j}{4\pi\epsilon}\frac{1}{|\mathbf{r}-\mathbf{R}^{(0)}_j|}\right]\psi_{\nu_b}(\mathbf{r})\delta_{\nu_a\nu_b}. \end{aligned} \tag{2.18}$$

Electron-electron The electron-electron interaction given by Eq. (2.5f) and may be written as $H_{\text{elec-elec}}(\{\mathbf{r}_j\}) = \frac{1}{2}\sum_{j'\neq j} H_{\text{elec-elec}}(\mathbf{r}_{j'} - \mathbf{r}_j)$. In second quantization this may be expressed as

$$H_{\text{elec-elec}} = \frac{1}{2}\sum_{\nu_i\nu_j\nu_k\nu_l} V_{\nu_i\nu_j,\nu_k\nu_l} c^\dagger_{\nu_i} c^\dagger_{\nu_j} c_{\nu_l} c_{\nu_k}, \tag{2.19}$$

with $V_{\nu_i\nu_j,\nu_k\nu_l}$ being the Coulomb intercation matrix element [53].

[4] The polarization vector has the property $\boldsymbol{\xi}_\mu = -\boldsymbol{\xi}_{\overline{\mu}}$, as $\mathbf{u}(\mathbf{r})$ must be Hermitian [53].

Summary

We have sketched the derivation of a Hamiltonian describing a quantum system of interacting light and matter, which is summarized by

Non-interacting part $H_0 = H_{0,\text{elec}} + H_{0,\text{rad}} + H_{0,\text{ph}}$	**Interacting part** $H_{\text{int}} = H_{\text{elec-elec}} + H_{\text{elec-rad}} + H_{\text{elec-ph}}$
$H_{0,\text{elec}} = \sum_\nu \hbar\omega_\nu c_\nu^\dagger c_\nu$	$H_{\text{elec-elec}} = \frac{1}{2}\sum_{\nu_i\nu_j\nu_k\nu_l} V_{\nu_i\nu_j,\nu_k\nu_l} c_{\nu_i}^\dagger c_{\nu_j}^\dagger c_{\nu_l} c_{\nu_k}$
$H_{0,\text{rad}} = \sum_n \hbar\omega_n \left(a_n^\dagger a_n + \frac{1}{2}\right)$	$H_{\text{elec-rad}} = \sum_{\nu_a\nu_b,n} \hbar g^n_{\nu_a\nu_b} c_{\nu_a}^\dagger c_{\nu_b} (a_n^\dagger + a_n)$
$H_{0,\text{ph}} = \sum_\mu \hbar\omega_\mu \left(b_\mu^\dagger b_\mu + \frac{1}{2}\right)$	$H_{\text{elec-ph}} = \sum_{\nu_a\nu_b,\mu} M^\mu_{\nu_a\nu_b} c_{\nu_a}^\dagger c_{\nu_b} \left(b_\mu + b_{\bar{\mu}}^\dagger\right)$
External classical field	$W(t) = E_{\text{clas}}(t) \sum_{\nu_a\nu_b} d_{\nu_a\nu_b} c_{\nu_a}^\dagger c_{\nu_b}$

These Hamiltonians constitute the main building blocks in analyzing the dynamics of different quantum systems in the next chapters. In Chapter 3-5 we focus on coupling between a two-level emitter and a quantized electromagnetic field in a one-dimensional waveguide, where we only treat coupling to the environment by a loss rate of the emitter. In Chapter 8-10 we specifically consider interaction between the electronic states of a semiconductor quantum dot and a cavity field, specifically focussing on the contributions from phonons.

Chapter 3

Single-photon scattering

One of the simplest systems in which to investigate the coupling between a few-photon non-linearity and a propagating photon pulse, is a two-level emitter (TLE) coupling to an infinite one-dimensional waveguide. A physical realization of such a system has e.g. been demonstrated by A. Goban et al. [62] by trapping a Caesium atom in the vicinity of a photonic crystal waveguide, demonstrating a coupling efficieny of the TLE to the waveguide modes of 32 %. A much higher coupling efficiency may, however, be achieved in solid state systems, in which the TLE is placed inside the high-index materials. A recent experiment by M. Arcari et al. [45] demonstrates a coupling efficiency of 98 % between a semiconductor quantum dot and a line defect in a photonic crystal slab, as sketched in Fig. 3.1. A higher coupling for the quantum dot is achieved as the emitter is inside the high-index material, although the solid environment also introduce additional scattering processes from phonons, which we will elaborate on in Chapter 8–10. The purpose of this chapter is to clarify the dynamics of a single photon scattering on the TLE, as it is an important building block for a solid understanding of two-photon scattering, where the non-linearity of the TLE is addressed.

The scattering of an incoming single-photon wavepacket on the TLE will depend strongly on the spectral and spatial properties of the photon relative to the TLE. Pulses with a very narrow bandwidth have a very small probability of exciting the TLE, as the energy of the pulse is spread across a wide spatial range. In this regime, the TLE is well-known to behave as a linear scatterer in the few-photon limit with the transmission spectrum sketched in Fig. 3.2(a). If the narrow-spectrum photon is resonant with the emitter transition, the pulse is fully reflected. The reason for this is explained in Fig. 3.2(b), by expanding a right-propagating photon in an equal superposition of even and odd waveguide modes. While the even modes has an anti-node at the emitter position, the odd modes has a node and thus does not interact with the emitter. As the field scattered from a dipole will be out of phase with the incoming light, the even mode attains a phase shift of π, whereas the odd modes propagates past the emitter. Thus, by summing up the contributions, the scattered even and odd mode interfere destructively in the right (transmitted) port, and thus the

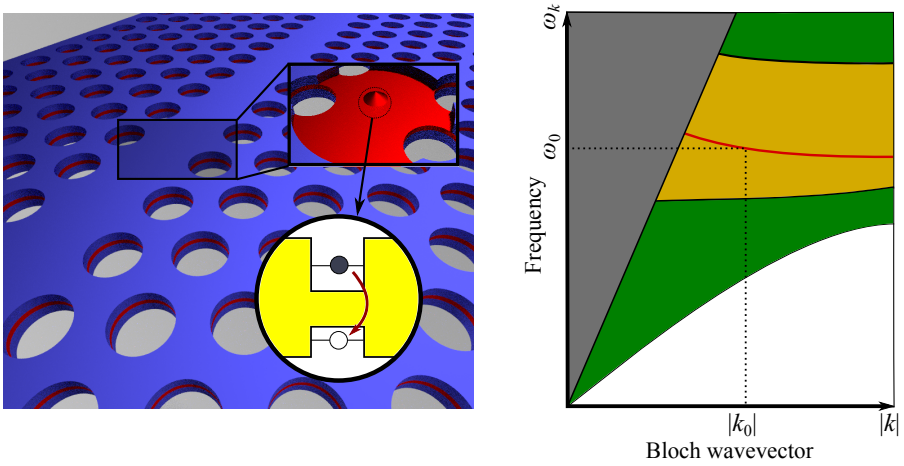

Figure 3.1: (Left) Illustration of a TLE embedded in a one-dimensional waveguide, exemplified by a line defect in a photonic crystal slab containing a quantum dot. (Right) Schematic illustration of the corresponding band diagram showing the slab modes (green area) with a bandgap (yellow area) containing a line defect mode (red line). The resonance frequency of the emitter, ω_0, lies inside the bandgap, and we consider only propagating modes below the light cone (shaded grey).

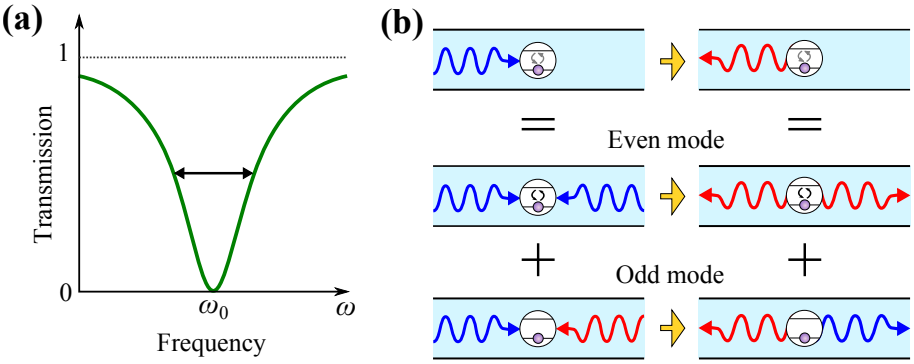

Figure 3.2: (a) Transmission spectrum of a lossless TLE with transition frequency ω_0 inside the waveguide for a continuous wave with frequency ω. The spectral width of the transmission dip is proportional to the decay rate of the emitter. (b) Interference effects for a continuous wave in the case $\omega = \omega_0$, with the incoming field (left column) and the scattered field (right column). The incoming field (top row) may be expanded as a sum of and even mode (middle row) and an odd mode in the waveguide (bottom row), with the red and blue colors indication fields which are out of phase. The even mode has an anti-node at the emitter position and gains a phase shift of π upon scattering, whereas the odd mode has node and thus passes the emitter without interacting.

resonant photon pulse is fully reflected. If the emitter has a non-zero loss rate to other modes than the waveguide modes, the reflection is no longer perfectly 100 % [63].

For single-photon pulses with spectral linewidths comparable to that of the TLE, the TLE still behaves linearly, as the saturation of the TLE first plays a role if a second photon is present. Following different approaches to describe the single-photon scattering [64, 65, 66, 67], we calculate the excitation dynamics of the TLE for input single-photon pulses with different spectra, and we determine the resulting scattering probabilities. We demonstrate how the incoming pulse is mostly affected by the emitter when the pulse spectrum is as narrow as possible for resonant excitation, as this would reflect the pulse fully. The emitter, however, is populated the most when the bandwidth of the pulse and the emitter linewidth are comparable, making this regime interesting for investigating the emitter non-linearity.

Lastly, we introduce a numerical scheme for solving the single-photon scattering for arbitrary pulses, which Chapter 4 will be generalized to two-photon scattering. A full understanding of the mathematical approaches and results in the single-photon case is thus important when expanding the model to considering two-photon scattering, as will be done in the next chapters.

3.1 The model

The system Hamiltonian in the Schrödinger picture for a single TLE interacting with a quantized electromagnetic field is given by Eqs. (2.6), (2.8), and (2.12), neglecting the contribution to the energy from the vacuum field, as this does not affect the system dynamics,

$$H = \hbar\omega_0 c^\dagger c + \sum_\lambda \hbar\omega_\lambda a_\lambda^\dagger a_\lambda + \hbar \sum_\lambda [g_\lambda a_\lambda c^\dagger + g_\lambda^* a_\lambda^\dagger c]. \tag{3.1}$$

Here λ is a generalised quantum number describing polarisation and propagation degrees of freedom, and each mode is described by creation and annihilation operators $a_\lambda^\dagger$ and a_λ, respectively. Furthermore $c^\dagger = c_e^\dagger c_g$ is the creation operator for an excitation of the TLE, moving an electron from the ground state to the excitated state. The transmission frequency of the emitter is denoted ω_0, and the coupling between the TLE and the optical mode λ is described by the dipole interaction by the strength g_λ from in Eq. (2.13). In Eq. (3.1) the rapidly-oscillation interaction terms containing $a_\lambda^\dagger c^\dagger$ and $a_\lambda c$ have been neglected by the rotating wave approximation, valid when the electromagnetic field has frequencies close to the emitter resonance, with low field intensities [68].

We assume that the waveguide is sufficiently small, such that it only supports a single mode (for each direction of propagation) at a specific frequency, as sketched for the photonic crystal waveguide in Fig. 3.1. In this case, the mode index λ corresponds to the continuous-mode variable k, being the wavenumber of the plane wave modes. Here $k > 0$ or $k < 0$ implies a waveguide mode propagating in the forward or backward direction, respectively. For the infinite waveguide, these modes will be plane wave modes.

With these assumptions, the sum over all modes in the waveguide reduces to $\sum_\lambda = \lim_{L\to\infty}(L/2\pi)\int_{-\infty}^{\infty}\mathrm{d}k$, with L being the length of the 1D waveguide, and $2\pi/L$ the spacing between the modes in reciprocal space. Continuous mode operators are defined as $a(k) = \lim_{L\to\infty}\sqrt{(L/2\pi)}a_\lambda$, preserving the commutator relationship $[a(k), a^\dagger(k')] = \delta(k-k')$ [69, 50]. Moreover, the continuous version of the waveguide mode frequencies and coupling strength is defined as $\omega(k) = \omega_\lambda$ and $g(k) = \lim_{L\to\infty}\sqrt{(L/2\pi)}g_\lambda$, respectively. The system Hamiltonian becomes

$$H = \hbar\omega_0 c^\dagger c + \int_{-\infty}^{\infty}\mathrm{d}k\,\hbar\omega(k)a(k)^\dagger a(k) + \hbar\int_{-\infty}^{\infty}\mathrm{d}k\,\left[g(k)a(k)c^\dagger + \mathrm{h.c.}\right], \quad (3.2)$$

with h.c. indicating a term which is the Hermitian conjugate of the previous term.

The calculations are most easily carried out in a frame rotating with a carrier frequency of the emitter, ω_0, described by the transformation $T(t) = \exp[-\mathrm{i}\omega_0 t(c^\dagger c + \sum_\lambda a_\lambda^\dagger a_\lambda)]$. The transformed Hamiltonian is given by $\tilde{H} = T^\dagger(t)HT(t) + \mathrm{i}\hbar\frac{\partial T^\dagger}{\partial t}T(t) = \tilde{H}_0 + \tilde{H}_I$, resulting in

$$\tilde{H} = \int_{-\infty}^{\infty}\mathrm{d}k\,\hbar(\omega(k)-\omega_0)a(k)^\dagger a(k) + \hbar\int_{-\infty}^{\infty}\mathrm{d}k\,\left[g(k)a(k)c^\dagger + \mathrm{h.c.}\right]. \quad (3.3)$$

The incoming photon wavepackets are assumed to have a small bandwidth (on the order of 10^9 rad s^{-1}) compared to the QD transition frequency ($\sim 10^{15}$ rad s^{-1}). This allows a linearization of the dispersion relation (for each direction of propagation), obtained by a Taylor expansion of the dispersion relation $\omega(k)$ around ω_0, see Fig. 3.1,

$$\omega(k) - \omega_0 = \left.\frac{\partial\omega}{\partial k}\right|_{k=\pm k_0}(k \mp k_0) = v_g(|k| - k_0), \quad (3.4)$$

valid for photons propagating in both directions, with $k_0 > 0$ defined such that $\omega(k_0) = \omega_0$, and with the group velocity $v_g = \frac{\partial\omega}{\partial k}|_{k=k_0}$.

3.2 A single system excitation

We consider a single excitation in the emitter-waveguide system, assuming no losses of the excitation to external reservoirs[1], which would be a reasonable approximation for the QD–photonic crystal waveguide coupling demonstrated in Ref. [45]. The system state may at all times be written as a superposition of the excitation being in one of the waveguide modes or as an electronic excitation in the emitter,

$$|\psi(t)\rangle = \int_{-\infty}^{\infty}\mathrm{d}k\,C^g(k,t)a^\dagger(k)|\phi\rangle + C^e(t)c^\dagger|\phi\rangle, \quad (3.5)$$

[1] For non-negligible loss, e.g. due to the presence of other modes or due to scattering with phonons, external reservoirs to which the system couples may be introduced. In the limit of weak coupling to a reservoir of harmonic oscillators, dissipation rates of the system states may be derived [70]. Alternatively, the dynamics may be treated using a quantum jump approach [71] or reduced density matrices [72, 73], which however are computationally more challenging.

with $|\phi\rangle$ being the quantum state with the emitter in its ground state and no photons in the waveguide. The wavefunction is normalized such that $\langle\psi(t)|\psi(t)\rangle = \int_{-\infty}^{\infty} \mathrm{d}k\, |C^g(k,t)|^2 + |C^e(t)|^2 = 1$ at all times, in the loss-free case.

The system dynamics are calculated by applying the time-dependent Schrödinger equation, $\mathrm{i}\hbar\partial_t|\psi(t)\rangle = H|\psi(t)\rangle$, and projecting onto the orthogonal states $c^\dagger|\phi\rangle$ and $a^\dagger(k')|\phi\rangle$, giving a system of coupled differential equations for the expansion coefficients,

$$\partial_t C^e(t) = -\mathrm{i}\int_{-\infty}^{\infty} \mathrm{d}k\, g(k) C^g(k,t), \tag{3.6a}$$

$$\partial_t C^g(k,t) = -\mathrm{i}[\omega(k)-\omega_0]C^g(k,t) - \mathrm{i}g^*(k)C^e(t). \tag{3.6b}$$

By formally integrating Eq. (3.6b) from an initial time t_i to t, and inserting the expression for $C^g(k,t)$ back into Eq. (3.6a), we obtain

$$\partial_t C^e(t) = -\mathrm{i}\int_{-\infty}^{\infty} \mathrm{d}k\, g(k) C^g(k,t_i)\mathrm{e}^{-\mathrm{i}[\omega(k)-\omega_0](t-t_i)} - \int_{-\infty}^{\infty} \mathrm{d}k\, |g(k)|^2 \int_{t_i}^{t} \mathrm{d}t'\, C^e(t')\mathrm{e}^{-\mathrm{i}[\omega(k)-\omega_0](t-t')}. \tag{3.7}$$

The intergrand in the last term of Eq. (3.7) may be simplified by using the assumption from the previous section that the decay rate of the emitter is much lower than the carrier frequency of the pulse. In that case, $C^e(t')$ varies slowly compared to the exponential and may be pulled outside the integral, as the integral only has non-zero contributions for $t' \approx t$. By this, the lower limit of the integration may also be expanded to $t_i \to -\infty$ without changing the value of the integral. This is well-known as the Wigner-Weisskopf approximation [74], by which the system does not have any memory of the past (also sometimes called the Markov approximation).

By complex integration, the remaining integral reduces to

$$\int_{-\infty}^{t} \mathrm{d}t'\, \mathrm{e}^{-\mathrm{i}[\omega(k)-\omega_0](t-t')} = -\mathrm{i}\mathcal{P}\left\{\frac{1}{\omega(k)-\omega_0}\right\} + \pi\delta(\omega(k)-\omega_0), \tag{3.8}$$

with $\mathcal{P}$ indicating the principal value. The first term induces a frequency shift, commonly known as the Lamb shift [50], which is omitted by including this as a re-normalization of the basic transition frequency of the emitter, ω_0. By defining the constant $\Gamma = 2\pi\int_{-\infty}^{-\infty} \mathrm{d}k\, |g(k)|^2\delta(\omega(k)-\omega_0)$, we arrive at

$$\partial_t C^e(t) = -\mathrm{i}\int_{-\infty}^{\infty} \mathrm{d}k\, g(k) C^g(k,t_i)\mathrm{e}^{-\mathrm{i}[\omega(k)-\omega_0](t-t_i)} - \frac{\Gamma}{2}C^e(t). \tag{3.9}$$

Hence, Γ is spontaneous decay rate of the emitter population, $|C^e(t)|^2$, into both propagation directions of the waveguide. Under the narrow bandwidth assumptions, $g(k)$ is approximately contrant, $g(k) \approx g(k_p) = \sqrt{\Gamma v_g/(4\pi)}$ [43].

3.2.1 Input state

To solve Eq. (3.9) we consider a incident, forward-propagating single photon as the initial condition. A single-photon state existing in a 1D continuum is in

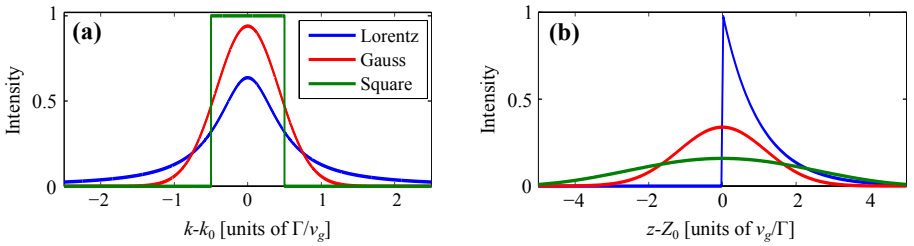

Figure 3.3: (a) Intensity spectra, $|\xi(k)|^2$, for the three single-photon wavepackets in Eqs. (3.12a)-(3.12c), here plotted for $\sigma = \Gamma/v_g$. (b) Corresponding spatial pulse profiles, $|\xi(z)|^2$, where large values of z correspond to the front part of the pulse, arriving first at the position of the emitter.

general described by the state

$$|\xi\rangle = \int_{-\infty}^{\infty} \mathrm{d}k\, \xi(k) a^\dagger(k)|\phi\rangle. \tag{3.10}$$

The state describes a superposition of excited states in the 1D continuum with the photon wavepacket $\xi(k)$, seen by applying $\langle\phi|a(k')$ from the left

$$\langle\phi|a(k')|\xi\rangle = \int_{-\infty}^{\infty} \mathrm{d}k\, \xi(k)\delta(k-k') = \xi(k'), \tag{3.11}$$

We consider three transform-limited incoming pulse shapes propagating in the forward direction, being a Lorentzian, a Gaussian, and a step-function [75, 76] pulse, which are given by the wavepackets

$$\xi_{\mathrm{Lor}}(k) = \frac{\sqrt{\sigma/(2\pi)}}{k - k_p - \mathrm{i}\sigma/2} \mathrm{e}^{-\mathrm{i}Z_0(k-k_p)}, \tag{3.12a}$$

$$\xi_{\mathrm{Gauss}}(k) = (\pi\sigma'^2)^{-1/4} \mathrm{e}^{-(k-k_p)^2/(2\sigma'^2)} \mathrm{e}^{-\mathrm{i}Z_0(k-k_p)}, \tag{3.12b}$$

$$\xi_{\mathrm{square}}(k) = \sigma^{-1/2}\theta(\sigma/2 - |k-k_p|) \mathrm{e}^{-\mathrm{i}Z_0(k-k_p)}, \tag{3.12c}$$

all with the carrier frequency $v_g k_p$, and where $\sigma' = (2\sqrt{\ln(2)})^{-1}\sigma$ for the Gaussian wavepacket, with $\theta(k)$ is the Heaviside step function. All wave packets have a full width–half maximum (FWHM) of the intensity spectrum of σ, and the wavepackets are normalised such that $\int_{-\infty}^{\infty} \mathrm{d}k\, |\xi(k)|^2 = 1$. Additionally, $Z_0 < 0$ is the position at which the pulse starts behind the emitter at $t = t_i$, with the origo of the spatial axis being at the emitter position. The intensity spectra of the input pulses are shown in Fig. 3.3 together with the spatial pulse profiles, defined as the Fourier transform $\xi(z) = (2\pi)^{-1/2} \int_{-\infty}^{\infty} \mathrm{d}k\, \xi(k) \exp[\mathrm{i}kz]$.

3.2.2 Dynamics

Assuming that the incoming single-photon wavepacket has a carrier frequency which is resonant with the emitter, and that the pulses starts infinitely far away from the pulse $Z_0 \to -\infty$, the QD excitation probability, $P_e(t) = |C^e(t)|^2$, may

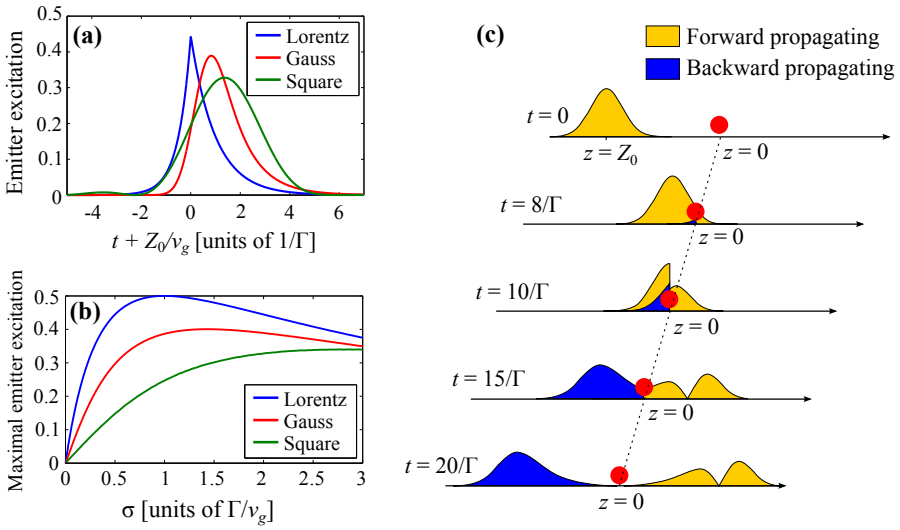

Figure 3.4: (a) Emitter excitation probability for an incoming single-photon wavepacket starting in $z = Z_0 < 0$ with $\sigma = 2\Gamma/v_g$, for the wavepackets in Eqs. (3.13a)-(3.13c), resonant with the emitter, $k_p = k_0$. (b) Maximal emitter excitation during the scattering event for incoming pulses with different values of σ, also with $k_p = k_0$. (c) Excitation density in the waveguide for light propagating in the forward (yellow) and backward (blue) direction for a Gaussian pulse scattering on the emitter at $z = 0$ (red). Figure (c) is reproduced from [77].

be determined by solving Eq. (3.9) with the initial conditions $C^g(k, t_i) = \xi(k)$ and $C^e(t_i) = 0$ for the pulse shapes in Eqs. (3.12a)-(3.12c),

$$P_e^{\mathrm{Lor}}(t) = \frac{2\Gamma v_g \sigma}{(\sigma v_g + \Gamma)^2}\left[\mathrm{e}^{\sigma v_g \tau}\theta(-\tau) + \mathrm{e}^{-\Gamma\tau}\theta(\tau)\right], \tag{3.13a}$$

$$P_e^{\mathrm{Gauss}}(t) = \frac{\sqrt{\pi}\Gamma}{4 v_g \sigma'}\mathrm{e}^{-\Gamma\tau + \Gamma^2/(4\sigma'^2 v_g^2)}\left[1 - \mathrm{erf}\left(\frac{\Gamma - 2v_g^2\sigma'^2\tau}{2\sqrt{2}\sigma' v_g}\right)\right]^2, \tag{3.13b}$$

$$P_e^{\mathrm{square}}(t) = \frac{\Gamma}{4\pi v_g \sigma}\mathrm{e}^{-\Gamma\tau}\left|E_1\left(\frac{\mathrm{i}\sigma v_g - \Gamma}{2}\tau\right) - E_1\left(\frac{-\mathrm{i}\sigma v_g - \Gamma}{2}\tau\right)\right|^2, \tag{3.13c}$$

with $\tau = t + Z_0/v_g$ being the time in a frame relative to the initial position of the pulse. Additionally, the error function is defined as $\mathrm{erf}(x) = \frac{2}{\sqrt{\pi}}\int_0^x \mathrm{d}q\, \mathrm{e}^{-q^2}$, and E_1 is the exponential integral defined as $E_1(z) = \int_1^\infty \mathrm{d}q\, \mathrm{e}^{-qz} q^{-1}$.

The excitation probabilities are illustrated in Fig. 3.4(a) for $\sigma = 2\Gamma/v_g$. Especially from the Lorentzian pulse it is apparent that the rate of dot *excitation* depends on the linewidth of the emitter, whereas the rate of the emitter *de-excitations* is determined by Γ - see also Eq. (3.13a). The maximal emitter excitation sketched in Fig. 3.4(b). The emitter is maximally excited for a Lorentzian input with $\sigma = \Gamma/v_g$, as the Lorentzian spectrum exactly corresponds to the spectrum of pulse emitter from the emitter by spontaneous emission (although time-reverted). As the square pulse has the largest mismatch between the spectrum of the emitter and the photon, the pulse energy

can never efficiently couple to the emitter and thus results in the lowest maximal emission probability for the square pulse. The maximal attainable emitter population of $1/2$ stems from the phenomenon in Fig. 3.2, as only maximally half of the photon energy may couple to the emitter.

The properties of the scattered pulse may be examined by calculating the energy distribution across the waveguide at a time t during the scattering event. We describe it by the waveguide excitation density, $N_z(z,t)$, measured in units of of inverse length. It is calculated using Eq. (3.6b), and is defined as

$$N_z(z,t) = \langle\psi(t)|a(z)a^\dagger(z)|\psi(t)\rangle \tag{3.14}$$

$$= \frac{1}{2\pi}\left|\int_{-\infty}^{\infty} \mathrm{d}k\, C^g(k,t)\mathrm{e}^{\mathrm{i}kz}\right|^2. \tag{3.15}$$

The excitation density is sketched in Fig. 3.4(c) for scattering of a Gaussian pulse. Due to the finite spatial width of the pulse (and thus non-zero bandwidth), there is a probability that the pulse scatters in both directions, and moreover the spatial pulse profile may be significantly changed by the scattering.

The scattered state may be obtained by calculating $C^g(k,t)$ for $t \to \infty$. An easier way to obtain the scattered state is, however, by exploiting that the emitter acts as linear scatterer for a single-photon packet, and thus the scattered wavepacket may be calculated by treating each frequency component of the incoming pulse individually. For an input pulse as in Eq. (3.10) which propagates in the forward direction, the wavepacket of the scattered state is

$$\begin{aligned}\xi_{\mathrm{scat}}(p) &= \int_{-\infty}^{\infty} \mathrm{d}k\, \xi(k)\left[\bar{t}(k)\delta(p-k) + \bar{r}(k)\delta(p+k)\right] \\ &= \xi(p)\bar{t}(p) + \xi(-p)\bar{r}(-p),\end{aligned} \tag{3.16}$$

where the transmission and reflection coefficients for scattering on the emitter is [66],

$$\bar{t}(k) = \frac{k-k_0}{k-k_0+\mathrm{i}\tilde{\Gamma}/2}, \qquad \bar{r}(k) = \frac{-\mathrm{i}\tilde{\Gamma}/2}{k-k_0+\mathrm{i}\tilde{\Gamma}/2}, \tag{3.17}$$

with $\tilde{\Gamma} = \Gamma/v_g$. The spectrum for the transmitted part, $|\xi(p)\bar{t}(p)|^2$, and for the reflected part, $|\xi(-p)\bar{r}(-p)|^2$, is shown in Fig. 3.5(a). The frequency components of the pulse closest to the transition energy of the emitter interact most strongly, and those at the exact frequency of the emitter ($k = k_0$) are perfectly reflected [64]. The probability the photon is scattered is obtained by integrating over all pulse frequencies, $P_{\mathrm{r}} = \int_{-\infty}^{\infty} \mathrm{d}p\, |\xi(-p)\bar{r}(-p)|^2$. For a Lorentzian input, the reflection probability becomes

$$P_{\mathrm{r,Lor}}(\Delta) = \frac{(\tilde{\Gamma}+\sigma)\tilde{\Gamma}}{(\tilde{\Gamma}+\sigma)^2 + 4\Delta^2}, \tag{3.18a}$$

with the detuning between the emitter and the pulse defined as $\Delta = k_p - k_0$. For a resonant Gaussian pulse, $\Delta = 0$,

$$P_{\mathrm{r,Gauss}}(\Delta=0) = \frac{\tilde{\Gamma}\sqrt{\pi}}{2\sigma'}\mathrm{e}^{\tilde{\Gamma}^2/(2\sigma')^2}\left[1 - \mathrm{erf}\left(\frac{\tilde{\Gamma}}{2\sigma'}\right)\right], \tag{3.18b}$$

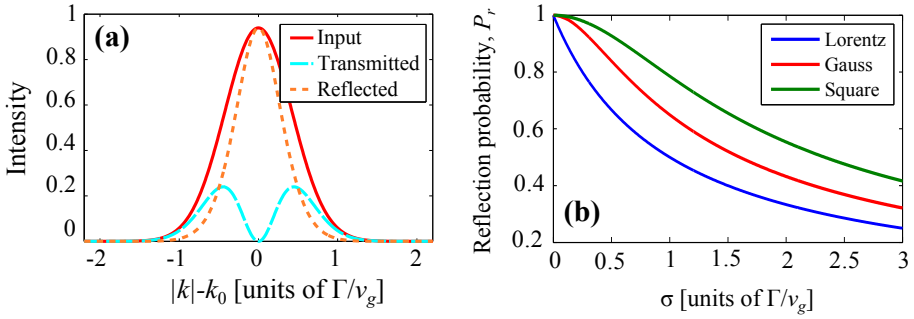

Figure 3.5: (a) Intensity spectra of an incoming Gaussian pulse, $|\xi_{Gauss}(k)|^2$, and the resulting spectra of the transmitted and reflected field, assuming resonant excitation of the emitter, $\Delta = 0$, and $\sigma = 1\,\Gamma/v_g$. (b) Reflection probabilities as a function of the bandwidth, σ, for the three pulses in Eqs. (3.12a)-(3.12c).

and for a square pulse

$$P_{\mathrm{r,square}}(\Delta) = \frac{\tilde{\Gamma}}{2\sigma}\left[\arctan\left(\frac{2\Delta+\sigma}{\tilde{\Gamma}}\right) - \arctan\left(\frac{2\Delta-\sigma}{\tilde{\Gamma}}\right)\right]. \tag{3.18c}$$

A comparison of the resulting reflection probabilities is shown in Fig. 3.5(b) for each of the three single-photon wavepackets in Eqs. (3.12a)-(3.12c). As σ decreases, a larger part of the pulse interacts strongly with the emitter, increasing the reflection probability, and P_r reaches unity for resonant monochromatic pulses ($\sigma \to 0$). In the opposite limit of $\sigma \to \infty$, only a vanishing fraction of frequency components overlap with the spectrum of the emitter, resulting in complete transmission since the pulse does not interact with the emitter. Since the Lorentzian has the largest spread of frequency components for a given FWHM, it interacts least with the emitter and correspondingly results in the lowest reflection probability for a given σ for the three considered pulses.

3.3 Numerical Implementation

In order to calculate the dynamics for an arbitrary input, we propose a scheme to solve Eqs. (3.6a) and (3.6b) numerically, see Appendix B for details. The continuum of waveguide modes is discretized into N discrete plane wave modes divided into two sub-intervals; with $N/2$ of the points centered around $-k_0$ and the other half around k_0. This is sufficient as only modes with $|k|$ close to ω_0/v_g interacts with the emitter. In these sub-intervals, the grid points are equidistantly with the spacing dk. With this discretization, Eqs. (3.6a) and (3.6b) now constitute a system of coupled linear differential equations.

Several numerical approaches exits to solve a large systems of coupled linear differential equations. When determining the full temporal evolution of the system, we implement a standard explicit Runge–Kutta (4,5) stencil [78]. In order to obtain the long-time dynamics of the state without being concerned about the intermediate dynamics, the Arnoldi method is useful, which is an

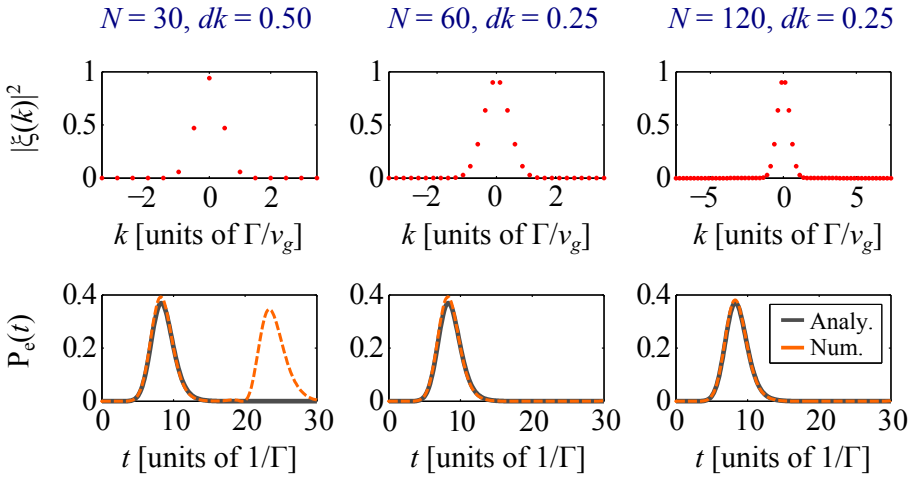

Figure 3.6: Each column correspond to a solution with N and dk (in units of $\tilde{\Gamma}$) shown above each column. (Top row) Discretized spectral wavepacket of the input pulse. (Bottom row) Calculated emitter excitation using the Runge–Kutta stencil (solid line) and the analytical solution from Eq. (3.13b) (dashed line). In all simulations, $\sigma = 1\,\tilde{\Gamma}$, $\Delta = 0$.

iterative technique used to approximate the eigenvalues of large sparse matrices [79, 80].

An example calculation of the emitter excitation probability is sketched in Fig. 3.6 for various choices of N and dk, where dk at least must be smaller than the bandwidth of the pulse to resolve it properly. In the first column of Fig. 3.6 we see that only a few points in k-space ($N = 30$) actually catches the dynamics quite well at small times. At higher times, the QD is re-excited in the numerical simulation, due to an insufficient calculation domain: When discretizing the k-modes in an infinite waveguide, this corresponds to chopping the waveguide down to a finite length of $l = 2\pi/dk$ with periodic boundary conditions. The pulses emitted by the QD has propagated through the numerical boundaries and reappears at the QD after a time $t_{\text{reapp}} = 2\pi/(dk \cdot v_g)$, which gives an indication of the upper time limit for which the numerical simulations are valid. In the second column of Fig. 3.6, dk is decreased while keeping $N \cdot dk$ constant, i.e. doubling t_{reapp}, and thus the numerical result is valid within the shown temporal domain.

A deviation appears between the numerical and the analytic result in the first two examples in Fig. 3.6 due to numerical inaccuracies. By keeping dk constant but increasing N, the width of the calculation domain increases, as from the second to the third column in Fig. 3.6, and we get a result closer to the analytic expression for the emitter excitation. This is analyzed in detail in Fig. 3.7, which illustrates the relative deviation in the maximal emitter population between the numerical result and the analytic from Eq. (3.13b) for varying N and dk. It is clearly seen that the error is minimized when the product $N \cdot dk$ is maximized, i.e. when maximizing the span of k-modes. This is due to the fact that the discretized k-array has a finite span, and

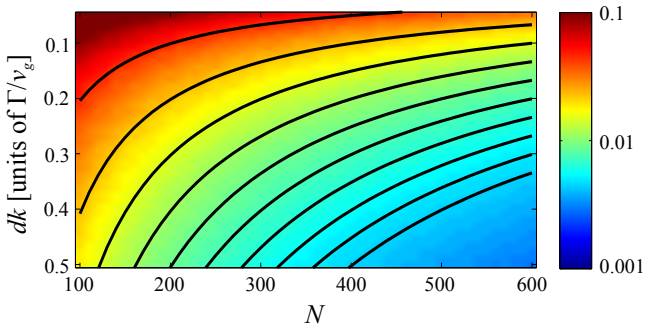

Figure 3.7: Relative deviation between the maximum emitter excitation obtained by the numerical and analytical solution for simulations with varying N and dk. The black lines are contours for constant values the span of the calculation domain which is $\sim N \cdot dk$.

thus we numerically omit modes, into which the emitter could decay. This is also explains why the numerical result always gives a higher maximal emitter excitation compared to the analytic value, as some decay channels are "missing" in the numerical implementation.

Thus, the choice of N and σ has to be with a sufficiently high σ to resolve the temporal dynamics properly, but this also implies a high N such that the normalization condition is obeyed.

3.4 Summary

In this chapter we have described the dynamics of a quantum system in which a single-photon pulse scatters on a lossless, two-level emitter inside an infinite one-dimensional waveguide using standard approaches [64, 66, 67]. The results are valid under the rotating wave approximation and under the Wigner–Weisskopf approximation, by which the emitter is assumed to have no memory of its past.

We have demonstrated how to determine analytical expression for the temporal evolution of the emitter population for input photons with a Gaussian, a Lorentzian and a square-shaped intensity spectrum. With the transmission and reflection matrix elements for a single emitter [66], we determined analytic expressions for the transmission and reflection probabilities. The pulse is affected the most by the emitter, if the linewidth of the pulse is much smaller than the emitter linewidth, in which case a resonant pulse would be fully reflected by the emitter. The emitter is, however, exited the most, when the bandwidth of the input pulse matches the linewidth of the emitter. This becomes important in system where the emitter non-linearity is to be exploited. One downside with this setup is, however, that these pulses have a non-zero probability of propagating being scattered into both directions of the waveguide, which may complicate implementation in optical gates. But, as we will demonstrate later in the thesis, there are different ways to circumvent this, e.g. by placing the emitter close to the end facet of a waveguide [64].

The possibilities with the emitter–waveguide systems are rich, and several functionalities of emitter–waveguide systems have been discussed, such as a single-photon router by using multiple emitters and waveguides [81]. For emitters with more than two energy levels [82], proposals have been made using the waveguide–emitter systems as single-photon frequency converters [83] and single-photon transistors [43, 84]. Furthermore the approaches demonstrated in this chapter may also be used to analyze more advanced scatterers such as waveguides interacting with emitters inside optical cavities [85, 86].

With this detailed understanding of the single-photon scattering, we proceed to considering two-photon scatting in the following chapters. Due to the saturability of the emitter, the two-photon scattering dynamics becomes much more complex. In Chapter 4 the scattering is examined using the numerical scheme from Section 3.3, supported by analytical calculations of the emitter excitation for two uncorrelated, Gaussian pulses, using an approach similar to the approach in Section 3.2. The transmission properties are specifically considered in Chapter 5, using the scattering matrix formalism [66], in which non-linear two-photon scattering matrix elements are introduced.

Chapter 4

Two-photon scattering — Wavefunction approach

4.1 Introduction

A model for describing two-photon scattering on a two-level emitter is developed in this chapter, as an extension of the single-excitation results from Chapter 3. The dynamics of two-photon scattering is, however, much more complex than the single-photon case, as the non-linear emitter can induce correlations between the photons caused by elastic multi-photon scattering processes [66, 87]. Existing methods for analyzing the multiple-photon scattering problem — such as the input-output formalism [66], the real-space Bethe ansatz [87, 88], or the Lehmann-Symanzik-Zimmermann formalism [89] — focus on the long-time limit of the scattered state [67] and necessitate the computation of complicated scattering elements or Laplace transforms [90]. Another recent approach demonstrates a master equation formalism derived by starting from the Itō Langevin equation, where also the emitter excitation is calculated [72], although without relating the emitter excitation to the scattering-induced correlations. Some specific considerations have been demonstrated using a wavefunction description of the system [91], e.g. the demonstration of stimulated emission of an emitter inside a waveguide [92], and scattering of a two-photon wavepacket in a photonic tight-binding waveguide [93, 94, 95]. Applications which utilize a TLE nonlinearity have been proposed, such as photon sorters and Bell state analyzers [96]. In all these cases the non-linearity of the emitter leads to rich scattering dynamics and scattering-induced correlations. It is the interplay between these highly non-trivial scattering properties and the excitation dynamics of the emitter which we seek to clarify in this chapter.

To do so we study two-photon scattering on a quantum emitter in a one-dimensional waveguide using a wavefunction approach as introduced in Chapter 3, in which the entire system state is explicitly calculated at all times during the scattering process, and which therefore provides a detailed picture of the scattering dynamics. This approach relies on a direct solution of the Schrödinger equation by expanding the complete state in a basis formed by

the TLE and the optical waveguide modes. This allows us to explore varying widths and separations of the incoming photons, and provides a convenient and detailed visualization of the temporal dynamics of the scattering process. As a special case, we show that the approach agrees with the above-mentioned methods in the post-scattering limit, discussed further in Chapter 5. For co-propagating pulses, we find that the transmission properties of the emitter depend crucially on the pulse width and separation, with closer spaced pulses giving rise to a larger proportion of scattered light. For counter-propagating coincident pulses we find that the non-linearity of the emitter can give rise to significant pulse-dependent directional correlations in the scattered photonic state. These correlations can be detected by a reduction in coincident clicks in a Hong-Ou-Mandel measurement setup, analogous to a linear beam splitter. Thus, the emitter may act as a non-linear beam-splitter, but only in the regime where the spectral width of the photon pulses is similar to the emitter decay rate.

This chapter is structured as follows: In Section 4.2 we introduce the two-excitation model and formalism as an extension of the model in Chapter 3. In Section 4.3 we analyse the scattering dynamics for two co-propagating photon pulses; we examine how the properties of the scattered state depend on the emitter excitation and consider the scattering-induced correlations between the photons. In Section 4.4 we study scattering of counter-propagating pulses, elucidating the analogy of the quantum emitter and a non-linear beam-splitter.

The chapter is based on the journal publication *Scattering of two photons on a quantum emitter in a one-dimensional waveguide: exact dynamics and induced correlations.* New Jour. Phys. **17**, 023030 (2015) by A. Nysteen, P. T. Kristensen, D. P. S. McCutcheon, P. Kaer, and J. Mørk.

4.2 Two-excitation model

The model dynamics are described by the Hamiltonian derived in Eq. (3.3) in a frame rotating with the carrier frequency of the emitter,

$$\tilde{H} = \int_{-\infty}^{\infty} \mathrm{d}k\, \hbar(\omega(k)-\omega_0)a(k)^\dagger a(k) + \hbar\int_{-\infty}^{\infty} \mathrm{d}k\, \left[g(k)a(k)c^\dagger + \mathrm{h.c.}\right], \quad (4.1)$$

where $\omega(k)$ is given by the Taylor expansion in Eq. (3.4), with $k > 0$ ($k < 0$) describing propagating in the forward (backward) direction which in this example is the right (left) direction in the waveguide. As discussed in Chapter 3, experimentally high coupling rates between a QD a photonic crystal waveguide makes it reasonable to omit losses in the calculations [45]. This allows us to expand a general state of the system in a basis spanned by all the possible system states containing two excitations. The two-excitation basis states are $a^\dagger(k_1)a^\dagger(k_2)|\phi\rangle$ and $a^\dagger(k)c^\dagger|\phi\rangle$, with the former describing two excited plane wave modes with wavevectors k_1 and k_2, and the latter describing the states where the emitter is in its excited state and a single waveguide mode with

wavevector k is excited. The total state at time t is written as

$$|\psi(t)\rangle = \frac{1}{\sqrt{2}}\int_{-\infty}^{\infty} \mathrm{d}k_1 \int_{-\infty}^{\infty} \mathrm{d}k_2\, C^{\mathrm{g}}(k_1,k_2,t)a^\dagger(k_1)a^\dagger(k_2)|\phi\rangle + \int_{-\infty}^{\infty} \mathrm{d}k\, C^{e}(k,t)a^\dagger(k)c^\dagger|\phi\rangle \tag{4.2}$$

where the expansion coefficients $C^{\mathrm{g}}(k_1,k_2,t)$ and $C^{e}(k,t)$ are in the rotating frame, and $|\phi\rangle$ indicates the emitter ground state and vacuum state of the waveguide. We note that since the photons are fundamentally indistinguishable, $[a^\dagger(k),a^\dagger(k')]=0$, (and indeed $a^\dagger(k_1)a^\dagger(k_2)|\phi\rangle = a^\dagger(k_2)a^\dagger(k_1)|\phi\rangle$), the coefficients of the two-photon terms must be symmetric, $C^{\mathrm{g}}(k_1,k_2,t) = C^{\mathrm{g}}(k_2,k_1,t)$. Normalization of the state requires

$$\langle\psi(t)|\psi(t)\rangle = \int_{-\infty}^{\infty} \mathrm{d}k_1 \int_{-\infty}^{\infty} \mathrm{d}k_2\, |C^{\mathrm{g}}(k_1,k_2,t)|^2 + \int_{-\infty}^{\infty} \mathrm{d}k\, |C^{e}(k,t)|^2 = 1, \tag{4.3}$$

and we can interpret $\int_{-\infty}^{\infty}\mathrm{d}k\,|C^e(k,t)|^2$ as the probability that the TLE is measured in its excited state, while the probability of measuring two photons in modes of index k_1 and k_2 for $k_1\neq k_2$ is $2|C^{\mathrm{g}}(k_1,k_2,t)|^2$, and $|C^{\mathrm{g}}(k_1,k_1,t)|^2$ for $k_1=k_2$.

Inserting Eq. (4.2) into the time-dependent Schrödinger equation, and using the Hamiltonian in Eq. (4.1) leads to a system of coupled differential equations for the expansion coefficients, analogously to the single photon case in Eqs. (3.2),

$$\partial_t C^{\mathbf{e}}(k,t) = -\mathrm{i}\Delta\omega(k)C^{\mathbf{e}}(k,t) - \mathrm{i}\sqrt{2}\int_{-\infty}^{\infty}\mathrm{d}k'\, g(k')C^{\mathrm{g}}(k,k',t), \tag{4.4a}$$

$$\partial_t C^{\mathrm{g}}(k_1,k_2,t) = -\mathrm{i}[\Delta\omega(k_1)+\Delta\omega(k_2)]C^{\mathrm{g}}(k_1,k_2,t) - \frac{\mathrm{i}}{\sqrt{2}}\big[g^*(k_1)C^{\mathbf{e}}(k_2,t) + g^*(k_2)C^{\mathbf{e}}(k_1,t)\big]. \tag{4.4b}$$

By discretizing the k-continuum of modes as described in Section 3.3, Eqs. (4.4a) and (4.4b) become a system of coupled linear differential equations. In general we solve Eqs. (4.4a) and (4.4b) numerically using the scheme in Section 3.3 – see Appendix B for details about the numerical implementation. In specific cases, Eqs. (4.4a) and (4.4b) may be solved analytically, e.g. when examining stimulated emission from a TLE [92, 97].

We note that in contrast to the linear nature of the discretized equations, the Heisenberg equations of motion for the system operators used in the scattering matrix approach result in a set of coupled nonlinear differential equations, whose solution must instead be obtained using e.g. the input–output formalism [66].

4.2.1 Two-photon input state

Eqs. (4.4a) and (4.4b) can in principle be solved for any initial state of the total system containing two excitations. We build onto the aforementioned

models for investigating stimulated emission [92, 97] by employing two single-photon pulses in the waveguide as the initial condition, and we investigate their scattering on the TLE for various pulse widths and separations. The two-photon input states can be experimentally produced using, for example, parametric down-conversion, as has been demonstrated [98, 99, 100]. In general, such a process creates two correlated photons, but the properties of the down-conversion crystal can be modified in such a way that uncorrelated photons are produced [101].

The general form of a two-photon state is written as

$$|\beta\rangle = \frac{1}{\sqrt{2}} \int_{-\infty}^{\infty} \mathrm{d}k \int_{-\infty}^{\infty} \mathrm{d}k' \, \beta(k,k') a^\dagger(k) a^\dagger(k') |0\rangle, \tag{4.5}$$

with $\beta(k,k')$ the two-photon wavepacket given in two-dimensional k-space. The bosonic nature of the photons implies symmetry of the two-photon wavepacket, $\beta(k,k') = \beta(k',k)$, and the normalisation condition is then

$$\langle\beta|\beta\rangle = \int_{-\infty}^{\infty} \mathrm{d}k \int_{-\infty}^{\infty} \mathrm{d}k' \, |\beta(k,k')|^2 = 1. \tag{4.6}$$

If we assume an initial condition corresponding to two photons described by Eq. (4.5), by comparison with Eq. (4.2), we find the corresponding initial conditions for the wavefunction coefficients $C^{\mathrm{e}}(k,0) = 0$ and $C^{\mathrm{g}}(k,k',0) = \beta(k,k')$.

We define a general symmetric two-photon Gaussian state as $\beta(k,k') = K\left[\beta_0(k,k') + \beta_0(k',k)\right]$ with

$$\beta_0(k,k') = f\big(k - k_{\mathbf{p},1} + k' - k_{\mathbf{p},2}\big)\xi_1(k)\xi_2(k'), \tag{4.7}$$

where $\xi_i(k) = {\sigma_i'}^{-1/2}\pi^{-1/4} \exp\left[-\mathrm{i}Z_{0,i}(k - k_{\mathbf{p},i}) - (k - k_{\mathbf{p},i})^2/(2{\sigma_i'}^2)\right]$ is a Gaussian single-photon wavepacket as defined in Eq. (3.12b). It has a FWHM of the intensity spectrum of $\sigma_i = 2\sqrt{\ln(2)}\sigma_i'$, $Z_{0,i}$ as the initial position of the pulse center, and where positive or negative $k_{\mathbf{p},i}$ corresponds to a wavepacket propagating to the right (forward) or left (backward), respectively. K is a normalization parameter, and $f(k,k')$ is a function describing phase matching, which for simplicity may be assumed to be a Gaussian, $f(k) = \exp\left[-k^2/(2{\sigma_p'}^2)\right]$ [102]. The correlation between the two photons is described by the parameter σ_p', which for parametric down-converted photons corresponds to the bandwidth of the pump laser [102]. The correlation parameter σ_p' is inversely proportional to the correlation length between the photons, and thus $\sigma_p' \to \infty$ corresponds to fully uncorrelated photons, and in such a case $\beta_0(k,k')$ factorizes into two single-photon wavepackets. We also define the real-space representation of the two-photon wave-packet by the Fourier transform

$$\beta(z,z') = \frac{1}{2\pi} \int_{-\infty}^{\infty} \mathrm{d}k \int_{-\infty}^{\infty} \mathrm{d}k' \, \beta(k,k') \mathrm{e}^{\mathrm{i}kz + \mathrm{i}k'z'}. \tag{4.8}$$

In addition to the two-photon wavepacket, described by the functions $\beta(k,k')$ and $\beta(z,z')$, it is also useful to define the expectation value of the photon

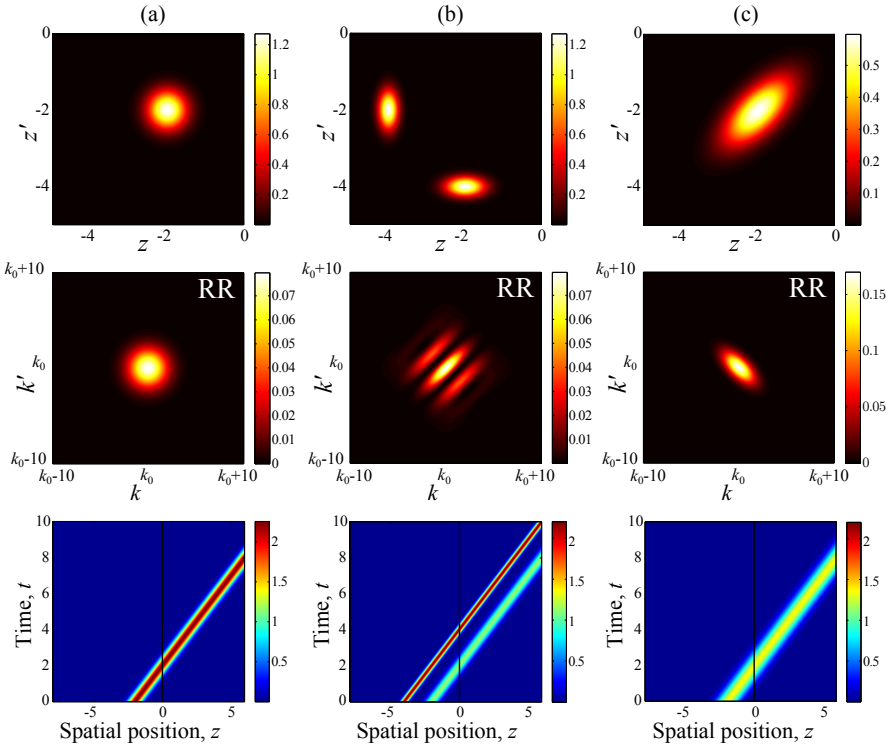

Figure 4.1: Absolute value of the two-photon wavepacket in real space, $|\beta(z,z')|$ (upper row), in reciprocal space, $|\beta(k,k')|$ (middle row), and the photon density $N(z,t)$ (lower row) for three different two-photon states, and with no emitter positioned in the waveguide. The three columns correspond to initial photonic states which are co-propagating coincident uncorrelated pulses of equal width ($\sigma_1' = \sigma_2' = 2$, $Z_{0,1} = Z_{0,2} = -2$, and $\sigma_p' \to \infty$, column (a)), uncorrelated spatially separated pulses of unequal widths ($\sigma_1' = 2$, $\sigma_2' = 4$, $Z_{0,1} = -2$, $Z_{0,2} = -4$, and $\sigma_p' \to \infty$, column (b)), and coincident highly correlated pulses of equal width ($\sigma_1' = \sigma_2' = 2$, $Z_{0,1} = Z_{0,2} = -2$, and $\sigma_p' = (3/4)\sigma_1'$, column (c)).

density at a time t and position z as $N_z(z,t) = \langle\psi(t)|a^\dagger(z)a(z)|\psi(t)\rangle$, where $a(z) = (2\pi)^{-1/2}\int \mathrm{d}k\, a(k)\mathrm{e}^{\mathrm{i}kz}$ annihilates a photon at position z, equivalent to the single-photon definition in Eq. (3.15). In terms of the wavefunction coefficients, the explicit form of $N_z(z,t)$ is given by

$$N_z(z,t) = 2\int_{-\infty}^{\infty}\mathrm{d}k\left|\frac{1}{\sqrt{2\pi}}\int_{-\infty}^{\infty}\mathrm{d}k'\, C^{\mathrm{g}}(k,k',t)\mathrm{e}^{\mathrm{i}k'z}\right|^2 + \left|\frac{1}{\sqrt{2\pi}}\int_{-\infty}^{\infty}\mathrm{d}k\, C^{\mathbf{e}}(k,t)\mathrm{e}^{\mathrm{i}kz}\right|^2. \tag{4.9}$$

Since a lossless system is assumed, the number of excitations is conserved, implying $\int_{-\infty}^{\infty}\mathrm{d}z\, N(z,t) = 2$ at all times.

To gain some intuition as to how these three descriptions of the two-photon state appear, we first consider three different input states in the waveguide containing no TLE (such that wavepackets propagate along the waveguide but no other dynamics are present). The three rows in Fig. 4.1 correspond to the absolute value of the initial real-space photon wavepacket $|\beta(z,z')|$, the initial k-space wavepacket $|\beta(k,k')|$, and the photon density as a function of time $N(z,t)$, for input states which correspond to two coincident uncorrelated photons of equal width column (a), two spatially separated uncorrelated photons of different width column (b), and two coincident highly-correlated photons column (c). We note that in comparing columns (a) and (b), the separated nature of the two pulses in (b) is clearly visible, as too is the inequality of the two pulse widths, as is evident from the elliptical shape of the wavepactet amplitudes in the top row. We also see oscillations appearing the k-space representation for the spatially separated pulses in column (b). These oscillations have a period $|Z_{0,1} - Z_{0,2}|^{-1}$ and are a signature of interference between the two separated pulses. For the correlated pulses in column (c) we see that the wavepacket is elongated along the diagonal line $z = z'$ in real-space, and along the $k = -k'$ direction in frequency space. This means that position measurements of the two photons will share positive correlations, whereas frequency measurements will be anti-correlated. Finally, we note that the photon density plots in the lower row provide us with an overall picture of the dynamics for all times, but do not capture all the features present in the photon wavepackets.

4.3 Co-propagating pulses

We now turn to the main focus of this chapter, and consider the evolution of the two photon state as it scatters on a TLE placed inside the waveguide. In order to solve Eqs. (4.4a) and (4.4b), we discretize the continuum of waveguide modes and numerically solve the resulting finite set of differential equations, as described in Appendix B. In the following calculations we assume frequency-independent coupling constants, $g(k) = g$, which is well justified owing to the assumption that the TLE linewidth is narrow compared to the carrier frequency of the wavepackets, as discussed in Chapter 3; in general, the numerical approach employed here may handle frequency dependent coupling constants and more complex dispersion relations.

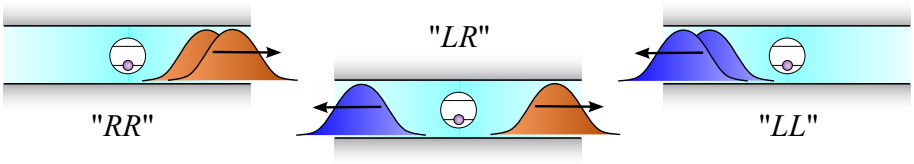

Figure 4.2: Illustration of the three possible scattering outcomes for the propagations of the scattered photons, where each pulse may propagate either in the right, "R", or left, "L", direction.

Convergence tests were carried out by comparison with the scattering properties of a single photon from the previous chapter for two temporally separated photons. For two identical coincident photons, we determine an analytical expression for the emitter population at all times. The approach is similar to the analytical approach in Chapter 3, and exploits distinguishing slowly and fast oscillating terms in the differential equations for the expansion coefficients as in the Wiegner–Weisskopf approximation. The derivation is based on a method presented in Refs. [91, 92] but is rather lengthy, so we refer to Appendix A for further details. We determine the emitter population for two co-propagating Gaussian pulses analytically, and this results is used to perform convergence-checks of the numerical implementation, see Section B.2 for details. In the long-time limit our results agree with the scattering matrix approach of Refs. [66, 67], which we describe in detail in Chapter 5.

In all plots, parameters with units of time or length are normalized to Γ^{-1} and v_g/Γ respectively. A pulse with a spectral width of $\sigma' = 1$ thus corresponds to a spatial width of $\sigma' = v_g/\Gamma$.Finally, for plotting in z-space, we used a frequency of $\omega_0 = 10^{15}$ s^{-1}.

4.3.1 Scattering dynamics

As an illustrative example of two-photon scattering, we first consider the scattering of two identical, coincident and uncorrelated single-photon pulses with carrier frequencies resonant with the TLE. Except for the inclusion of a TLE here, the input is identical to that of column (a) in Fig. 4.1; both photons are initially located left of the TLE, $Z_{0,1} = Z_{0,2} < 0$, and propagate to the right, $k_{p,1} = k_{p,2} > 0$. The scattered states are divided into three sub-categories: both being in the region right of the TLE, "RR", one on each side, "LR", and both photons to the left of the TLE, "LL", as sketched in Fig. 4.2.

The resulting dynamics are shown in Fig. 4.3. The spatial photon density, $N_z(z,t)$, is illustrated in the left of Fig. 4.3, and it represents the expectation value of position measurements of the two photons over many scattering events. We see that part of the energy is transmitted, and part is reflected. On the incoming side of the emitter ($z < 0$), a standing wave pattern is clearly visible, which is a result of interference between the incoming and reflected part of the pulse.

The upper row on the right shows the evolution of the spatial wavepacket at three representative times, corresponding to the onset of the scattering $t = 3.0$,

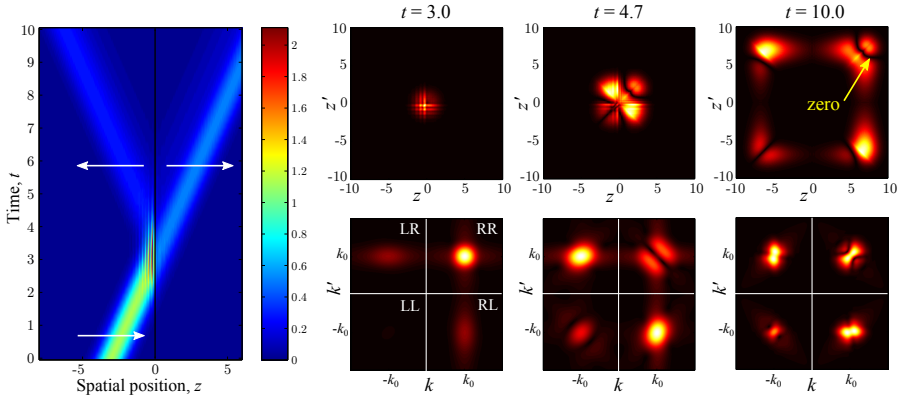

Figure 4.3: Left: Photon density, $N_z(z,t)$ for an initially uncorrelated ($\sigma_p' \to \infty$) coincident two-photon state scattering on an emitter placed at $z = 0$, using widths $\sigma_1' = \sigma_2' = 1$ and initial centre positions $Z_{0,1} = Z_{0,2} = -3$. The position of the emitter at $z = 0$ is indicated by the black solid line. Right: Absolute value of the two-photon wavepacket shown at three representative times during the scattering event, both in z-space (upper row) and k-space (lower row). In the k-space plots, we show only the regions centred around $k, k' = \pm k_0$, which we label LL (origin $(-k_0, -k_0)$), RR (origin (k_0, k_0)), LR (origin $(-k_0, k_0)$), and RL (origin $(k_0, -k_0)$).

during the scattering $t = 4.7$, and in the post-scattering long-time limit $t = 10.0$. We notice that after the scattering event, both photons clearly propagate away from the TLE as expected. An equivalent conclusion may also be drawn from the wavepacket in k-space as shown in the lower row of Fig. 4.3, where the scattered field has components propagating in the "RR", "LR", or "LL" directions. Due to the bosonic nature of the photons, the configurations "LR" and "RL" cannot be distinguished. At early times, e.g. at $t = 3.0$ in Fig. 4.3, the scattering is dominated by single photon processes, which can be seen by the fact that the two-photon wavepacket is elongated along the k and k' axes. This means that only a single photon has been broadened by its interaction with the TLE emitter, whilst the other remains unchanged. At larger times, features of two-photon scattering processes appear, which can be seen by the more complex shapes of the two-photon wavepackets. We discuss these features in more detail below.

It is interesting to compare the scattering dynamics in Fig. 4.3 with the case of two pulses which are sufficiently separated in space such that the TLE excitation induced by the first pulse has essentially decayed before the arrival of the second pulse. This is shown in Fig. 4.4, and in this case the scattering behaviour resembles two 'copies' of the single-photon scattering case [64]. Even though the carrier frequency of the pulse is resonant with the TLE, a non-zero transmission is obtained in this single-photon scattering limit because of the finite temporal widths of the input pulses. These features are in contrast to

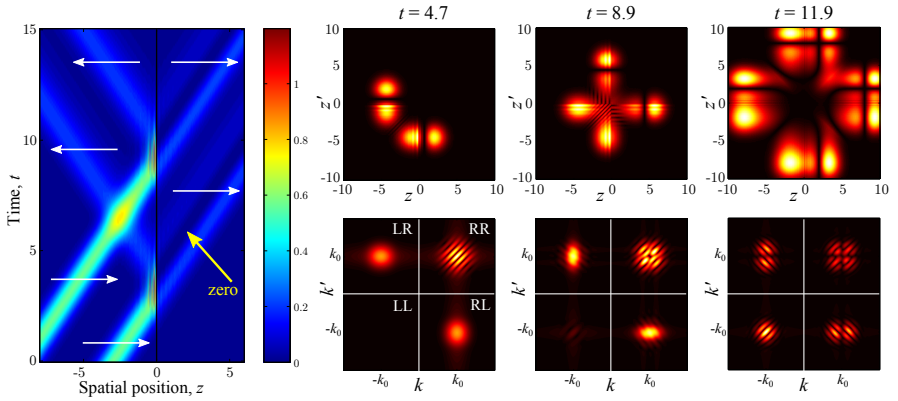

Figure 4.4: Left: Photon density, $N_z(z,t)$ for an uncorrelated ($\sigma_p' \to \infty$) two-photon state scattering on the emitter placed at $z = 0$, using widths $\sigma_1' = \sigma_2' = 1$ and initial centre positions $Z_{0,1} = -3$ and $Z_{0,2} = -9$. The position of the emitter at $z = 0$ is indicated by the black solid line. Right: Absolute value of the two-photon wavefunction shown at three different times during the scattering event, both in z-space (upper row) and k-space (lower row). In the k-plots, only the regions centred around $k, k' = \pm k_0$ are shown.

the case in which a spectrally narrow continuous wave pulse is incident on the emitter, which gives zero transmission on resonance because of destructive interference between the scattered and input fields [70, 85]. In this single-photon scattering limit, the TLE fully reflects frequency components of the incoming pulse which are close to the TLE resonance, as no two-photon processes are apparent. Hence, the spectrum of the transmitted pulse does not contain components at these frequencies, see e.g. the spectrum in Fig. 4.4 at $t = 11.9$. This is in contrast to the coincident case in Fig. 4.3, where two-photon processes allow for transmission of pulse components close to the TLE resonance.

During the initial phase of the scattering, the k-space wavefunctions in both Fig. 4.3 and Fig. 4.4 broaden and demonstrate interaction with states which are detuned from the TLE by several TLE linewidths. This may be seen at times $t = 3.0$ and $t = 4.7$ in Fig. 4.3, but these frequencies do not appear in the final scattered state at $t = 10.0$. This phenomenon may be understood as arising from the energy-time uncertainty relation, as processes taking place at short times allow for larger uncertainties in energy. Lastly, for the case of spatially separated pulses in Fig. 4.4, a dip is present in the transmitted waveguide excitation. This feature is a consequence of destructive interference between the initial photon wavepacket and the emitted photon, and manifests in the form of a dip in the spectrum of the transmitted pulse at the emitter transition frequency [64]. This dip is not apparent in the plot of $N(z,t)$ for the case of two initially coincident pulses in Fig. 4.3, but is present in the two-photon wavepacket in z-space as indicated for $t = 10.0$. Physically, it means that a photon may be detected at a position corresponding to the dip, but

if the first photon is detected there, the probability of detecting the second photon at that position is zero, exemplifying that the single-photon scattering features manifest themselves in two-photon scattering, although they may not be apparent from the photon density $N(z,t)$.

To summarise, we have illustrated the full scattering dynamics of two photons on a TLE by calculating the total system state at all times. For well-separated uncorrelated single-photon pulses, the dynamics may be well approximated by the single-photon results [64]. As the displacement between the pulses becomes smaller, non-trivial dynamics can be induced due to the saturation of the TLE. The approach we use here naturally accommodates this regime of two photon scattering.

4.3.2 Transmission and reflection properties

In order to investigate the transmission properties of the TLE, we consider the relative number of photons propagating to the left and right during the scattering process. We can calculate the total number of photons propagating to the right as

$$N_{\mathrm{R}}(t) = \int_0^\infty \mathrm{d}k\, \langle\psi(t)|a^\dagger(k)a(k)|\psi(t)\rangle \tag{4.10}$$

$$= 2\int_0^\infty \mathrm{d}k \int_{-\infty}^\infty \mathrm{d}k'\, |C^{\mathrm{g}}(k,k',t)|^2 + \int_0^\infty \mathrm{d}k\, |C^{\mathbf{e}}(k,t)|^2, \tag{4.11}$$

while the total number propagating to the left, is given by a similar expression with the integration range over k changed to $]-\infty, 0]$,

$$N_{\mathrm{L}}(t) = \int_{-\infty}^0 \mathrm{d}k\, \langle\psi(t)|a^\dagger(k)a(k)|\psi(t)\rangle. \tag{4.12}$$

The excitation probability of the TLE is given by

$$P_{\mathbf{e}}(t) = \langle\psi(t)|c^\dagger c|\psi(t)\rangle = \int_{-\infty}^\infty \mathrm{d}k\, \left|C^{\mathbf{e}}(k,t)\right|^2, \tag{4.13}$$

and normalization of the total state ensures $N_{\mathrm{R}}(t) + N_{\mathrm{L}}(t) + P_{\mathbf{e}}(t) = 2$; there is a total of two excitations in the system at all times. We therefore define the *relative* transmission to the right and left as $T_{\mathrm{R}}(t) = N_{\mathrm{R}}(t)/2$ and $T_{\mathrm{L}}(t) = N_{\mathrm{L}}(t)/2$.

In Fig. 4.5(a) we show the left and right transmission coefficients, together with the TLE excitation as a function of time, for the two cases of perfectly overlapping (solid) and non-overlapping pulses (dashed) introduced in Figs. 4.3 and 4.4 respectively. From these plots a clear reduction in the reflective nature of the TLE when the two pulses are coincident is evident, clearly illustrating that the first photon induces partial transparency in the TLE, minimising the interaction between the TLE and the second photon[1]. Also evident is a temporal delay between excitation of the TLE and the accumulation of the reflected

[1] Due to the symmetry, the maximum achievable TLE excitation for a single-pulse excitation from a single side is 1/2, as discussed with Fig. 3.2(b). A value of 1/2 is only obtained for a pulse with a temporal shape which is exactly the inverse of a pulse emitted by the TLE [103]. Such a pulse would render the TLE completely transparent.

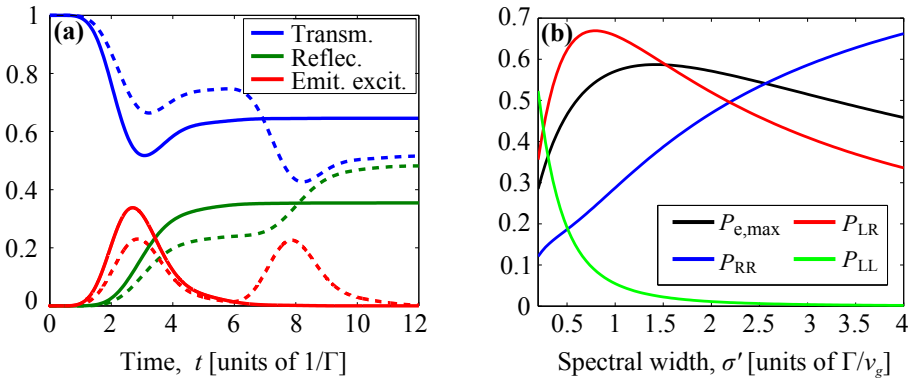

Figure 4.5: (a) Transmission $T_R(t)$ (blue) and reflection $T_L(t)$ (green), together with relative TLE excitation, $P_e(t)/2$ (red), for parameters corresponding to the two cases of perfectly overlapping (solid) and non-overlapping (dashed) pulses shown in Figs. 4.3 and 4.4 respectively. (b) Maximum TLE excitation and the directional scattering probabilities as a function of the wavepacket k-space width, σ', for two coincident but uncorrelated, single-photon pulses with the same width and carrier frequency, resonant with the TLE transition.

field, demonstrating non-instant scattering due to the finite decay rate of the TLE.

The transmission and reflection coefficients do not contain information regarding scattering-induced correlations between the photons, and to that end we define scattering probabilities for the three possible directional outcomes of the scattering process. In the long-time limit, the probability that both photons propagate to the right is given by

$$P_{RR} = \frac{1}{2}\lim_{t\to\infty}\int_0^\infty \mathrm{d}k \int_0^\infty \mathrm{d}k' \,\langle\psi(t)|a^\dagger(k)a^\dagger(k')a(k')a(k)|\psi(t)\rangle \quad (4.14)$$

$$= \lim_{t\to\infty}\int_0^\infty \mathrm{d}k \int_0^\infty \mathrm{d}k' \,|C^{\mathrm{g}}(k,k',t)|^2, \quad (4.15)$$

while P_{LL} is given by a similar expression with the integration ranges changed to $[-\infty, 0]$. The probability of having one photon travelling in each of the two directions is

$$P_{LR}(t) = 2\lim_{t\to\infty}\int_{-\infty}^0 \mathrm{d}k \int_0^\infty \mathrm{d}k' \,|C^{\mathrm{g}}(k,k',t)|^2. \quad (4.16)$$

The scattering probabilities P_{RR}, P_{LR}, and P_{LL} are thus obtained by integrating the two-photon wavepacket over the corresponding quadrant(s) in Fig. 4.3 or Fig. 4.4 in either z- or k-space.

At long times well past the scattering event, when the TLE has fully decayed to its ground state, the probabilities we have defined satisfy $P_{RR} + P_{LL} + P_{LR} = 1$. In contrast to the quantities T_R and T_L, the probabilities P_{RR}, P_{LL},

and P_{LR} contain information regarding the directional correlation between the individual photons. The correlations depend crucially on the width of the photon wavepacket, as well as the initial emitter excitation. To investigate this, Fig. 4.5(b) shows the directional scattering probabilities as a function of the width of two equal coincident input pulses, together with the maximal emitter excitation, $P_{\mathbf{e},\max}$. The scattering of monochromatic pulses (infinitely small σ') is well-known from Chapter 3 ; all of the pulse is reflected when the carrier frequency is resonant with the emitter transition, agreeing with our results here in the limit of a small σ'. Here the TLE excitation remains low due to the low optical power in the pulse. Spectrally broad pulses have a small overlap with the TLE in k-space, resulting in a small degree of interaction and thus also a low value of $P_{\mathbf{e},\max}$ and a high value of P_{RR}. The largest $P_{\mathbf{e},\max}$ is obtained for $\sigma' \sim \Gamma/v_{\mathrm{g}}$ which is also the parameter regime where P_{LR} dominates. This occurs when the spectral overlap between the wavepacket of the input state and the TLE emission spectrum is large.

4.4 Counter-propagating pulses

We now turn to the case where the TLE is illuminated by two counter-propagating single-photon pulses, one photon from each side of the TLE. The corresponding waveguide excitation dynamics is shown in Fig. 4.6, for excitation pulses with a carrier frequency resonant with the TLE transition energy. Due to the symmetry of the scattering problem around $z = 0$, the expectation value of the photon density is the same for the left and right propagating components of the pulse.

Closer inspection of the two-photon wavepacket on the right of Fig. 4.6 reveals interesting features regarding the induced correlations. We see that P_{LR} is much smaller than P_{RR} and P_{LL}. This indicates a strong directional correlation between the two scattered photons as the final state suggests both photons will be measured propagating in the same direction with high probability. We note that this property cannot be inferred from the photon density plot. This phenomenon is analogous to the well-known two-photon interference which gives rise to the Hong-Ou-Mandel dip, wherein two identical photons impinging from opposite sides of an optical beam-splitter coalesce and are measured in the same output arm [104]. In the present case, however, the effect is only partial due to the non-zero spectral width of the input pulses and the TLE saturation, and as a consequence P_{LR} is not zero. This beam splitter-like effect has been observed in Ref. [105] for coupled optical waveguides described by a tight-binding model between the individual sites.

4.4.1 Induced correlations

We now turn our attention to the correlations induced in the two-photon-state as a result of the scattering process. First, it is important to establish in which degrees of freedom the photons can be correlated. We distinguish between two correlation types, which we refer to as 'directional' and 'modal'. Directional

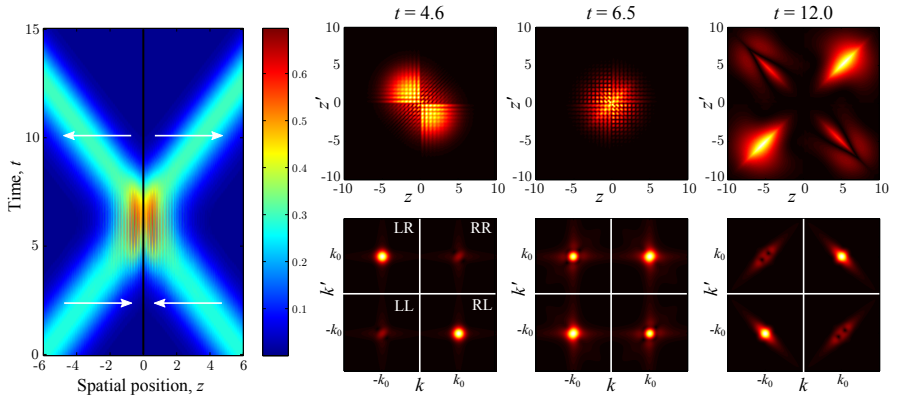

Figure 4.6: Left: Photon density, $N_z(z,t)$ for an initially uncorrelated ($\sigma'_p \to \infty$) two-photon state scattering on the emitter placed at $z = 0$, using pulse widths $\sigma'_1 = \sigma'_2 = 0.5$ and initial centre positions $Z_{0,1} = Z_{0,2} = -6$. The position of the emitter at $z = 0$ is indicated by the black line. Absolute value of the two-photon wavefunction shown at three different times during the scattering event, both in z-space (upper row) and k-space (lower row). In the k-space plots, only the intervals centred at $k, k' = \pm k_0$ are shown.

correlations are those present in measurement statistics acquired from detecting the *direction of propagation* of each of the two photons, and are captured by the quantities P_{ij} for $\{i,j\} \in \{\mathrm{R},\mathrm{L}\}$. If the propagation direction of one photon depends on the measured propagation direction of the other, the two are said to have directional correlations. Modal correlations, on the other hand, are concerned with measurement statistics obtained when detecting the *position* of each photon, assuming a given configuration of propagation directions. These modal correlations are contained in the correlation parameter σ'_{p}, defined for the input state in Eq. (4.7). Modal correlations are more traditionally described in terms of the well-known second order $g^{(2)}$ correlation function [106], which is typically employed when describing intensity correlations. A generic two-photon state may be correlated according to one of these measures, but fully uncorrelated in the other. Fig. 4.1(c) shows an example of such a state. The elliptical shape of the wavepacket in real-space is a signature of modal correlations, but the state can have no directional correlations, since both photons are propagating to the right.

The scattering of co-propagating photons shown in Fig. 4.6 induces strong directional correlations. Modal correlations are also induced, as can be seen from the elliptical shape of the wavefunction in z-space and k-space, meaning that the emitted photons are anti-correlated in k-space and correlated in z-space. This can be further appreciated by comparison with the state shown in Fig. 4.1(c), which was defined to have modal correlations. These correlations have been demonstrated in previous works both theoretically [91] and experimentally [107] for co-propagating photons. The induced anti-correlation in

k-space can be understood as a four-wave mixing process, where elastic scattering of two photons of almost identical energy results in one photon with higher energy and one with lower energy. This gives rise to the elliptical shape of the wavefunction in k-space, cf. the spectrum in Fig. 4.6 at $t = 12.0$. The correlation in z-space implies a larger probability of detecting the second photon spatially close to the first, i.e. photon bunching. Modal correlations such as these are not present in the scattered state from a conventional linear optical beam splitter; the modal entanglement observed here is caused by a non-linear scattering process between the incoming and emitted photons, which is mediated by the excitation of the TLE.

In order to relate the induced quantum correlations in the photonic state to the TLE excitation dynamics, we require a measure of the induced correlations, which can be facilitated by entanglement theory. There are several proposals in the literature of how to quantify the degree of entanglement (quantum correlations) between individual subsystems [108, 109, 110], particularly for distinguishable systems each of which may be in one of only two states, e.g. two spatially separated spin-half particles. These measures include the fidelity, the concurrence, the negativity, and the entropy of entanglement [38], each of which has a different operational meaning, and may be more or less appropriate given the problem at hand. For two indistinguishable particles e.g. two bosons in the same two-photon Hilbert space, extensions to the distinguishable case have to be made [111, 112, 113]. If the indistinguishable bosons can each occupy more than two states, as is the case for the state expressed by Eq. (4.5) (where the number of states is equal to the dimension of each particle sub-Hilbert space), there are fewer ways to quantify the entanglement. Among these is the von Neumann entropy of the reduced single-particle density matrix [112, 114], which quantifies the modal entanglement by the degree to which the state of the second photon is affected by a k-space measurement on the first.

In order to explore the extent to which our system behaves as a beam-splitter, we quantify the amount of directional entanglement present in the scattered state. To do this, the two-photon state may be projected onto a two-dimensional Hilbert space with each photon being in either a left or a right propagating state, giving three basis states, $|LL\rangle$, $|LR\rangle$, and $|RR\rangle$. This projected system is identical to the case of two indistinguishable two-state particles discussed above, for which the entanglement may be quantified by the fidelity, i.e. by comparison to a maximally entangled state. We focus here only on entangled states with a different number of particles in each direction and thus compare to two of the four Bell-states only,

$$|\Phi^{\pm}\rangle = \frac{1}{\sqrt{2}}\left[|LL\rangle \pm |RR\rangle\right]. \tag{4.17}$$

Here $|LL\rangle$ and $|RR\rangle$ are states with the same modal correlations as the parts of the calculated scattered state where both photons propagate to the left or both to the right, respectively. For pure states as in Eq. (4.5), the fidelities with respect to the maximally entangled states projected onto the $|L\rangle$ and $|R\rangle$ basis are defined as the overlap between the scattered state and the maximally

entangled state, $F^{\pm}_{\rm prob} = |\langle\Phi^{\pm}|\psi\rangle|^2$ [38], With this definition of $|LL\rangle$ and $|RR\rangle$ as stated above, the fidelity solely measure the directionally induced correlations, whereas a perfect 50-50 beam splitter would have a fidelity of 1. The fidelities exceed 1/2 only if $|\psi\rangle$ is a non-classical state, and can therefore be interpreted as a measure of the directional entanglement.

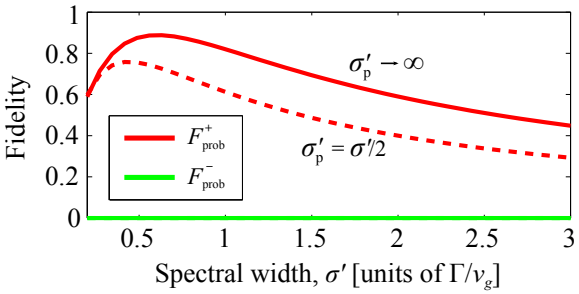

Figure 4.7: Directional entanglement, quantified by F_{prob}, plotted versus the spectral width of the photon wavepacket. Here we consider two identical, single-photon wavepackets impinging on the TLE from each side, initially equidistant from the TLE, and both being resonant with the TLE transition (i.e. the conditions are the same as those of Fig. 4.6 for which $\sigma'_1 = \sigma'_2 = 0.5$ and $\sigma'_p \to \infty$). Cases of initially uncorrelated states, $\sigma'_p \to \infty$, and spatially correlated states, $\sigma'_p = \sigma'_1/2$ are shown, and the wavepacket widths are always equal $\sigma'_1 = \sigma'_2 = \sigma'$.

For two identical photons scattering on the TLE from each side, as in Fig. 4.6, the input state has $F^{\pm}_{\rm prob} = 0$, as the overlap with the initial state $|LR\rangle$ is zero. The fidelity for the scattered state is shown in Fig. 4.7 for varying widths of the input pulses. $F^{-}_{\rm prob}$ is zero for the scattered state, at both $|LL\rangle$ and $|RR\rangle$ in Eq. (4.17) are obtain by a single-photon reflection in the input $|LR\rangle$, by which the resulting phase on $|LL\rangle$ and $|RR\rangle$ has to be the same.

The correlated input state, where both photons have a larger probability of scattering on the TLE at the same time, leads to a smaller fidelity at the output than for two uncorrelated photons at the input. For the initially correlated states, such as that shown in in Fig. 4.1(c), the spectrum of the photons is tighter than the uncorrelated case in Fig. 4.1(a), but the spatial distribution is broadened, resulting in a lower probability of having both of the photons at the TLE at the same time; this decreases the induced correlations and correspondingly leads to a smaller fidelity.

In the limit of large σ', only a small fraction of the pulse interacts with the TLE, giving a fidelity which approaches zero. In the small σ' limit, the incoming pulse is temporally broad, resulting in a low light intensity at the TLE position at all times, and hence, to a good approximation, the TLE remains in its ground state. As the TLE only induces non-linearities when it is excited, a two-photon packet with small σ' scatters as if the two photons were scattering individually on the TLE, giving the scattered state $|LR\rangle$. We note that the maximum fidelity is obtained when the linewidth of the Gaussian input pulses

is comparable with the decay rate of the TLE, i.e. for full-width half maximum of the incoming pulse on the order $\sigma = 2\sqrt{\ln(2)}\sigma' \approx 1.0$. In this case excitation of the TLE is high, and a highly directionally entangled state is produced.

4.5 Summary

In conclusion, we have developed a wavefunction approach to study the scattering of two photons on a two-level emitter in a one-dimensional waveguide. Our method benefits from the simple mathematical form, and provides the full temporal dynamics of the scattering event, as well as a detailed description of the scattering-induced correlations. For co-propagating pulses, we saw that the excitation of the emitter strongly influences its transparency. This results in transmission and reflection coefficients which depend sensitively on the separation between the two input pulses. For counter-propagating pulses, the emitter–waveguide system shows beam-splitter like features, generating directional correlations in the scattered two-photon state, occurring most strongly when the emitter excitation is largest. Unlike a conventional linear optical beam-splitter, however, the finite decay rate of the emitter introduces nonlinearities which manifest as additional bunching effects. Finally, we note that our model could be extended to more complicated scattering scenarios, such as several quantum dots with possibly additional levels [115, 82, 116]. The numerical approach we use also allows for the investigation of the role of waveguide dispersion, as well as non-Markovian coupling to the scattering object by including frequency-dependent coupling coefficients in the system. Lastly, another strength of this numerical approach is the possibility of several, spatially separated emitters. Other approaches such as the scattering matrix formalism becomes very complex for two-photon scattering, due to recursive terms where energy may oscillate back and forth between the scatterers [116], which we plan to look into in future studies.

Chapter 5

Two-photon scattering — Scattering matrix approach

In this chapter we discuss another approach to analyse two-photon scattering on a non-linearity, namely the scattering matrix formalism. For typical scattering experiments where an input state is sent toward a scattering region, the problem is often treated mathematically by the scattering matrix formalism. The state of the photon pulse long after the scattering process is related to the to the initial state through the scattering matrix operator S, which is equal to the evolution operator in the interaction picture from time $-\infty$ to ∞. For non-linear scatterers, the scattering matrix will in general be frequency dependent, and is given by

$$S = \lim_{\substack{t_i \to -\infty \\ t_e \to \infty}} \mathrm{e}^{\mathrm{i}H_0 t_e} \mathrm{e}^{-\mathrm{i}H(t_e - t_i)} \mathrm{e}^{-\mathrm{i}H_0 t_i} \tag{5.1}$$

with H_0 being the non-interaction part of the system Hamiltonian, H [66]. Thus, if the scattering matrix elements for a specific scatterer has been determined, the post-scattering may be determined using standard algebra. It is, however, not trivial to determine the scattering matrix elements for few-photon non-linearities, due to possible non-linear scattering processes where the energy between multiple input photons may be changed, as demonstrated in the previous chapter.

The scattering elements may be determined by various methods, such as the input-output formalism [66], the Bethe Ansatz [87, 88], and the Lehmann-Symanzik-Zimmermann formalism [89]. These approaches have been exploited to calculate the scattering matrix elements for two-photon states in various systems such as a single emitter [66, 67], an emitter inside an optical cavitiy [117], an emitter coupled to a ring resonator [118], and a non-linear optical cavity [119]. In contrast to the numerical approach in Chapter 4, the scattering matrix calculations complicate when considering scatterers which consist of multiple elements, and also for spatially separated scatterers due to recursive terms, corresponding to energy bounding back and forth between the scatterers. The two-photon scattering matrix for spatially separated two-level

emitters[1] was, however, recently determined [116]. The evaluated scattering matrix elements are usually evaluated by assuming no excitation losses to external reservoirs, but dissipation may be included according to the description in Rephaeli et al. [63].

Until now, a big focus has been on considering scattering of co-propagating two-photon pulses using the scattering matrix formalism. We employ in this chapter the scattering matrix formalism to examine the case of counter-propagating photons, as we saw in the previous chapter that this could lead to very strong correlations between the photons. By this mathematical approach we may exactly address the correlations induced specifically by the emitter non-linearity. We obtain very simple expressions for the scattering probabilities of a two-photon pulse with a Lorentzian spectrum, despite the complex scattering dynamics. Furthermore we define suitable fidelity measurements to quantify the induced correlations, taking into account both the induced changes in the propagation direction, spectrum and phase of the photons.

If the non-linearities are to be implemented in larger optical circuits with various photon gates, it may be of high importance for the overall effectiveness that the properties of the photons does not change through a gate, as this may devour the photon manipulations subsequent gates. This raises questions regarding the feasibility of integrating a large number of photonic gates needed to create complex optical circuits. The purpose of this work is to explore how two-photon pulses are altered by the scattering process, and investigate how these alterations depend on the level of induced non-linearities. Interestingly, we find that non-linearaties can actually suppress spectral and phase changes, thereby increasing the similarity of the scattered and input photons. As such, even when correctly accounting for all properties of the scattered photonic state, fidelities between the scattered and a desired directionally entangled state as high as 80% can still be achieved.

This chapter is organized as follows: In Section 5.1 we introduce our model system. In Section 5.2 we review the scattering of a single-photon pulse on a two-level-emitter, and we introduce fidelity measures to quantify the similarity between the incoming and scattered photons. In Section 5.3 the formalism is applied to scattering of two counter-propagating single-photon pulses, where our fidelity measures are used to analyse induced correlations and spectral changes, and how these relate to the level of non-linearities.

The chapter is based on the submitted publication *Strong non-linearity-induced correlations for counter-propagating photons scattering on a two-level emitter.* arXiv:1502.04729 (2015) by A. Nysteen, D. P. S. McCutcheon, and J. Mørk.

[1] For scatterers spaced by only a few wavelengths, the rotating wave approximation may however not be valid, as virtual photons may be exchanged between the atoms [120].

5.1 General theory

In contrast to the previous sections, we specifically distinguish the different propagating modes by dividing the waveguide modes into two subsets, being the right (mode index 1) and left (mode index 2) propagating modes, see Fig. 5.1. Each of the subsets describe a chiral waveguide, i.e. where propagation is only allowed in one direction, and we choose the orientation of the spatial axis in each subsets such that all modes have a positive wavevector, k. In the following we limit ourselves to lossless systems, though we note that this assumption could be relaxed by coupling our system to additional external reservoirs [70, 63]. Additionally, we neglect waveguide dispersion in the considered frequency interval, and we assume a localized scatterer (dipole approximation), i.e. that the scattering occurs only at a single point in space, all as discussed in Chapter 3. Instead of describing the Hamiltonian in a frame rotating with the emitter frequency as in the previous chapters, we follow the notation of Fan et. al [66] and use the carrier frequency of the pulse, ω_p, to describe the rotating frame, when employing the scattering matrix approach. With this, the system dynamics are given by the Hamiltonian from Eq. (3.3), given in a frame rotating with the pulse frequency, ω_p,

$$\begin{aligned}\tilde{H} = \hbar\Delta c^\dagger c + \sum_{i=1}^{2}\int_0^\infty \mathrm{d}\tilde{k}\,\hbar(\omega(\tilde{k})-\omega_\mathrm{p})\tilde{a}_i(\tilde{k})^\dagger\tilde{a}_i(\tilde{k}),\\ + \sum_{i=1}^{2}\hbar g\int_0^\infty \mathrm{d}\tilde{k}\,\left[\tilde{a}_i(\tilde{k})c^\dagger + \mathrm{h.c.}\right]\end{aligned} \tag{5.2}$$

Here each mode in subsystem 1 and 2 is characterized by a wavevector $\tilde{k} > 0$, annihilation operator $\tilde{a}_i(\tilde{k})$ and energy $\hbar\omega(\tilde{k})$. By writing the Hamiltonian in this way we implicitly consider a single polarization of the waveguide modes, and we assume a direction and frequency-independent coupling strength between the emitter and waveguide, g, as discussed in Section 3.2. The emitter excitation is described by the fermionic creation operator $c^\dagger = c_e^\dagger c_g$, and the emitter frequency detuning from the pulse is Δ.

We limit ourselves to consider input pulses where the two photon pulses have the same carrier frequency. We relate the frequencies of the waveguide modes $\omega(\tilde{k})$ by a linearization in similarity with Eq. (3.4),

$$\omega(\tilde{k}) \approx \omega_p + v_g(\tilde{k}-k_p) \tag{5.3}$$

with k_p is the carrier wavevector of the pulses, and $v_g = (\partial\omega/\partial\tilde{k})|_{\tilde{k}=k_p}$ the group velocity.

As each of the subsystems are chiral, no absolute value of k appears in Eq. (5.3), by which we may introduce annihilation and creation operators directly in the moving frame, $a_i(k) = \tilde{a}(k+k_p)$, with $k = \tilde{k} - k_p$ being the wavevector in the rotating frame [66]. The resulting Hamiltonian is

$$H = \hbar\Delta c^\dagger c + \hbar v_g\sum_{i=1}^{2}\int_{-\infty}^{\infty}\mathrm{d}k\,k\,a_i^\dagger(k)a_i(k) + \hbar g\sum_{i=1}^{2}\int_{-\infty}^{\infty}\mathrm{d}k[\sigma_+ a_i(k) + \mathrm{h.c.}] \tag{5.4}$$

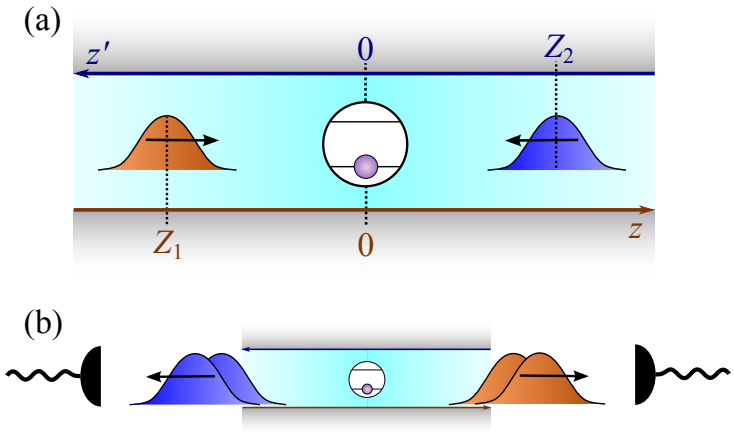

Figure 5.1: (a) Two counter-propagating single-photon pulses propagate toward a two-level system in its ground state. (b) The post-scattering state may be measured by detectors in each chiral waveguide mode sub-group.

We note that in obtaining Eq. (5.4) we have extended the lower limits of integration from $-k_p$ to $-\infty$. This approximation is justified since we will be interested in pulses with wavevectors centered around $k = \tilde{k} - k_p = 0$, where the bandwidth of the pulses is much smaller than k_p, as discussed in Chapter 3.

5.2 Single-photon scattering

Before we consider the scattering of two photons, we first review the single-photon scattering case and introduce the scattering matrix formalism for an arbitrary, localized quantum scatterer. We consider cases for which the scatterer initially is in its ground state. Following Fan et al. [66], the single-photon scattering matrix for a localized scatterer is given by the matrix elements

$$ {}_1\langle p|S^{(1)}|k\rangle_1 = {}_2\langle p|S^{(1)}|k\rangle_2 = \bar{t}(k)\delta(p-k), \tag{5.5} $$

$$ {}_2\langle p|S^{(1)}|k\rangle_1 = {}_1\langle p|S^{(1)}|k\rangle_2 = \bar{r}(k)\delta(p-k). \tag{5.6} $$

Here we use the shorthand notation, $|k\rangle_i = a_i^\dagger(k)|\phi\rangle$, with $|\phi\rangle$ being the system state corresponding to no excitations in the waveguide and the emitter in its ground state. Furthermore, $\bar{t}(k)$ and $\bar{r}(k)$ are the frequency-dependent single-photon transmission and reflection coefficients, respectively[2]. The delta-functions reflect momentum conservation, and as no external loss channels are present, $|\bar{t}(k)|^2 + |\bar{r}(k)|^2 = 1$.

An arbitrary single photon state propagating in subsystem 1 is written

$$ |\xi_0\rangle = \int_{-\infty}^{\infty} \mathrm{d}k\, \xi(k) a_1^\dagger(k)|\phi\rangle, \tag{5.7} $$

[2]The scattering matrix element deviates slightly from Eq. (3.16) by the sign in the δ-functions, which is due to the choice in this chapter that all waveguide modes have positive k (with the direction being given by the subset number).

where $\xi(k)$ is the wavepacket in momentum space. The post-scattering state corresponding to the incoming state expressed in Eq. (5.7) is defined as $|\xi\rangle_{t\to\infty} = S^{(1)}|\xi_0\rangle$. It is obtained by inserting the identity operator

$$\mathcal{I} = \sum_{i=1,2} \int_{-\infty}^{\infty} \mathrm{d}p\, |p\rangle_{ii}\langle p|, \tag{5.8}$$

from which we find

$$|\xi\rangle_{t\to\infty} = \int_{-\infty}^{\infty} \mathrm{d}p\, \bar{t}(p)\xi(p)|p\rangle_1 + \int_{-\infty}^{\infty} \mathrm{d}p\, \bar{r}(p)\xi(p)|p\rangle_2. \tag{5.9}$$

The two terms above reflect the fact that the photon can be transmitted or reflected. The scattering probabilities are defined as

$$P_i = {}_{t\to\infty}\langle\xi| \int_{-\infty}^{\infty} \mathrm{d}p\, |p\rangle_{ii}\langle p|\xi\rangle_{t\to\infty}, \tag{5.10}$$

with the transmission and reflection probabilities corresponding to $i = 1$ and $i = 2$ respectively. These probabilities are

$$P_1 = \int_{-\infty}^{\infty} \mathrm{d}p\, |\bar{t}(p)\xi(p)|^2, \qquad P_2 = \int_{-\infty}^{\infty} \mathrm{d}p\, |\bar{r}(p)\xi(p)|^2. \tag{5.11}$$

The theory above applies to any localized scatterer interacting with two chiral waveguide modes. We now specifically consider the emitter-waveguide system sketched in Fig. 5.1 and described by the Hamiltonian Eq. (5.4). In this system the reflection and transmission coefficients may be found through calculation of the single-photon scattering matrix elements [66], which gives

$$\bar{t}(k) = \frac{k-\Delta}{k-\Delta+\mathrm{i}\Gamma/(2v_g)}, \qquad \bar{r}(k) = \frac{-\mathrm{i}\Gamma/(2v_g)}{k-\Delta+\mathrm{i}\Gamma/(2v_g)}, \tag{5.12}$$

where $\Gamma = 4\pi g^2/v_g$ is the decay rate of the emitter as derived in Section 3.2. The matrix elements were used to calculate the single-photon scattering probabilities in Section 3.2.1 for incoming single photons with various spectral wavepackets. In this chapter we will consider the Lorentzian and Gaussian single-photon spectral wavepackets[3], Eqs. (3.12a)-(3.12b). All wave packets are normalised such that $\int_{-\infty}^{\infty} \mathrm{d}k\, |\xi(k)|^2 = 1$, and have a bandwidth (full width–half maximum of the intensity spectrum) of σ.

5.2.1 Scattering fidelities

If many emitters are to be implemented in a larger sequence of photonic devices or gates, it may be of importance that scattered photons maintain their spectral properties, i.e. the pulse shape and phase variation across the pulse. We therefore seek to define measures to compare the scattered state with some

[3] As the scattering matrix formalism maps an input state at $t \to -\infty$ to $t \to \infty$, the spatial origin of the pulses in Eqs. (3.12a)-(3.12b) does not affect the dynamics, and we may set $Z_0 = 0$ without loss of generality.

desired output state, given e.g. as the ideal output in a specific photon gate. We define three measures for this purpose, each with a different physical significance. We use the quantum state fidelity [38] as a measure of the degree to which the scattered state is quantum mechanically identical to the desired state (neglecting overall phase differences),

$$F_{\text{full}} \quad = \quad |\langle \xi_{\text{des}} | \xi \rangle_{t\to\infty}|^2, \tag{5.13}$$

where $|\xi_{\text{des}}\rangle$ is the desired state. To exemplify the fidelity calculations in the single-excitation case, we assume that the desired state is identical to the input state. Physically, this could correspond to a system where two identical photons are created, after which one of them is reflected from scattering on an emitter and then is to interfere with the second photon at 50-50 beam splitter. In this Hong-Ou-Mandel-type interference experiment, the photons will exit the beam splitter in the same arm, but only if the arrive at the beam splitter at the same time *and* they have the same photon properties, i.e. that $F_{\text{full}} = 1$. With this example, we find

$$F_{\text{full}} = \left| \int_{-\infty}^{\infty} \mathrm{d}p\, \bar{r}(p) |\xi(p)|^2 \right|^2. \tag{5.14}$$

For cases in which the phase of the scattered state is unimportant, but we only have interest in how the intensity in the pulses are distributed spectrally, the similarity between the scattered and the desired pulse may be characterized by

$$F_{\text{int}} = \left(\int_{-\infty}^{\infty} \mathrm{d}p\, |\bar{r}(p)||\xi(p)|^2 \right)^2. \tag{5.15}$$

This fidelity measure would be relevant when comparing the energy distributions in the scattered and desired pulse, which could be achieved by introducing spectrometers in a setup as sketched in Fig. 5.1(b), but disregarding the arrival times at the detectors. It can be seen to be the limiting form of a spatial definition of a fidelity measure, defined as

$$F_{\text{spat}}(\delta z) = \left| \int_{-\infty}^{\infty} \mathrm{d}z\, \xi^*(z) \xi_{\text{scat}}(z - \delta z) \right|^2, \tag{5.16}$$

where $\xi_{\text{scat}}(z)$ is the spatial representation of the scattered wavepacket, which after the scattering may be displaced by δz in the rotating frame due to a delay caused by the absorption in the emitter. Using the defined Fourier transform and Hölder's inequality, we find F_{int} is an upper bound for this spatial fidelity,

$$\max_{\delta z} F_{\text{spat}}(\delta z) = \max_{\delta z} \left| \int_{-\infty}^{\infty} \mathrm{d}p\, |\xi(p)|^2 \bar{r}(p) \mathrm{e}^{\mathrm{i}\delta z \cdot p} \right|^2 \leq F_{\text{int}}. \tag{5.17}$$

Thus, if it for some systems is too complicated to evaluate F_{spat} at each detuning, F_{int} provides a good upper bound for F_{spat}.

Finally, when neither the phase nor the spectral distribution are important, the scattered state may be projected onto a basis which merely counts the

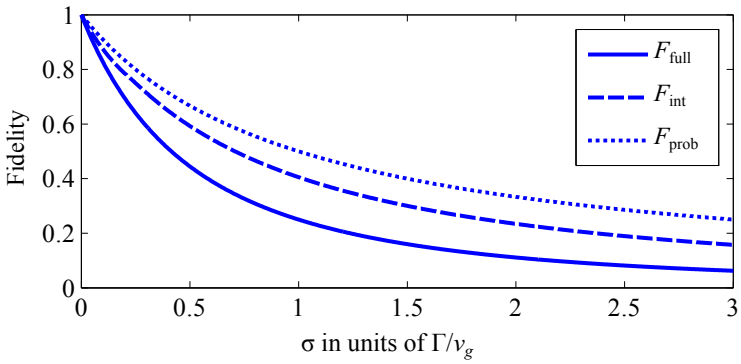

Figure 5.2: The three fidelity measures from Eqs. (5.14), (5.15), and (5.18) for scattering of a single-photon pulse on a resonant emitter, using the Lorentzian pulse spectrum from Eq. (3.12a).

number of photons in each waveguide mode, e.g. as in Fig. 5.1(b). The fidelity in this case simply becomes the probability of detecting a photon in the desired output mode (being the reflected field in the considered example),

$$F_{\text{prob}} = P_r. \tag{5.18}$$

analogous to the definition in Eq. (4.17).

We evaluate F_{full}, F_{int}, and F_{prob} for a resonant Lorentzian input, and show the results in Fig. 5.2. For F_{full} and F_{prob} we find the exact expressions

$$F_{\text{full}} = \frac{(\tilde{\Gamma})^2}{(\tilde{\Gamma}+\sigma)^2+4\Delta^2}, \tag{5.19}$$

$$F_{\text{prob}} = \frac{(\tilde{\Gamma}+\sigma)\tilde{\Gamma}}{(\tilde{\Gamma}+\sigma)^2+4\Delta^2}, \tag{5.20}$$

where $\tilde{\Gamma} = \Gamma/v_g$. From Fig. 5.2 we see that $0 \leq F_{\text{full}} \leq F_{\text{int}} \leq F_{\text{prob}} \leq 1$. This reflects the progressively less stringent criteria of these three measures. As the desired state in each case is a fully reflected state as discussed in Chapter 3, the fidelities are largest for small FWHMs.

5.3 Two-photon scattering

We now turn to the main focus of this chapter and extend our formalism to describe the scattering of two-photon states, first generalizing to an arbitrary localized scatterer. In the single-photon case, energy conservation implied that an approximately monochromatic single-photon wavepacket would scatter without changing its frequency. In the two-photon case, energy conservation only demands that the *sum* of the energies of the two incoming and two scattered photons is conserved. According to Fan et al. [66], we can define a two-photon scattering matrix, $S^{(2)}$, in a similar way to $S^{(1)}$, which contains terms describing single-photon scattering, and also additional terms stemming from two-photon

scattering processes. The additional terms involve four-wave mixing mechanisms between the two incoming and two scattered photons [66, 121].

In the rotating frame, a general two-photon state in the momentum representation is written as

$$\begin{aligned}|\beta\rangle = &\tfrac{1}{\sqrt{2}}\int_{-\infty}^{\infty}\mathrm{d}k\int_{-\infty}^{\infty}\mathrm{d}k'\,\beta_{11}(k,k')a_1^\dagger(k)a_1^\dagger(k')|\phi\rangle\\ &+\tfrac{1}{\sqrt{2}}\int_{-\infty}^{\infty}\mathrm{d}k\int_{-\infty}^{\infty}\mathrm{d}k'\,\beta_{22}(k,k')a_2^\dagger(k)a_2^\dagger(k')|\phi\rangle\\ &+\int_{-\infty}^{\infty}\mathrm{d}k\int_{-\infty}^{\infty}\mathrm{d}k'\,\beta_{12}(k,k')a_1^\dagger(k)a_2^\dagger(k')|\phi\rangle,\end{aligned}\tag{5.21}$$

normalized such that $\int_{-\infty}^{\infty}\mathrm{d}k\int_{-\infty}^{\infty}\mathrm{d}k'\,(|\beta_{11}(k,k')|^2+|\beta_{12}(k,k')|^2+|\beta_{22}(k,k')|^2)=1$. Introducing the notation $|kk'\rangle_{ii'}=\{{}_{i'i}\langle k'k|\}^\dagger=a_i^\dagger(k)a_{i'}^\dagger(k')|\phi\rangle$, the two-photon scattering elements are [66]

$$\begin{aligned}{}_{jj'}\langle pp'|S^{(2)}|kk'\rangle_{ii'} = &\,\alpha_{ji,k}\alpha_{j'i',k'}\delta(k-p)\delta(k'-p')\\ &+\alpha_{j'i,k}\alpha_{ji',k'}\delta(k-p')\delta(k'-p)\\ &+\tfrac{1}{4}B_{pp'kk'}\delta(p+p'-k-k'),\end{aligned}\tag{5.22}$$

for $i,j\in\{1,2\}$, and where

$$\alpha_{ji,k}=\begin{cases}\bar{t}(k) & \text{if } i=j\\ \bar{r}(k) & \text{if } i\neq j\end{cases}\tag{5.23}$$

are the single photon reflection and transmission matrix elements. Here $B_{pp'kk'}$ describes interactions between the two incoming and the two scattered photons, and is determined by the specific localized scatterer considered. As in the single-photon case, to find the scattered state, we insert the identity operator, which is now given by

$$\mathcal{I}=\int_{-\infty}^{\infty}\mathrm{d}p\int_{-\infty}^{\infty}\mathrm{d}p'\left[\frac{1}{2}|p'p\rangle_{1111}\langle pp'|+|p'p\rangle_{2112}\langle pp'|+\frac{1}{2}|p'p\rangle_{2222}\langle pp'|\right].\tag{5.24}$$

In this chapter we specifically considering two incoming, counter-propagating photons. Thus β_{12} is the only non-zero expansion coefficient in Eq. (5.21), which results in the post-scattering state

$$\begin{aligned}|\beta\rangle_{t\to\infty} = &\int_{-\infty}^{\infty}\mathrm{d}p\int_{-\infty}^{\infty}\mathrm{d}p'\Bigg\{\\ &\frac{1}{2}\Big[(\bar{t}(p)\bar{r}(p')+\bar{r}(p)\bar{t}(p'))\beta_{12}(p,p')+\tfrac{1}{4}b_{12}(p,p')\Big]a_1^\dagger(p)a_1^\dagger(p')\\ &+\Big[(\bar{r}(p)\bar{r}(p')+\bar{t}(p)\bar{t}(p'))\beta_{12}(p,p')+\frac{1}{4}b_{12}(p,p')\Big]a_1^\dagger(p)a_2^\dagger(p')\\ &+\frac{1}{2}\Big[(\bar{t}(p)\bar{r}(p')+\bar{r}(p)\bar{t}(p'))\beta_{12}(p,p')+\frac{1}{4}b_{12}(p,p')\Big]a_2^\dagger(p)a_2^\dagger(p')\quad\Bigg\}|\phi\rangle.\end{aligned}\tag{5.25}$$

The first term in each of the three square brackets in Eq. (5.25) represents single photon scattering processes, containing the appropriate combinations of transmission and reflection coefficients connecting the initial and final photon configurations. I.e. to obtain the output state with photons in different modes, either both must be reflected, $\bar{r}(p)\bar{r}(p')$, or both transmitted, $\bar{t}(p)\bar{t}(p')$, given in the third line of Eq. (5.25). Multi-photon process are contained in the pulse-dependent contribution $b_{12}(p,p')$, which describes processes induced by the emitter non-linearity, and is given by

$$b_{12}(p,p') = \int_{-\infty}^{\infty} \mathrm{d}k\, \beta_{12}(k, p+p'-k) B_{pp'k(p+p'-k)}. \tag{5.26}$$

We define P_{11} (P_{22}) as the probability that both photons are measured propagating in waveguide mode 1 (mode 2), and P_{12} the probability that one photon propagates in each waveguide mode. From Eq. (5.25) we find

$$P_{11} = \frac{1}{2}\int_{-\infty}^{\infty}\mathrm{d}p \int_{-\infty}^{\infty}\mathrm{d}p' \left|(\bar{t}(p)\bar{r}(p') + \bar{r}(p)\bar{t}(p'))\beta_{12}(p,p') + \frac{1}{4}b_{12}(p,p')\right|^2, \tag{5.27}$$

$$P_{12} = \int_{-\infty}^{\infty}\mathrm{d}p \int_{-\infty}^{\infty}\mathrm{d}p' \left|(\bar{t}(p)\bar{t}(p') + \bar{r}(p)\bar{r}(p'))\beta_{12}(p,p') + \frac{1}{4}b_{12}(p,p')\right|^2, \tag{5.28}$$

with $P_{11} = P_{22}$ and $P_{11} + P_{12} + P_{22} = 1$.

As for the single photon case, we will be interested in comparing the scattered two-photon state described by Eq. (5.25) to some desired state using the fidelity measures we have introduced in Eqs. (5.14), (5.15), and (5.18). In Chapter 4 we demonstrated numerically how a two-level emitter may act as a non-linear beam splitter. Thus, it would of relevance to compare the scattered to a scattered state obtained by replacing the emitter with a 50-50 beam splitter, which preserves the shape and phase of the input photons. In this case the desired state would be

$$\begin{aligned}|\beta_{\mathrm{des}}\rangle = \frac{1}{\sqrt{2}}\int_{-\infty}^{\infty}\mathrm{d}k \int_{-\infty}^{\infty}\mathrm{d}k'\, \beta_{12}(k,k') \\ \times \left[\frac{1}{\sqrt{2}}a_1^\dagger(k)a_1^\dagger(k') + \frac{1}{\sqrt{2}}a_2^\dagger(k)a_2^\dagger(k')\right]|\phi\rangle.\end{aligned} \tag{5.29}$$

With this desired state our fidelity measures become

$$F_{\mathrm{full}} = \left|\int_{-\infty}^{\infty}\mathrm{d}p \int_{-\infty}^{\infty}\mathrm{d}p' \beta_{12}^*(p,p')\beta_{12}'(p,p')\right|^2 \tag{5.30}$$

$$F_{\mathrm{int}} = \left[\int_{-\infty}^{\infty}\mathrm{d}p \int_{-\infty}^{\infty}\mathrm{d}p' |\beta_{12}(p,p')|\,|\beta_{12}'(p,p')|\right]^2 \tag{5.31}$$

$$F_{\mathrm{prob}} = P_{11} + P_{22} \tag{5.32}$$

with $\beta_{12}'(p,p') = (\bar{t}(p)\bar{r}(p') + \bar{r}(p)\bar{t}(p'))\beta_{12}(p,p') + \frac{1}{4}b_{12}(p,p')$.

5.3.1 Two-level emitter

The theory presented above is valid for any localized scatterer. We now specifically consider the two-level-emitter–waveguide system described by Eq. (5.4), and focus here only on pulses starting equidistantly from the emitter. Furthermore, we only treat pairs of input pulses with the same spectral linewidth, although the formalism can be straightforwardly extended to more general cases. For a two-level-emitter the single photon transmission and reflection matrix elements $\bar{t}(k)$ and $\bar{r}(k)$ are given by Eq. (5.12), while the two-photon scattering element is [66]

$$B_{pp'kk'} = \mathrm{i}\frac{\sqrt{\Gamma}}{\pi} s(p)s(p')[s(k) + s(k')], \tag{5.33}$$

where

$$s(k) = \frac{\sqrt{\Gamma}/v_g}{k - \Delta + \mathrm{i}\Gamma/(2v_g)}. \tag{5.34}$$

We only consider uncorrelated photon input states, and as such $\beta(k, k')$ is a symmetrized product of two single-photon wavepackets $\beta(k, k') = [\xi(k)\xi'(k') + \xi'(k)\xi(k')]$, which is normalized as $\int_{-\infty}^{\infty} \mathrm{d}k \int_{-\infty}^{\infty} \mathrm{d}k' \, |\beta(k, k')|^2 = 1$.

We begin our analysis of the scattered state by considering correlations in photon detection events in the two waveguide mode subsets, as depicted in Fig. 5.1(b). In this case no information regarding the spectrum and phase of the scattered photons is obtained, and the appropriate fidelity measure is F_{prob}, which is equal to 1 minus the probability of detecting a coincidence in the two detectors, i.e. for $F_{\mathrm{prob}} = 1$ no coincidence events are measured (a perfect Hong-Ou-Mandel dip would be observed). In Fig. 5.3(a), F_{prob} is calculated for Gaussian and Lorentzian input pulses for zero detuning ($\Delta = 0$), for which the interaction between the pulses and emitter is greatest. We see that very high fidelities are obtained, reaching values of $\sim 80\%$ for the Lorentzian input and $\sim 90\%$ for the Gaussian. This is equivalent to the result in Fig. 4.7, wheremaximal correlations are achieved in the regime where the emitter and pulse linewidth are similar. Interestingly, although the Lorentzian pulse shape is well-known to be the optimal pulse shape for maximally exciting the two-level emitter with a single photon [103], it is not the optimal shape for maximizing the directional correlations in the scattered state.

The high fidelities obtained demonstrate that the scattered states are highly directionally entangled, in analogy with the effect of an optical beam-splitter. However, in contrast to the classical beam splitter, the high correlation seen here is induced solely by non-linearities. To demonstrate that the high directional correlations indeed stem from non-linearities, in Fig. 5.3(a) we also show the case where the non-linear two-photon interaction term $b_{12}(p, p')$ has been artificially set to 0 (dashed curves). For an uncorrelated two-photon input pulse which is resonant with the emitter and which has a symmetric spectral wavefunction amplitude, $|\xi(-k)|^2 = |\xi(k)|^2$, as is the case here, Eq. (5.27) reduces

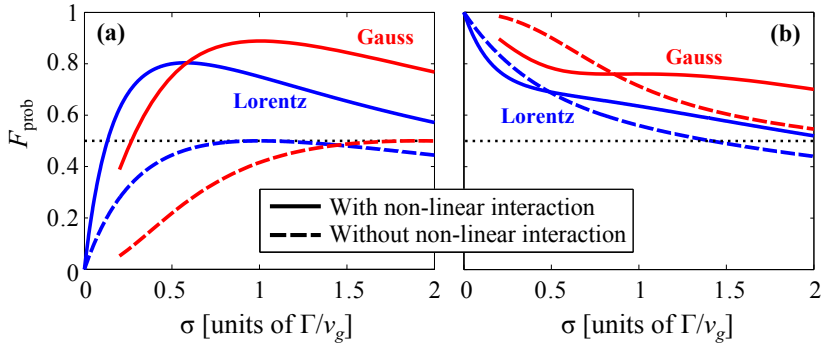

Figure 5.3: Degree of directional entanglement F_{prob} plotted for varying incoming pulse widths, shown for both Lorentzian and Gaussian input pulses (solid lines). The corresponding values obtained when neglecting two-photon scattering terms are also shown (dashed lines). (a) Pulse and emitter are resonant, $\Delta = 0$. (b) Pulse and emitter detuned by $\Delta = \Gamma/(2v_g)$.

to

$$P_{11} = a(1-a), \quad \text{with} \quad a = \int_{-\infty}^{\infty} \mathrm{d}p \, \frac{(\tilde{\Gamma}/2)^2}{p^2 + (\tilde{\Gamma}/2)^2} |\xi(p)|^2, \tag{5.35}$$

showing that P_{11} maximally attains the value $1/4$, occurs when $a = 1/2$. Thus, $F_{\mathrm{prob}} = 2P_{11}$ never exceeds $1/2$, as confirmed in Fig. 5.3(a), which indicates that no directional entanglement is present in the scattered state [38]. For $b_{12}(p, p') = 0$, the emitter behaves as a linear component (e.g. a lossless optical cavity) and cannot mediate interactions between the two photons. As such, the scattering process is determined entirely by interference effects, which, unlike an optical beam-splitter, cannot create entanglement in this system when the pulses are resonant with the emitter.

A more direct analogy with a 50/50 beam splitter can be obtained by detuning the input pulses by half the emitter linewidth, $\Delta = \Gamma/(2v_g)$. For this value of the detuning, a monochromatic single-photon pulse will be reflected/transmitted with 50% probability (whereas at $\Delta = 0$ a monochromatic single-photon pulse is fully reflected). Fig. 5.3(b) shows F_{prob} for $\Delta = \Gamma/(2v_g)$, and we confirm that $F_{\mathrm{prob}} \to 1$ as $\sigma \to 0$ as expected. The change in the fidelity due to the non-linearities now becomes smaller than in the resonant case, as the interaction between the pulse and the emitter is less efficient off resonance. Interestingly, in this case, for small σ, the non-linear interaction actually deteriorates the beam splitting effect, since now the directional entanglement can be generated by interference effects only.

For a Lorentzian input analytic expressions for $P_{11,\mathrm{Lor}} = P_{22,\mathrm{Lor}}$ may be derived. We find

$$P_{11,\mathrm{Lor}} = \frac{3\tilde{\Gamma}\sigma(3\sigma+\tilde{\Gamma})(\sigma+\tilde{\Gamma}) + 4\Delta^2\tilde{\Gamma}(\sigma+2\tilde{\Gamma})}{\left[(3\sigma+\tilde{\Gamma})^2 + 4\Delta^2\right]\left[(\sigma+\tilde{\Gamma})^2 + 4\Delta^2\right]}, \tag{5.36}$$

with $\tilde{\Gamma} = \Gamma/v_g$. The maximum value on resonance ($\Delta = 0$) is obtained for

$\sigma/\tilde{\Gamma} = 3^{-1/2} \approx 0.57$, at which point $P_{11,\mathrm{Lor}} \approx 0.40$ (and $F_{\mathrm{prob}} = 2P_{11,\mathrm{Lor}} \approx 0.8$), in agreement with Fig. 5.3(a). In comparison, with no non-linear terms, $b_{12}(p,p') = 0$, the scattering probability becomes

$$P^{\mathrm{one}}_{11,\mathrm{Lor}} = \frac{\sigma\tilde{\Gamma}(\sigma+\tilde{\Gamma})^2 + 4\Delta^2\tilde{\Gamma}(\sigma+2\tilde{\Gamma})}{\left[(\sigma+\tilde{\Gamma})^2+4\Delta^2\right]^2}, \tag{5.37}$$

which has an on-resonance maximum for $\sigma = \tilde{\Gamma}$, giving $F_{\mathrm{prob}} = 2P^{\mathrm{one}}_{RR,\mathrm{Lor}} = 1/2$. Thus, for the Lorentzian pulse, non-linearities increase the scattering probability by a factor of $P_{11,\mathrm{Lor}}/P^{\mathrm{one}}_{11,\mathrm{Lor}} = 1 + 2/(1+3\sigma/\tilde{\Gamma})$ on resonance. For $\sigma \to \infty$, the interaction with the emitter becomes infinitely weak and no enhancement is present. In the opposite limit of $\sigma \to 0$, the enhancement factor is 3.

5.3.2 Scattering fidelities

As discussed above, if the scatterer is to be implemented in a larger optical circuit, in addition to considering in which *direction* the photons scatter, the *amplitude* and *phase* of the different frequency components may also be important. In such a case, F_{prob} is no longer a sufficient fidelity measure, since it contains only directional information. As illustrated in Fig. 5.4, where we plot the intensity spectrum of a scattered Gaussian wavepacket, the spectra of the scattered pulses change significantly during the scattering process. For input pulses with a narrow spectral linewidth compared to the emitter (1st row), the pulse power at the emitter position remains low due to the corresponding broad spatial profiles of the pulses. In that case, the non-linearity is only weakly addressed, and the individual photons are predominately reflected. A weak non-linearity-induced four-wave mixing process is signified by the appearance of diagonal features, as one photon achieves a larger energy, while the energy of the other decreases. When the pulse and emitter linewidths are comparable (2nd row), the predicted strong directional correlation is induced [121], with the pulse profile being almost preserved. For spectrally broad pulses (3rd row), only the near-resonant part of the spectrum interacts with the emitter. We see that the spectral components at the emitter frequency are absent from the transmitted pulse since these have been reflected without significant two-photon effects.

Interestingly, the fact that the pulse spectrum is almost perfectly preserved when the pulse and emitter linewidths are comparable (2nd row) can be attributed to non-linearities. This can be seen in the 4th row, where we again show the initial and scattered spectra for the case $\sigma = \tilde{\Gamma}$, but where we have artificially set the non-linear term equal to zero, $b_{12} = 0$. By comparison with the 2nd row, we can clearly see that the non-linearities not only give rise to the directional entanglement, but also suppress changes to the spectral shape.

To quantify both the spectral and phase deviations between the scattered and the desired state, all three fidelities defined in Eqs. (5.30)-(5.32) are shown in Fig. 5.5. By comparing F_{prob} to F_{int}, i.e. taking into account the difference in the spectra of the scattered and desired pulse (but not the phase), we see

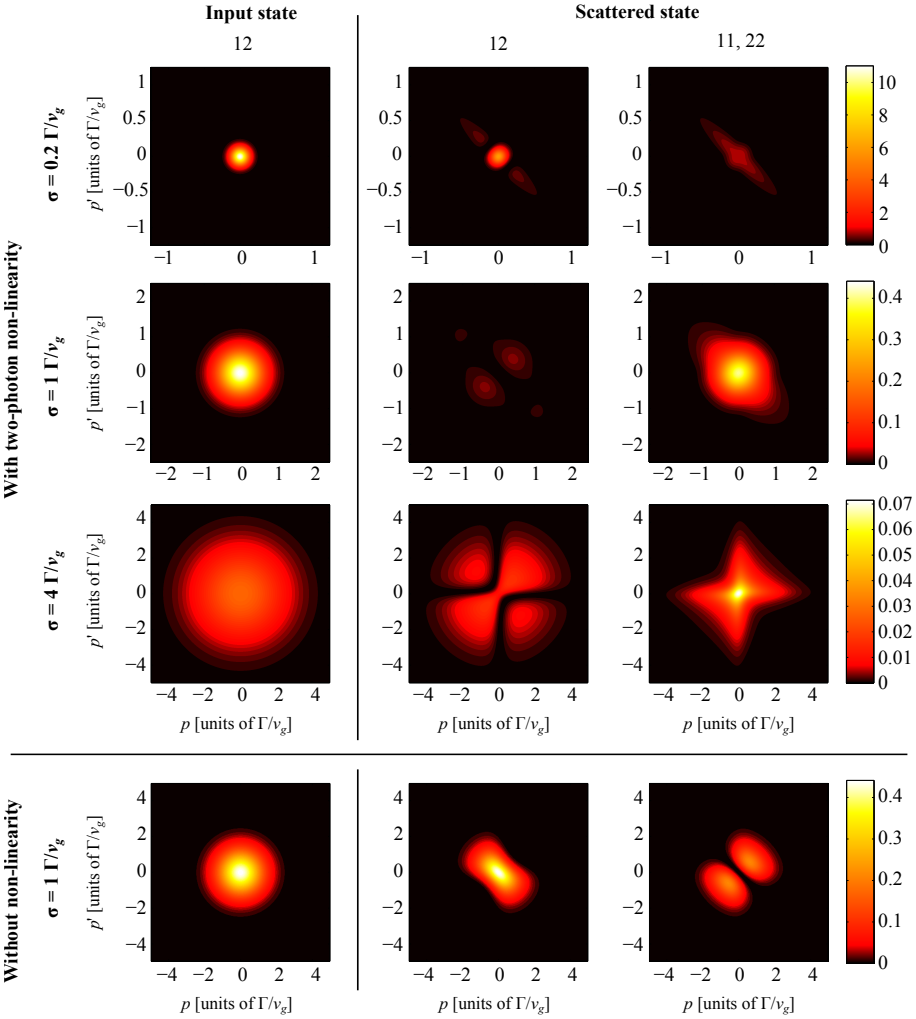

Figure 5.4: Intensity spectrum of an incoming Gaussian two-photon state for two counter-propagating photons (left column), and the resulting two-photon intensity spectra for the scattered state (middle and right columns) for photons scattering in different directions, 12, and where both photons propagate in the same direction, 11 (identical to 22), with $\Delta = 0$. The spectral width of the input pulses is varied: $\sigma = 0.2\,\tilde{\Gamma}$ (1st row), $\sigma = 1\,\tilde{\Gamma}$ (2nd row), and $\sigma = 4\,\tilde{\Gamma}$ (3rd row). The intensity spectra are also shown for scattering with the non-linearity turned off, $b_{12}(p, p') = 0$, using $\sigma = 1\,\tilde{\Gamma}$ (4th row).

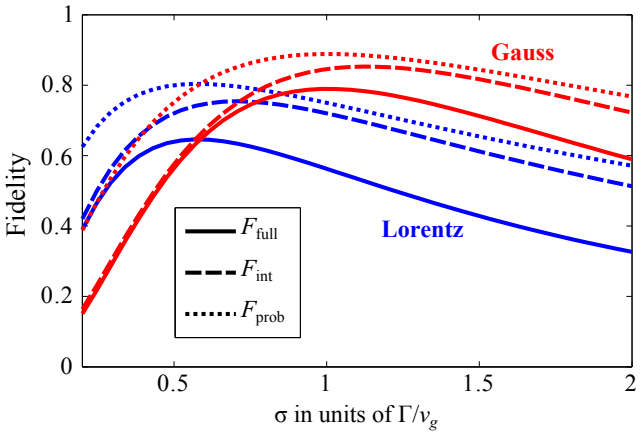

Figure 5.5: Fidelities from Eqs. (5.30)-(5.32) plotted for varying width of the input pulses, shown both for Gaussian and Lorentzian inputs on resonance with the emitter.

that the fidelity becomes lower, and most significantly so for pulses with a small spectral linewidth. This can be understood from Fig. 5.4, where we see that the scattered wavepacket for the spectrally narrow input (1st row) is clearly influenced by strong four-wave mixing effects. For pulses with larger widths, these effects are weaker, since a larger fraction of frequency components are detuned from the emitter transition and therefore interact only weakly.

Scattering-induced phase differences across the pulses may be examined by comparison of F_{int} and F_{full}. As illustrated in Fig. 5.5, these fidelities are almost equal for spectrally narrow pulses, whereas significant deviations are seen for spectrally broad pulses. This may be explained by considering the simpler single-photon scattering case. From Eq. (5.12), we see that a resonant, monochromatic pulse will be reflected with a phase shift of π, whereas spectrally broader pulses attain a phase shift from $\pi/2$ to $3\pi/2$ across the pulse spectrum. Thus, spectrally broad pulses experience larger decreases in the fidelity due to phase mismatching with our given desired state.

As the phase changes correspond to modifications to the spatial profile of the pulse, we specifically consider how the spatial pulse profile (here analogous to the temporal shape) is changed during the scattering process. To clearly illustrate the effect of the non-linear scattering on the spatial profile, we evaluate the photon density at a specific point of the photon wavepacket in the rotating frame, defined in the same way as in Eq. (4.9),

$$N_z(z,\infty) =_{t\to\infty} \langle\beta|a^\dagger(z)a(z)|\beta\rangle_{t\to\infty}, \tag{5.38}$$

where $a(z) = (2\pi)^{-1/2}\int_{-\infty}^{\infty} \mathrm{d}k\, a(k)\exp[\mathrm{i}kz]$ is the annihilation operator for an excitation at a position z in a frame rotating with the pulses. For Gaussian and Lorentzian input pulses, the photon density is plotted in Fig. 5.6. For both pulse shapes, we see that a delay occurs due to interaction with the emitter, and furthermore the non-linearity improves the similarity between the scattered and incoming field. The Gaussian pulse is observed to preserve its

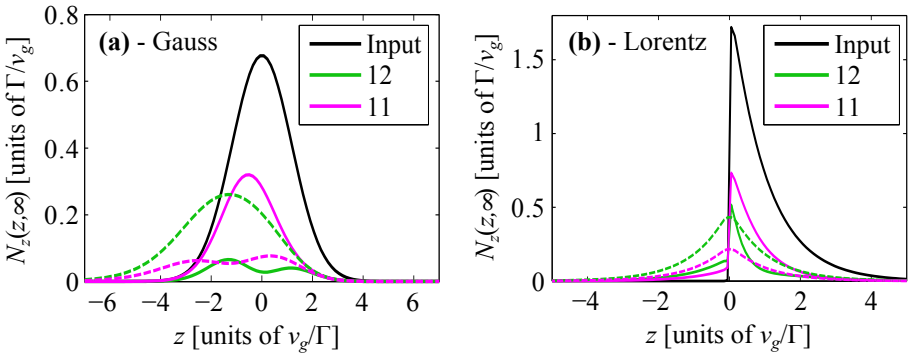

Figure 5.6: The photon density in the moving frame, $N_z(z,\infty)$, calculated for the input pulse and for photons in the same (11 identical to 22) or in different modes after the scattering (12) for resonant input pulses with $\sigma = 1\tilde{\Gamma}$ and $\Delta = 0$. The largest values of z correspond to the front part of the pulse, and the solid (dashed) lines include (do not include) the non-linear two-photon interaction, $b_{12}(p,p')$. (a) Gaussian wavepacket (b) Lorentzian wavepacket.

spatial symmetry, as compared to the Lorentzian input pulse. This is due to the fact that the part of the photon pulses which is absorbed by the emitter is re-emitted with an exponential shape that is spatially reversed compared to the input pulse, which explains why F_{prob} deviates significantly from F_{int} for large spectral linewidths in Fig. 5.5.

5.4 Summary

We have analytically demonstrated that the non-linearity of a two-level-emitter can induce strong pulse-dependent directional correlations (entanglement) in the scattered state of two initially counter propagating photons, as predicted numerically in Chapter 4. These correlations are maximized for photons with spectral widths comparable to that of the emitter, and also depend on the specific spectral shape of the photons. Furthermore, we have investigated how the spectra and phase of the photons are affected by the scattering process, and introduced different fidelity measures to quantify the similarity of the scattered and input photons. Interestingly, for photons with spectral widths comparable to the emitter linewidth (where the directional correlations are maximized), the non-linearity of the emitter acts to suppress changes in the spectra and phase of the photons. As such, even when taking all properties of the scattered state into account, a comparison to perfect directionally entangled photons with preserved spectra and phases gives fidelities as high as $\sim 80\%$ for Gaussian pulse shapes. A comparison of our fidelity measures indicates that when engineering photonic gate structures and other functionalities using two-level-emitters, it is important to also consider spectral and phase changes when determining the efficiency and scalability of non-linear photonic devices.

Compared to the wavefunction approach in Chapter 4, the scattering matrix approach is advantageous if one is only interested in the long-time scattered

state. This may be calculated computationally faster than in the wavefunction approach, whereas it necessitates a derivation of scatterer-specific one- and two-photon scattering matrix elements. This becomes complex for multi-component scatterers or spatially separated scatterers, as compared to the wavefunction approach. Thus, the method to analysing two-photon scattering on a non-linearity should be chosen depending on the specific problem and the desired information about the scattering process.

Chapter 6

Controlled phase gate

In this chapter we discuss how the results and understanding of non-linear two-photon scattering from the previous chapters may be employed in proposals for two-photon conditional gates and switches, where the presence of one photon influences the scattering of the second photon. Conditional two-qubit gates such as the CNOT gate or the controlled-phase (c-phase) gate are a fundamental building block in the universal set of gates operations required in the standard picture of quantum computing [3].

Using only beam splitters, phase shifters, and photon detectors, T. Ralph proposed in 2002 a scheme for a CNOT gate [122], where the non-linearities were obtained by projective measurements on ancilla arms. Due to its probabilistic nature, the succes probability of the gate is $1/9$, where a success is indicated by a specific measurement outcome in the ancilla arms. The gate has been experimentally implemented using free-space optics [16], and has also recently been implemented in an all-optical semiconductor platform using directional couplers and quantum dots in micropillars as single-photon sources [123]. A disadvantage with the gate is its probabilistic nature, as the low success rate have major influence is several subsequent gates are to be employed. One method to enhance the performance of these probabilistic gate is by quantum teleportation [15], which however relies on using multiple ancilla waveguides and photon detectors. As this quickly results in large structures for implementation, current research focusses on implementation the conditional gate operations in a deterministic setup instead.

Several recent experimental results demonstrate the possibility of creating deterministic controlled phase gates and photonic switches between the polarisation state of a single photon and the spin state of an emitter. It has both been demonstrated experimentally for Rubidium atoms coupled strongly to optical cavities [40, 124, 39] and recently also for a quantum dot inside a photonic crystal cavity [42]. By applying single-qubit rotations to the atom mediated by $\pi/2$-pulses from external lasers, the atom–cavity systems may work as conditional gates for qubit state encoded in the polarisation of two temporally separated photons. This was originally proposed by Duan and Kimble [125], and has been applied to a variety of systems, including also proposals with NV

centers [126].

Deterministic switching operations between two photons may also be realized using other encodings than in the polarisation degree of freedom. For an emitter strongly coupled to an optical cavity, the atom dresses the energy levels of the cavity, given rise to energy levels of the dressed cavity which are not equally spaced [24]. By using different frequencies of the control and the signal photons, the frequencies may be chosen such that the signal only may couple to the cavity if the control photon is present [44, 127, 128].

A different proposal by R. Johne et al. [129] describes a scheme for a controlled-phase gate for two indistinguishable, temporally separated photons. Here the control photon is captured as an excitation of a QD inside an optical cavity by electrically detuning the emitter out of resonance with the cavity. The emitter is detuned such that the energy for exciting the bi-exciton state of the QD exactly matches the energy of the incoming signal photon. Thus, the signal photon can only couple to the emitter if the control photon was present to excite the QD - giving the conditional operation. An advantage of using this scheme is that the non-linearity-induced distortions in the photon spectra as discussed in the previous chapters do not occur [130], as the photons do not scatter at the same time. We will look further into this type of gate in the next chapter.

In this chapter we propose an experimental setup for a deterministic controlled-phase gate for two uncorrelated, indistinguishable photons in the dual-rail representation, which employs two two-level emitters as non-linear components. The gate works best for input pulses with spectral linewidths comparable to the linewidth of the emitter, which is also where the largest non-linear interaction is expected, cf. the previous chapters. In this regime, the presence of one photon prevent the second photon from scattering on the emitter - in analogy with the effect discussed above for the strongly coupled emitter–cavity systems.

In contrast to the deterministic gates discussed above, our proposal does not rely on any external modulations such as lasers to prepare or alter the emitter state, and it does not need any dynamical trapping processes, which may be a large benefit when discussing implementations. We demonstrate a gate fidelity of almost 80 %, which primarily limited by the non-linearity-induced spectral changes.

In Section 6.1 the requirements for a controlled-phase gate is discussed, and we introduce the individual gate components. In Section 6.2 we introduce our gate proposal and evaluate the performance using the scattering matrix formalism introduced in Chapter 5. The results presented in this chapter are from an ongoing research collaboration with Mikkel Heuck and Prof. Dirk Englund from the Quantum Photonics Group at Massachusetts Institute of Technology.

6.1 The controlled phase gate

In a controlled phase (c-phase) gate, the state of a control qubit determines whether a signal qubit attains a phase shift of π or not [38]. Denoting the qubit

states by $|'0'\rangle$ and $|'1'\rangle$, an ideal c-phase would act on the combined qubit state as

$$\begin{aligned}
|'0_c'\rangle|'0_s'\rangle &\longrightarrow |'0_c'\rangle|'0_s'\rangle \\
|'0_c'\rangle|'1_s'\rangle &\longrightarrow \exp[i\theta_s]|'0_c'\rangle|'1_s'\rangle \\
|'1_c'\rangle|'0_s'\rangle &\longrightarrow \exp[i\theta_c]|'1_c'\rangle|'0_s'\rangle \\
|'1_c'\rangle|'1_s'\rangle &\longrightarrow \exp[i\theta_c+i\theta_s+i\pi]|'1_c'\rangle|'1_s'\rangle
\end{aligned}$$

with c (s) referring to the control (signal). Here it is implied that non-linear interaction occurs when both photons are in the '1' state, giving the additional phase shift of π. In a specific gate structure, each individual photon may also attain a phase of θ_s or θ_c when entering the gate in the '1' state compared to entering the gate in the '0' state. This is, however, without accounting for the presence of the other photon. The core of the c-phase gate is, however, that when both qubits are in the '1' state, an additional phase shift of π is gained on the total state, in addition to θ_s and θ_c, requiring non-linear interaction between the qubits.

In our proposal, each flying qubit is encoded in a dual-rail representation of propagating photon pulse, i.e. a photon may be in one of two waveguides, characterized by the '0' and '1' states respectively. For the c-phase gate to work optimally for pulsed input for our requirements, the scattered state at the output should fulfil:

- The control and signal photon must be distinguishable at the output arms. Thus, all scattering processes which have a probability of scattering both photons into either the control or signal arms, introduce errors in the gate operation, and these processes must be minimized.

- For the gate to be implemented in larger photonic circuits, the gate cannot alter the spectrum and temporal shape of the pulse, as this could decrease the performance of succeeding gates. Thus we require that the spectra of the control and signal photon pulses are changed as little as possible when passing the gate, i.e. by maximizing the fidelity between the input and output states, with the fidelity measures defined in Chapter 5.

- The gate-induced phase must be the same across the full spectral width of the pulse (delays taken into account). If it is not, the photon pulses might not interfere/interact perfectly with other photons, decreasing the performance in following gates.

6.1.1 Gate components

Three types of optical components are used to realize the c-phase gate: directional couplers, phase shifters and end-coupled emitters.

Directional coupler: The setup employs a directional coupler as shown in Fig. 6.1(a) which may be realized in various waveguide technologies, such as

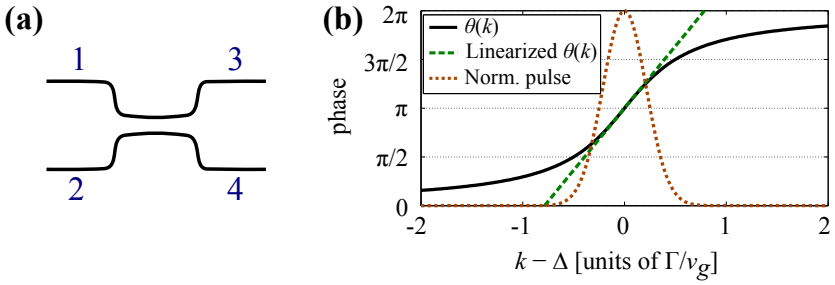

Figure 6.1: (a) Directional coupler, relating the state in the input arms, 1 and 2, to the output arms, 3 and 4, through the symmetrical beam splitter relation, cf. Eq. (6.1). (b) The phase attained by a single-photon wavepacket scattering on a lossless, end-coupled resonant emitter, $\theta(k)$, (black solid line) and a linearisation of $\theta(k)$, see Eq. (6.3) (green dashed line). By comparison, the spectrum of a resonant Gaussian wavepacket with spectral FWHM of $\sigma = \tilde{\Gamma}/2$ is shown (red dotted line) (where the intensity has been scaled to match the plotting window).

silica-on-silicon ridge waveguides [131], photonic ridge waveguide circuits in GaAs [132], and in photonic crystals waveguides [133]. The length of the coupling region is chosen such that the creation operators for the input and output states are related by the symmetrical beam splitter relation [132]

$$\begin{bmatrix} a_3^\dagger \\ a_4^\dagger \end{bmatrix} = \frac{1}{\sqrt{2}} \begin{bmatrix} 1 & \mathrm{i} \\ \mathrm{i} & 1 \end{bmatrix} \begin{bmatrix} a_1^\dagger \\ a_2^\dagger \end{bmatrix}, \tag{6.1}$$

Phase shifter: Phase shifters are exploited to alter the phase of the pulses by a momentum-dependent phase, $\varphi = k\delta L$, with δL being the additional optical path length, either induced by a change in the refractive index of the material or by a longer arm length. Spatially, the linear phase change is equivalent to a delay of the pulse (obtained by Fourier-transforming the output pulse).

End-coupled emitter: As illustrated in the previous chapters, the nonlinearity of a two-level emitter inside a waveguide induces very strong correlations in a two-photon state. We also observed that for pulses with finite temporal width, it is unavoidable that the incoming photon pulses scatter in different directions, giving higher demands for the gate structure. One way to circumvent this is by making the system one-sided, i.e. by placing the emitter close to a terminated waveguide, necessitating that the full pulse is reflected back. Furthermore, the interaction between the pulse and the emitter is increased, as the decay rate of the emitter is halved (cannot couple to waveguide modes propagating in both directions) [64], making it possible for a perfect (Lorentzian) single-photon pulse to excite the emitter fully. A trade-off using this one-sided setup is, however, that the input and output of the gates are in the same arms.

The frequency-dependent transmission coefficient of an emitter coupled to a chiral (with propagating restricted to a single direction) waveguide is [88, 63],

$$t(k) = \frac{k - \Delta - \mathrm{i}(\Gamma - \gamma)/(2v_g)}{k - \Delta + \mathrm{i}(\Gamma + \gamma)/(2v_g)}, \tag{6.2}$$

with k being the momentum in a frame rotating with the carrier frequency of the pulse. The momentum detuning of the emitter from the pulse is Δ, and Γ denotes the emitter decay rate (which is halved compared to the decay rate defined in Chapter 3). Emitter losses are introduced by the substitution $\Delta \to \Delta - \mathrm{i}\gamma/(2v_g)$ in the single-photon scattering elements, with γ being the loss rate of the emitter into other modes than the waveguide modes [63].

Some insight may be gained about the scattering-induced phase by considering the loss-less case. For $\gamma = 0$, $|t(k)| = 1$, and thus $t(k)$ may also be described by a complex phase, $t(k) = \mathrm{e}^{\mathrm{i}\theta(k)}$, such that an incoming single-photon pulse with a spectral wavepacket $\xi(k)$ results in a scattered wavepacket of $\xi_{\mathrm{scat}}(k) = \mathrm{e}^{\mathrm{i}\theta(k)}\xi(k)$. This phase is shown in Fig. 6.1 in the case $\gamma = 0$. If the incoming single-photon pulse has a carrier frequency corresponding to the emitter transition, $\Delta = 0$, and if the pulse has a sufficiently narrow spectrum compared to the linewidth of the emitter, $\theta(k)$ may be approximated by a Taylor expansion,

$$t(k) = \exp\left[\mathrm{i}\pi + \mathrm{i}4k/\tilde{\Gamma} + O(k^3)\right], \tag{6.3}$$

with $O(k^3)$ containing terms of third order or higher in k. Pulses with a narrow spectral width compared to the emitter linewidth will, apart from a constant phase shift of π, gain a phase of $4k/\tilde{\Gamma}$, which in time is exactly equivalent to a temporal delay of $\Delta t = 4/\Gamma$. This delay is caused by the interactions with the emitter due to absorption and re-emission. For spectrally broader pulses, higher order terms in k do have an influence and introduces different chirping effects, as seen from Eq. (6.3) and the discussion in Chapter 3.

6.2 Gate setup

Our proposal for a c-phase gate is illustrated in Fig. 6.2, which works for two uncorrelated single-photon pulses with the same spectral wavefuntion, where the control and single photon are represented in a dual-rail basis. The '1' arms (inner arms) are connected by a 50-50 directional coupler, and at each output port of the coupler is an end-coupled two-level emitter. The coupler creates a superposition state of two photon being either in the upper or lower arm on the right side of the beam splitter. Thus, when the photon state scatters on the emitters, it only contains component with two photons, and thus the full state is affected by the non-linearity. In this way, the non-linearity may be exploited the most. The outer arms ('0' arms) contain a phase shifter to compensate for delays in the '1' arms, as predicted by Eq. (6.3). Note, that due to the choice of directional coupler, the output port of the '1' control and signal states are flipped, as indicated in Fig. 6.2. A similar setup is discussed in [96, 134], but here with the purpose of using it as photon sorter, quantum non-demolition detector, and Bell-state analyzer.

As the gate proposal is one-sided, meaning that the input and output arms of the gate are the same, the whole setup may be "unfolded" to a chiral scheme (where the waveguides only allow propagation in one direction), if the overall phase due to the reflection is omitted. An important requirement is, however,

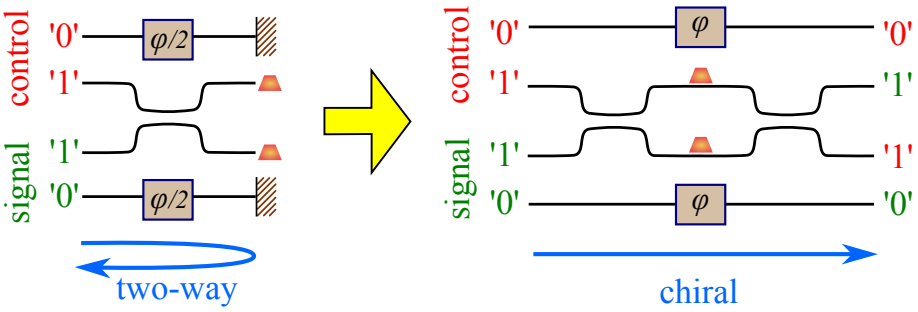

Figure 6.2: (Left) Proposal for controlled phase gate in the dual rail representation using a directional coupler, phase shifters, and two identical emitters placed close to two terminated waveguides, with identical coupling strengths to the waveguide modes. The hatched brown sections describe perfectly reflecting mirrors. (Right) The c-phase setup may be "unfolded" to a chiral scheme, if the overall phase induced by the reflection is omitted. Note that the '1' states in this scheme is interchanged at the output ports.

that the emitters are identical and couples to the waveguide modes with the same coupling strength. If this is not the case, the scattered photons will not interfere perfectly on the way back through the coupler, which will result in a decrease of the gate efficiency.

For the gate to work properly, the input states $|"0_c"\rangle|"0_s"\rangle$, $|"1_c"\rangle|"0_s"\rangle$, and $|"0_c"\rangle|"1_s"\rangle$, which induce only linear scattering effects, and the input state $|"1_c"\rangle|"1_s"\rangle$, which gives non-linear interaction, must all provide the desired output states in the c-phase gate. This may only be achieved perfectly if input and output photons of the gate have the same intensity spectrum and no undesired phase changes across the pulse, induced by scattering on the emitters. These scattering-induced changes are investigated below, treating the linear and non-linear case separately. The scattered states are calculated using the scattering matrix formalism introduced in Chapter 5.

6.2.1 Linear gate interactions

Apart from the $|"1_c"\rangle|"1_s"\rangle$ input, the c-phase gate in Fig. 6.2 behaves linearly, as two photons never are present simultaneously at the emitters.

The input state $|"0_c"\rangle|"0_s"\rangle$ simply attains a phase shift of $\varphi = k\delta L$ for each photons due to the phase shifters.

The input states with a single photon in one of the '1' arms, $|"0_c"\rangle|"1_s"\rangle$ and $|"1_c"\rangle|"0_s"\rangle$, scatters as

$$\int_{-\infty}^{\infty} \mathrm{d}k\, \xi(k) a^{\dagger}_{c/s,1}(k)|\phi\rangle \rightarrow \int_{-\infty}^{\infty} \mathrm{d}k\, [-it(p)]\, \xi(p) a^{\dagger}_{c/s,1}(p)|\phi\rangle \tag{6.4}$$

whereas the other photon attains a phase shift of φ. The factor of $-\mathrm{i}$ appears from coupling forth and back through the directional coupler, as seen in Eq. (6.1).

In the scattering with the emitter, it is important that the spectrum is unchanged and that the phase across the pulse is constant (up to a linear

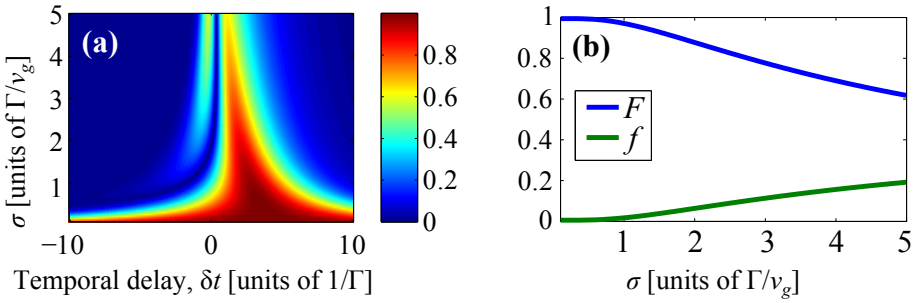

Figure 6.3: (a) Fidelity between an incoming Gaussian pulse with spectral width σ and the state scattered on a resonant two-level emitter close to a terminated waveguide. A temporal delay, δt, is allowed in the fidelity calculation. (b) The maximal F at a given σ and the corresponding value of f.

phase, as we may account for delays by the phase shifters in the '0' arms). The similarity between the spectral wavepacket of the input and scattered photon is measured by the earlier introduced fidelity between the spectral wavefunction of the gate input, $\xi(k)$, and the output wavefunction with the spectral wavepacket $t(k)\xi(k)$. According to the discussion in Section 5.2.1, the relevant fidelity measure to use would be $F_{\text{spat}}(\delta z)$, as it takes spectral deviations between the pulses into account, but allows a spatial/temporal detuning of the pulses in the output arms (which we may account for using the phase shifters). We use a shorthand notation for $F_{\text{spat}}(\delta z)$ in this chapter,

$$F(\delta z) = \left| \int_{-\infty}^{\infty} \mathrm{d}p\, t(p) |\xi(p)|^2 \mathrm{e}^{\mathrm{i}\delta z \cdot p} \right|^2 \tag{6.5}$$

where the spatial delay is analogous to a temporal delay of $\delta t = \delta z / v_g$. Assuming Gaussian wavepackets with a spectral bandwidth (FWHM of the intensity spectrum) of σ as given in Eq. (3.12b), the resulting fidelity for a photon resonant with the emitter, $\Delta = 0$, is illustrated in Fig. 6.3(a) by plotting F as a function of σ and δt. The fidelity is maximized in the continuous wave limit, $\sigma \to 0$, for all delays due to the fact that two plane waves overlap perfectly. In the regime $\sigma \sim \tilde{\Gamma}$, where non-linear interactions are expected to be the strongest, a high value of F may still be achieved. As expected from Eq. (6.3), the high fidelities are obtained at delays corresponding to $\delta t \sim 4/\Gamma$ when $\sigma \lesssim \tilde{\Gamma}$.

Apart from having a large F, it is important that the phase across the pulse (apart from a linear phase change - corresponding to a delay) is not changes by the scattering event. As a measure to compare phases between the incoming and scattered photons, we introduce

$$f = \frac{1}{4} \int_{-\infty}^{\infty} \mathrm{d}p \left| \xi(p) + t(p)\xi(p) \mathrm{e}^{\mathrm{i}v_g \delta t \cdot p} \right|^2 . \tag{6.6}$$

which is evaluated at the value of δt which maximizes F. With this measure, $0 \leq f \leq 1$, with $f = 1$ corresponding to two pulses being in phase at all k, and $f = 0$ to pulses being out of phase by exactly π at all values of k. The maximal

value of F at a specific σ is plotted together with f in Fig. 6.3(b) as a function of σ. For small values of σ, f is close to zero, as expected from Eq. (6.3), as the scattered pulse attains a constant phase of π upon scattering.

Summarizing the linear scattering results, a single photon in one of the '1'-arms attains a phase shift of π and a temporal delay. The linear operations work optimally when the spectral width of the incoming pulses is much smaller than the emitter linewidth. In the regime, where the non-linearities may be addressed the best $\sigma \sim \tilde{\Gamma}$, the pulse spectrum is still preserved with more than 95% fidelity as seen in Fig. 6.3, if we choose the optimal delays for the emitter-induced temporal delay. This may be done by tuning the induced delay in the phase shifters to match the emitter-induced delay.

6.2.2 Non-linear gate interactions

The non-linear interaction occurs for the input state $|"1_c"\rangle|"1_s"\rangle$. The non-linear scattering is treated in the same way as in Chapter 5, but here we are considering a chiral waveguide [66], and we take the directional coupler into account when calculating the scattered state of the entire gate. The gate input for two uncorrelated, identical photons and the corresponding gate output are

$$\begin{aligned} |\psi_{\text{in}}\rangle &= \int_{-\infty}^{\infty} \mathrm{d}k \int_{-\infty}^{\infty} \mathrm{d}k'\, \xi(k)\xi(k') a_{c1}^{\dagger}(k) a_{s1}^{\dagger}(k')|\phi\rangle \\ \rightarrow |\psi_{\text{scat}}\rangle &= -\int_{-\infty}^{\infty} \mathrm{d}p \int_{-\infty}^{\infty} \mathrm{d}p'\, \beta_{\text{scat}}(p,p') a_{c1}^{\dagger}(p) a_{s1}^{\dagger}(p')|\phi\rangle \end{aligned} \tag{6.7}$$

with

$$\beta_{\text{scat}}(p,p') = \beta_{\text{scat}}^{\text{linear}}(p,p') + \frac{1}{2} b(p,p') \tag{6.8}$$

with the linear contribution $\beta_{\text{scat}}^{\text{linear}}(p,p') = t(p)t(p')\xi(p)\xi(p')$ and a non-linear scattering contribution with

$$b(p,p) = \int_{-\infty}^{\infty} \mathrm{d}k\, \xi(p)\xi(p') B_{pp'k(p+p'-k)} \tag{6.9}$$

where $B_{pp'k(p+p'-k)}$ is defined in Eq. (5.33).

For the c-phase gate to work properly, the scattered state of Eq. (6.7) must differ by an overall phase of π compared to the linear case, where the two photons do not interact, i.e. to a scattered state as in Eq. (6.7) but with $\beta_{\text{scat}}^{\text{linear}}(p,p')$ instead of $\beta_{\text{scat}}(p,p')$. As before, the pulse spectrum must also remain unchanged. To quantify the scattering-induced effects, we employ two-photon versions of the fidelities from Eqs. (6.5) and (6.6),

$$F = \left| \int_{-\infty}^{\infty} \mathrm{d}p \int_{-\infty}^{\infty} \mathrm{d}p' \left[\beta_{\text{scat}}^{\text{linear}}(p,p')\right]^{*} \beta_{\text{scat}}(p,p') \mathrm{e}^{\mathrm{i}v_g \delta t (p+p')} \right|^2 \tag{6.10}$$

taking into account that each photon may be delayed by an identical temporal delay of δt, and

$$f = \frac{1}{4} \int_{-\infty}^{\infty} \mathrm{d}p \int_{-\infty}^{\infty} \mathrm{d}p' \left| \beta_{\text{scat}}(p,p') + \beta_{\text{scat}}^{\text{linear}}(p,p') \mathrm{e}^{\mathrm{i}v_g (p+p')\delta t} \right|^2 \tag{6.11}$$

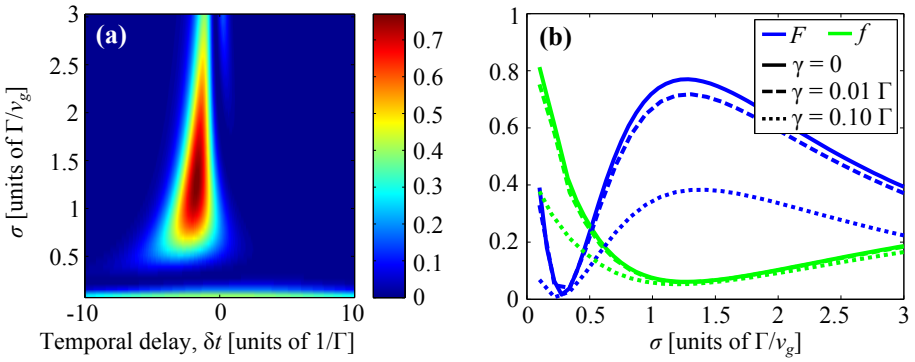

Figure 6.4: (a) The fidelity F for the scattered two-photon state for a gate input of $|"1_c"\rangle|"1_s"\rangle$ compared to a similar setup with the non-linearities artificially turned off, assuming $\gamma = 0$. The input pulses are resonant with the emitter and have a Gaussian spectrum with a spectral width σ. The temporal delays describes the delay of $\beta_{scat}^{linear}(p,p')$ compared to $\beta_{scat}(p,p')$. (b) The maximal F at a given σ and the corresponding value of f. The fidelities are evaluated for different loss rate in the emitter, $\gamma = 0$ (solid line), $\gamma = 0.01\Gamma$ (solid line), and $\gamma = 0.10\Gamma$ (dotted line).

with f is evaluated at the delay which maximizes F, in similarity with the linear cases.

The calculated fidelities are shown in Fig. 6.4. The largest values of F are obtained at $\sigma \sim 1.2\tilde{\Gamma}$, consistent with the results in Chapter 5. Most importantly we see that for these values of σ, f is very close to zero, demonstrating that the gate actually works as a controlled phase gate, as the non-linearity induces a phase difference of π. In the linear case, both photons would attain a phase shift of π according to Eq. (6.3), giving a total of 2π for the two-photon state. In the non-linear case, one photon "blocks" the coupling to the emitter for the second photon, and thus only a single phase shift of π is attained.

In Fig. 6.4(a), the maximal fidelities all appear for negative values of δt. This implies that when the non-linearity is "off", the pulse will actually propagate slower through the gate than when the non-linearity is "on". This is due to the fact that both photons may interact with the emitter in the linear case and attain large delays, than compared to when the non-linearity is "on".

The limiting factor in the gate functionality is two fundamental properties in the scattering. First, the phase gained upon scattering from the coefficient $\bar{t}(k)$ introduce phase differences across the pulse. When the pulses are sufficiently narrow, the attained phase is linear, which we may correct for by introducing phase shifters. However for spectrally broader pulser, the scattering induces other variations in the phase of the scattered pulse, which decreases the fidelity. From this point of view, the input pulse should be as narrow as possible, but this brings us to the second point: The non-linearity is only efficient when the bandwidth of the pulses is similar to the emitter linewidth. Thus we cannot use spectrally narrow pulses, and must accept the error from the scattering-induced changes in phase. However, the non-linearity impose changes on the spectrum due to four-wave mixing as demonstrated in Chapter 4, which also

results in lower gate fidelities.

In the optimal case, the fidelity becomes almost 80 %, as shown Fig. 6.1(b), when accounting for the non-linearity-induced change in the pulse shape and phase. When taking emitter losses into account, F decreases even further, and for loss rates of $\gamma = 0.1\Gamma$, F is reduced to 40%. Thus it is very important to effectively couple the emitter to the waveguide. For a semiconductor quantum dot inside a photonic crystal waveguide, coupling efficiencies between the emitter and the waveguide of up to 98% has been achieved [45].

6.3 Summary

We have proposed a setup for a deterministic controlled phase gate for two identical, uncorrelated single photon pulses, which exploits the intrinsic non-linearity of two-level emitters. Our calculations demonstrate fidelities for the gate operations just below 80%. This is limited by linear scattering-induced changes in the phase of the pulse, and also by non-linearity-induced changes in the pulse spectrum and phase, as discussed in Chapter 4. The interaction with the emitters also causes a delay in the '1'-arms, but this is accounted for by phase shifters in the '0' arms.

The setup depends strongly on having two *resonant* emitters, which couples with *identical* strengths to the waveguides. If the emitters are not exactly identical, the gate performance would decrease, as it relies on perfect interference between the states scattered on the two emitters. If only a single emitter were used in the present setup, only half of the pulse would be affected by the non-linearity, decreasing the performance of the gate, especially deteriorating the interference at the directional coupler after the scattering. In standard quantum dot samples, quantum dots are grown at random positions and with different resonant frequencies [61], and thus it may be difficult to fulfil both criteria at the same time. Site-controlled growing of the quantum dots has been demonstrated [135, 136], although it still appears a challenge to precisely control the transition frequencies of the individual dots. Another possibility would be to trap identical atoms close to the facets of the inner waveguides [62, 39], as they by nature would be resonant. This may, however, not be suitable for on-chip integration in larger optical circuits.

As the input and output arms are the same in Fig. 6.2, an implementation of the gate necessitates the use of optical components such as circulators [137] to direct the output into new waveguides. A way to circumvent this is to exploit "uni-directional" non-linearities, i.e. non-linearities which only couple to a subset of modes propagating in *one* direction of the waveguide. With these, the chiral scheme in Fig. 6.2 could be directly implemented. An example of such is chiral spin-photon interfaces, which has recently has been demonstrated experimentally for a quantum dot inside a photonic crystal waveguide using polarized light [138]. Other candidates are whispering-gallery-type resonators, such as ring resonators, microtoroids, microdisks or microspheres [139] created in a material with a strong non-linearity (typically a $\chi^{(2)}$ non-linearity). As we will discuss in the following chapter, recent developments allow fabrication of very high Q-resonator cavities. If the intrinsic non-linearity dominates the losses,

a splitting of the energy spectrum will appear, in similarity with strong coupling in an emitter-cavity system. If the coupling between counter-propagating modes in the ring is zero, the transmission of a strongly non-linear resonator may be described by Eq. (6.2), making ring resonators viable candidates for the proposed gate scheme. Non-linear optical cavities do, however, also suffer from the demonstrated non-linear processes which alter the spectrum of the scattered photons [119].

The proposed fidelity of the deterministic gate of almost 80 % is relatively good, compared to the fact that no external manipulations are required during the gate operation, in contrast to many other proposals. The fidelity is, however, difficult to improve further using only passive components, as it is limit by intrinsic properties of the photon scattering.

Chapter 7

Controlled phase gate - Using dynamical capture

The performance of the controlled phase gate in the previous chapter was deteriorated by side-effects when two photons of the same frequency scatter on a non-linearity at the same time. In this chapter we investigate possibilities of circumventing these side-effects by employing the recently proposed "interaction-free" gate schemes [140, 141], which exploit the quantum Zeno blockade (QZB) [142]. The QZB occurs when frequent or continuous measurements are performed on a quantum system, which will inhibit the unitary evolution of the system. In optical systems, the "measurements" may be facilitated by a strong optical non-linear interaction with another photon. We will specifically consider an optical cavity with a large quadratic ($\chi^{(2)}$) material non-linearity, giving rise to sum-frequency generation [143]. As will be demonstrated in the following, the presence of one (control) photon in the cavity will prohibit the coupling of another (signal) photon into the cavity, as the control photon continuously "probes" the cavity. In that sense, the QZB is analogous to the photon blockade in a strongly coupled emitter–cavity system [24].

Recently Sun et al. [141] made a theoretical proposal of a c-phase gate, which employs a lithium niobate (LiNbO3) ring resonator, as LiNbO3 has a high intrinsic ($\chi^{(2)}$) non-linearity. In the scheme, a temporally broad (control) photon probes the cavity during the time where second (signal) photon scatters. When the control is "on", it prohibits the signal for entering the cavity, giving the conditional gate operation and predicts fidelities of up to 98 % (although they do not take into account that the temporal shape of the control is reversed). The scheme proposed by Sun et al. does however not work for identical photons as the gate in Chapter 6, as their proposal relies on using photons of different frequencies. This enables the signal and control photon to be distinguished at the output, which would not be possible when using two identical photons, and the gate does not seem suitable for large-scale integration in general quantum circuits.

A method to overcome this when using two identical photons is proposed in a scheme for a c-phase gate by Johne et al. [129], in which the control

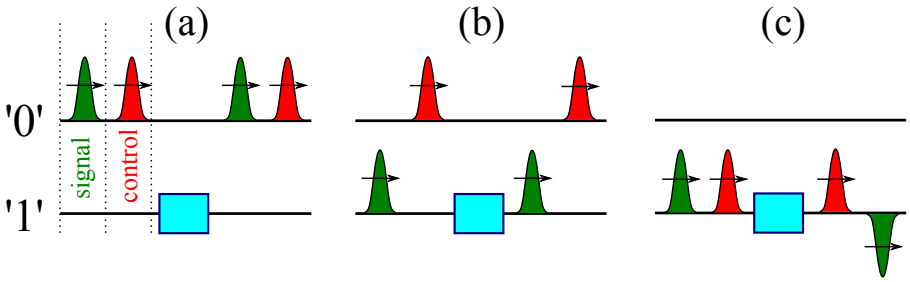

Figure 7.1: Phenomenological gate structure of the dynamical capture c-phase gate, with each qubit being encoded in a one-way dual-rail representation, and where the control (red) and signal (green) photons are distinguished by a temporal separation. The control pulse may be dynamically captured in the yet unspecified object indicated by the blue box. (a) Both photons in the '0' state goes through the gate unaffected. (b) Ideally the signal photon has the same phase before and after the scattering, as the control is in arm '0'. (c) If both photons are in the '1' arm, the presence of a captured control photon impose a phase shift of π on the signal. Note than if the control photon is in '1', the temporal ordering of the pulses is reversed at the output [129].

photon and signal photon are distinguished by a temporal separation in the waveguide. The scheme employs a method where the firstly arriving (control) photon is captured and stored in a state with another frequency, as illustrated phenomenologically in Fig. 7.1. When considering two photons of the same frequency, this shifting of frequency is necessary; otherwise a capture of the control photon would also mean that the interaction channel for the signal would be shut off, by which the non-linear interaction cannot occur. In Ref. [129] the scattering object is facilitated by a QD inside an optical cavity. The QD is detuned exactly to the point where the frequency of the succeeding signal photon matches the bi-exciton transition in the QD — which it may only couple to, if the control is present. After the scattering of the signal photon, the control photon will be released again, and thus no frequency-mixing processes like the four-wave mixing process we allowed during the gate operation, predicting fidelities of close to 90 % for an ideal loss-less QD [129].

In this chapter we discuss if it would be feasible to combine the idea of Sun et al. [141] and Johne et al. [129]. One major benefit of using a ($\chi^{(2)}$) compared to a QD in the gating scheme is that it is not restricted to low-temperature operations due to phonon coupling. Furthermore the rings have an inherent uni-directional scattering into only a single direction of the waveguide, and thus no combination of end-coupled QDs and circulators are necessary, as in the proposal in Chapter 6. However, the dynamical capture scheme sets requirements of the possibility of tuning the frequency of the resonator modes [144, 145, 146]. We first discuss the possibility of achieving sufficiently high non-linear coefficients in Section 7.1. Secondly we focus on the full gate operation, which is divided into several stages: capture of control photon, scattering of signal photon, and release of control photon. In Section 7.2 we estimate the efficiency of the individual steps. We demonstrate how a theoretically larger

fidelity may be obtained using this gate scheme as compared to the passive scheme in Chapter 6, but is also sets high fabricational requirements on the ring properties and timing possibilities during the gate operation.

The research presented in this chapter is from an ongoing research collaboration with Mikkel Heuck and Prof. Dirk Englund from the Quantum Photonics Group at Massachusetts Institute of Technology.

7.1 Requirements for ring-resonator non-linearity

In this section we estimate the requirements on the magnitude of the non-linearity compared to the losses in order for the QZB scheme to work. To do so, we specifically consider three energies in the ring resonator, ω_1, ω_2, and $\omega_3 = \omega_1 + \omega_2$, and we assume the that a single non-degenerate mode exists at each frequency. In ring resonators, sum-frequency generation may populate the sum-state, but an additional condition apart from conservation of energy has to be fulfilled, namely quasi-phase matching (QPM) condition. For disk resonators, QPM is usually obtained by a periodical poling of the disk [147, 148, 141]. In reality it is possible to obtain a structure with a set of frequencies as stated above, but it requires numerical (and sometimes analytical, when possible) investigations for the specific structure to find possible sets of $\{\omega_1, \omega_2, \omega_3\}$ [149, 150, 141].

Following Ref. [141], the Hamiltonian of the three-mode system may be described by

$$H = \sum_{j=1}^{3} \hbar\omega_j a_j^\dagger a_j + \hbar\left(U a_3^\dagger a_2 a_1 + U^* a_1^\dagger a_2^\dagger a_3\right), \tag{7.1}$$

where U is the non-linear coupling coefficient describing sum-frequency generation between the considered resonator modes. It has the form

$$U = \frac{\chi^{(2)}}{2}\sqrt{\frac{\hbar\omega_1\omega_2\omega_3}{\epsilon_0}}\int_V \mathrm{d}\mathbf{r}\, D(\mathbf{r})\Phi_1(\mathbf{r})\Phi_2(\mathbf{r})\Phi_3^*(\mathbf{r}), \tag{7.2}$$

with $\chi^{(2)}$ being the non-linear coefficient, $\Phi_j(\mathbf{r})$ the spatial mode profile of mode j, and $D(\mathbf{r})$ being a function describing the spatial dependence determined by the fabricated QPM pattern [141, 149]. Thus, a high value of U depend on a high value of the non-linear coefficient, but also on the modal overlap between the spatial wavefunctions of the three modes. As detailed calculations of possibly attainable values of U are given in Ref. [141] for a LiNbO3 resonator, we will not elaborate further on the calculation details here, but simply refer to their calculations.

Eq. (7.1) is derived under a no-loss assumption. However, losses of the cavity system may be included as coupling to external reservoirs for each of the three ring modes according to Refs. [149, 70, 151], giving an effective Hamiltonian on the form

$$H_{\text{eff}} = \sum_{j=1}^{3} \hbar\tilde{\omega}_j a_j^\dagger a_j + \hbar\left(U a_3^\dagger a_2 a_1 + U^* a_1^\dagger a_2^\dagger a_3\right), \tag{7.3}$$

with $\tilde{\omega}_j = \omega_j - \mathrm{i}\gamma_j/2$, where γ_j is the loss rate of energy in mode j in the resonator. If the ring is initially populated by two photons, one with frequency ω_1 and one with frequency ω_2, the system state is

$$|\psi(t)\rangle = C_{12}(t)a_1^\dagger a_2^\dagger|\phi\rangle + C_3(t)a_3^\dagger|\phi\rangle, \tag{7.4}$$

with $|\phi\rangle$ describes the vacuum state, and where the expansion coefficient are not normalized, due to the presence of loss. The temporal evolution of the system is determined by the time-dependent Schrödinger equation, $\mathrm{i}\hbar\partial_t|\psi(t)\rangle = H_{\mathrm{eff}}|\psi(t)\rangle$, providing equations of motion for the expansion coefficients,

$$\partial_t C_{12}(t) = -\mathrm{i}(\tilde{\omega}_1 + \tilde{\omega}_2)C_{12} - \mathrm{i}U^* C_3(t), \tag{7.5}$$

$$\partial_t C_3(t) = -\mathrm{i}\tilde{\omega}_3 C_3 - \mathrm{i}U C_{12}(t). \tag{7.6}$$

The corresponding eigenvalues of the differential equation system are

$$\lambda_\pm = -\left(\mathrm{i}\omega_3 + \sum_{j=1}^{3}\frac{\gamma_j}{4}\right) \pm \mathrm{i}\sqrt{|U|^2 - \left(\frac{\gamma_1+\gamma_2-\gamma_3}{4}\right)^2}. \tag{7.7}$$

In similarity with the Jaynes Cummings model, two regimes exist describing the dynamical evolution of the system. If the non-linearity is strong, $4|U| > \gamma_1 + \gamma_2 - \gamma_3$, two new non-degenerate eigenstates form, $|\lambda_-\rangle$ and $|\lambda_+\rangle$, being superpositions between the two states $a_1^\dagger a_2^\dagger|\phi\rangle$ and $a_3^\dagger|\phi\rangle$, see Fig. 7.2(a,b). These levels may be properly resolved if the splitting between the new states is much larger than the loss-induced broadening, which from Eq. (7.7) occurs when $|U|^2 \gg [(\gamma_1+\gamma_2)^2 + \gamma_3^2]/8$. If U is sufficiently large as illustrated in Fig. 7.2(b), the splitting may be exploited in the c-phase gate in the way, that when a control photon proves the cavity, an incoming signal photon cannot couple, giving the conditional operation in the gate.

The task is now to determine realistic values for U and the loss rates for this specific configuration. The needed calculations for the non-linear coefficient in a LiNbO3 resonator have already carried out by Sun et al. in Ref. [141]. Here the magnitude of the non-linear parameter, U, is estimated from the mode profiles of a whispering gallery mode using Eq. (7.2), based on calculations from [152]. A figure of merit for the non-linear parameter is $\chi^{(2)}Q/V$, with Q being the quality factor of the resonator more and V the mode volume. A realistically obtainable value[1] of U is estimated to be $U = 337\,\mathrm{MHz}$ for a disk LiNbO3 resonator with a diameter of $40\,\mu$m, using the available micro-fabrication technology. We assume that one of the loss rates is dominating the others, denoted by γ, e.g. corresponding to a mode which couples to a waveguide mode, as we will discuss below. For the gate to work properly, a maximum allowed loss rate is $\gamma_{\max} = 2\sqrt{2}|U|$. Assuming that the wavelength of the light is $\lambda = 1.31\,\mu$m, and that the decay rate of all modes is identical, the minimal quality factor of each mode must be $Q_{\min} = \omega_0/\gamma_{\max} = 2\pi c/(2\sqrt{2}|U|\lambda n_{\mathrm{ref}}) = 7\times10^5$, using a the refractive index of lithium niobate of $n_{\mathrm{ref}} = 2.22$ [153].

[1] In Ref. [141] they even use a value of 610 MHz in their theoretical calculations, although this seems large compared to realistically obtained values nowadays. It may, however, be possible to achieve soon with the rapid improvements in micro- and nanofabrication.

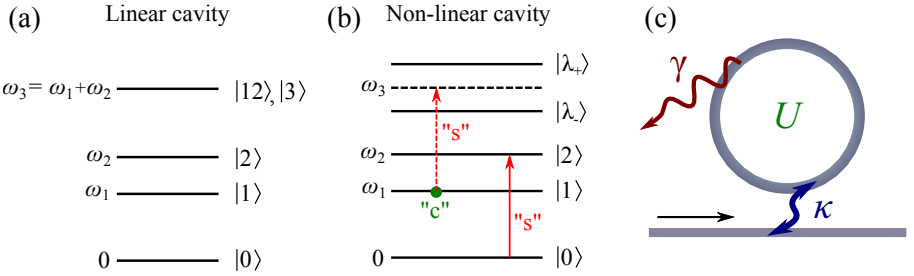

Figure 7.2: (a) Level scheme for a linear cavity, which have transitions corresponding to the frequencies ω_1, ω_2, and $\omega_3 = \omega_1 + \omega_2$. (b) Level scheme for a non-linear cavity where the non-linear coefficient exceeds the losses, which results in a splitting of the sum-frequency level due to the QZB, according to Eq. (7.7). If a control photon (green) of frequency ω_1 is present in the cavity, a signal photon (red) with frequency ω_2 cannot couple to the resonator. (c) A non-linear ring resonator coupled to a one-dimensional waveguide, with indications of the rate of population transfer to/from the ring, κ, and a loss rate of population out of the system, γ (which may be different for each cavity mode).

The quality factor of a resonator mode may be divided into two contributions, $Q^{-1} = Q_i^{-1} + Q_c^{-1}$, where Q_i is given by the intrinsic losses and Q_c is given by the coupling rates to other external modes, e.g. to a waveguide. The intrinsic losses are typically bending losses and absorption. Due to the high refractive index of LiNbO3, the bending losses are not the limiting factor on Q_i [154]. The limiting factor is in general material absorption, which according to Ref. [141] has a reasonable limitation of $Q_i \gtrsim 10^9$ with the existing structures. To overcome the internal losses, Q_c should be less than $\sim 10^8$.

In our proposal, the non-linear resonator is be coupled to a one-dimensional waveguide, corresponding to the functionality of the blue box in Fig. 7.1. In that case Q_c will be directly related to the decay rate of the energy in the ring into the waveguide modes, κ, as $Q_c = \omega/\kappa$, with ω being the carrier frequency of the pulses. This coupling may be realized physically e.g. by coupling to integrated planar waveguides [155], demonstrating a Q above 10^8. To specifically consider the effect of the non-linear interaction, we make the crude approximation that the control photon is already "trapped" in the cavity at a frequency ω_1 (i.e. it cannot couple to the continuum of waveguide modes) when the signal is impinging – we will comment on this approximation later on. We also for simplicity assume that the sum-frequency state at ω_3 cannot couple to the waveguide modes. With these approximations, the dynamics may be described by the single-photon scattering model in Chapter 3, where the total Hamiltonian now to be given by

$$H_{\text{wg–one ring}} = H_{\text{eff}} + \int_0^\infty \mathrm{d}k\, \hbar\omega(k) a^\dagger(k) a(k) + \hbar\sqrt{\frac{\kappa v_g}{2\pi}} \int_0^\infty \mathrm{d}k \left[a^\dagger(k) a_2 + a_2^\dagger a(k) \right], \qquad (7.8)$$

where H_{eff} is given in Eq. (7.3), and with $a(k)$ being the annihilation operator

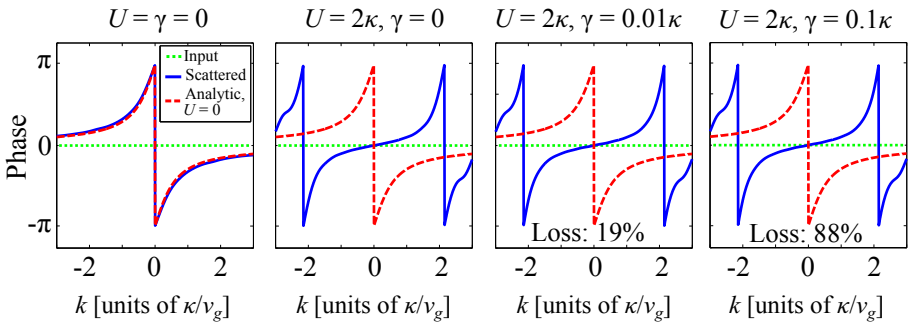

Figure 7.3: Phase of an incoming single-photon pulse (green dotted line) and the scattered photon (solid blue line) when scatterings from a waveguide onto a non-linear ring resonator with the non-linear coefficient of U. The loss rate, γ, is assumed to be the same for each mode of the ring. In the cases with $\gamma \neq 0$, the loss of population during the scattering is indicated in the plot, calculated for an incoming pulse with a bandwidth identical to the emitter linewidth.

of a plane wave mode in the waveguide with momentum k and energy $\omega(k)$. Furthermore the QD decay rate has been replaced by κ, and the lower bound on the integration is 0, as we assume no back-scattering from the ring. In deriving Eq. (7.8), we furthermore assumed a constant coupling parameter from the gate cavity to all modes in the waveguide equal to $\sqrt{\frac{\kappa v_g}{2\pi}}$, in similarity with Section 3.2.

According to the proposed gate scheme in Fig. 7.1, the phase of the signal photon should by changed by π, if the control is present in the resonator. In order to estimate the gained phase, we employ the numerical model in Chapter 3. In Fig. 7.3 we sketch the phase gained at the different frequency components of the pulse for different values of U and γ, assuming that the internal losses for all modes are identical $\gamma = \gamma_1 = \gamma_2 = \gamma_3$ (the coupling to the waveguide modes is described by κ, which thus is not included in the rate γ_2).

At resonance, a narrow-bandwidth signal photon will gain a phase shift of π when $U = 0$, i.e. corresponding to the absence of a captured control photon. When $U \neq 0$, the signal can no longer couple to the cavity and does not gain a π phase shift. As discussed in the previous chapter in Fig. 6.1(b), the bandwidth of the incoming pulse must be sufficiently narrow compared to the spectral linewidth of the resonator mode, as the gate to a maximum allows a linear phase change across the pulse (corresponding to a temporal delay, which may be accounted for). Furthermore, U must be sufficiently large compared to the pulse bandwidth such that the linear phase condition is still fulfilled across the spectrum of the incoming pulse, if a control photon is present in the cavity. As demonstrated in Fig. 7.3, the gained phase remains almost the same for the shown loss rates of up to at least $\gamma = 0.1\kappa$. The limiting factor here is the fact that more than 80 % of the pulse energy is lost.

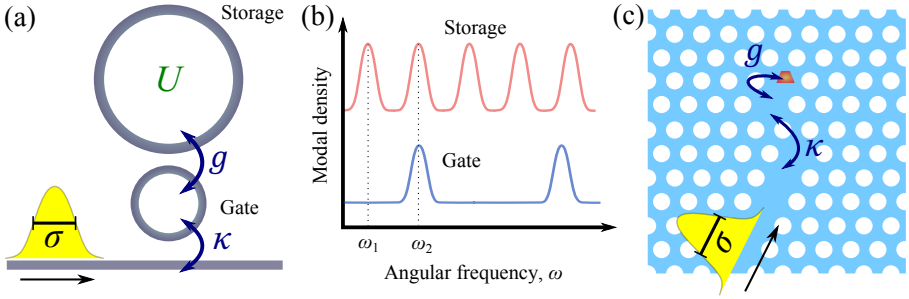

Figure 7.4: (a) Double-resonator system, in which a gate ring is introduced as compared to Fig. 7.2(c). The coupling rate from the waveguide to the first ring is still denoted κ, but an additional coupling occurs between the rings, described by the coupling strength g. (b) Desired modal density in the storage and gate rings at the time where the signal photon scatteres with frequency ω_1 (with a possible control photon at ω_2) (c) An equivalent system, consisting of QD inside an end-coupled optical cavity, as described in Ref. [129].

7.2 Dynamical capture

Above we have estimated the requirements for the non-linearity and losses for the part of the gate operation where a control photon may have been captured and the signal photon is impinging. However, with the one-ring setup in Fig. 7.2(c), the control excitation may in principle decay into the continuum of waveguide modes as nothing hinders the coupling. In order to prevent this, we introduce a *gate*-ring as sketched in Fig. 7.4(a,b). When the control photon is captured at a mode with frequency ω_1 in the *storage* (inner) ring, it cannot couple to the waveguide, as no mode is present in the gate at that frequency. In contrast, an incoming signal photon with frequency ω_2 may couple to a mode in the storage ring through the gate ring. This capture principle is the same as for an emitter inside an optical cavity at the end of a waveguide [129], as illustrated in Fig. 7.4(c).

The full scheme will thus be as follows: First a incoming control photon of frequency ω_2 is captured in the storage cavity by detuning the mode of the captured photon to a frequency ω_1. Secondly, the signal photon of frequency ω_2 scatters and attains a phase shift depending on the presence of the control photon. Lastly, the control photon is released again at a frequency ω_2 by detuning the storage back. Below, we will go through the steps; first by considering capture and release of the control photon, followed by a detailed discussion of the scattering of the signal photon for the presence/absence of the control photon.

7.2.1 Capture and release of the control photon

In the first step where the control photon is captured, ideally all of the energy in the photon must be captured in the storage. We assume that the control photon initially is resonant with both a mode in the gate and in the storage, at the frequency ω_2 in Fig. 7.4. The idea is to capture the control by detuning

the storage exactly when it is populated the most. Here we only consider the possibility of tuning the resonances of the storage. In that case, the control photon must have a specific spectral and temporal shape in order to be fully absorbed. The optimal may be determined by reversing the capture process, i.e. by determining the pulse shape of an emitted photon if the storage initially is excited.

To determine this, we define a Hamiltonian for the double-ring system valid for a single excitation, in analogy with the derivations in Chapter 3,

$$H_{\text{wg-double-ring}} = \hbar g(a_{\text{s}}^{\dagger}a_{\text{g}} + a_{\text{g}}^{\dagger}a_{\text{s}}) + \hbar\sqrt{\frac{\kappa v_g}{2\pi}}\int_0^{\infty} \mathrm{d}k\, \left[a^{\dagger}(k)a_{\text{g}} + a_{\text{g}}^{\dagger}a(k)\right], \quad (7.9)$$

with a_{s} and a_{g} being annihilation operators for the considered mode in the storage and gate resonator, respectively (we do not include transitions to other modes here). The coupling rate g is proportional to the rate at which energy is transferred between the rings. The single-excitation state of the system is

$$|\psi(t)\rangle = C_{\text{s}}(t)a_{\text{s}}^{\dagger}|\phi\rangle + C_{\text{g}}(t)a_{\text{g}}^{\dagger}|\phi\rangle + \int_0^{\infty}\mathrm{d}k\, C_{\text{wg}}(k,t)a^{\dagger}(k,t)|\phi\rangle, \quad (7.10)$$

with $|C_{\text{s/g}}(t)|^2$ being the population in the storage/gate ring at time t, and with $\int_{k_1}^{k_2}\mathrm{d}k\,|C_{\text{wg}}(k,t)|^2$ being the possibility having a photon with momentum between k_1 and $k_2 > k_1$ at time t. In a similar way as in Chapter 3, we use the time-independent Schrödinger equation to determine differential equations for the expansion coefficients. In a frame rotating with the frequency of the modes in the gate and storage, which is assumed to be the same, we arrive at

$$\partial_t C_{\text{s}}(t) = -\mathrm{i}gC_{\text{g}}(t), \quad (7.11a)$$

$$\partial_t C_{\text{g}}(t) = -\frac{\kappa}{2}C_{\text{g}}(t) - \mathrm{i}gC_{\text{s}}(t), \quad (7.11b)$$

where the coupling to the waveguide modes may described by κ mode with narrow linewidths compared to the carrier frequencies of the pulses, in analogy to Γ in Eq. (3.9). By solving these equations, the spontaneously emitted pulse shape is given by the temporal wavepacket

$$\xi(t) = \mathrm{i}\frac{g\sqrt{\kappa}}{J}\mathrm{e}^{-\kappa t/4}\left[\mathrm{e}^{\mathrm{i}Jt/2} - \mathrm{e}^{-\mathrm{i}Jt/2}\right], \quad (7.12)$$

where $J = \sqrt{4g^2 - \kappa^2/4}$ is either real or purely imaginary, depending on if the system is in the strong or weak coupling regime, respectively.

Using the numerical approach in Section 3.3 with a temporally reversed version of Eq. (7.12) as input, we calculate the full scattering dynamics, see Fig. 7.5. In Fig. 7.5(a), the resulting gate and storage populations are shown. The idea is to detune the storage exactly when the population of the storage is at its maximum, here $t/\kappa \sim 13$. To illustrate the scattering dynamics clearly, we evaluate the spectral density in the waveguide, $N_k(k,t) = \langle\psi(t)|a^{\dagger}(k)a(k)|\psi(t)\rangle$, and the spatial photon density in the waveguide, $N_z(z,t)$, given in Eq. (3.15). These are plotted in Fig. 7.5(b,c), and specifically we notice, that the temporal shape of the pulse is reversed for the scattered pulse.

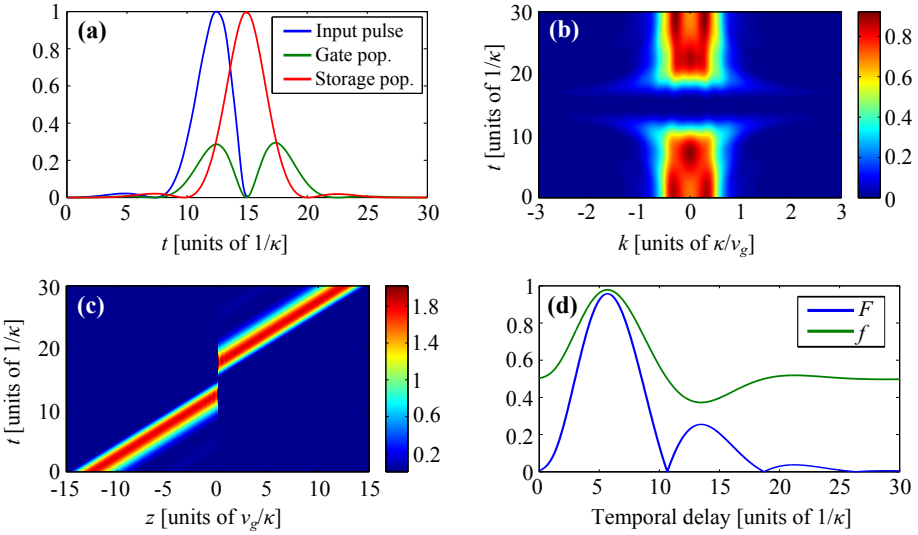

Figure 7.5: (a) Gate (green) and storage (red) popultion for an incoming single-photon pulse with the temporal shape from Eq. (7.12) (blue), shown for $g = \kappa/2$. (b) Spectral density in waveguide, $N_k(k,t)$. (c) Spatial photon density in the waveguide, $N_z(z,t)$. (d) The fidelity measure F from Eq. (6.5) describes the fidelity between the incoming and scattered pulse, plotted for varying temporal delays when calculating the fidelity. f describes the relative phases between the pulses, as defined in Eq. (6.6).

This reversion explains why the fidelity, F, between the scattered pulse and the incoming pulse is not perfectly 1 (when delay is taken into account) in Fig. 7.5(d). This fidelity measure is the same as used in the previous chapter in Eq. (6.5), where F is evaluated at the optimal delay. When accounting for scattering-induced delays, the relative phase measure f from Eq. (6.6) is close to 1, stating that the scattered and incoming pulse are in phase. This is due to the fact that the pulse interacts with both cavities, and thus attains a total phase shift of 2π.

Actually, as demonstrated in Ref. [156], a Gaussian pulse as in Eq. (3.12b) may approximate the "perfect" excitation pulse very well when the bandwidth of the Gaussian, σ (in units of 1/m as in Eq. (3.12b)), is $\sim \kappa/v_g$ and when the the combined two-ring system is on the border between strong and weak coupling, where the loss rate of the mode in the gate ring is similar to the rate at which energy is exchanged between the two ring resonators. The resulting dynamics are calculated in the same way as for the "perfect" pulse, for a Gaussian pulse with $\sigma v_g = \kappa$ see Fig. 7.6. Even though a part of the Gaussian pulse does not couple to the emitter (as seen from the small leakage in Fig. 7.6(c)), the fidelities in Fig. 7.6(d) are on the same order as for the "perfect" pulse. This is due to the fact that the Gaussian pulse has a symmetric temporal shape, which compensates for the non-perfect coupling. For both pulse shapes, high fidelities of $> 95\%$ are obtained, and thus both of them seem applicable in the given ring setup.

Choosing the "perfect" pulse as an example, we illustrate the capture and

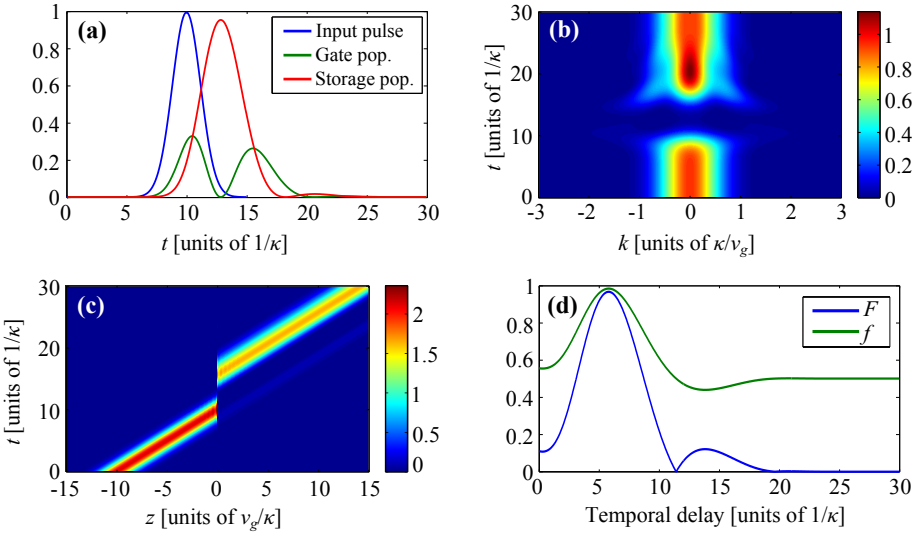

Figure 7.6: (a) Gate (green) and storage (red) popultion for an incoming single-photon pulse with a Gaussian spectrum as in Eq. (3.12b) with bandwidth $\sigma v_g = \kappa$ (blue), shown for $g = \kappa/2$. (b) Spectral density in waveguide, $N_k(k,t)$. (c) Spatial photon density in the waveguide, $N_z(z,t)$. (d) The fidelity measure F and phase comparison parameter f from Eqs. (6.5) and (6.6), plotted for varying temporal delays.

release in Fig. 7.7, where the storage instantaneously[2] is detuned by an amount of either $\delta\omega = 9\kappa$ or $\delta\omega = 10\kappa$, and the resulting fidelities are calculated. As F remains the same for the two different detunings, a significant difference appears in the values of the relative phase measure, f. For $\delta\omega = 10\kappa$, the input and output pulse are in phase, whereas the case $\delta\omega = 9\kappa$ results in pulses almost completely out of resonance. This is explained by the fact that when the frequency of the stored pulse is shifted, the stored pulse gains an additional phase of $\delta\omega \cdot t_{\mathrm{cap}}$ with t_{cap} being the capture time of the control. Thus, in order to obtain high efficiencies for the photon capture/release, a very precise timing is required both to perform the detuning at the correct time, but also timing the release (compared to the detuning magnitude) very precisely.

The required magnitude of the frequency detuning, $\delta\omega$, depends on how long the operation time of the gate is, as the control according to the gate scheme cannot to decay while the signal is scattering. The effective decay rate may be calculated from Eqs. (7.11a) and (7.11b) by including a term $-\mathrm{i}\delta\omega C_{\mathrm{S}}(t)$ in Eq. (7.11a) to account for the detuning. We estimate the effective decay rate of a captured control excitation in the storage from the eigenvalue of the differential equation system in Eqs. (7.11a) and (7.11b) with the smallest magnitude of its real part. In the large detuning limit[3], this real part would

[2] The detuning speed depends in practice of the limitations in the detuning process. As an example, electro-optical modulation in LiNbO3 may be on the order of 10 GHz [146].

[3] For small detunings and large values of g, the real part of the eigenvalues of the differential equation system would be describe the decay of the dressed states.

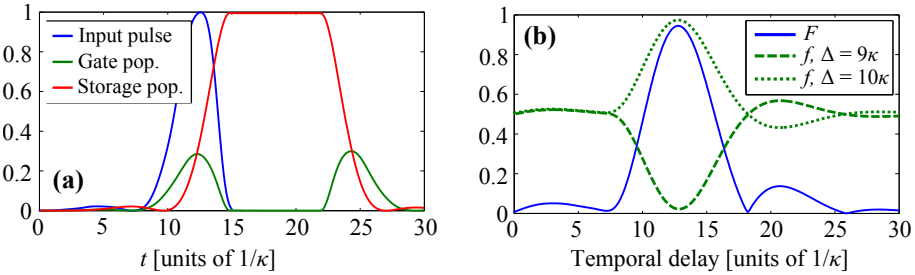

Figure 7.7: (a) Capture of control photon (blue) by detuning the gate by a frequency $\delta\omega = 10$, exactly when the storage is populated the most, and releasing it again after a time of $t_{cap} = 7/\kappa$. (b) Fidelity, F, and relative phase measure, f, shown for two different detunings, with F having the same value at both detunings. F peaks at a later time compared to in Fig. 7.5, corresponding to an additional delay of t_{cap}.

correspond to the decay of the energy for the detuned storage mode,

$$\kappa_{\mathrm{stor,eff}} = \frac{\kappa}{2} - \left|\mathrm{Im}\left\{\sqrt{4g^2 - (\kappa/2 - \mathrm{i}\delta\omega)^2}\right\}\right|. \tag{7.13}$$

The effective decay rate is shown in Fig. 7.8 in the case $g = \kappa/2$ and should in principle be very small compared to $1/t_{\mathrm{op}}$, where t_{op} is the total time for a full c-phase gate operation. A high value of $\delta\omega$, however, also demands more from the physical mode detuning process. Furthermore, for the specific practical gate setup, the energy of the detuned state cannot match any states in the gate, as this destroy the gate performance. Thus a lot of issues have to be taken into account when determining the value of $\delta\omega$ to be used in a given setup. An estimate of the time which the control has to be captured in can be roughly estimated from the example in Fig. 7.7(a) to be a time $\approx 20/\kappa$. For the control photon not to decay during this period, a reasonable estimate would be $\kappa_{\mathrm{stor,eff}}/\kappa < 10^{-2}$, which from Fig. 7.8 necessitates a detuning of at least 10 linewidths of the gate resonator mode. This is significantly larger than for the existing LiNbO3 tunable resonators, which allows switching corresponding to a few linewidths [145, 146]. Although with an improvement in the Q-factors of the resonator modes, this could be achievable.

7.2.2 Scattering of the signal photon

We now turn to consider the core operation of the gate, namely the phase shift imposed on the signal photon if it is in arm "1", depending on whether the control was in "1" as thus was captured, or if was in "0" and was not captured. According to the gate scheme, the phase of the signal should have an additional π, if the control was captured. Furthermore we require that the properties of the signal photon is not altered upon scattering, apart from a scattering-induced temporal delay.

If the conditions mentioned in the previous sections are fulfilled, such that a control photon is perfectly captured in the highly non-linear storage ring, the signal cannot couple to the storage, as we discussed in Section 7.1. Assuming

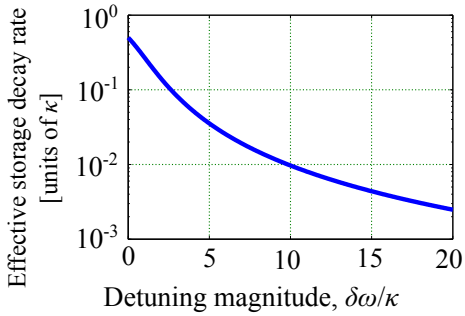

Figure 7.8: Effective decay rate of the captured control photon, $\kappa_{stor,eff}$, from Eq. (7.13), here shown for $g = \kappa/2$.

that no backscattering is present in the resonators, scattering of the signal photon may simply be described by the one-ring transmission coefficient in Eq. (6.2) [151, 157]. Equivalently, the fidelity and relative phase between the input and scattered signal pulses are as calculated in Fig. 6.3, but with the time scale normalized to κ instead of Γ. For low values of σ, the signal gains a phase shift of π, with a fidelity close to 1. In the regime where the capture is optimal, $\sigma v_g \sim \kappa$, a fidelity of $F \sim 95\,\%$ is still achieved.

If the control photon, however, was in arm "0" while the signal was in "1", the scattered signal photon should in-phase with the incoming photon, according to Fig. 7.1. The resulting scattering fidelities are shown in Fig. 7.9, evaluated for $g = \kappa/2$, $g = \kappa$, and $g = 2\kappa$. For low valus of σ, f is very close to 1, indicating that the scattered state is in phase with the input photon. And with a value of F of more than $95\,\%$ even at $\sigma v_g \sim \kappa$, the pulse shape is well preserved upon scattering. For large values of g, the rings are strongly coupling and a frequency splitting occurs, preventing the signal from entering the rings. This explains why the highest fidelities are achieved at close to zero temporal delay Fig. 7.9(c), as the signal simply does not couple to the rings. Summarizing, the signal photon is scattered with high fidelity in both cases, and with the desired phases according to the c-phase scheme.

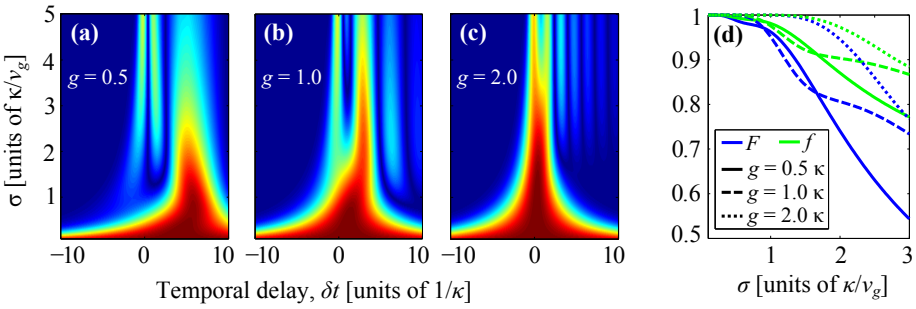

Figure 7.9: (a-c) The fidelity F between an incoming Gaussian pulse with spectral width σ and the state scattered on a two-ring system, shown for three different values of g (in units of κ). A temporal delay, δt, is allowed in the fidelity calculation. (d) The maximal F at a given σ (spectral FWHM of the input pulse) and the corresponding value of f.

7.3 Summary

In this chapter we have discussed the implementation of a control-phase gate presented by Johne et al. in Ref. [129] into a system of two coupled ring resonators. This is inspired by the continuously improvements in nano- and microfabrication which shows promising perspectives in achieving $\chi^{(2)}$-non-linearities at the single-photon level [140]. By storing the control photon in an optical cavity instead of in a QD, we expect less decoherence from the environment, which especially is significant if the gate is to work at room temperature.

The realization of a controlled-phase for two *identical* photons which employs dynamical capture of the control photon, requires high efficiency of all individual processes related to one full gate operation: eventual capture of control photon, scattering of signal photon, eventual release of control photon. The processes involving scattering of the signal photon shows high fidelities of more than 95 % for pulses with an optimal bandwidth for the dynamical capture. The dynamical capture and release of the control photon, however, relies on the possibility of shifting the frequency of the storage resonator very fast compared to the temporal extent of the pulse, and the magnitude of the detuning must be of several linewidths of the given resonator mode. This process therefore makes very high demands on the modulation probabilities of the materials, as they at the same time must have a high non-linear coefficient and Q-factor.

Electro-optically tunable microring resonators have been demonstrated in LiNbO3, but these have too low Q-values on the order $\sim 10^4$ [146, 145]. On the other hand, free-standing LiNbO3 ring resonators show very high Q-factors [155] on the order $Q \sim 10^8$, but to our knowledge are difficult to manipulate electro-optically. Recent fabrication processes for integrated LiNbO3 resonators with sub-mm dimensions with Q-factors of $\sim 10^5$ [158, 132], but with the present technology it seems a challenge to have at highly non-linear, high-Q, electro-optically tunable micro-resonator in LiNbO3 which fulfils the require-

ments for the gate implementation. If it becomes possible to fabricate such a resonator, a good control of the timing and release of the control photon is also necessitated.

The gate performance is limited by the one of the four possible input configurations with the lowest fidelity, being the four permutations of a control and signal in '0' and '1'. The case with the lowest fidelity is when both photons are in the '1' arm, where they are both interacting with the ring system, as also pointed out in Ref. [129]. The total fidelity is estimated to be close to 90 %, but we clearly see limiting factors in this gate in the practical implementation as compared to the gate in the previous chapter. This would be timing of the capture–release process, and the possibility to shift the resonator frequency sufficiently much, sufficiently fast. Regarding the aspect of capturing the control photon by storing it in a mode with another frequency, the idea proposed by Johne et al. in Ref. [129] may be easier to implement, as it relies on electrical tuning of the QD, in which the control is stored. It may, however, only be operated at low temperatures to avoid dephasing from phonon interaction.

With the increasing knowledge and instrumental power in the field of microfabrication, this scheme with dynamical capture in rings could be realized, if precisely-tunable, highly non-linear, high-Q, low mode volume ring resonators are constructed, which to our knowledge not yet has been fabricated with sufficient properties.

Chapter 8

Phonon-induced dynamics — Basic theory

As demonstrated in the previous chapters, solid-state implementations of few-photon non-linearities such as with semiconductor quantum dots (QDs) are promising for the realisation of a variety of integrated optical functionalities such as few-photon gates and single-photon sources [45]. However, due to the solid-state nature of the QDs, it is well-known that interactions with vibrational modes in the surrounding lattice introduce dephasing and may lead to loss of quantum mechanical coherence between the different system states. In particular, solid-state based cavity QED systems such as semiconductor micropillars [159, 160, 161] and photonic crystal cavities [162, 163] are strongly affected by dephasing induced by phonon scattering [47, 46, 164, 165, 166, 167, 48, 168]. Phonon-induced decoherence thus makes the observation of such effects as vacuum Rabi-oscillations [169] much more difficult than in atomic cavity QED systems and impairs the realization of a scalable solid-state platform for quantum information technology. For instance, indistinguishability requirements of subsequent emission events from a single-photon source places strict limitations on the amount of dephasing that can be accepted [49, 170, 171].

Recently it was demonstrated experimentally in that the usual Markovian model of pure dephasing is not sufficient to describe the system dynamics for a non-resonant coupled cavity-quantum dot system [46]. A non-Markovian description of the electron-phonon interaction is required to explain the additional coupling of the QD to the cavity through the emission/absorption of a phonon. Several approaches have been made recently to describe the electron-phonon coupling, showing asymmetric off-resonance coupling at low temperatures [48, 47]. These asymmetries stem from a lower probability for non-resonant couplings which requires absorption of a phonon, but a larger probability for emission of a phonon.

In this and the following two chapters we examine this asymmetry in detail. Specifically, we investigate how the confinement of both the electrical carriers (Chapter 9) and of the phonons (Chapter 10) affect the phonon-induced dynamics, and we discuss the possibilities of controlling the confinement in order

to be able to optimize the performance of the quantum systems. Our main focus will be on implementation in a GaAs platform, as the theory will be applied to an experiment made in this material platform [172].

This chapter provides the fundamental theory on the interaction between the QD and the phonons. In Section 8.1 the three major coupling mechanisms between phonons and electrons/holes are introduced. In Section 8.2 we derive specific equations of motion for a quantum system interacting weakly with a large bosonic reservoir, using standard open-system approaches [54, 173, 174, 175]. We employ the model considered by P. Kaer [173, 54], where the time-convolutionless formalism enables the inclusion of non-Markovian effects, which stem from a finite memory depth of the phonon reservoir [176, 177, 178]. The commonly-used Lindblad formalism [179] may be obtained from the time-convolutionless formalism in the limit where the reservoir correlation functions are delta functions in time, corresponding to memory-less reservoir, resulting in Markovian dynamics.

8.1 Electron-phonon coupling mechanisms

In crystals with two or more atoms per primitive basis, e.g. in GaAs, the vibrational modes may be divided into two classes of phonon, acoustic phonons and optical phonons [58]. These may be divided further into transverse (respectively TA and TO) phonons and longitudinal (LA and LO) phonons, which are characterized by their dispersion properties as illustrated in Fig. 8.1.

Acoustic phonons are characterized by lattice oscillations where the ions move in phase with each other. They have a linear dispersion close to the center of the Brillouin zone, Γ, where the phonon wavelength becomes infinitely large, corresponding to sound waves propagating in a lattice, hence the name *acoustic* phonons. Optical phonons, on the other hand, are quantized lattice vibrations where differently charged ions oscillate out of phase. This induces a dipole moment, and thus infrared radiation may excite these photons, which is why they are called *optical* photons.

The interaction between charge carriers and phonons is described by three major mechanisms:

- **Polar coupling**: Appears in crystals with two or more atoms in the primitive cell with different charge, when optical phonons are excited by an optical field [53, 180].
- **Deformation potentials**: Local site deformations caused by dilations associated with acoustical waves: For long-wavelength phonons, the displacement corresponds to a deformation of the crystal, shifting the electronic bands. [181].
- **Piezo-electric interaction**: In non-centrosymmetric materials, stress will induce a macroscopic polarization, well-known as the piezo-electric effect. The process also works the other way around, where acoustic phonons will induce a polarization which will interact with the electrons [53].

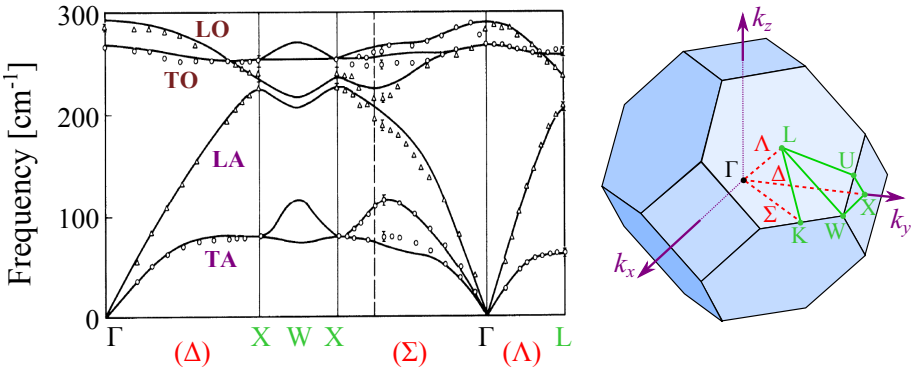

Figure 8.1: Dispersion curve for phonon modes in GaAs from theoretical calculations (solid lines) and experimental data points found using neutron diffraction [184], showing the phonon frequency as a function of the wavevector, $\mathbf{k}$. The different branches correspond to the four classes of phonons, TA, LA, TO, and LO. GaAs crystallizes in a Zinc-blende structure, which has a truncated octahedron shaped Brillouin zone, shown in the figure to the right, with indications of the high-symmetry points.

In the considered QD structure, acoustic phonons will introduce a broadening of the zero phonon line, whereas the polar coupling to optical phonons give rise to phonon sidebands in the absorption spectrum well separated from the zero phonon line [182].

In a bulk GaAs material at low temperatures, the LA phonon modes have energies of < 10 meV [173]. When only considering this energy regime, longitudinal optical phonons do not contribute to the dynamics due to their large energies, ~ 37 meV in GaAs [173]. The piezoelectric interaction depends strongly on the separation of the electron and hole wavefunctions. In GaAs the deformation potential is dominating the piezoelectric coupling, but a material like GaN possesses strong polarisation charges at the interfaces which gives a strong build in polarisation, in which the piezoelectric interaction will be much stronger than the deformation potential coupling [183]. In this thesis, we thus limit ourselves to only consider the coupling to LA phonons through the deformation potential coupling.

8.1.1 Deformation potential

Following derivations in [185, 186, 187, 188], we for simplicity consider a non-degenerate band close to Γ in Fig. 8.1. The deformation potential is defined as the energy change of an electronic level per unit strain. To the leading order, the energy shift is proportional to the relative volume change $\delta\mathcal{V}/\mathcal{V}$, and the interaction Hamiltonian may be written as

$$H_{\mathrm{e/h}}^{(\mathrm{DP})} = \Delta E_{\mathrm{c/v}} = D_{\mathrm{e/h}} \frac{\delta\mathcal{V}}{\mathcal{V}} = D_{\mathrm{e/h}} \mathrm{Tr}\{\hat{\sigma}\}, \tag{8.1}$$

with $D_{\mathrm{e/h}}$ being the deformation potential constant for the electron/hole, $\mathcal{V}$ is the volume of a unit cell of the crystal, and $\mathrm{Tr}\{\hat{\sigma}\}$ is the trace of the strain

tensor. When $D_{\mathrm{e/h}} < 0$, the bottom of the energy band is shifted toward higher energies when the crystal is compressed.

For a homogeneous material, small strains obey Hooke's law [58],

$$\sigma_{ij} = \frac{1}{2}\left(\frac{\partial u_i}{\partial r_j} + \frac{\partial u_j}{\partial r_i}\right), \tag{8.2}$$

where u_i are the vector components of the local displacement field of the phonons, $\mathbf{u}(\mathbf{r})$. This reduces Eq. (8.1) to

$$H_{\mathrm{e/h}}^{(\mathrm{DP})} = D_{\mathrm{e/h}} \boldsymbol{\nabla} \cdot \mathbf{u}(\mathbf{r}), \tag{8.3}$$

with $\mathbf{u}(\mathbf{r}) = (u_x(\mathbf{r}), u_y(\mathbf{r}), u_z(\mathbf{r}))$. Initially we assume bulk phonon modes, for which $\mathbf{u}(\mathbf{r})$ is given in Eq. (2.16). As seen from Eq. (8.3), transverse phonon modes do not contribute to the Hamiltonian, and thus only *longitudinal acoustic* phonons contribute to the deformation potential coupling. The Hamiltonian simplifies to

$$H_{\mathrm{e/h}}^{(\mathrm{DP})}(\mathbf{r}) = -D_{\mathrm{e/h}} \sum_{\mathbf{k}} k \sqrt{\frac{\hbar}{2\varrho V \omega_{\mathrm{LA}}(\mathbf{k})}} \left(b_{-\mathbf{k},\mathrm{LA}}^{\dagger} + b_{\mathbf{k},\mathrm{LA}}\right) \mathrm{e}^{\mathrm{i}\mathbf{k}\cdot\mathbf{r}}. \tag{8.4}$$

with $\omega_{\mathrm{LA}}(\mathbf{k})$ being the dispersion relation for the longitudinal acoustic phonons, ϱ the material density, V the phonon quantization volume, and $b_{\mathbf{k},\mathrm{LA}}$ the annihilation operator for an LA phonon with the wavevector $\mathbf{k}$. In the literature, the minus sign is commonly (but not always) taken into the definition of $D_{\mathrm{e/h}}$, such that the commonly given values of the deformation potential already contain this minus sign [185] — we will adopt this notation from now on.

The corresponding Hamiltonian in second quantization is obtained by calculating the matrix element of Eq. (8.4) in the electron/hole single-particle basis as discussed in Chapter 2,

$$H_{\mathrm{e/h}}^{(\mathrm{DP})} = \sum_{\mathbf{k},\nu\nu'} D_{\mathrm{e/h}} k \sqrt{\frac{\hbar}{2\varrho V \omega_{\mathrm{LA}}(\mathbf{k})}} \mathcal{F}_{\mathrm{e/h},\nu\nu'}(\mathbf{k}) \left(b_{-\mathbf{k},\mathrm{LA}}^{\dagger} + b_{\mathbf{k},\mathrm{LA}}\right) c_{\nu}^{\dagger} c_{\nu'}, \tag{8.5}$$

with c_ν being the annihilation operator in the single-particle electron/hole basis, and with $k = |\mathbf{k}|$. The form factor, $\mathcal{F}$, is given by with the form factor given by

$$\mathcal{F}_{\mathrm{e/h},\nu\nu'}(\mathbf{k}) = \int \mathrm{d}\mathbf{r}\, \psi_{\mathrm{e/h},\nu}^{*}(\mathbf{r}) \psi_{\mathrm{e/h},\nu'}(\mathbf{r}) \mathrm{e}^{\mathrm{i}\mathbf{k}\cdot\mathbf{r}}. \tag{8.6}$$

It describes the overlap between the electronic confinement and the phonon confined, with the latter being described by plane waves, as we assume bulk phonon modes. The form factor has the symmetry properties $\mathcal{F}_{\mathrm{e/h},\nu\nu'}(\mathbf{k}) = \mathcal{F}_{\mathrm{e/h},\nu'\nu}^{*}(-\mathbf{k})$.

By comparing Eq. (8.5) with the general form of the electron-phonon interaction in Eq. (2.17), the interaction matrix element is given as

$$M_{\mathrm{e/h},\nu\nu'}^{(\mathrm{DP})}(\mathbf{k}) = D_{\mathrm{e/h}} k \sqrt{\frac{\hbar}{2\varrho V \omega_{\mathrm{LA}}(\mathbf{k})}} \mathcal{F}_{\mathrm{e/h},\nu\nu'}(\mathbf{k}), \tag{8.7}$$

At some other symmetry points in the crystal, where the bands are degenerate, e.g. at X or L point in Fig. 8.1, the $D_{\mathrm{e/h}}$ in Eq. (8.1) is not a scalar but rather a tensor and more complex equations involving also TA phonons must be considered [57].

Having established the fundamental form of the interaction Hamiltonian, we will in the following determine the dynamics of a quantum system which couples weakly to a bosonic reservoir, where the coupling in our case will be described by the Hamiltonian in Eq. (8.5).

8.2 Open quantum systems

In open quantum systems, where a small system interacts with a many-body environment, a common approach to determine the system dynamics is by a quantum master-equation [189]. We give a general derivation here, and we employ the interaction Hamiltonian from Eq. (8.5) later. The environment is modelled as a reservoir, R, which interacts with the system, S, and thus the combined R+S system is described by the total Hilbert space $\mathcal{H}_{\mathrm{total}} = \mathcal{H}_{\mathrm{S}} \otimes \mathcal{H}_{\mathrm{R}}$. By tracing out the reservoir degrees of freedom from the density matrix of the total system, $\rho_{\mathrm{full}}(t)$, the system dynamics may be described by the reduced density matrix operator, $\rho(t) = \mathrm{Tr}_{\mathrm{R}}\left\{\rho_{\mathrm{full}}(t)\right\}$. From the reduced density matrix, the expectation value of all operators belonging to $\mathcal{H}_{\mathrm{S}}$ may be calculated as

$$\langle \hat{O} \rangle = \mathrm{Tr}_{\mathrm{R}\oplus\mathrm{S}}\left\{\hat{O}\rho_{\mathrm{full}}(t)\right\} = \mathrm{Tr}_{\mathrm{S}}\left\{\hat{O}\mathrm{Tr}_{\mathrm{R}}\left\{\rho_{\mathrm{full}}(t)\right\}\right\} = \mathrm{Tr}_{\mathrm{S}}\left\{\hat{O}\rho(t)\right\}. \tag{8.8}$$

The Hamiltonian of the total system is separated into three parts: a part only related to the system, H_{S}, a part only related to the reservoir, H_{R}, and a term H_{SR} expressing the interaction between S and R,

$$H = H_{\mathrm{S}} + H_{\mathrm{R}} + H_{\mathrm{SR}} = H_0 + H_{\mathrm{SR}}. \tag{8.9}$$

We here consider time-independent Hamiltonians only, and use $H_0 = H_{\mathrm{S}} + H_{\mathrm{R}}$ as short-hand notation for the non-interacting parts of the Hamiltonian.

The time evolution of the total density matrix in the Schrödinger picture is given by

$$\partial_t \rho_{\mathrm{full}}(t) = \frac{1}{\mathrm{i}\hbar}\left[H, \rho_{\mathrm{full}}(t)\right]. \tag{8.10}$$

If the interaction is weak, $\rho_{\mathrm{full}}(t)$ may advantageously be considered in the interaction picture,

$$\tilde{\rho}_{\mathrm{full}}(t) = \mathrm{e}^{\frac{\mathrm{i}}{\hbar}H_0 t}\rho_{\mathrm{full}}(t)\mathrm{e}^{\frac{-\mathrm{i}}{\hbar}H_0 t}. \tag{8.11}$$

in which the fast motion stemming from H_0 is suppressed. Using Eq. (8.10) and the unitary properties of the operator $\mathrm{e}^{\mathrm{i}\hbar^{-1}H_0 t}$, the equation of motion for $\tilde{\rho}_{\mathrm{full}}(t)$ becomes

$$\partial_t \tilde{\rho}_{\mathrm{full}}(t) = \frac{1}{\mathrm{i}\hbar}\left[\tilde{H}_{\mathrm{SR}}(t), \tilde{\rho}_{\mathrm{full}}(t)\right], \tag{8.12}$$

where

$$\tilde{H}_{\mathrm{SR}}(t) = \mathrm{e}^{\frac{\mathrm{i}}{\hbar}H_0 t} H_{\mathrm{SR}} \mathrm{e}^{\frac{-\mathrm{i}}{\hbar}H_0 t}. \tag{8.13}$$

By formally integrating Eq. (8.12) from an initial time, t_0, up to t to obtain an expression for $\tilde{\rho}_{\mathrm{full}}$ and inserting this back into Eq. (8.12), we arrive at

$$\partial_t \tilde{\rho}_{\mathrm{full}}(t) = \frac{1}{\mathrm{i}\hbar}\left[\tilde{H}_{\mathrm{SR}}(t), \tilde{\rho}_{\mathrm{full}}(t_0)\right] - \frac{1}{\hbar^2}\int_{t_0}^{t} \mathrm{d}t' \, \left[\tilde{H}_{\mathrm{SR}}(t), \left[\tilde{H}_{\mathrm{SR}}(t'), \tilde{\rho}_{\mathrm{full}}(t')\right]\right]. \tag{8.14}$$

The reduced density matrix operator may equivalently be defined in the interaction picture,

$$\tilde{\rho}(t) = \mathrm{e}^{\frac{\mathrm{i}}{\hbar}H_{\mathrm{S}} t} \rho(t) \mathrm{e}^{-\frac{\mathrm{i}}{\hbar}H_{\mathrm{S}} t}. \tag{8.15}$$

Here the interaction picture for ρ is defined purely by the free Hamiltonian of the system, H_{S}, as the reservoir has been traced out. It may be obtained from $\tilde{\rho}_{\mathrm{full}}(t)$ in Eq. (8.11)

$$\begin{aligned} \mathrm{Tr}_{\mathrm{R}}\left\{\tilde{\rho}_{\mathrm{full}}(t)\right\} &= \mathrm{Tr}_{\mathrm{R}}\left\{\mathrm{e}^{\frac{\mathrm{i}}{\hbar}H_0 t} \rho_{\mathrm{full}}(t) \mathrm{e}^{\frac{-\mathrm{i}}{\hbar}H_0 t}\right\} && (8.16)\\ &= \mathrm{e}^{\frac{\mathrm{i}}{\hbar}H_{\mathrm{S}} t} \mathrm{Tr}_{\mathrm{R}}\left\{\mathrm{e}^{\frac{\mathrm{i}}{\hbar}H_{\mathrm{R}} t} \rho_{\mathrm{full}}(t) \mathrm{e}^{\frac{-\mathrm{i}}{\hbar}H_{\mathrm{R}} t}\right\} \mathrm{e}^{-\frac{\mathrm{i}}{\hbar}H_{\mathrm{S}} t} && (8.17)\\ &= \tilde{\rho}(t). && (8.18) \end{aligned}$$

where we in the last equality exploit the cyclic property of the trace. With this, tracing over the reservoir in Eq. (8.14) leads to

$$\begin{aligned} \partial_t \tilde{\rho}(t) = \frac{1}{\mathrm{i}\hbar}\mathrm{Tr}_{\mathrm{R}}\left\{\left[\tilde{H}_{\mathrm{SR}}(t), \tilde{\rho}_{\mathrm{full}}(t_0)\right]\right\} \\ - \frac{1}{\hbar^2}\int_{t_0}^{t} \mathrm{d}t' \, \mathrm{Tr}_{\mathrm{R}}\left\{\left[\tilde{H}_{\mathrm{SR}}(t), \left[\tilde{H}_{\mathrm{SR}}(t'), \tilde{\rho}_{\mathrm{full}}(t')\right]\right]\right\}. \end{aligned} \tag{8.19}$$

Eq. (8.19) is still exact, but to eliminate the reservoir-related terms, several approximations must be carried out.

8.2.1 The Born-Markov approximation

At the initial time, t_0, we assume that no correlations exist between the system and the reservoir. This corresponds to a factorizable density matrix operator,

$$\rho_{\mathrm{full}}(t_0) = \rho(t_0) \otimes R_0, \tag{8.20}$$

with R_0 being the initial density operator for the reservoir.

If the reservoir is very large and the coupling between the system and reservoir is weak, the reservoir may be assumed to be approximately in the thermal state $R_0 = \frac{\exp(-\beta H_{\mathrm{R}})}{\mathrm{Tr}_{\mathrm{R}}\{\exp(-\beta H_{\mathrm{R}})\}}$ at all times, with $\beta = 1/(k_B T)$ defined from Bolzman's constant, k_B, and the temperature, T. We assume that H_{SR} contains terms with exactly one bosonic operator, $b^\dagger$ or b, e.g. as in Eq. (8.5). Because R_0 contains only terms with an even number of bosonic operators (seen by a

Taylor-expansion of the exponential in the expression for R_0 because H_{R} contains only quadratic terms in bosonic operators), $\tilde{H}_{\mathrm{SR}}(t)R_0$ will contain an odd number of bosonic operators. In that case $\mathrm{Tr}_{\mathrm{R}}\left\{\tilde{H}_{\mathrm{SR}}(t)R_0\right\} = 0$ due to the fact that expectation values of operators with an odd number of operators will be zero, i.e. $\langle n|b^\dagger|n\rangle = \langle n|b|n\rangle = 0$. Therefore, the first term in Eq. (8.19) becomes zero. The assumption about the reservoir remaining in the same thermal state moreover allows a factorization of $\rho_{\mathrm{full}}(t)$ at all times,

$$\tilde{\rho}_{\mathrm{full}}(t) = \tilde{\rho}(t) \otimes R_0 + O(H_{\mathrm{SR}}), \tag{8.21}$$

where the deviations from the uncorrelated state should be on the order of H_{SR} due to the weak coupling [175].

To proceed, we make our first major approximation, the so-called Born approximation. When inserting Eq. (8.21) into Eq. (8.19), we neglect terms higher than second order in H_{SR},

$$\partial_t\tilde{\rho}(t) = -\frac{1}{\hbar^2}\int_{t_0}^{t}\mathrm{d}t'\,\mathrm{Tr}_{\mathrm{R}}\left\{\left[\tilde{H}_{\mathrm{SR}}(t),\left[\tilde{H}_{\mathrm{SR}}(t'),\tilde{\rho}(t')\otimes R_0\right]\right]\right\}. \tag{8.22}$$

This gives a closed integro-differential equation for the density operator $\rho(t)$ of the system in the interaction picture. More detailed analysis of the Born approximation may be carried out by the *projection operator formalism*, see [176] for details.

To further simplify Eq. (8.22), we have to specify the interaction Hamiltonian. Thus we assume that H_{SR} as in Eq. (8.5) may be written on the form

$$H_{\mathrm{SR}} = \sum_{\nu\nu'} P_{\nu\nu'} \otimes B_{\nu\nu'}, \tag{8.23}$$

where $P_{\nu\nu'}$ is a system operator and $B_{\nu\nu'}$ is a reservoir operator. Using this notation and omitting the use of $\otimes$, we have

$$\partial_t\tilde{\rho}(t) = -\frac{1}{\hbar^2}\int_{t_0}^{t}\mathrm{d}t'\,\mathrm{Tr}_{\mathrm{R}}\Bigg\{\sum_{\nu_1\nu_2\nu_1'\nu_2'}\Big[\tilde{P}_{\nu_1\nu_1'}(t)\tilde{B}_{\nu_1\nu_1'}(t), \Big[\tilde{P}_{\nu_2\nu_2'}(t')\tilde{B}_{\nu_2\nu_2'}(t'),\tilde{\rho}(t')R_0\Big]\Big]\Bigg\}. \tag{8.24}$$

The system part may now be distinguished from the reservoir part. This may be realized by exploiting the cyclic property of the trace and by evaluating the expectation value when averaging over all reservoir degrees of freedom, $\mathrm{Tr}_{\mathrm{R}}\{OR_0\} = \langle O\rangle$, giving

$$\begin{aligned}\partial_t\tilde{\rho}(t) = -\frac{1}{\hbar^2}\int_{t_0}^{t}\mathrm{d}t' \sum_{\nu_1\nu_1'\nu_2\nu_2'}\Big\{ & \\ \Big[\tilde{P}_{\nu_1\nu_1'}(t)\tilde{P}_{\nu_2\nu_2'}(t')\tilde{\rho}(t') - \tilde{P}_{\nu_2\nu_2'}(t')\tilde{\rho}(t')\tilde{P}_{\nu_1\nu_1'}(t)\Big]\langle\tilde{B}_{\nu_1\nu_1'}(t)\tilde{B}_{\nu_2\nu_2'}(t')\rangle & \\ + \Big[\tilde{\rho}(t')\tilde{P}_{\nu_2\nu_2'}(t')\tilde{P}_{\nu_1\nu_1'}(t) - \tilde{P}_{\nu_1\nu_1'}(t')\tilde{\rho}(t')\tilde{P}_{\nu_2\nu_2'}(t)\Big]\langle\tilde{B}_{\nu_2\nu_2'}(t')\tilde{B}_{\nu_1\nu_1'}(t)\rangle\Big\}. & \end{aligned} \tag{8.25}$$

Due to the t' dependence of $\tilde{\rho}$ in the integral (and not t), the evolution of $\rho(t)$ is non-Markovian, meaning that the evolution depends on the past due to interaction with earlier states that are reflected back.

The Markov approximation

To handle Eq. (8.25), further approximations have to be introduced. A commonly used but simple approach is the Markov approximation described in [174, 175, 176] which is obtained by the substitution $\tilde{\rho}(t') \to \tilde{\rho}(t)$ such that the time evolution only depends on the present state $\tilde{\rho}(t)$. This assumption seems reasonable if we consider a large bath in thermal equilibrium, since we expect minor changes to be equalized so fast that they do not affect the dynamics of the system. The Markov approximation is only valid if the correlation time of the reservoir τ_R is small compared to the time scale describing changes in $\tilde{\rho}(t)$ described by H_{SR} [175]. What is important is that the substitution is made in the interaction picture such that Eq. (8.25) still contains memory related to the dynamics caused by H_{S}, and in that way the system behaviour is still non-Markovian in our description.

The Born- and Markov-approximations together are often just denoted the Born-Markov approximations. The important point for the assumptions is that the time scale over which the system varies is much larger than decay times of the reservoir correlation functions.

The dynamics of $\rho(t)$ is only governed by the Hamiltonian of the system, H_{S}, and may be described using the transformation operator [173]

$$U_{\mathrm{S}}(t,t_0) = \mathrm{e}^{-\mathrm{i}\hbar^{-1}H_{\mathrm{S}}(t-t_0)}, \tag{8.26}$$

which obeys the Schrödinger equation

$$\mathrm{i}\hbar\partial_t U_{\mathrm{S}}(t,t_0) = H_{\mathrm{S}}U_{\mathrm{S}}(t,t_0). \tag{8.27}$$

Transforming Eq. (8.25) back to the Schrödinger picture using U_S and Eq. (8.27), gives

$$\partial_t\rho(t) = \partial_t\Big\{U_{\mathrm{S}}(t,t_0)\tilde{\rho}(t)U_{\mathrm{S}}^\dagger(t,t_0)\Big\} = -\frac{\mathrm{i}}{\hbar}\left[H_{\mathrm{S}},\rho(t)\right] + S(t), \tag{8.28}$$

where $S(t)$ defines the time-local scattering terms induced by the reservoir,

$$S(t) = U_{\mathrm{S}}(t,t_0)\left(\partial_t\{\tilde{\rho}(t)\}\right)U_{\mathrm{S}}^\dagger(t,t_0). \tag{8.29}$$

By exploiting the properties of U_{S}, we have the two relations

$$\begin{aligned} U_{\mathrm{S}}(t,t_0)\tilde{\rho}(t')U_{\mathrm{S}}^\dagger(t,t_0) &= U_{\mathrm{S}}(t,t_0)U_{\mathrm{S}}^\dagger(t',t_0)\rho(t')U_{\mathrm{S}}(t',t_0)U_{\mathrm{S}}^\dagger(t,t_0) &(8.30)\\ &= U_{\mathrm{S}}(t,t')\rho(t')U_{\mathrm{S}}^\dagger(t,t'), &(8.31)\end{aligned}$$

and similarly

$$U_{\mathrm{S}}(t,t_0)\tilde{P}_{\nu_1\nu_1'}(t')U_{\mathrm{S}}^\dagger(t,t_0) = U_{\mathrm{S}}(t,t')P_{\nu_1\nu_1'}U_{\mathrm{S}}^\dagger(t,t'). \tag{8.32}$$

Using these, the time-local scattering term may be achieved from Eq. (8.25) by substituting $\tilde{\rho}(t') \to \tilde{\rho}(t)$, before transforming back to the Schrödinger picture,

$$\begin{aligned} S(t) = -\frac{1}{\hbar^2}\int_{t_0}^{t} \mathrm{d}t' \sum_{\nu_1\nu_1'\nu_2\nu_2'} \Big\{ & \\ & \Big[P_{\nu_1\nu_1'} U_{\mathrm{S}}(t,t') P_{\nu_2\nu_2'} U_{\mathrm{S}}^{\dagger}(t,t') \rho(t) \\ & \quad - U_{\mathrm{S}}(t,t') P_{\nu_2\nu_2'} U_{\mathrm{S}}^{\dagger}(t,t') \rho(t) P_{\nu_1\nu_1'} \Big] \langle \tilde{B}_{\nu_1\nu_1'}(t) \tilde{B}_{\nu_2\nu_2'}(t') \rangle \\ & + \Big[\rho(t) U_{\mathrm{S}}(t,t') P_{\nu_2\nu_2'} U_{\mathrm{S}}^{\dagger}(t,t') P_{\nu_1\nu_1'} \\ & \quad - P_{\nu_1\nu_1'} \rho(t) U_{\mathrm{S}}(t,t') P_{\nu_2\nu_2'} U_{\mathrm{S}}^{\dagger}(t,t') \Big] \langle \tilde{B}_{\nu_2\nu_2'}(t') \tilde{B}_{\nu_1\nu_1'}(t) \rangle \Big\}. \end{aligned} \tag{8.33}$$

For a specific system, U_{S} may thus be determined from the system Hamiltonian, H_{S}, and P and B are given by the specific coupling mechanism between the system and the reservoir, described by H_{SR}.

8.3 Summary

In this chapter we have introduced the deformation potential coupling, being the major mechanism for interaction between the electronic carriers in a standard GaAs-based QD system and the surrounding environment, with the latter being modelled as a large phonon reservoir. The interaction strength is proportional to the overlap between the spatial modes of the electronic carriers and the phononic modes, characterized by a form factor, Eq. (8.6).

Using a quantum master equation [173, 175, 174], an equation of motion for the reduced density matrix of the system has been derived in Eq. (8.28) using the time-convolutionless formalism, where the phonon reservoir degrees of freedom has been traced out. The influence of the phonons appear as a non-Markovian time-local scattering term, Eq. (8.33), additional to the pure evolution of the system.

In the next two chapters we solve Eq. (8.28) with the interaction Hamiltonian in Eq. (8.5) to examine how the electronic and phononic confinement may be engineered in order to alter the phonon-induced dynamics. For the phonon confinement, the interaction matrix element becomes more complicated, as the bulk phonon description breaks down.

Chapter 9

Phonon-induced dynamics — The electronic confinement

In this chapter we investigate the role of carrier confinement on phonon scattering in a semiconductor quantum dot (QD). We employ the comprehensive theoretical model described in Chapter 8 that takes into account the non-Markovian nature of the phonon reservoir [48], thus avoiding the standard approach of describing phonon-induced decoherence by a pure dephasing rate [190, 191]. Surprisingly, we find that deformation potential scattering may be completely quenched under certain conditions, depending on the degree of confinement of the involved electronic states. The effect is investigated in detail for two cases.

Firstly in Section 9.1, we consider photoluminescence spectroscopy of a single QD and find that the luminescence is suppressed at certain detunings due to a quenching of phonon scattering. Approximate analytic results show that the effect originates from the difference in the spatial confinement of electrons and holes, usually neglected in theoretical treatments. Secondly in Section 9.2, we find that quenching of phonon scattering strongly affects pure dephasing in coupled QD-cavity systems. Expanding the description to realistic QD structures, which are analyzed numerically, conditions for reducing phonon scattering are established. Lastly in Section 9.3, the phonon model is applied to an experimental measurement of the decay rate of a QD inside a L3 photonic crystal cavity, by which we are able to map out the effective phonon density of states, which to our knowledge has not been demonstrated before [172].

Other approaches towards controlling the degree of phonon scattering use phononic bandgap structures for suppressing vibrational modes [192] or considers QDs near surfaces [193], which will be discussed in the next chapter. Structures with simultaneous photonic and phononic bandgaps have been discussed theoretically [194] and experimentally realized [195] with phononic bandgaps in the GHz-regime. In cavity QED, the most relevant phonons belong to the

acoustic branch with energies in the THz-regime, hence the present phononic band gap structures are primarily of interest for improving the optomechanical coupling [196].

The chapter is based on the journal publication *Proposed Quenching of Phonon-Induced Processes in Photoexcited Quantum Dots due to Electron-Hole Asymmetries.* Phys. Rev. Lett. **110**, 087401 (2013) by A. Nysteen, P. K. Nielsen, and J. Mørk. Experimental results are included from the journal publication: *Measuring the effective phonon density of states of a quantum dot in cavity quantum electrodynamics.* Phys. Rev. B **88**, 045316 (2013) by K. H. Madsen, P. K. Nielsen, A. Kreiner-Møller, S. Stobbe, A. Nysteen, J. Mørk, and P. Lodahl.

9.1 Photoluminescence excitation

At first we consider a two-level QD with transition energy $\hbar\omega_{\mathrm{QD}}$ illuminated by a CW laser with frequency ω_{L} in a standard photoluminescence excitation experiment. We consider InGaAs material systems and limit ourselves to detunings below 10 meV and low temperatures (here 4 K), where the deformation potential coupling between electrons and longitudinal acoustic phonons constitutes the dominating coupling mechanism, as discussed in Section 8.1. Following Chapter 2, the Hamiltonian for the QD excited by the laser has the form

$$H_{\mathrm{S}} = \hbar(\omega_{\mathrm{QD}} - \omega_{\mathrm{L}})c_e^\dagger c_e + \hbar\Omega(c_e^\dagger c_g + c_g^\dagger c_e), \tag{9.1}$$

here written in a frame rotating with the frequency of the laser, and where $\hbar\Omega$ corresponding to a Rabi-frequency induced by the laser. The QD excited and ground state annihilation (creation) operators are c_e and c_g ($c_e^\dagger$ and $c_g^\dagger$) respectively. The phonon bath is described by Eq. (2.10),

$$H_{0,\mathrm{ph}} = \sum_{j,\mathbf{k}} \hbar\omega_j(\mathbf{k}) b_{j,\mathbf{k}}^\dagger b_{j,\mathbf{k}}, \tag{9.2}$$

where the 1/2-term also is omitted as it does not contribute to the dynamics. Finally, the interaction between the electrons (e)/holes (h) and the phonons for bulk phonon modes is given by Eq. (8.5),

$$H_{\text{e-ph}} = \sum_{j,\mathbf{k}} \left(M_{j,hh}^{\mathbf{k}} c_g^\dagger c_g + M_{j,ee}^{\mathbf{k}} c_e^\dagger c_e\right)\left(b_{j,-\mathbf{k}}^\dagger + b_{j,\mathbf{k}}\right). \tag{9.3}$$

As the interlevel in the QD is much larger than the phonon energies considered in this theses, we set the matrix elements $M_{j,he}^{\mathbf{k}}$ and $M_{j,eh}^{\mathbf{k}}$ to zero because the interlevel distance is much larger than the phonon energies considered in this thesis.

Initially we consider spherical-parabolic confinement potentials, giving the electron and hole wavefunctions

$$\phi_\nu(\mathbf{r}) = \pi^{-3/4} w_\nu^{-3/2} \exp\left[-r^2/(2w_\nu^2)\right], \tag{9.4}$$

with $\nu \in \{e, h\}$ representing the electron and the hole respectively. The differences in carrier confinement lead to wavefunctions with different effective widths for electrons (w_e) and holes (w_h).

As derived in Eq. (8.28), the reduced density matrix describing the quantum system evolves according to

$$\partial_t \rho(t) = -\mathrm{i}\hbar^{-1}[H_\mathrm{S}, \rho(t)] + S_\mathrm{LA}(t) + L(t). \tag{9.5}$$

Here $L(t)$ represents losses included through the Lindblad formalism [179], which accounts through the rate Γ, for the decay of the excited QD state into subsystems which are not described by H_S. $S_\mathrm{LA}(t)$ describes the non-Markovian coupling between the electron/hole and the phonon reservoir. It is calculated from Eq. (8.33), which is carried out in detail in [173]. We will not go through the deviations here, but simply note that $S_\mathrm{LA}(t)$ contains a correlation function describing the phonon reservoir,

$$D^{\gtrless}(t) = \sum_{\mathbf{k}} |M^{\mathbf{k}}|^2 \left[(2n_{\mathbf{k}} + 1)\cos(\omega_{\mathbf{k}} t) \mp \mathrm{i}\sin(\omega_{\mathbf{k}} t)\right]. \tag{9.6}$$

where $\mathbf{k}$ is the phonon wavevector, and $n_{\mathbf{k}} = 1/[\exp(\hbar\omega_{\mathbf{k}}/k_B T) - 1]$ is the average thermal occupation number of the phonon mode $\mathbf{k}$ at temperature T. It is related to the phonon bath operators in Eq. (8.33) as $D^{\gtrless}(t-t') = \langle \tilde{B}(\pm[t-t'])\tilde{B}(0)\rangle$ and contains information about the memory depth of the phonon reservoir. For bulk phonons, $D^{\gtrless}(t)$ decays within 5 ps [173, 197]. Furthermore $M^{\mathbf{k}} = M^{\mathbf{k}}_{ee} - M^{\mathbf{k}}_{hh}$ is the effective electron/hole-phonon coupling matrix element with the interaction strengths given by Eq. (8.7). When evaluating $M^{\mathbf{k}}$, we consider bulk phonons with a linear dispersion relation, $\omega_{\mathbf{k}} = c_l|\mathbf{k}|$, with c_l being the velocity of longitudinal acoustic waves, here defined as the slope of the dispersion curve in Fig. 8.1 close to the Γ-point in reciprocal space.

Solving Eq. (9.5) numerically[1] with the confinement of the electronic carriers given by Eq. (9.4), we calculate the stationary population of an InAs QD embedded in GaAs for varying detuning between the laser and the QD ground state resonance, see Fig. 9.1a. Comparing the black and blue curve in Fig. 9.1a shows that the QD, as is well-known [164, 198], may be populated by a phonon-assisted process when the laser and the QD are off-resonant. However, when the widths of the electron and hole wavefunction differ, as for the red curve, the QD population and thus the photoluminescence intensity is suppressed at a specific detuning. As we shall show, this implies quenching of phonon scattering.

The strength of the carrier-phonon scattering is quantified by the effective phonon spectrum, $\mathcal{D}(\omega)$, describing how the phonon modes interact with the QD at a given temperature. It is obtained by calculating the real part of $D^{>}(t)$ from Eq. (9.6) in frequency domain [173, 48],

$$\mathcal{D}(\omega) = \pi \sum_{\mathbf{k}} |M^{\mathbf{k}}|^2 \Big[n_{\mathbf{k}} \delta(\omega + \omega_{\mathbf{k}}) + (n_{\mathbf{k}} + 1)\delta(\omega - \omega_{\mathbf{k}}) \Big]. \tag{9.7}$$

[1] We consider parameters for GaAs, with deformation potentials $D_e = -14.6\,\mathrm{eV}$, $D_h = -4.8\,\mathrm{eV}$ [47, 182], $c_l = 5110\,\mathrm{m/s}$, and $\varrho = 5370\,\mathrm{kg/m^3}$. See Appendix C for elaborating discussions of the parameters.

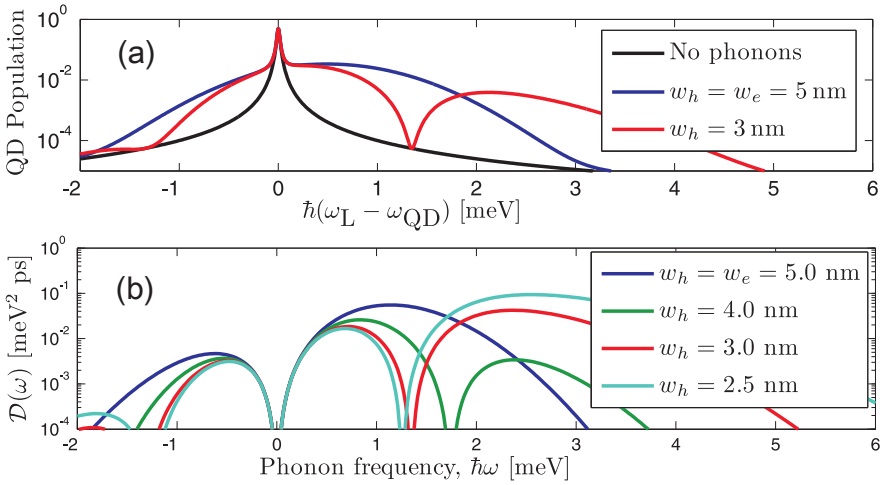

*Figure 9.1: (**a**) Stationary population of a bare QD, when excited by a CW field, corresponding to a Rabi-frequency $\hbar\Omega = 10\,\mu eV$. The black curve describes the case without phonon-assisted coupling, and the QD decay rate is $\Gamma = 1\,ns^{-1}$. (**b**) The effective phonon spectrum for spherical wavefunctions for varying w_h and w_e. For both plots, $w_e^3 + w_h^3$ is kept constant, and $T = 4\,K$.*

A positive frequency implies a phonon of energy $\hbar\omega$ being emitted into the surrounding lattice, whereas a negative frequency indicates the absorption of a phonon of energy $\hbar|\omega|$ from the surrounding environment.

For spherical wavefunctions, cf. Eq. (9.4), the effective phonon spectrum reduces to

$$\mathcal{D}(\omega) = \frac{\hbar}{4\pi\varrho c_l^5}\frac{\omega^3}{1-\mathrm{e}^{-\beta\hbar\omega}} \times \left[D_e \mathrm{e}^{-\omega^2 w_e^2/(4c_l^2)} - D_h \mathrm{e}^{-\omega^2 w_h^2/(4c_l^2)}\right]^2, \tag{9.8}$$

and is shown in Fig. 9.1b. The magnitude of $\mathcal{D}(\omega)$ is generally smaller for $\omega < 0$ compared to $\omega > 0$ due to the low probability of thermally excited phonons. As seen from Eq. (8.6), a spatially narrow wavefuntion is wide in $\mathbf{k}$-space and thus interacts with many phonon modes, explaining why $\mathcal{D}(\omega)$ broadens and increases in magnitude as w_h decreases. At non-zero temperature, $\mathcal{D}(\omega)$ has two zeros at

$$\omega^2 = \frac{4c_l^2}{w_e^2 - w_h^2}\ln\left(\frac{D_e}{D_h}\right), \tag{9.9}$$

except for the trivial zero at $\omega = 0$. In materials where $D_e/D_h > 0$, like GaAs [47, 182], dips thus appear in the effective phonon spectrum for non-zero phonon energies when $w_e \neq w_h$. The dips appear exactly when $|M^{\mathbf{k}}| \propto |D_e\mathcal{F}_e(k = \omega/c_l) - D_h\mathcal{F}_h(k = \omega/c_l)| = 0 \Rightarrow D_e\mathcal{F}_e(k = \omega/c_l) = D_h\mathcal{F}_h(k = \omega/c_l)$.

Based on this we provide a simple physical explanation for the quenching of phonon-induced processes. The deformation potential interaction occurs in

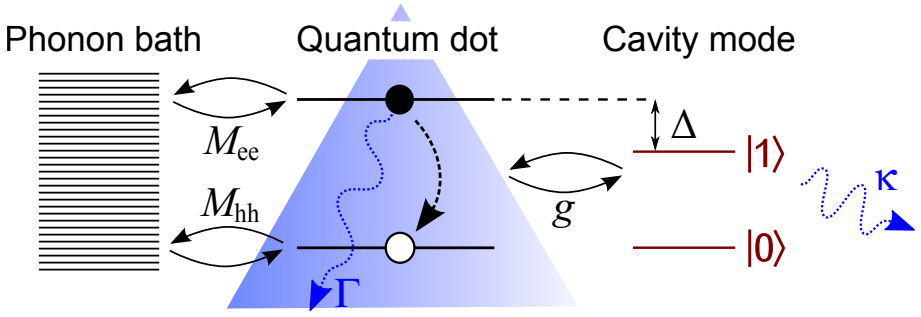

Figure 9.2: Coupled cavity–QD system interacting with a phonon reservoir. The light-matter coupling strength is g, the QD–cavity detuning is Δ (positive for the case shown), and $M_{ee/hh}$ are electron/hole–phonon coupling matrix elements. Γ is the QD population decay rate, and κ is the leakage rate from the optical cavity.

general due to the different values of the deformation potential constant in the conduction and valence band. However, for a specific detuning, this can be compensated by a difference in the confinement of the electron and the hole through the form factor in Eq. (8.6). In the case of identical electron and hole wavefunctions, $w_e = w_h$, the zeros appear at infinite frequency, and the effect is not apparent.

9.2 Coupled QD–cavity system

Quenching of phonon processes has interesting consequences for cavity QED. Instead of illuminating the QD with a laser, the QD is now placed inside a single-mode optical cavity, detuned by $\Delta = \omega_{\mathrm{QD}} - \omega_{\mathrm{cav}}$ from the QD resonance, see Fig. 9.2. H_{S} in Eq. (9.5) is replaced by the combined QD-cavity system Hamiltonian, Eqs. (2.8) and (2.12),

$$H_{\mathrm{S}} = \hbar\Delta c_e^\dagger c_e + \hbar g(a c_e^\dagger c_g + a^\dagger c_g^\dagger c_e) \tag{9.10}$$

where $\hbar\omega_{\mathrm{cav}}$ is the cavity photon energy, a ($a^\dagger$) is the annihilation (creation) operator for the cavity photons, and g is the optical interaction strength, see e.g. Ref [173]. Furthermore, the escape of photons through the cavity is included via a rate κ in the Lindblad term $L(t)$ in Eq. (9.5).

Solving Eq. (9.5), the QD decay curves in Fig. 9.3a are obtained. The structure of the phonon bath results in an asymmetry, expressed in the possibility of the QD to couple to a red-tuned (lower energy, $\Delta > 0$) cavity by the emission of an acoustic phonon, but a lack of coupling to a blue-tuned (higher energy, $\Delta < 0$) cavity by phonon absorption at low temperatures, where the population of thermally excited phonons is low [47, 48]. This is in accordance with $\mathcal{D}(\omega)$ in Fig. 9.1b. In the limit of $|\Delta| \to \infty$, the QD and the cavity decouple, and the QD decays with the rate Γ. By single-exponential fits to the QD decay curves, the lifetime of the excited QD state is extracted, see Fig. 9.3b.

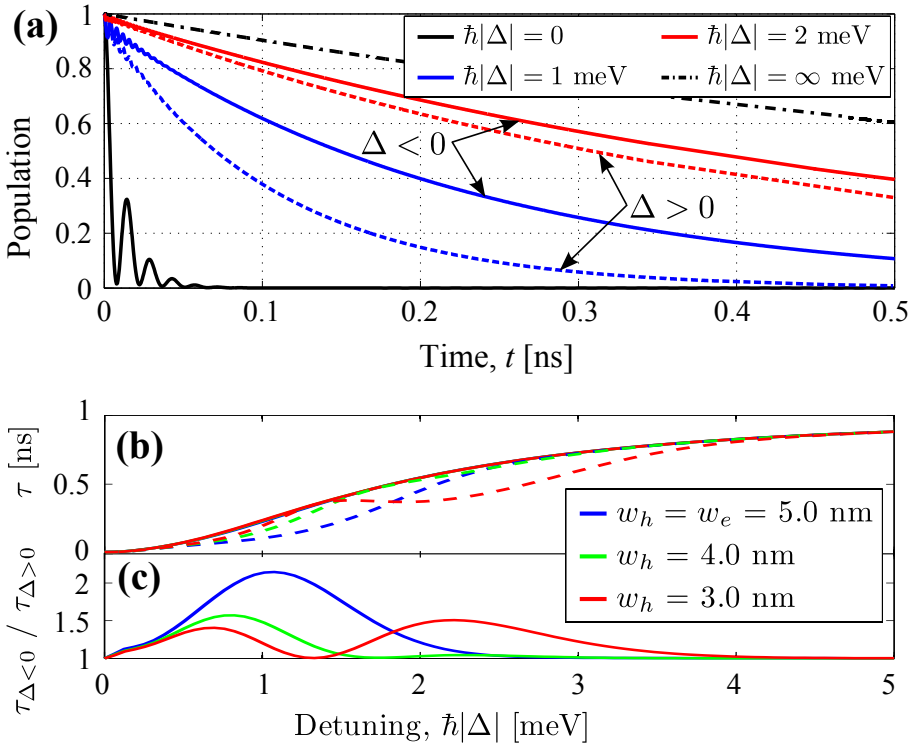

Figure 9.3: (**a**) *Time evolution of the population of an initially excited QD for different detunings. The solid (dashed) curve is for negative (positive) detuning, and the electron and the hole are equally confined,* $w_e = w_h = 5\,nm$. *The temperature is* $T = 4\,K$, *and we use* $\hbar g = 150\,\mu eV$, $\Gamma = 1\,ns^{-1}$, *and* $\hbar\kappa = 100\,\mu eV$. (**b**) *Lifetimes,* τ, *of the excited QD state plotted versus detuning for different values of* w_e *and* w_h, *keeping the volume parameter* $w_e^3 + w_h^3$ *constant. The solid (dashed) curves indicate negative (positive) detunings.* (**c**) *The degree of asymmetry versus detuning.*

From this we determine the lifetime ratio $\tau_{\Delta<0}/\tau_{\Delta>0}$, see Fig. 9.3c. Surprisingly, for $w_e \neq w_h$, a non-zero QD–cavity detuning exists, where no lifetime asymmetry is present.

To examine the physical origin of the lifetime asymmetry, we consider the total decay rate of the excited QD state when $\Delta \gg g$ as derived in Ref. s[173],

$$\Gamma_{\rm tot} \approx \Gamma + 2g^2 \frac{\gamma_{\rm tot}}{\gamma_{\rm tot}^2 + \Delta^2} \left[1 + \frac{1}{\hbar^2 \gamma_{\rm tot}} \mathcal{D}(\omega = \Delta) \right], \tag{9.11}$$

with $\gamma_{\rm tot} = (\Gamma + \kappa)/2$. The total QD decay rate, $\Gamma_{\rm tot}$, has two contributions besides the decay rate Γ. The first term in the square brackets represents the usual Purcell enhancement rate, while the second term represents the decay of the QD through the cavity by the simultaneous emission/absorption of a phonon. Thus, the behaviour of $\mathcal{D}(\omega)$ translates directly into the behaviour

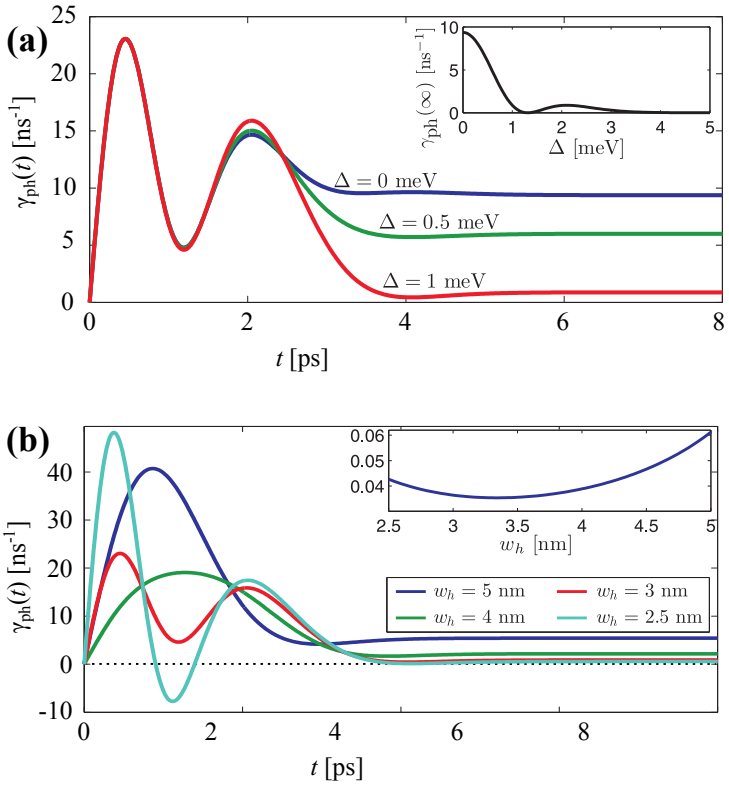

*Figure 9.4: (**a**) Time evolution of phonon-induced dephasing rate for different QD-cavity detunings. Inset shows the long-time value of the dephasing rate versus detunings, $w_h = 3$ nm, $w_e = 6$ nm, and $T = 4$ K. (**b**) Time evolution of phonon-induced dephasing rate for different wavefunction widths, keeping $w_e^3 + w_h^3$ constant, and $\Delta = 1$ meV. The inset quantifies the short-time scattering by showing the integrated value of $\gamma_{ph}(t)$ from $t = 0$ to 3 ps for different wavefunction widths. Parameter values as in Fig. 9.3.*

of the lifetime ratio plot in Fig. 9.3c, such that non-zero QD-cavity detunings exist where phonons do not affect the lifetime of the excited QD state.

The suppression of the effective phonon density is expected to affect not only the QD lifetime, but all phonon-induced effects such as pure dephasing. The degree of single-photon indistinguishability [170] is typically quantified as the ratio between the coherence time and lifetime of the emitter [171], here given by the ratio $\Gamma_{\text{tot}}/(\Gamma_{\text{tot}} + 2\gamma_{\text{ph}})$, with γ_{ph} being the pure dephasing contribution from the phonons. This hints at the importance of having a high decay rate compared to the pure dephasing rate.

The phonon-induced pure dephasing rate[2] is calculated from the phonon

[2] γ_{ph} corresponds to Re$\{\gamma_{12}\}$ in Ref. [173].

bath correlation function [173], and we find it to be given by

$$\gamma_{\rm ph}(t) = \mathrm{Re}\Big\{\hbar^{-2}(1-K)\int_0^t \mathrm{d}t'\,\mathcal{D}^<(t') + \hbar^{-2}K\int_0^t \mathrm{d}t'\,\cos\left(t'\sqrt{\Delta^2+4g^2}\right)\mathcal{D}^<(t')\Big\}, \tag{9.12}$$

where $K = 4\lambda_+^2/(1+\lambda_+^2)^2$ with $\lambda_+ = \Delta/(2g) + \sqrt{\Delta^2/(2g)^2+1}$. As seen from Fig. 9.4a, the initial behaviour of $\gamma_{\rm ph}(t)$ is governed by the bare QD-phonon coupling, whereas the long-time value depends on the cavity detuning. On the short time scale, the phonons participate in non-energy conserving virtual processes, and the electrons interact with the full phonon spectrum $\mathcal{D}(\omega)$. The long-time value $\gamma_{\rm ph}(t\to\infty)$, on the other hand, implies a Fourier transform of $\mathcal{D}(t)$ and depends only on $\mathcal{D}(\omega=0)$, which is zero, and $\mathcal{D}(\omega=\pm\sqrt{\Delta^2+4g^2})$, corresponding to sampling the spectrum at the polaritonic eigenenergies.

The phonon-induced dephasing of the QD–cavity system may be reduced by minimizing the short-time or long-time scattering. The former may be achieved by reducing the overall amplitude of $\mathcal{D}(\omega)$, as illustrated in the inset of Fig. 9.4b for $w_h \sim 3.4\,\mathrm{nm}$, compare with Fig. 9.1b. The reduction of long-time scattering is obtained by using a QD–cavity detuning such that $\sqrt{\Delta^2+4g^2}$ coincides with a dip in $\mathcal{D}(\omega)$, as seen from the inset in Fig. 9.4a. It turns out that for the indistinguishability of single photons, the reduction of the overall amplitude is the most important [49]. The coupling to excited shells in the QD through virtual phonon interactions induces additional pure dephasing [167]. However, for $T < 10\,\mathrm{K}$ this amounts to a weak background, with no qualitative effect on our result. Furthermore, for the dot sizes considered here, the next electronic energy levels are well-separated compared to the acoustic phonon energies [199], and these levels are neglected.

QD structures realized by epitaxial growth are not spherically symmetric [200], and to investigate the quenching for more realistic structures, we model truncated conical QD structures by solving the one-band effective mass Schrödinger equation using the Finite Element Method (FEM) [201]. Strain-induced effects [200] were not included, but since the strain strongly depends on the QD geometry, material and growth conditions, it may further suppress or enhance phonon scattering, thus presenting another option for engineering the basic properties.

The effective phonon spectrum obtained with the FEM wavefunctions is shown in Fig. 9.5a for an InAs QD and wetting layer embedded in a GaAs barrier[3]. The overall amplitude of the spectrum is the largest, when the carriers are strongly confined in two directions, i.e. for the tallest dot, compared to the shallow dot where the carriers are only strongly confined in one direction. These results are qualitatively explained by the form factor in Eq. (8.6).

To examine the role of material composition, we consider an $\mathrm{In}_y\mathrm{Ga}_{1-y}\mathrm{As}$ QD, where the amount of gallium in the QD and wetting layer is varied. Increas-

[3] We use $E_{g,\mathrm{GaAs}} = 1.424\,\mathrm{eV}$, $E_{g,\mathrm{InAs}} = 0.359\,\mathrm{eV}$, $m^*_{c,\mathrm{GaAs}} = 0.0665m_0$, $m^*_{c,\mathrm{InAs}} = 0.027m_0$, $m^*_{v,\mathrm{GaAs}} = 0.38m_0$, $m^*_{v,\mathrm{InAs}} = 0.34m_0$, and a wetting layer thickness of 0.2 nm [201, 202].

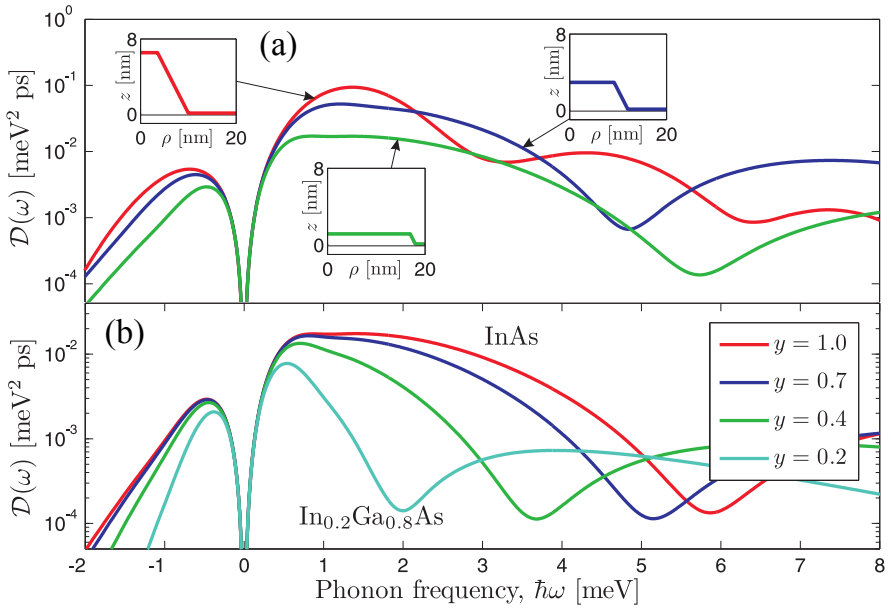

*Figure 9.5: (**a**) Effective phonon spectrum using the FEM-computed wavefunctions for the three QDs shown in the insets with matching colors, $T = 4\,K$. The QD volume and side slope are kept constant. (**b**) The effective phonon spectrum for the shallow dot in (a) for different QD material compositions, $In_yGa_{1-y}As$.*

ing the gallium concentration shrinks the band offsets [202], and the effective mass changes, giving $\mathcal{D}(\omega)$ in Fig. 9.5b. Thus, w_e and w_h both increase, resulting in a lower overall amplitude of $\mathcal{D}(\omega)$. Due to the heavier hole mass, the asymmetry between the electron and hole wavefunctions also increases, moving the dip in the spectrum towards lower frequencies, as predicted by the spherical model in Eq. (9.9) when $w_e^2 - w_h^2$ increases. The dip position may hereby be changed by the QD growth parameters. For small gallium concentrations, the confinement energies may become comparable to the Coulomb energy, in which case the exitonic nature of the electron–hole pair must be taken into account.

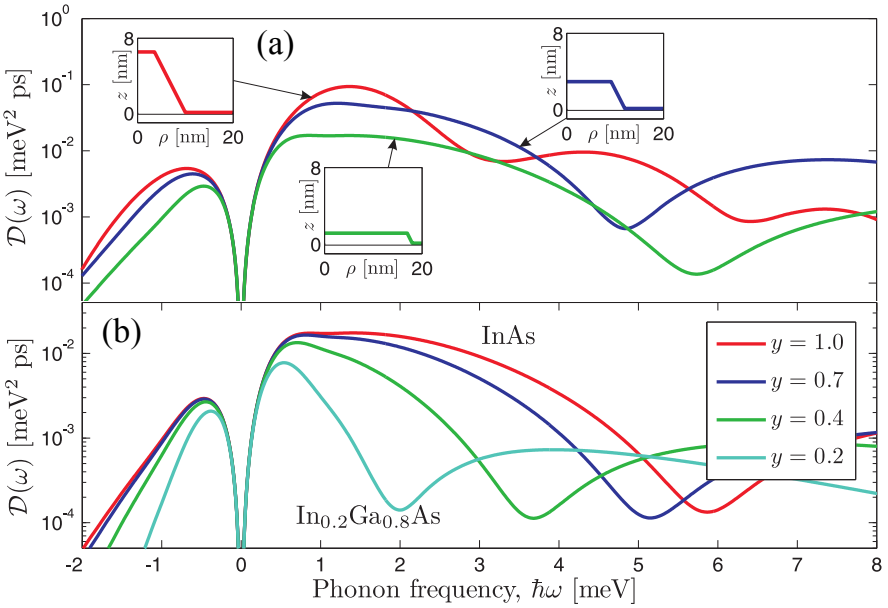

Figure 9.6: (**a**) *Effective phonon spectrum using the FEM-computed wavefunctions for the three QDs shown in the insets with matching colors,* $T = 4\,K$. *The QD volume and side slope are kept constant.* (**b**) *The effective phonon spectrum for the shallow dot in (a) for different QD material compositions,* $In_yGa_{1-y}As$.

9.3 Experimental investigation

Experimental investigations of the dependence of the QD–cavity detuning on the QD decay rate has recently been carrier out by Kristian H. Madsen and Asger Kreiner-Møller at the Niels Bohr Institute in the Quantum Photonics Group, headed by Prof. Peter Lodahl [172]. To our knowledge, this is the first demonstration of modelling the decay rates with a macroscopic model which allows us to extract the effective phonon density of states.

The detuning dependence is investigated in a standard L3 cavity in a photonic crystal membrane containing self-assembled quantum dots, see Fig. 9.7(a). The Purcell-enhancement is spectrally much broader than expected from the standard Markovian Jaynes Cummings model [203, 24], given by the first two terms in Eq. (9.11). Instead, the experimental data may be modelled very well by including the phonon contribution to the decay rate of the emitter as the last term in Eq. (9.11). In Fig. 9.7(b) the effective phonon spectrum is extracted from the experimental data, accounting for the fact that the measurements were carried out at different temperatures by plotting the temperature-independent quantity $\mathcal{D}(\omega=\Delta)\mathrm{sgn}(\Delta)\,(1-\exp[-\hbar\omega/(k_BT)])$.

The grown QDs were known to have a smaller height compared to widths, and thus the spherical electronic confinement in Eq. (9.4) would not be a sufficient description. Instead, the extracted data was fitted to match phonon interaction with an elliptical carrier wavefunction,

$$\phi_\nu(\mathbf{r}) = \pi^{-3/4} w_{\nu,\rho}^{-1} w_{\nu,z}^{-1/2} \mathrm{e}^{-\rho^2/(2w_{\nu,\rho}^2)} \mathrm{e}^{-z^2/(2w_{\nu,z}^2)},$$

given in cylindrical coordinates with ρ describing the radial dependence, where the radial width is given by $w_{\nu,\rho}$ and the height by $w_{\nu,z}$. We determine the effective phonon spectrum by evaluating Eq. (9.7) with the elliptical carrier confinement,

$$\mathcal{D}(\omega) = \frac{\hbar}{4\pi\varrho c_l^5} \frac{\omega^3}{1-\mathrm{e}^{-\beta\hbar\omega}} \Big[D_e^2 \mathrm{e}^{-\omega^2 w_{e,\rho}^2/(2c_l^2)} f_{ee}(\omega) + D_h^2 \mathrm{e}^{-\omega^2 w_{h,\rho}^2/(2c_l^2)} f_{hh}(\omega) - 2D_e D_h \mathrm{e}^{-\omega^2 (w_{e,\rho}^2 + w_{h,\rho}^2)/(4c_l^2)} f_{eh}(\omega) \Big], \qquad (9.13)$$

requiring $w_{\nu,\rho} \geq w_{\nu,z}$, and with

$$f_{\nu\nu'}(\omega) = \int_0^1 \mathrm{d}x\, \mathrm{e}^{\frac{\omega^2 b_{\nu\nu'}^2}{4c_l^2} x^2},$$

where $b_{\nu\nu} = \sqrt{2}\sqrt{w_{\nu,\rho}^2 - w_{\nu,z}^2}$, and $b_{eh} = \sqrt{b_{ee}^2 + b_{hh}^2}/\sqrt{2}$. Eq. (9.13) reduces to Eq. (9.8) in the limit $w_{h,\rho} = w_{h,z}$, $w_{e,\rho} = w_{e,z}$.

The experimental data points are fitted to Eq. (9.13) using the material parameters from Appendix C, and is seen to match the theoretical model very well. The confinement lengths for the QD wavefunctions are extracted to be: $l_{e,\rho} = 3.4$ nm, $l_{e,z} = 1.4$ nm, $l_{h,\rho} = 3.9$ nm, and $l_{h,z} = 2.3$ nm. However, to make the fit agree, $\mathcal{D}(\omega)$ has been scaled by a factor of 5.57 compared to Eq. (9.13). This scaling does, however, seem reasonable when accounting

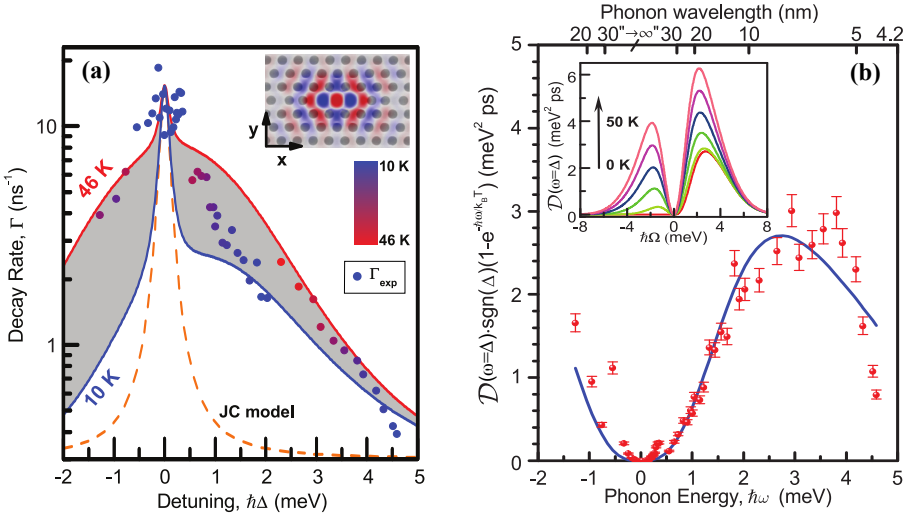

Figure 9.7: (a) Experimentally measured decay rates of a QD in an L3 photonic crystal cavity for varying detuning cavity–QD detunings (with the color specifying the experimental temperature). The emitter decay rate evaluated theoretically using Eq. (9.11) for the smallest and largest temperature used in the experiments (solid curves), and in the case where no phonon coupling is present (dashed line), i.e. the standard Jaynes Cummings model [203]. (b) A plot of the effective phonon spectrum, extracted experimentally for the L3-system, where the temperature dependence has been factored out. The inset shows the theoretical behaviour of the effective phonon spectrum when the temperature is increased. The parameters used for the L3 cavity are $\hbar\kappa = 195\,\mu eV$, $\hbar g = 22\,\mu eV$, and $\hbar\Gamma = 0.2\,\mu eV$. Reproduced from [172].

for the uncertainty in the material constants, especially the uncertainty in c_l, as it appears to the fifth power — see Appendix C and [164] for elaborating discussions.

When employing the elliptical confinement in the calculations, the zeros in the effective phonon spectrum for non-zero detunings only appear in the spherical limit. For non-spherical wavefunctions, a dip in the spectrum is however still present in similarity with Fig. 9.5, at which detunings the phonon-contribution to the decay rate would be low. The extracted widths of the wavefunctions indicate a dot geometry where the height is much smaller than the width. According to Fig. 9.5 the position of the dip would be at detunings of ∼5–6 meV. But as the phonon contribution to the QD lifetime in Eq. (9.11) is proportional to $(\gamma_{\text{tot}}^2 + \Delta^2)^{-1}$, it becomes a challenge to measure these phonon-contributions to the lifetime at such large detunings, as they are very small. This may explain why we are not able to observe any dips in the extracted effective phonon spectrum in Fig. 9.7(b).

9.4 Summary

In this chapter we have applied the non-Markovian model of the phonon dynamics from Chapter 8 to describe the dynamics of a QD driven by a slightly

detuned laser. We expanded this to consider the decay dynamics of a QD inside an optical cavity. In both cases we predict how that electron-phonon scattering may be suppressed due to differences in the spatial confinement of electrons and holes. Physically we explain this by a balancing between the electronic confinement and the effect on the deformation potential coupling on the energy bands in the QD. We suggest that the effect may be measured by photoluminescence excitation spectroscopy, but also that it should strongly affect the decoherence properties of cavity QED systems.

We derived an expression for the phonon spectrum of ellipsoidal wavefunctions of the electrons and holes, and it is able to reproduce recent experimental results very well. In the experiment, we were however not able to observe any of the dips in the effective phonon spectrum due to the electron-hole asymmetry. The wavefunction dimensions extracted from the experiment estimates that the dip in the phonon spectrum appear for QD–cavity detunings of $\sim$ 4-5 meV. But at these detuning values, the phonon contribution to the measured lifetime is also very low according to Eq. (9.11), making the dip very difficult to measure. In another recent experiment in Ref. [198], a dip is observed in the intensity spectrum of a QD pumped by a detuned laser at a detuning of $\sim$ 1 meV, which could be due to these electron-hole asymmetries. It was, however, not possible to facilitate a collaboration for further investigations.

We demonstrated in Eq. (9.12) that the phonon-induced dephasing has two contributions: In the long time limit depends on sampling the effective phonon spectrum at two specific points, $\mathcal{D}(\omega = \pm\sqrt{\Delta^2 + 4g^2})$. In the short-time limit, however, phonons may participate in non-energy-conserving virtual processes, which corresponds to sampling the effective phonon at all frequencies. Both of these contributions have to be minimized in order to reduce the phonon-induced dephasing the most.

In later works [73, 49], P. Kaer et al. have specifically investigated how the phonon-induced dephasing affects the indistingushability of photons emitted from a single-photon source created with a QD inside an optical cavity such as a micropillar. Here it is shown that the short-time non-Markovian interaction has the largest significance on the indistinguishability of the emitted photons. These effects are minimized when the integral of the effective phonon spectrum is minimized, shown by the inset in Fig. 9.4, providing optical values of the electronic and hole confinements. One must however keep in mind, that these depend on the material parameters of the quantum dot and the barrier.

We expect this new approach for suppressing phonon interactions to be important for the reduction of decoherence in devices for quantum information technology, like single-photon sources and switches. This is combined with the possibility of also engineering the phononic confinement, as will be discussed in the following chapter.

Chapter 10

Phonon-induced dynamics — The phononic confinement

In experimental setups which employ QDs, a bulk description of the phonons is usually employed, even though the sample with the QDs have a finite extent. The question is, however, for which structures the bulk assumption is valid, and whether the confinement of phonon may be exploited to improve the performance of a quantum system, i.e. to improve the performance of a single-photon source.

The simplest approach to consider phonon confinement is by confining them in a single spatial direction, i.e. in an infinite slab. It is well-known that the phonon reservoir changes properties when describing the coupling to a QD close to a surface [204, 205]. These descriptions have been expanded to include the infinite slab structure, where the calculations show that the emitted phonons have a possibility of being scattered at the surface and interact with the QD carriers again, which will introduce modulations in the QD absorption spectrum [206, 207, 193].

A specific interest has been in predicting the dynamics in a double-quantum dot system placed in an infinite slab [208]. The double-dot systems are viable candidates as solid-state qubits with the qubit states represented by an excitation in either of the dots, where the coefficients of the system may be controlled by electrically controlling the tunneling rate between the qubits. The performance of the qubits are, however, deteriorated by phonon-assisted coupling between the quantum dots. By placing the emitters at optimal positions in the slab, the phonon-induced effects may however be suppressed, due to changes in the phonon modes as compared to bulk phonons [208, 209, 210, 211].

In this chapter, we extend the approaches above to investigate how these suppressions apply to a cavity–QD-system suspended in an infinite slab. Using the theory from the previous chapters we have an approach to directly address the phonon reservoir. Physically such a system could correspond to the L3

cavity in a photonic crystal slab as in Section 9.3. We show how the decay rate of the emitter may be either enhanced or suppressed (compared to bulk), depending on the detuning from the cavity modes. The enhancement/suppression depends on the energies of the vibrational modes in the slab, and we show how a slight change in the detuning can alter the phononic contribution to the decay rate significantly. The enhancement or reduction is most significant when the slab is thinnest, and we estimate that for a slab thickness of more than ~ 70 nm, a bulk description of the phonon modes is sufficient.

In Section 10.1 the vibrational modes of an infinite slab is described, and we discuss the changes in the electron-phonon coupling mechanism as compared to bulk phonons. The resulting dynamics are calculated in Section 10.2, and the effective phonon spectrum is determined. The results are based on *Reducing dephasing in coupled quantum dot-cavity systems by engineering the carrier wavefunctions.* Proceedings of SPIE, the International Society for Optical Engineering **8271**, 82710E (2012) by A. Nysteen, P. K. Nielsen, and J. Mørk.

10.1 Phonon modes in an infinite slab

For an isotropic elastic continuum the ion displacement at a position $\mathbf{r}$ obeys the wave equation [206],

$$\partial_t^2 \mathbf{u} = c_t^2 \nabla^2 \mathbf{u} + (c_l^2 - c_t^2)\boldsymbol{\nabla}(\boldsymbol{\nabla} \cdot \mathbf{u}), \tag{10.1}$$

where c_t and c_l are the velocity of the transverse and longitudinal sound waves in bulk semiconductors, respectively, and obey $c_l > c_t$. The boundary conditions to Eq. (10.1) stem from the assumption of a *free-standing* slab, requiring that the normal components of the stress tensor vanish at the slab surface. For the vibrational modes in an infinite slab, the solution of Eq. (10.1) is on the form

$$\mathbf{u}(\mathbf{r}, t) = \sum_n \int \mathbf{u}_n(\mathbf{k}_\parallel, z) \mathrm{e}^{\mathrm{i}\mathbf{k}_\parallel \cdot \mathbf{r}_\parallel - \mathrm{i}\omega_n t} \frac{\mathrm{d}\mathbf{k}_\parallel}{(2\pi)^2}, \tag{10.2}$$

where the phonons are described by a continuum of plane waves in the in-plane directions and by a discrete set of eigenmodes $\mathbf{u}_n(\mathbf{k}_\parallel, z)$ in the z-direction depending on the in-plane wavevector, $\mathbf{k}_\parallel$ [206].

Typically, vibrational modes of a slab are divided into shear, dilatational and flexural waves [193]. According to Eq. (8.3), the deformation potential coupling allows coupling only between electrons and *longitudinal* acoustic phonons with the assumptions discussed in Section 8.1, and thus the shear waves will not be considered. Examples of the grid displacements for dilatational and flexural modes are shown in Fig. 10.1.

Following [193, 212], the carrier–phonon interaction matrix element for the deformation potential interaction for dilatational modes simplifies to

$$M_{n,\nu\nu} = D_\nu \mathcal{G}_n \mathcal{F}_{n,\nu}, \tag{10.3}$$

where D_ν is the deformation potential of the electron/hole, and $\mathcal{G}_n$ is a factor containing the dispersion relation of the phonon subband n, ω_n. The spatial

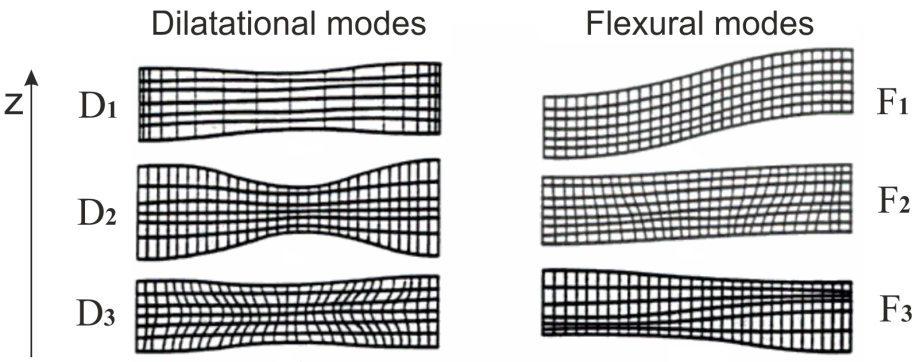

Figure 10.1: Illustration of the grid displacement for the three lowest-order dilatational (symmetric) and flexural (anti-symmetric) modes. Illustration from [188].

overlap between the electronic and phononic wavefunctions is contained in the form factors, analogous to the bulk form factor in Eq. (8.6),

$$\mathcal{F}_{n,\nu,\mathrm{dil}} = \int_{\mathrm{slab}} \mathrm{d}\mathbf{r}\, |\phi_\nu(\mathbf{r})|^2 \mathrm{e}^{\mathrm{i}\mathbf{k}_\parallel \cdot \mathbf{r}_\parallel} \cos(k_{l,n} z), \tag{10.4}$$

$$\mathcal{F}_{n,\nu,\mathrm{flex}} = \int_{\mathrm{slab}} \mathrm{d}\mathbf{r}\, |\phi_\nu(\mathbf{r})|^2 \mathrm{e}^{\mathrm{i}\mathbf{k}_\parallel \cdot \mathbf{r}_\parallel} \sin(k_{l,n} z), \tag{10.5}$$

The electronic confinement is included in a simple way by assuming a quantum dot with spherical wavefunction placed in with its center in the middle of the slab, and with $z = 0$ as a symmetry plane. With this configuration the electrons will only interact with the dilatational (symmetric) slab modes and not the flexural (anti-symmetric) modes, with the latter caused by a vanishing integral in Eq. (10.5) as the integrand has an odd-symmetry in the z-direction with the given assumptions.

For bulk phonon modes, $\mathcal{G}_n$ has a simple form as in Eq. (8.7), which however is more complex for phonon modes in a slab — see Ref. [193] for the specific expression for $\mathcal{G}_n$. The dispersion relation for the dilatational modes, which is employed when evaluating $\mathcal{G}_n$, is obtained from Ref. [193], and it is illustrated in Fig. 10.2

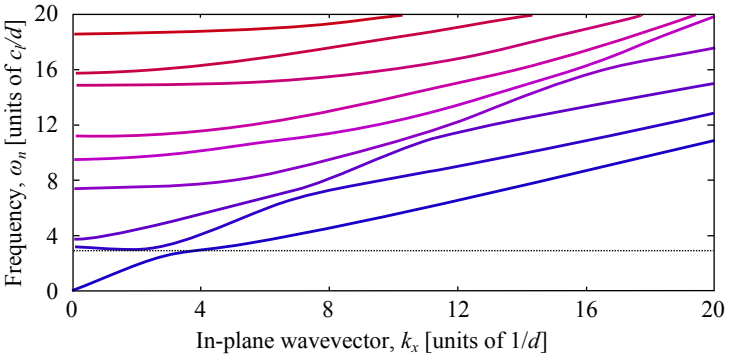

Figure 10.2: Phonon dispersion for dilatational modes, relating the frequency of the phonon modes in the nth band to the phonon wavevector, both normalized to the thickness of the slab, d. The dashed line indicates a minimum of the second band at $\omega d/c_l = 2.98$. Reproduced from [213].

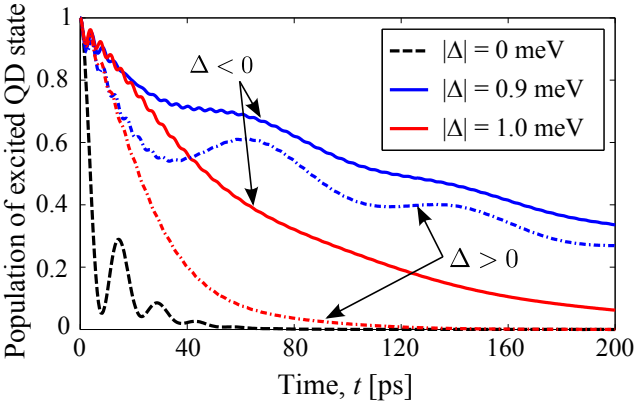

Figure 10.3: Population of the initially excited QD state as a function of time with a slab thickness of $d = 10\,nm$ at $T = 10\,K$. The solid (dash-dot) line is for negative (positive) detuning. The initial oscillations at $\Delta = 0$ are Rabi-oscillations in the strong-coupling limit.

10.2 Dynamics

Eq. (9.5) is solved numerically by assuming an initially excited QD state, using the material parameters in Appendix C and with spherical wavefunctions as in Eq. (9.4). To emphasize the changes induced by the *phononic* confinement, we make the crude approximation that the electron and hole have the same confinement length, $w_e = w_h = 5\,\text{nm}$. The resulting QD decay is illustrated in Fig. 10.3 for various QD–cavity detunings, where an asymmetry exist between positive/negative detuning due to the emission/absorption of a phonon, as discussed in Chapter 9. For bulk phonons we expect the fastest decay at the lowest detunings, where the coupling to the cavity through the Purcell effect is strongest. This is however not the case in Fig. 10.3 for the slab configuration, where the detuning is varied only slightly. To investigate this interesting feature further, we examine the lifetime asymmetry in detail.

The lifetime variation with detuning is calculated by extracting the lifetime of the excited QD state by a single-exponential fit to the decay curves in Fig. 10.3. As a measure of the asymmetry, we plot the lifetime ratio $\tau_{\Delta<0}/\tau_{\Delta>0}$ as a function of the QD-cavity detuning, see Fig. 10.4. At small slab thicknesses we clearly see the effect of both suppressed and enhanced electronic interaction on the lifetime asymmetry.

As we saw in the previous chapters that the effective phonon spectrum contains details information about the phonon-induced features, the spectrum in Eq. (9.7) is evaluated using the new expression for the interaction matrix elements from Eq. (10.3). A plot of the effective phonon spectrum in provided in Fig. 10.5. It shows the same features as seen in the lifetime plot in Fig. 10.4, where both suppressed and enhanced phonon interaction can be observed, dependent on the value of Δ. Due to the limited amount of sampling points in the detuning-array, we are not able to catch the suppressed and enhanced phonon modes properly for the slab with $d = 30\,\text{nm}$ in the lifetime plot, but they are clearly seen in the effective phonon spectrum. For a slab thickness of $d = 70$ nm, the suppression/enhancement not pronounced in the spectrum any more as compared to the bulk case (except for very small detunings).

In the calculations we include a finite lifetime of the phonons to account for other dephasing processes of the phonon reservoir such as anharmonic effects as described in Eq. (2.9) which from Ref. [214] is estimated to be 600 ps at 10 K. These are accounted for by multiplying $\mathcal{D}^{\gtrless}(t)$ in Eq. (9.6) with $\exp[-t/600\,\text{ps}]$. For bulk phonon, this factor is insignificant, as the correlation time of the reservoir (i.e. the memory depth) is only around 5-10 ps [173]. However, in the slab, longer memory depths are observed as the phonons may be reflected from the slab surfaces and interact with the QD again, and thus the correction for other dephasing processes must included.

The enhanced electron-phonon coupling stems from interaction with a resonant vibrational mode of the slab and arises from a van-Hove singularity in the phonon density of states. This is seen in Fig. 10.2 as a minimum in the second phonon band of the dispersion curves [213, 207], equivalent to a theoretically infinite phonon density of states. The resonance peak appears in Eq. (9.6) at $\omega = 2.98 \cdot c_l/d$, with d being the thickness of the slab. The resonance peak

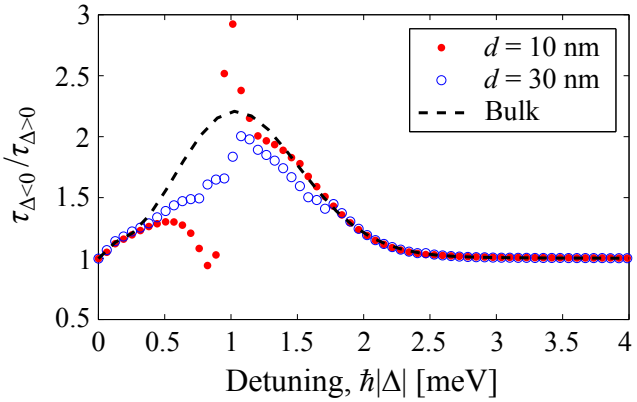

Figure 10.4: Lifetime of the excited QD state vs. the detuning for different slab widths, plotted for $T = 10\,K$, and compared to the case of bulk phonons. The point where the lifetime asymmetry drops below 1 is due to inaccuracies in fitting a single-exponential to the decay curves in Fig. 10.3.

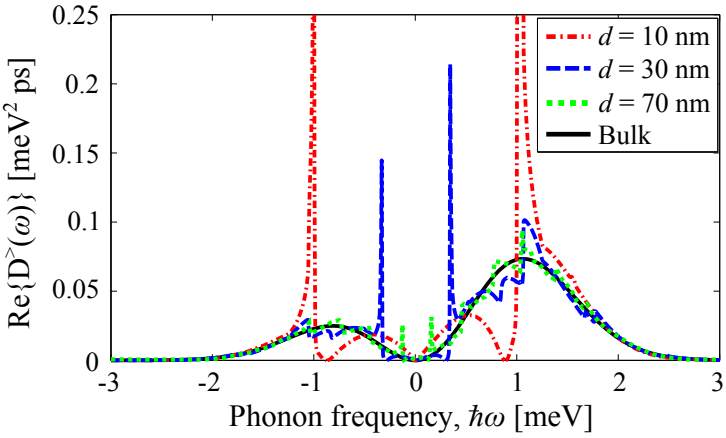

Figure 10.5: Effective phonon spectrum versus phonon frequency plotted for different slab thickness at $T = 10\,K$.

moves closer to $\omega = 0$ as the thickness of the slab increases. However, the amplitude of the resonance peak will decrease with increasing d, since a phonon emitted from the QD has a smaller probability of interacting with the surface rather than disappearing into the infinite extend of the slab. At $d = 10\,\text{nm}$ the travel time for a photon from the QD to the surface and back is $\sim 4\,\text{ps}$, which exactly corresponds to the fast oscillations in Fig. 10.3 for non-zero detuning.

Surprisingly, at slightly lower detunings than for the enhanced phonon modes, the interaction with the phonon modes is suppressed, which according to Eq. (9.11) gives the zeros in the lifetime asymmetry plot in Fig. 10.4. This system thus shows features of a coupled QD-cavity system where the system at a specific detuning does not experience any phonon-induced lifetime asymmetry, even when assuming identical widths of the wavefunction for the electron and the hole.

We should emphasize the assumptions and approximations made for the calculations. The large spikes in the effective phonon spectrum correspond to a strong electron-phonon interaction, which in the theory is assumed only to be a weak perturbation in Eq. (8.22). In a system where these phonon resonances is to be exploited, the assumption of small interaction strength should be tested. Furthermore, if very narrow slabs are used, the contrast between the GaAs material and the surrounding air introduces a quantum well for the electrons as well, which has to be taken into account. A full description where the flexural slab modes have to be taken into account, if we want to consider the possibility of placing the QD away from the center plane of the slab, or if we treat non-symmetric electronic wavefunction.

10.3 Summary

In conclusion we have demonstrated how the presence of an infinite slab around a coupled cavity-quantum dot system alters the dynamics significantly due to enhanced/suppressed electron-phonon interaction depending on the cavity-quantum dot detuning. The enhancement/suppression depends on how the QD–cavity detuning matches the vibrational modes of the slab, and by changing the detuning only slightly ~ 0.3 meV, the phonon contribution to the decay rate of the emitter may go from 0 to a large enhancement compared to the bulk case. We estimate that for a slab thickness of ~ 70 nm, the bulk description of the phonon modes is sufficient. In the experiment in Section 9.3, a slab thickness of ~ 150 nm was used, and the considerations in this chapter justify the bulk treatment of the phonons.

We believe that these effects of confining the phonons may have interesting applications in the creation of a coupled QD-cavity system with low dephasing, showing promising features e.g. for obtaining high indistinguishability in single-photon sources. An interesting perspective of the calculations would be to consider micropillar single-photon sources [32, 215]. Here the phonons are confined effectively in two dimensions, where one thus would expect a higher sensitivity of the phonon modes to confinement dimensions than compared to the slab. The electron-phonon interaction matrix elements will, however, also becomes more complex.

Chapter 11

Highlights and outlook

The work carried out in this thesis provides a fundamental description of photon–photon interaction in the presence of non-linearities such as a two-level system, and we discuss implementations, possibilities, and limitations when exploiting the non-linearities in conditional gates for quantum computation. When utilising solid-state implementations of the few-photon non-linearities such as semiconductor quantum dots, coupling to phonons may deteriorate the efficiency, and we discuss possibilities for suppressing the phonon-induced effects by manipulating the electronic and phononic confinement.

Highlights

We focus on a simple system in which propagating photons interact via a material non-linearity, namely in an infinite waveguide containing a two-level emitter. Single-photon scattering is well-understood, but the dynamics becomes much more complex for two-photon scattering due to saturation of the emitter. We consider two approaches for examining non-trivial two-photon interactions; a numerical wavefunction approach and the scattering matrix formalism. The wavefunction approach excels in determining the total system wavefunction at all times and makes it possible to relate the emitter excitation to the scattering-induced correlations. It may easily be expanded to consider more complicated scatterers, e.g. multiple quantum dots in a cavity or spatially separated scatteres. On the other hand, the scattering matrix formalism allows calculation of the scattered state faster than the full numerical approach. However, it relies on the calculation of a scatterer-specific two-photon scattering matrix which attains a simple expression for the simple two-level scatterer, but quickly becomes much more complex to evaluate if the scatterer is more complex.

With the two approaches we demonstrate that the largest non-linearity-induced correlations between two photons scattering on an emitter occurs when the emitter is excited the most. This happens when the bandwidth of the incoming photon pulses is similar to the linewidth of the emitter. For scattering of two initially counter-propagating photons we show how the emitter works as a non-linear beam splitter in this regime of input pulse bandwidths. We

demonstrate how the non-linearity may help preserving the spectral shapes of the photons. Even when accounting for all the scattering-induced changes phase and spectrum of the photons, the photon properties are preserved with almost 80 % in the non-linear beam splitter.

By employing the gained knowledge, we propose an experimental setup for a controlled-phase gate consisting of passive optical components and two emitters. We estimate a gate fidelity close to 80 %, limited by phase modulations upon scattering and inherent errors from four-wave-mixing processes caused by the non-linearity. We discuss another proposal for a controlled-phase gate consisting of a waveguide coupling to two ring resonators with a strong second-order non-linearity. The scheme suppresses the four-wave-mixing processes by dynamically capturing the first of two temporally separated photons. Theoretically the scheme promises higher fidelities than the other gate proposal, although the dynamical capturing relies on precise timing and control over cavity detunings, which in reality may be very difficult with the current technology.

When the non-linearities are implemented in solid-state environments, coupling to phonons may induce dephasing, limiting the coherent interactions. To understand how to minimize the phonon-induced effects, we apply a model by P. Kaer [173] which considers a non-Markovian coupling to a large phonon reservoir through the deformation potential coupling. We specifically investigate how the electronic and phononic confinement affect the dynamics of a quantum dot decay through coupling to an optical cavity. The theory is applied to an experimental measurement of the decay rate of a quantum dot inside an photonic crystal cavity, from which we are able to extract an effective phonon spectrum. When examining the electronic confinement, we find that the asymmetry between the electron and hole wavefunction in a quantum dot in a GaAs platform may be exploited to suppress the phonon-induced effects. We explain this suppression by a balancing of the electron-hole wavefuntion and the deformation potential coupling, occuring only in materials where the deformation interaction shifts the electron and hole energy bands in the same direction. Regarding the confinement of the phonons, we consider a quantum dot–cavity system with the dot placed in the center of an infinite slab. We demonstrate how the phonon-assisted coupling of the dot through the cavity may be either significantly suppressed or enhanced, depending on how the quantum dot–cavity detuning matches the energies of the vibrational modes in the slab. Furthermore we estimate that a bulk description of the phonon modes is sufficient for a slab thickness larger than ~ 70 nm, at least when describing the phonon-contribution the emitter decay rate. We believe that a full understanding of the possibilities of manipulating the electronic and phononic confinements will be important for reducing dephasing in quantum devices such as single-photon sources and non-linear gates.

Outlook and future directions

It is obvious that a large amount of work still has to be carried out in order to achieve an efficient, scalable platform for performing quantum computation

utilising few-photon non-linearities. This is both in the field of creating efficient single-photon sources, gates, and detectors in a scalable scheme — and also in combining them together in integrated circuits without large coupling losses between the different devices. In wake of recent breakthroughs, the following years will most likely bring many new achievements in the fundamental study of strongly interacting photons. As an example of the recent breakthroughs, a chiral spin-photon interface in a photonic crystal waveguide allows direction-specific emission to emitter depending on the spin state of a quantum dot [138]. New structures with non-linearities in the single-photon regime have also appeared, such as a graphene plasmon cavity coupling to a dielectric waveguide [216], which extends the perspectives of the possibilities with the few-photon non-linearities.

It would indeed be interesting to expand the numerical code to consider several spatially separated emitters and/or cavities in the waveguide, especially regarding investigation of sharp Fano resonances [217]. These structures require a significantly smaller energy detuning to change from being fully transmissive to fully reflective, as compared to a system with only a single emitter. These Fano-structures could high relevance when designing few-photon conditional gates.

Regarding the phonon-induced effects it would be worth making a more thorough investigation of varying the material compositions in order to change the electronic confinement and deformation potential constants such that the phonon-induced dephasing is suppressed the most in quantum devices. We also see promising perspectives in suppressing the dephasing by altering the phononic confinement, which may be done by an expansion of the presented model to more complicated phonon confinements such as in micropillars. The possibility of creating structures with simultaneous photonic and phononic bandgap has already been proposed, although with the purpose of enhancing the optomechanical coupling strength [218, 195]. The bandgap in the presented structures is, however, for vibrational modes with energies in the GHz regime, which are several magnitudes below the energies of the acoustic phonons. It would be interesting to examine if these structures could be exploited to suppress dephasing from acoustical phonons in the quantum dot systems.

Appendix

Appendix A

Analytical derivation of two-photon emitter excitation

In this appendix we demonstrate how to find an analytical expression for the emitter excitation probability, when a two-photon pulse consisting of two co-phopagating, uncorrelated single-photon pulses scatters on an emitter, which initially is in its ground state. We specifically determine the excitation probability for an input pulse consisting of two identical pulses with a Gaussian wavepacket, and we use this to verify the numerical implementation demonstrated in Chapter 4.

The procedure of the derivation follows Kojima et al. [91] and Valente et al. [92], starting from the Hamiltonian in Eq. (3.1), with the waveguide modes given as plane wave modes with a frequency ν. The waveguide modes are split into two subgroups, a and b, distinguished by the direction of propagating, and with different orientations of the spatial axis of the two modes, by which we may assume a positive value of the wavevector for all modes (removing the absolute value in the dispersion relation, Eq. (3.4)). With these notations, the Hamiltonian is

$$H = H_{\mathrm{1D}} + H_{\mathrm{atom}} + H_{\mathrm{int}}, \tag{A.1}$$

$$H_{\mathrm{1D}} = \sum_{\nu=0}^{\infty} \hbar\nu (a_\nu^\dagger a_\nu + b_\nu^\dagger b_\nu), \tag{A.2}$$

$$H_{\mathrm{atom}} = \hbar\nu_A c^\dagger c, \tag{A.3}$$

$$H_{\mathrm{int}} = -\mathrm{i}\sum_{\nu=0}^{\infty} \hbar g_\nu^a [a_\nu c^\dagger - c a_\nu^\dagger] - \mathrm{i}\sum_{\nu=0}^{\infty} \hbar g_\nu^b [b_\nu c^\dagger - c b_\nu^\dagger], \tag{A.4}$$

where $a_\nu^\dagger$ and $b_\nu^\dagger$ creates an excitation of frequency ν in the respective subgroup of waveguide modes, and $c^\dagger$ creates an excitation in the emitter. Here ν_A is the transmission frequency of the emitter, and g_ν^a and g_ν^b describing the coupling

strength of the emitter into the different directions of the waveguide. In this derivation we use slightly different definitions of rotating frames etc. compared to the remaining thesis, which however does not influence the results

We define the two-excitation state as,

$$|\psi(t)\rangle = \sum_{\nu=0}^{\infty} \psi_\nu^a(t) a_\nu^\dagger c^\dagger |\phi\rangle + \sum_{\nu=0}^{\infty} \psi_\nu^b(t) b_\nu^\dagger c^\dagger |\phi\rangle + \sum_{\nu_1,\nu_2=0}^{\infty} \Big[\phi_{\nu_1\nu_2}^{aa}(t) a_{\nu_1}^\dagger a_{\nu_2}^\dagger + \phi_{\nu_1\nu_2}^{ab}(t) a_{\nu_1}^\dagger b_{\nu_2}^\dagger + \phi_{\nu_1\nu_2}^{ba}(t) b_{\nu_1}^\dagger a_{\nu_2}^\dagger + \phi_{\nu_1\nu_2}^{bb}(t) b_{\nu_1}^\dagger b_{\nu_2}^\dagger \Big] |\phi\rangle. \tag{A.5}$$

The factor of $1/\sqrt{2}$ used in Eq. (4.5) is absorbed into the expansion coefficients of the state to ease the notation in the following for ϕ^{aa} and ϕ^{bb} (changing the normalization condition of the state). Furthermore we define the symmetric version of ϕ,

$$\Phi_{\nu_1\nu_2}^{\sigma_1\sigma_2} = \frac{\phi_{\nu_1\nu_2}^{\sigma_1\sigma_2} + \phi_{\nu_2\nu_1}^{\sigma_2\sigma_1}}{2}. \tag{A.6}$$

The expressions above are inserted in the time-dependent Schrödinger equation $\mathrm{i}\hbar\partial_t|\psi(t)\rangle = H|\psi(t)\rangle$. By projecting onto the different system states given in Eq. (A.5), a system of coupled differential equations is achieved,

$$\partial_t \psi_w^\sigma = -\mathrm{i}(\nu_A + w)\psi_w^\sigma - 2\sum_{\nu_2} \left(g_{\nu_2}^\sigma \Phi_{w\nu_2}^{\sigma\sigma} + g_{\nu_2}^{\bar\sigma} \Phi_{w\nu_2}^{\sigma\bar\sigma} \right), \tag{A.7a}$$

$$\partial_t \Phi_{w_1 w_2}^{\sigma_1\sigma_2} = -\mathrm{i}(w_1 + w_2)\Phi_{w_1 w_2}^{\sigma_1\sigma_2} + \frac{1}{2}\left(g_{w_2}^{\sigma_2}\psi_{w_1}^{\sigma_1} + g_{w_1}^{\sigma_1}\psi_{w_2}^{\sigma_2} \right), \tag{A.7b}$$

where $\sigma \in \{a, b\}$, and $\bar\sigma$ is the opposite of σ, i.e. $\bar a = b$. Defining the Fourier transform

$$\psi^\sigma(r,t) = \sum_{\nu=0}^{\infty} \psi_\nu^\sigma(t) \mathrm{e}^{\mathrm{i}k_\nu r}, \tag{A.8}$$

and using the relation

$$\sum_\nu \nu \psi_\nu^\sigma \mathrm{e}^{\mathrm{i}k_\nu r} = -\mathrm{i}c\partial_r \sum_\nu \psi_\nu^\sigma \mathrm{e}^{\mathrm{i}k_\nu r}, \tag{A.9}$$

Eq. (A.7a) becomes

$$[\partial_t + c\partial_r]\,\psi^\sigma(r,t) = -\mathrm{i}\nu_A \psi^\sigma(r,t) - 2\sum_{\nu w} \left(g_\nu^\sigma \Phi_{w\nu}^{\sigma\sigma}(t) + g_\nu^{\bar\sigma} \Phi_{w\nu}^{\sigma\bar\sigma}(t) \right) \mathrm{e}^{\mathrm{i}k_w r}. \tag{A.10}$$

The term $-\mathrm{i}\nu_A\psi^\sigma(r,t)$ is removed by introducing a rotating frame [92],

$$\tilde\psi^\sigma(t) = \psi^\sigma(t)\mathrm{e}^{\mathrm{i}\nu_A t}\mathrm{e}^{\mathrm{i}\omega_L^\sigma(t-r/c)}. \tag{A.11}$$

With this, Eq. (A.10) becomes

$$[\partial_t + c\partial_r]\tilde\psi^\sigma(r,t) = -\mathrm{e}^{\mathrm{i}\nu_A t + \mathrm{i}\nu_L^\sigma(t-r/c)} 2\sum_{\nu w} \left(g_\nu^\sigma \Phi_{w\nu}^{\sigma\sigma} + g_\nu^{\bar\sigma}\Phi_{w\nu}^{\sigma\bar\sigma} \right) \mathrm{e}^{\mathrm{i}k_w r}. \tag{A.12}$$

To determine expressions for the Φ's, we formally integrate Eq. (A.7b), assuming that the initial time is $t = 0$,

$$\Phi^{\sigma_1\sigma_2}_{w_1w_2}(t) = \Phi^{\sigma_1\sigma_2}_{w_1w_2}(0)\mathrm{e}^{-\mathrm{i}(w_1+w_2)t} + \frac{1}{2}\int_0^t \mathrm{d}t' \ \left[g^{\sigma_2}_{w_2}\psi^{\sigma_1}_{w_1}(t') + g^{\sigma_1}_{w_1}\psi^{\sigma_2}_{w_2}(t')\right]\mathrm{e}^{-\mathrm{i}(w_1+w_2)(t-t')}. \tag{A.13}$$

Inserting this into Eq. (A.12), we arrive at

$$[\partial_t + c\partial_r]\tilde{\psi}^\sigma(r,t) = -A^\sigma_1(r,t) - A^\sigma_2(r,t), \tag{A.14}$$

where

$$A^\sigma_1(r,t) = 2\sum_{wv}\left[g^\sigma_v\Phi^{\sigma\sigma}_{wv}(0) + g^{\overline{\sigma}}_v\Phi^{\sigma\overline{\sigma}}_{wv}(0)\right]\mathrm{e}^{\mathrm{i}\nu_A t + \mathrm{i}\nu^\sigma_L(t-r/c) - \mathrm{i}(w+v)t + \mathrm{i}k_w r}, \tag{A.15}$$

and

$$\begin{aligned} A^\sigma_2(r,t) \quad = \quad & \mathrm{e}^{\mathrm{i}\nu_A t+\mathrm{i}\nu^\sigma_L(t-r/c)}\sum_{wv_2}\left[g^\sigma_v\int_0^t \mathrm{d}t' \ \left[g^\sigma_v\psi^\sigma_w(t') + g^\sigma_w\psi^\sigma_v(t')\right]\mathrm{e}^{-\mathrm{i}(w+v)(t-t')}\right. \\ & \left. + g^{\overline{\sigma}}_v\int_0^t \mathrm{d}t' \ \left[g^{\overline{\sigma}}_v\psi^\sigma_w(t') + g^\sigma_w\psi^{\overline{\sigma}}_v(t')\right]\mathrm{e}^{-\mathrm{i}(w+v)(t-t')}\right]\mathrm{e}^{\mathrm{i}k_w r}. \end{aligned} \tag{A.16}$$

From here we make the Markov-approximation and thus assume that the coupling constants are independent of frequency, according to the discussion in Section 3.2.

Simplifying $A^\sigma_2(r,t)$

With Eq. (A.8), we may further divide $A^\sigma_2(r,t)$ into four terms,

$$A^\sigma_{2,1}(r,t) = g^\sigma g^\sigma\int_0^t \mathrm{d}t' \ \psi^\sigma(r - c(t-t'),t')\sum_\nu \mathrm{e}^{-\mathrm{i}\nu(t-t')+\mathrm{i}\nu_A t+\mathrm{i}\nu^\sigma_L(t-r/c)}, \tag{A.17a}$$

$$A^\sigma_{2,2}(r,t) = g^\sigma g^\sigma\int_0^t \mathrm{d}t' \ \psi^\sigma(-c(t-t'),t')\sum_w \mathrm{e}^{-\mathrm{i}w(t-t')+\mathrm{i}k_w r+\mathrm{i}\nu_A t+\mathrm{i}\nu^\sigma_L(t-r/c)}, \tag{A.17b}$$

$$A^\sigma_{2,3}(r,t) = g^{\overline{\sigma}} g^{\overline{\sigma}}\int_0^t \mathrm{d}t' \ \psi^\sigma(r - c(t-t'),t')\sum_\nu \mathrm{e}^{-\mathrm{i}\nu(t-t')+\mathrm{i}\nu_A t+\mathrm{i}\nu^\sigma_L(t-r/c)}, \tag{A.17c}$$

$$A^\sigma_{2,4}(r,t) = g^{\overline{\sigma}} g^\sigma\int_0^t \mathrm{d}t' \ \psi^{\overline{\sigma}}(-c(t-t'),t')\sum_w \mathrm{e}^{-\mathrm{i}w(t-t')+\mathrm{i}k_w r+\mathrm{i}\nu_A t+\mathrm{i}\nu^\sigma_L(t-r/c)}, \tag{A.17d}$$

We consider each term separately. For the first term, Eq. (A.17a), we transform ψ^σ to $\tilde{\psi}^\sigma$ using Eq. (A.11),

$$A^\sigma_{2,1}(r,t) = g^\sigma g^\sigma\int_0^t \mathrm{d}t' \ \tilde{\psi}^\sigma(r - c(t-t'),t')\sum_\nu \mathrm{e}^{-\mathrm{i}(\nu-\nu_A)(t-t')}. \tag{A.18}$$

Using the Wigner–Weisskopf approximation as in Section 3.2, $\tilde{\psi}$ may be moved outside the integral by assuming that it varies slowly compared to the temporal evolution in the exponential. The remaining part in the integral over time corresponds to half a delta-function (plus a Lamb shift), leading to a definition of the decay rate

$$\Gamma^{\sigma_1\sigma_2} = 2\pi g^{\sigma_1} g^{\sigma_2} \sum_{\nu} \delta(\nu - \nu_A), \tag{A.19}$$

leading to

$$A^{\sigma}_{2,1}(r,t) = \frac{\Gamma^{\sigma\sigma}}{2}\tilde{\psi}(r,t). \tag{A.20}$$

A similar statement applies to $A^{\sigma}_{2,3}(r,t)$ in Eq. (A.17c), which becomes

$$A^{\sigma}_{2,3}(r,t) = \frac{\Gamma^{\overline{\sigma}\sigma}}{2}\tilde{\psi}(r,t). \tag{A.21}$$

For Eq. (A.17b), we get

$$A^{\sigma}_{2,2}(r,t) = g^{\overline{\sigma}} g^{\sigma} \mathrm{e}^{-\mathrm{i}\delta^{\sigma}_{L} r/c} \int_0^t \mathrm{d}t'\, \tilde{\psi}^{\sigma}(-c(t-t'),t') \sum_{w} \mathrm{e}^{-\mathrm{i}(w-\nu_A)(t-t'-r/c)}, \tag{A.22}$$

where $\delta^{\sigma}_{L} = \nu^{\sigma}_{L} - \nu_A$ and $k_w = w/c$. Making that same assumption about a fast varying exponential, the only contribution to the w-sum is when $t-t'-r/c = 0$. As the integration only goes from $0 < t' < t$, this introduces two Heaviside step function,

$$A^{\sigma}_{2,2}(r,t) = \mathrm{e}^{-\mathrm{i}\delta^{\sigma}_{L} r/c} \Gamma^{\sigma\sigma} \theta(r)\theta(t-r/c)\tilde{\psi}^{\sigma}(-r,t-r/c), \tag{A.23}$$

with the propertiy that $\theta(0) \equiv 1/2$.

The last contribution in Eq. (A.17d) becomes

$$A^{\sigma}_{2,4}(r,t) = g^{\overline{\sigma}} g^{\sigma} \mathrm{e}^{-\mathrm{i}\delta^{\sigma}_{L} r/c + \mathrm{i}(\nu^{\sigma}_{L} - \nu^{\overline{\sigma}}_{L})t} \int_0^t \mathrm{d}t'\, \tilde{\psi}^{\overline{\sigma}}(-c(t-t'),t') \times \sum_{w} \mathrm{e}^{-\mathrm{i}(w-\nu_A)(t-t'-r/c)}. \tag{A.24}$$

With similar arguments as for $A^{\sigma}_{2,2}(r,t)$, we arrive at

$$A^{\sigma}_{2,4}(r,t) = \mathrm{e}^{-\mathrm{i}\delta^{\sigma}_{L} r/c + \mathrm{i}(\nu^{\sigma}_{L} - \nu^{\overline{\sigma}}_{L})t} \Gamma^{\overline{\sigma}\sigma} \theta(r)\theta(t-r/c)\tilde{\psi}^{\overline{\sigma}}(-r,t-r/c). \tag{A.25}$$

Thus Eq. (A.14) simplifies to

$$[\partial_t + c\partial_r]\tilde{\psi}^{\sigma}(r,t) = A^{\sigma}_{1}(r,t) - \frac{\Gamma^{\sigma\sigma} + \Gamma^{\overline{\sigma}\sigma}}{2}\tilde{\psi}^{\sigma}(r,t) - \theta(r)\theta(t-r/c)\mathrm{e}^{-\mathrm{i}\delta^{\sigma}_{L} r/c}\left[\Gamma^{\sigma\sigma}\tilde{\psi}^{\sigma}(-r,t-r/c) + \Gamma^{\overline{\sigma}\sigma}\mathrm{e}^{\mathrm{i}(\nu^{\sigma}_{L} - \nu^{\overline{\sigma}}_{L})t}\tilde{\psi}^{\overline{\sigma}}(-r,t-r/c)\right], \tag{A.26}$$

where $A^{\sigma}_{1}(r,t)$ only depends on the initial conditions of the ϕs. We define the total rate $\Gamma = \Gamma^{\sigma\sigma} + \Gamma^{\overline{\sigma}\overline{\sigma}} = \Gamma^{aa} + \Gamma^{bb}$, which according to Eq. (A.26) describes the rate of spontaneous emission of the emitter into both directions.

Solving Eq. (A.26)

To determine a solution to Eq. (A.26), we first consider a general differential equation on the form

$$[\partial_t + c\partial_r]f(r,t) \quad = \quad -\Gamma f(r,t) - A(r,t). \tag{A.27}$$

Applying a symmetric Fourier transform,

$$f(k,t) = \frac{1}{\sqrt{2\pi}}\int \mathrm{d}r\, f(r,t)\mathrm{e}^{-\mathrm{i}kr}, \quad f(r,t) = \frac{1}{\sqrt{2\pi}}\int \mathrm{d}k\, f(k,t)\mathrm{e}^{\mathrm{i}kr}, \tag{A.28}$$

Eq. (A.27) becomes

$$[\partial_t + \mathrm{i}kc + \Gamma]f(k,t) = -\frac{1}{\sqrt{2\pi}}\int \mathrm{d}r\, A(r,t)\mathrm{e}^{-\mathrm{i}kr}. \tag{A.29}$$

By multiplying each side with $\exp[(\Gamma + \mathrm{i}kc)t]$ and integrating over time, we arrive at

$$f(k,t) = f(k,0)\mathrm{e}^{-(\Gamma+\mathrm{i}kc)t} - \frac{1}{\sqrt{2\pi}}\int_0^t \mathrm{d}t' \int \mathrm{d}r\, A(r,t')\mathrm{e}^{-\mathrm{i}kr-(\Gamma+\mathrm{i}kc)(t-t')}. \tag{A.30}$$

Transforming back, we get

$$\begin{aligned} f(r,t) &= \frac{1}{\sqrt{2\pi}}\int \mathrm{d}k\, f(k,0)\mathrm{e}^{-(\Gamma+\mathrm{i}kc)t+\mathrm{i}kr} \\ &\quad - \frac{1}{2\pi}\int \mathrm{d}k \int_0^t \mathrm{d}t' \int \mathrm{d}r'\, A(r',t')\mathrm{e}^{-\mathrm{i}kr'-(\Gamma+\mathrm{i}kc)(t-t')+\mathrm{i}kr} \\ &= f(r-ct,0)\mathrm{e}^{-\Gamma t} - \int_0^t \mathrm{d}t' \int \mathrm{d}r\, A(r',t')\delta(r-r'-c(t-t'))\mathrm{e}^{-\Gamma(t-t')} \\ &= f(r-ct,0)\mathrm{e}^{-\Gamma t} - \int_0^t \mathrm{d}t'\, A\left(r-c(t-t'),t'\right)\mathrm{e}^{-\Gamma(t-t')}. \end{aligned} \tag{A.31}$$

This derived expression may be used to solve Eq. (A.26). By defining

$$B^\sigma(r,t) = \int_0^t \mathrm{d}t'\, A_1^\sigma\left(r-c(t-t'),t'\right)\mathrm{e}^{-\Gamma(t-t')/2}, \tag{A.32}$$

we may use Eq. (A.31) to write the solution for Eq. (A.26),

$$\begin{aligned} \tilde{\psi}^\sigma(r,t) &= \tilde{\psi}(r-ct,0)\mathrm{e}^{-\Gamma t/2} - B^\sigma(r,t) \\ &\quad - \int_0^t \mathrm{d}t'\, \theta(r-c(t-t'))\theta(t-r/c)\mathrm{e}^{-\mathrm{i}\delta_L^\sigma(r-c(t-t'))/c} \\ &\quad \times \Big[\Gamma^{\sigma\sigma}\tilde{\psi}^\sigma(-(r-c(t-t')),t-r/c) \\ &\qquad + \Gamma^{\overline{\sigma}\sigma}\mathrm{e}^{\mathrm{i}(\nu_L^\sigma-\nu_L^{\overline{\sigma}})t}\tilde{\psi}^{\overline{\sigma}}(-(r-c(t-t')),t-r/c)\Big]\mathrm{e}^{-\Gamma(t-t')/2}. \end{aligned} \tag{A.33}$$

For simplicity, we assume from here that $\nu_L^\sigma = \nu_L^{\overline{\sigma}} \equiv \nu_L$, i.e. that the carrier frequency of the incoming pulses is identical in both arms. We write Eq. (A.33) in a simple-looking form,

$$\tilde{\psi}^\sigma(r,t) = \tilde{\psi}(r-ct,0)\mathrm{e}^{-\Gamma t/2} - B^\sigma(r,t) - \Gamma^{\sigma\sigma} D^\sigma(r,t) - \Gamma^{\overline{\sigma}\sigma} D^{\overline{\sigma}}(r,t), \quad \text{(A.34)}$$

with

$$D^{\sigma_1}(r,t) = \theta(t-r/c)\int_0^t \mathrm{d}t'\,\theta(r-c(t-t'))\mathrm{e}^{-\mathrm{i}\delta_L(r-c(t-t'))/c} \times \tilde{\psi}^{\sigma_1}(-(r-c(t-t')),t-r/c)\mathrm{e}^{-\Gamma(t-t')/2}. \quad \text{(A.35)}$$

A transformation $R = r - c(t-t')$ gives

$$D^{\sigma_1}(r,t) = \theta(t-r/c)\frac{1}{c}\int_{r-ct}^{r} \mathrm{d}R\,\theta(R)\mathrm{e}^{-\mathrm{i}\delta_L R/c}\tilde{\psi}^{\sigma_1}(-R,t-r/c)\mathrm{e}^{-\frac{\Gamma}{2}\frac{r-R}{c}}. \quad \text{(A.36)}$$

The Heaviside-function in front of the integral modifies the lower limit of the integral. As $t \leq 0$ the integral is only non-zero when $r \leq 0$ due to $\theta(R)$ and thus gives a $\theta(r)$ in front,

$$D^{\sigma_1}(r,t) = \theta(t-r/c)\theta(r)\frac{1}{c}\int_0^r \mathrm{d}R\,\mathrm{e}^{-\mathrm{i}\delta_L R/c}\tilde{\psi}^{\sigma_1}(-R,t-r/c)\mathrm{e}^{-\frac{\Gamma}{2}\frac{r-R}{c}}. \quad \text{(A.37)}$$

We insert the expression for $\tilde{\psi}^\sigma$ from Eq. (A.34) and get

$$\begin{aligned} D^{\sigma_1}(r,t) = \theta(t-r/c)\theta(r)\frac{1}{c}\int_0^r \mathrm{d}R\,\mathrm{e}^{-\mathrm{i}\delta_L R/c}\Big\{ & \\ \tilde{\psi}^{\sigma_1}(-R-c(t-r/c),0)\mathrm{e}^{-\frac{\Gamma}{2}(t-r/c)} - B^{\sigma_1}(-R,t-r/c)\Big\}\mathrm{e}^{-\frac{\Gamma}{2}\frac{r-R}{c}} & \\ - \theta(t-r/c)\theta(r)\frac{1}{c}\int_0^r \mathrm{d}R\,\mathrm{e}^{-\mathrm{i}\delta_L R/c}\Big[D^{\sigma_1}(-R,t-r/c) & \\ + D^{\overline{\sigma_1}}(-R,t-r/c)\Big]\mathrm{e}^{-\frac{\Gamma}{2}\frac{r-R}{c}}. & \quad \text{(A.38)} \end{aligned}$$

A closer look on the last two lines shows that both $D^{\sigma_1}(-R,t-r/c)$ and $D^{\overline{\sigma_1}}(-R,t-r/c)$ contain a step function $\theta(-R)$. But as the integration limits only includes positive values of R, these integrations vanish and

$$\begin{aligned} D^{\sigma_1}(r,t) = \frac{1}{c}\theta(t-r/c)\theta(r)\int_0^r \mathrm{d}R\,\mathrm{e}^{-\mathrm{i}\delta_L R/c}\Big\{\tilde{\psi}^{\sigma_1}(r-R-ct,0)\mathrm{e}^{-\frac{\Gamma}{2}(t-r/c)} & \\ - B^{\sigma_1}(-R,t-r/c)\Big\}\mathrm{e}^{-\frac{\Gamma}{2}\frac{r-R}{c}}. & \quad \text{(A.39)} \end{aligned}$$

Thus $D^{\sigma_1}(r,t)$ is solely described by the initial conditions, and the final analytical solution is given by Eq. (A.34).

Simplifying the expression for $B^\sigma(r,t)$

The function $B^\sigma(r,t)$ is defined in Eq. (A.32) and is given by

$$B^\sigma(r,t) = \int_0^t \mathrm{d}t'\, A_1^\sigma\left(r - c(t-t'), t'\right) \mathrm{e}^{-\Gamma(t-t')/2}, \tag{A.40}$$

where $A_1^\sigma(r,t)$ is given in Eq. (A.15) as

$$A_1^\sigma(r,t) = 2\sum_{wv}\left[g^\sigma \Phi_{wv}^{\sigma\sigma}(0) + g^{\overline{\sigma}}\Phi_{wv}^{\sigma\overline{\sigma}}(0)\right] \mathrm{e}^{\mathrm{i}\nu_A t + \mathrm{i}\nu_L(t-r/c) - \mathrm{i}(w+v)t + \mathrm{i}k_w r}. \tag{A.41}$$

We define a Fourier transform of Φ equivalent to the one for ψ in Eq. (A.8),

$$\Phi^{\sigma_1\sigma_2}(r_1, r_2, t) = \sum_{\nu\nu'} \Phi_{\nu\nu'}^{\sigma_1\sigma_2}(t) \mathrm{e}^{\mathrm{i}k_\nu r_1 + \mathrm{i}k_{\nu'} r_2}. \tag{A.42}$$

With this, $A_1^\sigma(r,t)$ becomes

$$A_1^\sigma(r,t) = 2\left[g^\sigma \Phi^{\sigma\sigma}(r-ct, -ct, 0) + g^{\overline{\sigma}}\Phi^{\sigma\overline{\sigma}}(r-ct,-ct,0)\right] \mathrm{e}^{\mathrm{i}\nu_A t + \mathrm{i}\nu_L^\sigma(t-r/c)}. \tag{A.43}$$

By defining

$$\tilde{\Phi}^{\sigma_1\sigma_2}(r_1, r_2, 0) = \Phi^{\sigma_1\sigma_2}(r_1, r_2, 0) \mathrm{e}^{-\mathrm{i}\nu_L r_1/c - \mathrm{i}\nu_L r_2/c}, \tag{A.44}$$

we arrive at

$$A_1^\sigma(r,t) = 2\left[g^\sigma \tilde{\Phi}^{\sigma\sigma}(r-ct, -ct, 0) + g^{\overline{\sigma}}\tilde{\Phi}^{\sigma\overline{\sigma}}(r-ct,-ct,0)\right] \mathrm{e}^{-\mathrm{i}\delta_L t}. \tag{A.45}$$

Thus the expression for $B^\sigma(r,t)$ becomes

$$B^\sigma(r,t) = 2\int_0^t \mathrm{d}t'\, \mathrm{e}^{-\mathrm{i}\delta_L t' - \Gamma(t-t')/2}\Big[g^\sigma \tilde{\Phi}^{\sigma\sigma}(r-ct, -ct', 0) + g^{\overline{\sigma}}\tilde{\Phi}^{\sigma\overline{\sigma}}(r-ct,-ct',0)\Big]. \tag{A.46}$$

Summarizing the results

The solution for the ψ-expansion coefficient of the two-photon state is in the rotated frame given by

$$\tilde{\psi}^\sigma(r,t) = \quad \tilde{\psi}(r-ct,0)\mathrm{e}^{-\Gamma t/2} - B^\sigma(r,t) - \Gamma^{\sigma\sigma} D^\sigma(r,t) - \Gamma^{\overline{\sigma}\sigma} D^{\overline{\sigma}}(r,t), \tag{A.47}$$

where $B^\sigma(r,t)$, D^σ, and $D^{\overline{\sigma}}(r,t)$ are solely described by the initial conditions. They are given by

$$B^\sigma(r,t) = 2\int_0^t \mathrm{d}t'\, \mathrm{e}^{-\mathrm{i}\delta_L t' - \Gamma(t-t')/2}\Big[g^\sigma \tilde{\Phi}^{\sigma\sigma}(r-ct, -ct', 0) + g^{\overline{\sigma}}\tilde{\Phi}^{\sigma\overline{\sigma}}(r-ct,-ct',0)\Big], \tag{A.48}$$

and

$$D^{\sigma_1}(r,t) = \frac{1}{c}\theta(t-r/c)\theta(r)\int_0^r \mathrm{d}R\,\mathrm{e}^{-\mathrm{i}\delta_L R/c}\Big\{\tilde{\psi}^{\sigma_1}(r-R-ct,0)\mathrm{e}^{-\frac{\Gamma}{2}(t-r/c)} - B^{\sigma_1}(-R,t-r/c)\Big\}\mathrm{e}^{-\frac{\Gamma}{2}\frac{r-R}{c}}. \tag{A.49}$$

Assuming an initially excited QD, i.e. for all ϕ's, $\phi(r_1,r_2,0)=0 \rightarrow B^a(r,t) = B^b(r,t)=0$, and a one-way waveguide, $g^b=0$ (no coupling to the backwards propagating mode), the result becomes similar to the one of Valente et al. [92].

A.1 Example: Single-sided Gaussian two-photon input

As an example we calculate the emitter excitation,

$$\langle\psi(t)|c_e^\dagger c_e|\psi(t)\rangle = \sum_\nu |\psi_\nu^a(t)|^2 + \sum_\nu |\psi_\nu^b(t)|^2. \tag{A.50}$$

This is done in the case of identical gs, i.e. that the emitter couples with equal strength in to both directions of the waveguide. Furthermore we assume that the carrier frequency of the input pulses is equal to the QD transition frequency, i.e. $\delta_L = 0$.

A general, two-photon input state has the form

$$|\beta\rangle = K\int \mathrm{d}r_1 \int \mathrm{d}r_2\,\beta(r_1,r_2)a^\dagger(r_1)a^\dagger(r_2)|g,0,0\rangle, \tag{A.51}$$

where K is a normalization constant. Requiring that $\langle\beta|\beta\rangle = 1$, the normalization constant becomes

$$K^2 = \frac{1}{2\int \mathrm{d}r_1 \int \mathrm{d}r_2\,|\tilde{\beta}(r_1,r_2)|^2}, \tag{A.52}$$

where $\tilde{\beta}$ is a symmetric version of β, defined as

$$\tilde{\beta}(r_1,r_2) = \frac{\beta(r_1,r_2)+\beta(r_2,r_1)}{2}. \tag{A.53}$$

Assuming that the two-photon state initially exists in waveguide a only, we see by comparing Eq. (A.51) and Eq. (A.5) that the initial conditions are

$$\phi^{aa}(r_1,r_2,0) = K\beta(r_1,r_2), \tag{A.54}$$

$$\phi^{ab}(r_1,r_2,0) = \phi^{ba}(r_1,r_2,0) = \phi^{bb}(r_1,r_2,0) = \psi^a(r,0) = \psi^b(r,0). \tag{A.55}$$

As we are solving for the symmetrical version of ϕ, the first condition becomes

$$\Phi^{aa}(r_1,r_2,0) = K\tilde{\beta}(r_1,r_2). \tag{A.56}$$

Two independently created single photons

For simplicity, we assume that the two-photon state consists of two independently created single-photon states, $\beta(r_1, r_2) = \xi_1(r_1)\xi_2(r_2)$, with $\xi_i(r)$ being the spatial single-photon wavepacket. Assuming that the single-photon wavepacket amplitudes are normalized as

$$\int \mathrm{d}r\, |\xi_1(r)|^2 = \int \mathrm{d}r\, |\xi_2(r)|^2 = 1, \tag{A.57}$$

the normalization constant K becomes

$$\frac{1}{1 + \left| \int \mathrm{d}r\, \xi_1(r)\xi_2^*(r) \right|^2}. \tag{A.58}$$

With the initial conditions above, $B^b(r,t) = 0$, and the expression for $B^a(r,t)$ simplifies to

$$B^a(r,t) = K g_a \Bigg[\xi_1(r - ct) \int_0^t \mathrm{d}t'\, \mathrm{e}^{-\Gamma(t-t')/2} \xi_2(-ct') + \xi_2(r - ct) \int_0^t \mathrm{d}t'\, \mathrm{e}^{-\Gamma(t-t')/2} \xi_1(-ct') \Bigg]. \tag{A.59}$$

Gaussian input pulses

We assume input pulses with a Gaussian single-photon wavepacket as in Eq. (3.12b), which in a spatial representation is (given in the rotated frame described by Eq. (A.11)),

$$\xi_1(r) = \left(\frac{\sigma_1^2}{\pi} \right)^{1/4} \mathrm{e}^{-(r - r_{01})^2 \sigma_1^2/2}, \quad \xi_2(r) = \left(\frac{\sigma_2^2}{\pi} \right)^{1/4} \mathrm{e}^{-(r - r_{02})^2 \sigma_2^2/2}. \tag{A.60}$$

which corresponds to pulses with a FWHM of the intensity spectrum corresponding to $2\sqrt{\ln(2)}\sigma_{1/2}$. Using these, the normalization constant becomes

$$K^2 = \frac{1}{1 + \frac{2\sigma_1\sigma_2}{\sigma_1^2 + \sigma_2^2} \exp\left[-\frac{\sigma_1^2 \sigma_2^2 (r_{01} - r_{02})^2}{(\sigma_1^2 + \sigma_2^2)} \right]}. \tag{A.61}$$

For the simple case of similar wavepacket width, $\sigma_1 = \sigma_2 \equiv \sigma$, we get

$$K^2 = \frac{1}{1 + \exp[-\sigma^2 (r_{01} - r_{02})^2/2]}. \tag{A.62}$$

In calculating $B^a(r,t)$, a relevant integral is

$$\int_0^t \mathrm{d}t'\, \mathrm{e}^{-\Gamma(t-t')} \xi_i(-ct'). \tag{A.63}$$

Using the integral

$$f_i(x) = \int \mathrm{d}x\, \mathrm{e}^{-(x\sigma_i/\sqrt{2})^2 + x\Gamma/c} = \sqrt{\frac{\pi}{2}} \frac{1}{\sigma_i} \mathrm{e}^{\frac{\Gamma^2}{2c^2\sigma_i^2}} \operatorname{erf}\left[\frac{x\sigma_i}{\sqrt{2}} - \frac{\Gamma}{\sqrt{2}c\sigma_i} \right], \tag{A.64}$$

with may write Eq. (A.63) in a compact way by introducing the variable $x = ct' + r_{0i}$,

$$\int_0^t \mathrm{d}t'\, \mathrm{e}^{-\Gamma(t-t')/2}\xi_i(-ct') = \left(\frac{\sigma_i^2}{\pi}\right)^{1/4} \frac{1}{c}\mathrm{e}^{-\Gamma t/2} \int_{r_{0i}}^{ct+r_{0i}} \mathrm{d}x\, \mathrm{e}^{-x^2\sigma_i^2/4+\frac{\Gamma}{2}(x-r_{0i})/c} \tag{A.65}$$

$$= \left(\frac{\sigma_i^2}{\pi}\right)^{1/4} \frac{1}{c}\mathrm{e}^{-\frac{\Gamma}{2}(t+r_{0i}/c)} \left[f_i(ct+r_{0i}) - f_i(r_{0i})\right]. \tag{A.66}$$

Inserting this into Eq. (A.59), we arrive at

$$B^a(r,t) = \frac{Kg_a}{c}\mathrm{e}^{-\Gamma t/2}\sqrt{\frac{\sigma_1\sigma_2}{\pi}}\Big\{ \mathrm{e}^{-(r-ct-r_{01})^2\sigma_1^2/2}\mathrm{e}^{-\frac{\Gamma}{2}r_{02}/c}\left[f_2(ct+r_{02}) - f_2(r_{02})\right] + 1 \leftrightarrow 2\Big\}, \tag{A.67}$$

where $1 \leftrightarrow 2$ replaces a similar term where the indices of 1 and 2 are interchanged.

For the D-functions, the initial conditions give that $D^b(r,t) = 0$. For $D^a(r,t)$, we get

$$D^a(r,t) = -\frac{1}{c}\theta(t-r/c)\theta(r)\int_0^r \mathrm{d}R\, B^a(-R, t-r/c)\mathrm{e}^{-\frac{\Gamma}{2}(r-R)/c} \tag{A.68}$$

$$= -\frac{Kg_a}{c^2}\sqrt{\frac{\sigma_1\sigma_2}{2\pi}}\theta(t-r/c)\theta(r)\mathrm{e}^{-\Gamma t/2} \times \Big\{\mathrm{e}^{-\frac{\Gamma}{2}r_{02}/c}\left[f_2(ct-r+r_{02}) - f_2(r_{02})\right] \times \int_0^r \mathrm{d}R\, \mathrm{e}^{-(-R-ct+r-r_{01})^2\sigma_1^2/2+\frac{\Gamma}{2}R/c} + 1 \leftrightarrow 2\Big\}. \tag{A.69}$$

The integral is evaluated as before, using the substitution $x = R + ct - r + r_{01}$,

$$\int_0^r \mathrm{d}R\, \mathrm{e}^{-(-R-ct+r-r_{01})^2\sigma_1^2/2+\frac{\Gamma}{2}R/c} = \mathrm{e}^{\frac{\Gamma}{2}(-ct+r-r_{01})/c}\left[f_1(ct+r_{01}) - f(ct-r+r_{01})\right]. \tag{A.70}$$

This leads to

$$D^a(r,t) = \frac{Kg_a}{c^2}\sqrt{\frac{\sigma_1\sigma_2}{\pi}}\theta(t-r/c)\theta(r)\mathrm{e}^{-\Gamma t+\frac{\Gamma}{2}(r-r_{01}-r_{02})/c} \times \left\{\left[f_1(ct-r+r_{01}) - f_1(ct+r_{01})\right]\left[f_2(ct-r+r_{02}) - f_2(r_{02})\right] + 1 \leftrightarrow 2\right\}. \tag{A.71}$$

Summarizing the results for a Gaussian input

Summarizing, the excitation value of the emitter for two uncorrelated Gaussian input pulses is

$$P_e(t) = P_e^a(t) + P_e^b(t) = \int_{-\infty}^{\infty} \mathrm{d}r\, |\tilde{\psi}^a(r,t)|^2 + \int_{-\infty}^{\infty} \mathrm{d}r\, |\tilde{\psi}^b(r,t)|^2, \tag{A.72}$$

where

$$\tilde{\psi}^a(r,t) = -B^a(r,t) - \Gamma^{aa} D^a(r,t), \tag{A.73}$$

$$\tilde{\psi}^b(r,t) = -\Gamma^{ab} D^a(r,t), \tag{A.74}$$

with

$$B^a(r,t) = \frac{K g_a}{c} \mathrm{e}^{-\Gamma t/2} \sqrt{\frac{\sigma_1 \sigma_2}{\pi}} \Bigg\{ \mathrm{e}^{-(r-ct-r_{01})^2 \sigma_1^2/2} \mathrm{e}^{-\frac{\Gamma}{2} r_{02}/c} \Big[f_2(ct + r_{02}) - f_2(r_{02}) \Big] + 1 \leftrightarrow 2 \Bigg\}, \tag{A.75}$$

and

$$D^a(r,t) = \frac{K g_a}{c^2} \sqrt{\frac{\sigma_1 \sigma_2}{\pi}} \theta(t - r/c) \theta(r) \mathrm{e}^{-\Gamma t + \frac{\Gamma}{2}(r - r_{01} - r_{02})/c} \times \Bigg\{ \left[f_1(ct - r + r_{01}) - f_1(ct + r_{01}) \right] \left[f_2(ct - r + r_{02}) - f_2(r_{02}) \right] + 1 \leftrightarrow 2 \Bigg\}, \tag{A.76}$$

where

$$f_i(x) = \sqrt{\frac{\pi}{2}} \frac{1}{\sigma_i} \mathrm{e}^{\frac{\Gamma^2}{2c^2 \sigma_i^2}} \operatorname{erf}\left[\frac{x \sigma_i}{\sqrt{2}} - \frac{\Gamma}{\sqrt{2} c \sigma_i} \right], \tag{A.77}$$

and the normalization constant is

$$K^2 = \frac{1}{1 + \frac{2\sigma_1 \sigma_2}{\sigma_1^2 + \sigma_2^2} \exp\left[-\frac{\sigma_1^2 \sigma_2^2 (r_{01} - r_{02})^2}{(\sigma_1^2 + \sigma_2^2)} \right]}. \tag{A.78}$$

Appendix B

Numerical Implementation of wavefunction approach

In this appendix we discuss the numerical implementation to determine temporal evolution of the expansion coefficient of the total state of the quantum system, which is introduced in Section 3.3. We specifically show the scheme for a excitation of a single emitter, first for a single excitation, followed by two excitations, where the latter is used in Chapter 4.

B.1 Single excitation

The continuum of modes in the infinite waveguide is discretized into N modes divided into two sub-intervals, with $N/2$ of the points centered around $-k_0$ and the other half around k_0, as only modes with $|k|$ close to ω_0/v_g interacts with the emitter - i.e. in the interval $[-\tilde{k}_0 - \Sigma; -\tilde{k}_0 + \Sigma] \cup [\tilde{k}_0 - \Sigma; \tilde{k}_0 + \Sigma]$ with Σ being the width of the sub-intervals. The differential equations for the expansion coeffients, Eqs. (3.6a) and (3.6b), are disretized accordingly using $\int_{-\infty}^{\infty} \mathrm{d}k = dk \sum_k$, giving

$$\partial_t C^e(t) = -\mathrm{i}\, dk \sum_j g(k_j) C^g(k_j, t), \tag{B.1a}$$

$$\partial_t C^g(k_j, t) = -\mathrm{i}\Delta\omega(k_j) C^g(k_j, t) - \mathrm{i}g^*(k_j) C^e(t). \tag{B.1b}$$

To implement Eqs. (B.1a) and (B.1b) and a given initial condition numerically, all quantities have to be normalized. For simplicity, we assume a constant, real coupling constant g. To stick to the standard normalization, we normalize everything to v_g and the QD decay rate into the 1D continuum, which in Section 3.2 was shown to be $\Gamma = 4\pi g(k_0)^2/v_g$. Defining the normalized quantities

$$\tilde{k} = k(v_g/\Gamma), \quad \tilde{t} = t\Gamma, \tag{B.2}$$

we get the equations

$$\partial_{\tilde{t}} C^e(\tilde{t}) = -\mathrm{i}\frac{d\tilde{k}}{\sqrt{4\pi}} \sum_{\tilde{k}} C^g(\tilde{k},\tilde{t}), \tag{B.3a}$$

$$\partial_{\tilde{t}} C^g(\tilde{k},\tilde{t}) = -\mathrm{i}(|\tilde{k}| - \tilde{k}_0) C^g(\tilde{k},\tilde{t}) - \mathrm{i}\frac{1}{\sqrt{4\pi}} C^e(\tilde{t}), \tag{B.3b}$$

Numerically, the system of equations Eqs. (B.3a) and (B.3b) are implemented as a matrix problem,

$$\partial_{\tilde{t}} \mathbf{c}(\tilde{t}) = \mathbf{A}\mathbf{c}(\tilde{t}), \tag{B.4}$$

with the $\tilde{k}$-array divided into components $\tilde{k}_1, \tilde{k}_2, ..., \tilde{k}_N$. We choose the ordering

$$\mathbf{c}(\tilde{t}) = \left[C^e(\tilde{t}), C^g(\tilde{k}_1,\tilde{t}), C^g(\tilde{k}_2,\tilde{t}), \ldots, C^g(\tilde{k}_N,\tilde{t})\right]^T \tag{B.5}$$

and where $\mathbf{A}$ will be a time-independent matrix, given by

$$\mathbf{A} = -\mathrm{i}\begin{bmatrix} 0 & 1 & 1 & \cdots & 1 \\ 1 & |\tilde{k}_1| - \tilde{k}_0 & & & \\ 1 & & |\tilde{k}_2| - \tilde{k}_0 & & \\ \vdots & & & \ddots & \\ 1 & & & & |\tilde{k}_N| - \tilde{k}_0 \end{bmatrix} \tag{B.6}$$

with blank spaces corresponding to zeros. The initial condition is

$$\mathbf{c}_0 = [0, \xi(k_1), \xi(k_2), \ldots, \xi(k_N)] \tag{B.7}$$

with $\xi(\tilde{k})$ being the spectral single-photon wavepacket, e.g. as in Eqs. (3.12a)-(3.12c). The numerical single-photon results are discussed in Section 3.3, where they are also compared to the analytical result for the emitter excitation using a single-photon input pulse with a Gaussian spectrum.

B.2 Two excitations

In this section we expand the model of the single-excitation propagation to a two-excitation model, using the same principle to disretize Eqs. (4.4a) and (4.4a). Following the approach as in Eqs. (B.3a) and (B.3b), the dimensionless equation system becomes

$$\partial_{\tilde{t}} C^e(\tilde{k}_i,\tilde{t}) = -\mathrm{i}(|\tilde{k}_i| - \tilde{k}_0) C^e(\tilde{k}_i,\tilde{t}) - \mathrm{i}\sqrt{2}\frac{d\tilde{k}}{\sqrt{4\pi}} \sum_j C^g(\tilde{k}_i,\tilde{k}_j,\tilde{t}) \tag{B.8}$$

$$\partial_{\tilde{t}} C^g(\tilde{k}_i,\tilde{k}_j,\tilde{t}) = -\mathrm{i}\left(|\tilde{k}_i| - \tilde{k}_0 + |\tilde{k}_j| - \tilde{k}_0\right) C^g(\tilde{k}_i,\tilde{k}_j,\tilde{t}) - \frac{\mathrm{i}}{\sqrt{2}}\frac{1}{\sqrt{4\pi}}\left[C^e(\tilde{k}_i,\tilde{t}) + C^e(\tilde{k}_j,\tilde{t})\right] \tag{B.9}$$

Numerical implementation scheme

Numerically, the system of equations are implemented as a matrix differential problem,

$$\partial_{\tilde{t}}\mathbf{c}(\tilde{t}) = \mathbf{A}\mathbf{c}(\tilde{t}) \tag{B.10}$$

where $\mathbf{A}$ will be a time-independent matrix, and where we choose the ordering

$$\mathbf{c} = \left[C^e_{\tilde{k}_1}, C^e_{\tilde{k}_2}, ..., C^e_{\tilde{k}_N}, \tilde{C}^g_{\tilde{k}_1\tilde{k}_1}, \tilde{C}^g_{\tilde{k}_2\tilde{k}_1}, \tilde{C}^g_{\tilde{k}_3\tilde{k}_1}, ..., , \tilde{C}^g_{\tilde{k}_N\tilde{k}_1}, \tilde{C}^g_{\tilde{k}_1\tilde{k}_2}, \tilde{C}^g_{\tilde{k}_2\tilde{k}_2}, ..., \tilde{C}^g_{\tilde{k}_N\tilde{k}_N}\right]^T \tag{B.11}$$

with the indices of the $\tilde{k}$s referring to the position in the discretized k-array. With this definition, A will be a sparse matrix of dimensions $(N + N^2) \times (N + N^2)$.

The number of elements in $\mathbf{c}$ and $\mathbf{A}$ may be reduced by exploiting that $\tilde{C}^g_{\tilde{k}\tilde{k}'} = \tilde{C}^g_{\tilde{k}'\tilde{k}}$ due to the bosonic nature of the photon, and thus we would only have to include $N + [N + (N-1) + (N-2) + ... + 1] = N + (N+1)N/2$ rows and columns.

To verify the numerical implementation, the value of the maximal emitter excitation obtained numerically is compared with an analytical value. For an incoming two-photon state consisting of two identical, co-propagating Gaussian pulses, the analytical value of the emitter excitation is derived in Appendix A. The relative deviation between the two values is sketched in Fig. B.1 for varying values of dk and N, and in similarity with the single-photon results, the lowest deviation is obtained when the product $dk \cdot N$ is largest, i.e. when the span of the calculation domain is widest.

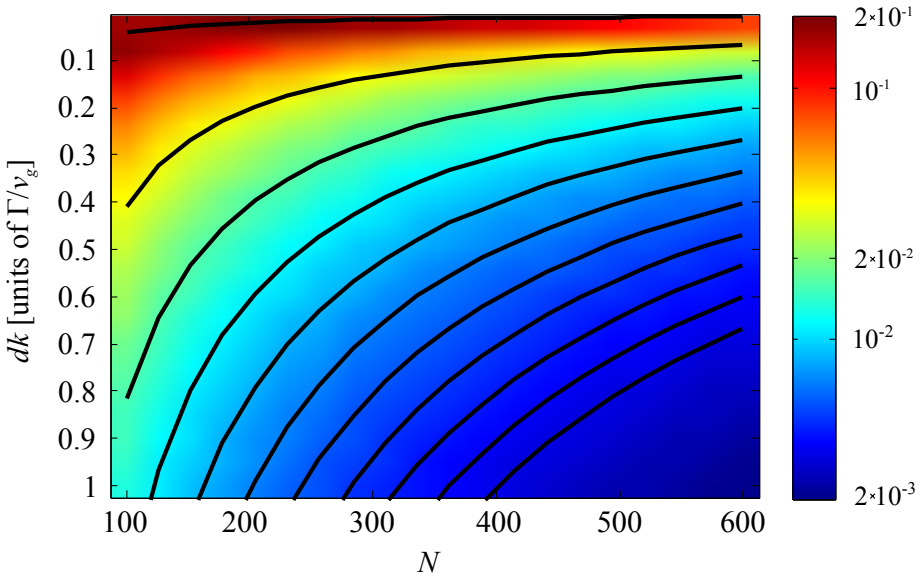

Figure B.1: Relative deviation between the maximum emitter excitation obtained by the numerical and analytical solution for a two-photon Gaussian pulse scattering on a two-level system, calculated for simulations with varying N and dk. The black lines are contours for constant values of the width of the k-array, $N \cdot dk$, and the spectral width of the input pulses is $\tilde{\sigma} = (2\sqrt{\ln(2)})^{-1}\sigma = 1.0\,\Gamma/v_g$.

Appendix C

Parameters for phonon calculations

The parameter values used in the phonon calculations in Chapters 9 and 10 are given in Table C.1, with elaborating comments below for some of the parameters.

Table C.1: Simulation Parameters

Parameter	Description	Value	Ref.
ϱ	Density of GaAs	$5.37\,\mathrm{g/cm^3}$	[182]
c_l	Velocity of LA waves in GaAs	$5.11\,\mathrm{km/s}$	a)
c_t	Velocity of TA waves in GaAs	$3.02\,\mathrm{km/s}$	b)
D_e	Def. potential for a electron in GaAs	$-14.6\,\mathrm{eV}$	c)
D_h	Def. potential for a hole in GaAs	$-4.8\,\mathrm{eV}$	c)
$\hbar g$	Electron-photon coupling strength	$150\,\mu\mathrm{eV}$	d)
Γ	Relaxation rate of excited state in QD	$1\,\mathrm{ns}^{-1}$	[200]
$\hbar\kappa$	Cavity population relaxation rate	$100\,\mu\mathrm{eV}$	[219]

a) c_l: The longitudinal sound velocity in GaAs may vary from 4.784–5.447 km/s depending on the direction of propagation compared to the various crystal planes in the GaAs crystal, $T = 77\,\mathrm{K}$ [220]. We use the value $c_l = 5.11\,\mathrm{km/s}$ used in articles dealing with electron-phonon interaction [47, 182], agreeing with the velocity obtained when averaging over all crystal directions in [220]. Other similar articles use a velocity of 5.15 km/s [221, 222].

b) c_t: The transverse sound velocity in GaAs varies from $2.479 - 3.35\,\mathrm{km/s}$ depending on the direction of propagation compared to the various crystal planes in the GaAs crystal, $T = 77\,\mathrm{K}$ [220]. We use the value $c_l = 3.02\,\mathrm{km/s}$ calculated as an average value of all the propagation directions of the value in [220], it and corresponds to values used in [223]. Other articles dealing with transverse sound waves use values from 2.80 km/s [221] to 3.35 km/s [207].

c) D_e, D_h: We adapt the values of the deformation potential from articles considering electron-acoustic phonon interaction, [182, 47], although it seems

there a big uncertainty in determining agreeing values when measuring the deformation potentials in different experiments. This is discussed in detail in [202].

[d] $\hbar g$: For QD in cavities coupling strengths for good cavities have been shown to be on the order $100 - 200\,\mu$eV [224, 26]. Thus we pick $g = 150\,\mu$eV as a reasonable value.

Bibliography

[1] M. Planck. Ueber das Gesetz der Energieverteilung im Normalspectrum. *Annalen der Physik*, 309(3):553–563, 1901.

[2] A. Einstein. Über einen die Erzeugung und Verwandlung des Lichtes betreffenden heuristischen Gesichtspunkt. *Annalen der Physik*, 322(6):132–148, 1905.

[3] T. D. Ladd, F. Jelezko, R. Laflamme, Y. Nakamura, C. Monroe, and J. L. O'Brien. Quantum computers. *Nature*, 464(7285):45–53, 2010.

[4] C. H. Bennett and G. Brassard. Quantum cryptography: Public key distribution and coin tossing. *Proceedings of IEEE International Conference on Computers, Systems and Signal Processing*, pages 175–179, 1984.

[5] A. K. Ekert. Quantum cryptography based on Bell's theorem. *Phys. Rev. Lett.*, 67:661–663, 1991.

[6] N. Gisin and R. Thew. Quantum communication. *Nat Photon*, 1(3):165–171, 2007.

[7] A. Politi, J.C. F. Matthews, and J. L. O'Brien. Shor's quantum factoring algorithm on a photonic chip. *Science*, 325:1221, 2009.

[8] H. J. Kimble. The quantum internet. *Nature*, 453(7198):1023–1030, 2008.

[9] S. Ritter, C. Nolleke, C. Hahn, A. Reiserer, A. Neuzner, M. Uphoff, M. Mucke, E. Figueroa, J. Bochmann, and G. Rempe. An elementary quantum network of single atoms in optical cavities. *Nature*, 484(7393):195–200, 2012.

[10] J. I. Cirac, P. Zoller, H. J. Kimble, and H. Mabuchi. Quantum state transfer and entanglement distribution among distant nodes in a quantum network. *Phys. Rev. Lett.*, 78:3221–3224, 1997.

[11] P. Kok, W. J. Munro, K. Nemoto, T. C. Ralph, J. P. Dowling, and G. J. Milburn. Linear optical quantum computing with photonic qubits. *Rev. Mod. Phys.*, 79:135–174, 2007.

[12] W. P. Bowen, N. Treps, R. Schnabel, and P. K. Lam. Experimental demonstration of continuous variable polarization entanglement. *Phys. Rev. Lett.*, 89:253601, 2002.

[13] K. Wagner, J. Janousek, V. Delaubert, H. Zou, C. Harb, N. Treps, J. F. Morizur, P. K. Lam, and H. A. Bachor. Entangling the spatial properties of laser beams. *Science*, 321(5888):541–543, 2008.

[14] E. Knill, R. Laflamme, and G. J. Milburn. A scheme for efficient quantum computation with linear optics. *Nature*, 409(6816):46–52, 2001.

[15] C. H. Bennett, G. Brassard, C. Crépeau, R. Jozsa, A. Peres, and W. K. Wootters. Teleporting an unknown quantum state via dual classical and Einstein-Podolsky-Rosen channels. *Phys. Rev. Lett.*, 70:1895–1899, 1993.

[16] J. L. O'Brien, G. J. Pryde, A. G. White, T. C. Ralph, and D. Branning. Demonstration of an all-optical quantum controlled-NOT gate. *Nature*, 426(6964):264–267, 2003.

[17] D. E. Chang, V. Vuletic, and M. D. Lukin. Quantum nonlinear optics – photon by photon. *Nat Photon*, 8(9):685–694, 2014.

[18] U. Banin, Y. Cao, D. Katz, and O. Millo. Identification of atomic-like electronic states in indium arsenide nanocrystal quantum dots. *Nature*, 400(6744):542–544, 1999.

[19] M. Bayer, O. Stern, P. Hawrylak, S. Fafard, and A. Forchel. Hidden symmetries in the energy levels of excitonic 'artificial atoms'. *Nature*, 405(6789):923–926, 2000.

[20] A. P. Alivisatos. Semiconductor clusters, nanocrystals, and quantum dots. *Science*, 271(5251):pp. 933–937, 1996.

[21] B. J. M. Hausmann, B. Shields, Q. Quan, P. Maletinsky, M. McCutcheon, J. T. Choy, T. M. Babinec, A. Kubanek, A. Yacoby, M. D. Lukin, and M. Lončar. Integrated diamond networks for quantum nanophotonics. *Nano Letters*, 12(3):1578–1582, 2012.

[22] A. Faraon, P. E. Barclay, C. Santori, K.-M. C. Fu, and R. G. Beausoleil. Resonant enhancement of the zero-phonon emission from a colour centre in a diamond cavity. *Nat Photon*, 5(5):301–305, 2011.

[23] M. H. Devoret and R. J. Schoelkopf. Superconducting circuits for quantum information: An outlook. *Science*, 339(6124):1169–1174, 2013.

[24] J.-M. Gérard. Solid-state cavity-quantum electrodynamics with self-assembled quantum dots. In *Single Quantum Dots*, volume 90 of *Topics in Applied Physics*, pages 269–314. Springer Berlin Heidelberg, 2003.

[25] K. M. Birnbaum, A. Boca, R. Miller, A. D. Boozer, T. E. Northup, and H. J. Kimble. Photon blockade in an optical cavity with one trapped atom. *Nature*, 436(7047):87–90, 2005.

[26] K. Hennessy, A. Badolato, M. Winger, D. Gerace, M. Atature, S. Gulde, S. Falt, E. L. Hu, and A. Imamoglu. Quantum nature of a strongly coupled single quantum dot-cavity system. *Nature*, 445(7130):896–899, 2007.

[27] D. Englund, A. Faraon, I. Fushman, N. Stoltz, P. Petroff, and J. Vuckovic. Controlling cavity reflectivity with a single quantum dot. *Nature*, 450(7171):857–861, 2007.

[28] J. C. F. Matthews, K. Busch. C. F., A. Politi, A. Stefanov, and J. L. O'Brien. Manipulation of multiphoton entanglement in waveguide quantum circuits. *Nat Photon*, 3(6):346–350, 2009.

[29] P. J. Shadbolt, Verde M. R., A. Peruzzo, A. Politi, A. Laing, M. Lobino, J. C. F. Matthews, M. G. Thompson, and J. L. O'Brien. Generating, manipulating and measuring entanglement and mixture with a reconfigurable photonic circuit. *Nat Photon*, 6(1):45–49, 2012.

[30] R. Bruck, B. Mills, B. Troia, D. J. Thomson, F. Y. Gardes, Y. Hu, G. Z. Mashanovich, V. M. N. Passaro, G. T. Reed, and O. L. Muskens. Device-level characterization of the flow of light in integrated photonic circuits using ultrafast photomodulation spectroscopy. *Nat Photon*, 9(1):54–60, 2015.

[31] F. Priolo, T. Gregorkiewicz, M. Galli, and T. F. Krauss. Silicon nanostructures for photonics and photovoltaics. *Nat Nano*, 9(1):19–32, 2014.

[32] J. Claudon, J. Bleuse, N. S. Malik, M. Bazin, P. Jaffrennou, N. Gregersen, C. Sauvan, P. Lalanne, and J.-M. Gerard. A highly efficient single-photon source based on a quantum dot in a photonic nanowire. *Nat Photon*, 4(3):174–177, 2010.

[33] P. Yao, V. S. C. Manga Rao, and S. Hughes. On-chip single photon sources using planar photonic crystals and single quantum dots. *Laser and Photonics Reviews*, 4(4):499–516, 2010.

[34] D. Sahin, A. Gaggero, Z. Zhou, S. Jahanmirinejad, F. Mattioli, R. Leoni, J. Beetz, M. Lermer, M. Kamp, S. Höfling, and A. Fiore. Waveguide photon-number-resolving detectors for quantum photonic integrated circuits. *Applied Physics Letters*, 103(11):–, 2013.

[35] R. H. Hadfield. Single-photon detectors for optical quantum information applications. *Nat Photon*, 3(12):696–705, 2009.

[36] G. N. Gol'tsman, O. Okunev, G. Chulkova, A. Lipatov, A. Semenov, K. Smirnov, B. Voronov, A. Dzardanov, C. Williams, and Roman Sobolewski. Picosecond superconducting single-photon optical detector. *Applied Physics Letters*, 79(6):705–707, 2001.

[37] F. Najafi, J. Mower, N. C. Harris, F. Bellei, A. Dane, C. Lee, X. Hu, P. Kharel, F. Marsili, S. Assefa, K. K. Berggren, and D. Englund. On-chip detection of non-classical light by scalable integration of single-photon detectors. *Nat Commun*, 6(5873), 2015.

[38] P. Kok and B. W. Lovett. *Introduction to Optical Quantum Information Processing*. Cambridge University Press, 2010.

[39] T. G. Tiecke, J. D. Thompson, N. P. de Leon, L. R. Liu, V. Vuletic, and M. D. Lukin. Nanophotonic quantum phase switch with a single atom. *Nature*, 508(7495):241–244, 2014.

[40] A. Reiserer, N. Kalb, G. Rempe, and S. Ritter. A quantum gate between a flying optical photon and a single trapped atom. *Nature*, 508(7495):237–240, 2014.

[41] W. Chen, K. M. Beck, R. Bücker, M. Gullans, M. D. Lukin, H. Tanji-Suzuki, and V. Vuletić. All-optical switch and transistor gated by one stored photon. *Science*, 341(6147):768–770, 2013.

[42] H. Kim, R. Bose, T. C. Shen, G. S. Solomon, and E. Waks. A quantum logic gate between a solid-state quantum bit and a photon. *Nat Photon*, 7(5):373–377, 2013.

[43] D. E. Chang, A. S. Sorensen, E. A. Demler, and M. D. Lukin. A single-photon transistor using nanoscale surface plasmons. *Nat Phys*, 3(11):807–812, 2007.

[44] T. Volz, A. Reinhard, M. Winger, A. Badolato, K. J. Hennessy, E. L. Hu, and A. Imamoğlu. Ultrafast all-optical switching by single photons. *Nat Photon*, 6(9):605–609, 2012.

[45] M. Arcari, I. Söllner, A. Javadi, S. Lindskov Hansen, S. Mahmoodian, J. Liu, H. Thyrrestrup, E. H. Lee, J. D. Song, S. Stobbe, and P. Lodahl. Near-unity coupling efficiency of a quantum emitter to a photonic crystal waveguide. *Phys. Rev. Lett.*, 113:093603, 2014.

[46] S. Ates, Ulrich S. M., A. Ulhaq, S. Reitzenstein, A. Löffler, S. Höfling, A. Forchel, and P. Michler. Non-resonant dot-cavity coupling and its potential for resonant single-quantum-dot spectroscopy. *Nat Photon*, 3(12):724–728, 2009.

[47] U. Hohenester. Cavity quantum electrodynamics with semiconductor quantum dots: Role of phonon-assisted cavity feeding. *Phys. Rev. B*, 81:155303, 2010.

[48] P. Kaer, T. R. Nielsen, P. Lodahl, A.-P. Jauho, and J. Mørk. Non-Markovian model of photon-assisted dephasing by electron-phonon interactions in a coupled quantum-dot–cavity system. *Phys. Rev. Lett.*, 104:157401, 2010.

[49] P. Kaer, P. Lodahl, A.-P. Jauho, and J. Mork. Microscopic theory of indistinguishable single-photon emission from a quantum dot coupled to a cavity: The role of non-Markovian phonon-induced decoherence. *Phys. Rev. B*, 87:081308, 2013.

[50] R. Loudon. *The Quantum Theory of Light*. Oxford University Press, third edition, 2000.

[51] C. Cohen-Tannoudji, J. Dupont-Roc, and G. Grynberg. *Photons and Atoms - Introduction to Quantum Electrodynamics.* John Wiley and Sons, 1989.

[52] W. Schäfer and M. Wegener. *Semiconductor Optics and Transport Phenomena.* Springer-Verlag, 2002.

[53] G. D. Mahan. *Many-Particle Physics.* Plenum Press, New York, 1990.

[54] P. Kær Nielsen. Fundamental properties of single-photon sources. Master's thesis, DTU Fotonik, 2008.

[55] H. Bruus and K. Flensberg. *Many-Body Quantum Theory in Condensed Matter Physics.* Oxford University Press, 2004.

[56] L. E. Ballentine. *Quantum Mechanics - A Modern Development.* World Scientific, 1998.

[57] M. A. Stroscio and M. Dutta. *Phonon in Nanostructures.* Cambridge University Press, 2004.

[58] C. Kittel. *Introduction to Solid State Physics.* John Wiley and Sons, eigth edition, 2004.

[59] C. Gerry and P. Knight. *Introduction to Quantum Optics.* Cambridge University Press, 2005.

[60] S. Stobbe, P. T. Kristensen, J. E. Mortensen, J. M. Hvam, J. Mørk, and P. Lodahl. Spontaneous emission from large quantum dots in nanostructures: Exciton-photon interaction beyond the dipole approximation. *Phys. Rev. B*, 86:085304, 2012.

[61] Q. D. Zhuang, J. M. Li, Y. P. Zeng, L. Pan, H. X. Li, M. Y. Kong, and L. Y. Lin. Structural characterization of InGaAs/GaAs quantum dots superlattice infrared photodetector structures. *Journal of Crystal Growth*, 200(3-4):375 – 381, 1999.

[62] A. Goban, C.-L. Hung, S.-P. Yu, J. D. Hood, J.A. Muniz, J.H. Lee, M.J. Martin, A. C. McClung, K. S. Choi, D. E. Chang, O. Painter, and H. J. Kimble. Atom–light interactions in photonic crystals. *Nat Commun*, 5(3808), 2014.

[63] E. Rephaeli and S. Fan. Dissipation in few-photon waveguide transport. *Photon. Res.*, 1(3):110–114, 2013.

[64] Y. Chen, M. Wubs, J. Mørk, and A. F. Koenderink. Coherent single-photon absorption by single emitters coupled to one-dimensional nanophotonic waveguides. *New J. Phys.*, 13(10):103010, 2011.

[65] J. T. Shen and S. Fan. Coherent photon transport from spontaneous emission in one-dimensional waveguides. *Opt. Lett.*, 30(15):2001–2003, 2005.

[66] S. Fan, Ş. E. Kocabaş, and J.-T. Shen. Input-output formalism for few-photon transport in one-dimensional nanophotonic waveguides coupled to a qubit. *Phys. Rev. A*, 82:063821, 2010.

[67] H. Zheng, D. J. Gauthier, and H. U. Baranger. Waveguide QED: Many-body bound-state effects in coherent and Fock-state scattering from a two-level system. *Phys. Rev. A*, 82:063816, 2010.

[68] Y. Wu and X. Yang. Strong-coupling theory of periodically driven two-level systems. *Phys. Rev. Lett.*, 98:013601, 2007.

[69] K. J. Blow, R. Loudon, S. J. D. Phoenix, and T. J. Shepherd. Continuum fields in quantum optics. *Phys. Rev. A*, 42:4102–4114, 1990.

[70] J.-T. Shen and S. Fan. Theory of single-photon transport in a single-mode waveguide. i. coupling to a cavity containing a two-level atom. *Phys. Rev. A*, 79:023837, 2009.

[71] C. W. Gardiner, A. S. Parkins, and P. Zoller. Wave-function quantum stochastic differential equations and quantum-jump simulation methods. *Phys. Rev. A*, 46:4363–4381, 1992.

[72] B. Q. Baragiola, R. L. Cook, A. M. Brańczyk, and J. Combes. N-photon wave packets interacting with an arbitrary quantum system. *Phys. Rev. A*, 86:013811, 2012.

[73] P. Kaer and J. Mørk. Decoherence in semiconductor cavity QED systems due to phonon couplings. *Phys. Rev. B*, 90:035312, 2014.

[74] V. Weisskopf and E. Wigner. Berechnung der natürlichen Linienbreite auf Grund der Diracschen Lichttheorie. *Zeitschrift für Physik*, 63(1-2):54–73, 1930.

[75] G. K. Gulati, B. Srivathsan, B. Chng, A. Cerè, D. Matsukevich, and C. Kurtsiefer. Generation of an exponentially rising single-photon field from parametric conversion in atoms. *Phys. Rev. A*, 90:033819, 2014.

[76] M. Keller, B. Lange, K. Hayasaka, W. Lange, and H. Walther. Continuous generation of single photons with controlled waveform in an ion-trap cavity system. *Nature*, 431(7012):1075–1078, 2004.

[77] Y. Chen, T. R. Nielsen, N. Gregersen, P. Lodahl, and J. Mørk. Finite-element modeling of spontaneous emission of a quantum emitter at nanoscale proximity to plasmonic waveguides. *Phys. Rev. B*, 81:125431, 2010.

[78] R. LeVeque. *Finite Difference Methods for Ordinary and Partial Differential Equations: Steady-State and Time-Dependent Problems.* SIAM, Society for Industrial and Applied Mathematics, 2007.

[79] W. E. Arnoldi. The principle of minimized iterations in the solution of the matrix eigenvalue problem. *Quarterly of Applied Mathematics*, 9:17–29, 1951.

[80] M. Knap, E. Arrigoni, W. von der Linden, and J. H. Cole. Emission characteristics of laser-driven dissipative coupled-cavity systems. *Phys. Rev. A*, 83:023821, 2011.

[81] W.-B. Yan and H. Fan. Single-photon quantum router with multiple output ports. *Scientific Reports*, 4:4820, 2014.

[82] C. Martens, P. Longo, and K. Busch. Photon transport in one-dimensional systems coupled to three-level quantum impurities. *New J. Phys.*, 15(8):083019, 2013.

[83] W.-B. Yan, J.-F. Huang, and H. Fan. Tunable single-photon frequency conversion in a Sagnac interferometer. *Sci. Rep.*, 3(3555), 2013.

[84] J. Hwang, M. Pototschnig, R. Lettow, G. Zumofen, A. Renn, S. Gotzinger, and V. Sandoghdar. A single-molecule optical transistor. *Nature*, 460(7251):76–80, 2009.

[85] A. Auffèves-Garnier, C. Simon, J.-M. Gérard, and J.-P. Poizat. Giant optical nonlinearity induced by a single two-level system interacting with a cavity in the Purcell regime. *Phys. Rev. A*, 75:053823, 2007.

[86] A. Blais, R.-S. Huang, A. Wallraff, S. M. Girvin, and R. J. Schoelkopf. Cavity quantum electrodynamics for superconducting electrical circuits: An architecture for quantum computation. *Phys. Rev. A*, 69:062320, 2004.

[87] J.-T. Shen and S. Fan. Strongly correlated two-photon transport in a one-dimensional waveguide coupled to a two-level system. *Phys. Rev. Lett.*, 98:153003, 2007.

[88] J.-T. Shen and S. Fan. Strongly correlated multiparticle transport in one dimension through a quantum impurity. *Phys. Rev. A*, 76:062709, 2007.

[89] T. Shi and C. P. Sun. Lehmann-symanzik-zimmermann reduction approach to multiphoton scattering in coupled-resonator arrays. *Phys. Rev. B*, 79:205111, 2009.

[90] J.-F. Huang, J.-Q. Liao, and C. P. Sun. Photon blockade induced by atoms with Rydberg coupling. *Phys. Rev. A*, 87:023822, 2013.

[91] K. Kojima, H. F. Hofmann, S. Takeuchi, and K. Sasaki. Nonlinear interaction of two photons with a one-dimensional atom: Spatiotemporal quantum coherence in the emitted field. *Phys. Rev. A*, 68:013803, 2003.

[92] D. Valente, Y. Li, J. P. Poizat, J M. Gérard, L. C. Kwek, M. F. Santos, and A. Auffèves. Optimal irreversible stimulated emission. *New J. Phys.*, 14(8):083029, 2012.

[93] P. Longo, P. Schmitteckert, and K. Busch. Dynamics of photon transport through quantum impurities in dispersion-engineered one-dimensional systems. *Journal of Optics A: Pure and Applied Optics*, 11(11):114009, 2009.

[94] P. Longo, P. Schmitteckert, and K. Busch. Few-photon transport in low-dimensional systems. *Phys. Rev. A*, 83:063828, Jun 2011.

[95] M. Moeferdt, P. Schmitteckert, and K. Busch. Correlated photons in one-dimensional waveguides. *Opt. Lett.*, 38(18):3693–3695, 2013.

[96] D. Witthaut, M. D. Lukin, and A. S. Sørensen. Photon sorters and QND detectors using single photon emitters. *EPL (Europhysics Letters)*, 97(5):50007, 2012.

[97] E. Rephaeli and S. Fan. Stimulated emission from a single excited atom in a waveguide. *Phys. Rev. Lett.*, 108:143602, 2012.

[98] C. Cinelli, G. Di Nepi, F. De Martini, M. Barbieri, and P. Mataloni. Parametric source of two-photon states with a tunable degree of entanglement and mixing: Experimental preparation of Werner states and maximally entangled mixed states. *Phys. Rev. A*, 70:022321, 2004.

[99] M. Ostermeyer, D. Korn, D. Puhlmann, C. Henkel, and J. Eisert. Two-dimensional characterization of spatially entangled photon pairs. *Journal of Modern Optics*, 56(17):1829–1837, 2009.

[100] G. Harder, V. Ansari, B. Brecht, T. Dirmeier, C. Marquardt, and C. Silberhorn. An optimized photon pair source for quantum circuits. *Opt. Express*, 21(12):13975–13985, 2013.

[101] W. P. Grice, A. B. U'Ren, and I. A. Walmsley. Eliminating frequency and space-time correlations in multiphoton states. *Phys. Rev. A*, 64:063815, 2001.

[102] K. Wang. Quantum theory of two-photon wavepacket interference in a beamsplitter. *Journal of Physics B: Atomic, Molecular and Optical Physics*, 39(18):R293, 2006.

[103] E. Rephaeli, J.-T. Shen, and S. Fan. Full inversion of a two-level atom with a single-photon pulse in one-dimensional geometries. *Phys. Rev. A*, 82:033804, 2010.

[104] C. K. Hong, Z. Y. Ou, and L. Mandel. Measurement of subpicosecond time intervals between two photons by interference. *Phys. Rev. Lett.*, 59:2044–2046, 1987.

[105] P. Longo, J. H. Cole, and K. Busch. The Hong-Ou-Mandel effect in the context of few-photon scattering. *Opt. Express*, 20(11):12326–12340, 2012.

[106] H. Zheng, D. J. Gauthier, and H. U. Baranger. Strongly correlated photons generated by coupling a three- or four-level system to a waveguide. *Phys. Rev. A*, 85:043832, 2012.

[107] I.-C. Hoi, T. Palomaki, J. Lindkvist, G. Johansson, P. Delsing, and C. M. Wilson. Generation of nonclassical microwave states using an artificial atom in 1d open space. *Phys. Rev. Lett.*, 108:263601, 2012.

[108] G. Vidal and R. F. Werner. Computable measure of entanglement. *Phys. Rev. A*, 65:032314, 2002.

[109] M. B. Plenio and S. Virmani. An introduction to entanglement measures. *Quantum Info. Comput.*, 7(1):1–51, 2007.

[110] V. Vedral and M. B. Plenio. Entanglement measures and purification procedures. *Phys. Rev. A*, 57:1619–1633, 1998.

[111] H. M. Wiseman and J. A. Vaccaro. Entanglement of indistinguishable particles shared between two parties. *Phys. Rev. Lett.*, 91:097902, 2003.

[112] G. Ghirardi and L. Marinatto. General criterion for the entanglement of two indistinguishable particles. *Phys. Rev. A*, 70:012109, 2004.

[113] K. Eckert, J. Schliemann, D. Bruss, and M. Lewenstein. Quantum correlations in systems of indistinguishable particles. *Annals of Physics*, 299(1):88 – 127, 2002.

[114] R. Paškauskas and L. You. Quantum correlations in two-boson wave functions. *Phys. Rev. A*, 64:042310, 2001.

[115] D. Witthaut and A. S. Sørensen. Photon scattering by a three-level emitter in a one-dimensional waveguide. *New J. Phys.*, 12(4):043052, 2010.

[116] M. Laakso and M. Pletyukhov. Scattering of two photons from two distant qubits: Exact solution. *Phys. Rev. Lett.*, 113:183601, 2014.

[117] T. Shi, S. Fan, and C. P. Sun. Two-photon transport in a waveguide coupled to a cavity in a two-level system. *Phys. Rev. A*, 84:063803, 2011.

[118] T. Shi and S. Fan. Two-photon transport through a waveguide coupling to a whispering-gallery resonator containing an atom and photon-blockade effect. *Phys. Rev. A*, 87:063818, 2013.

[119] J.-Q. Liao and C. K. Law. Correlated two-photon transport in a one-dimensional waveguide side-coupled to a nonlinear cavity. *Phys. Rev. A*, 82:053836, 2010.

[120] S. Derouault and M. A. Bouchene. One-photon wave packet interacting with two separated atoms in a one-dimensional waveguide: Influence of virtual photons. *Phys. Rev. A*, 90:023828, 2014.

[121] A. Nysteen, P. T. Kristensen, D. P. S. McCutcheon, P. Kaer, and J. Mørk. Scattering of two photons on a quantum emitter in a one-dimensional waveguide: exact dynamics and induced correlations. *New J. Phys.*, 17(2):023030, 2015.

[122] T. C. Ralph, N. K. Langford, T. B. Bell, and A. G. White. Linear optical controlled-NOT gate in the coincidence basis. *Phys. Rev. A*, 65:062324, 2002.

[123] M. A. Pooley, D. J. P. Ellis, R. B. Patel, A. J. Bennett, K. H. A. Chan, I. Farrer, D. A. Ritchie, and A. J. Shields. Controlled-NOT gate operating with single photons. *Applied Physics Letters*, 100:211103, 2012.

[124] I. Shomroni, S. Rosenblum, Y. Lovsky, O. Bechler, G. Guendelman, and B. Dayan. All-optical routing of single photons by a one-atom switch controlled by a single photon. *Science*, 345(6199):903–906, 2014.

[125] L.-M. Duan and H. J. Kimble. Scalable photonic quantum computation through cavity-assisted interactions. *Phys. Rev. Lett.*, 92:127902, 2004.

[126] C. Wang, Y. Zhang, R.-Z. Jiao, and G.-S. Jin. Universal quantum controlled phase gate on photonic qubits based on nitrogen vacancy centers and microcavity resonators. *Opt. Express*, 21(16):19252–19260, 2013.

[127] D. Englund, A. Majumdar, M. Bajcsy, A. Faraon, P. Petroff, and J. Vučković. Ultrafast photon-photon interaction in a strongly coupled quantum dot-cavity system. *Phys. Rev. Lett.*, 108:093604, 2012.

[128] R. Bose, D. Sridharan, H. Kim, G. S. Solomon, and E. Waks. Low-photon-number optical switching with a single quantum dot coupled to a photonic crystal cavity. *Phys. Rev. Lett.*, 108:227402, 2012.

[129] R. Johne and A. Fiore. Proposal for a two-qubit quantum phase gate for quantum photonic integrated circuits. *Phys. Rev. A*, 86:063815, 2012.

[130] S. Xu, E. Rephaeli, and S. Fan. Analytic properties of two-photon scattering matrix in integrated quantum systems determined by the cluster decomposition principle. *Phys. Rev. Lett.*, 111:223602, 2013.

[131] M. G. Thompson, A. Politi, J. C. F. Matthews, and J. L. O'Brien. Integrated waveguide circuits for optical quantum computing. *Circuits, Devices Systems, IET*, 5(2):94–102, 2011.

[132] J. Wang, A. Santamato, P. Jiang, D. Bonneau, E. Engin, J. W. Silverstone, M. Lermer, J. Beetz, M. Kamp, S. Höfling, M. G. Tanner, C. M. Natarajan, R. H. Hadfield, S. N. Dorenbos, V. Zwiller, J. L. O'Brien, and M. G. Thompson. Gallium arsenide (GaAs) quantum photonic waveguide circuits. *Optics Communications*, 327:49 – 55, 2014.

[133] A. Martinez, F. Cuesta, and J. Marti. Ultrashort 2-d photonic crystal directional couplers. *Photonics Technology Letters, IEEE*, 15(5):694–696, 2003.

[134] T. C. Ralph, I. Söllner, S. Mahmoodian, A. G. White, and P. Lodahl. Photon sorting, efficient bell measurements and a deterministic CZ gate using a passive two-level nonlinearity. *arXiv:1502.04261*, 2015.

[135] A. Mohan, P. Gallo, M. Felici, B. Dwir, A. Rudra, J. Faist, and E. Kapon. Record-low inhomogeneous broadening of site-controlled quantum dots for nanophotonics. *Small*, 6(12):1268–1272, 2010.

[136] A. Lyasota, S. Borghardt, C. Jarlov, B. Dwir, P. Gallo, A. Rudra, and E. Kapon. Integration of multiple site-controlled pyramidal quantum dot systems with photonic-crystal membrane cavities. *Journal of Crystal Growth*, 414:192 – 195, 2015.

[137] Z. Wang and S. Fan. Optical circulators in two-dimensional magneto-optical photonic crystals. *Opt. Lett.*, 30(15):1989–1991, 2005.

[138] I. Söllner, S. Mahmoodian, S. L. Hansen, L. Midolo, A. Javadi, G. Kiršanskė, T. Pregnolato, H. El-Ella, E. H. Lee, J. D. Song, S. Stobbe, and P. Lodahl. Deterministic photon-emitter coupling in chiral photonic circuits. *arXiv:1406.4295*, 2015.

[139] K. J. Vahala. Optical microcavities. *Nature*, 424(6950):839–846, 2003.

[140] D. V. Strekalov, A. S. Kowligy, Y.-P. Huang, and P. Kumar. Progress towards interaction-free all-optical devices. *Phys. Rev. A*, 89:063820, 2014.

[141] Y.-Z. Sun, Y.-P. Huang, and P. Kumar. Photonic nonlinearities via quantum Zeno blockade. *Phys. Rev. Lett.*, 110:223901, 2013.

[142] W. M. Itano, D. J. Heinzen, J. J. Bollinger, and D. J. Wineland. Quantum Zeno effect. *Phys. Rev. A*, 41:2295–2300, 1990.

[143] P. N. Butcher and D. Cotter. *The Elements of Nonlinear Optics*. Cambridge University Press, 1990.

[144] T. Tanabe, M. Notomi, H. Taniyama, and E. Kuramochi. Dynamic release of trapped light from an ultrahigh-Q nanocavity via adiabatic frequency tuning. *Phys. Rev. Lett.*, 102:043907, 2009.

[145] T.-J. Wang, C.-H. Chu, and C.-Y. Lin. Electro-optically tunable microring resonators on lithium niobate. *Opt. Lett.*, 32(19):2777–2779, 2007.

[146] A. Guarino, G. Poberaj, D. Rezzonico, R. Degl'Innocenti, and P. Gunter. Electro-optically tunable microring resonators in lithium niobate. *Nat Photon*, 1(7):407–410, 2007.

[147] D. Haertle. Domain patterns for quasi-phase matching in whispering-gallery modes. *Journal of Optics*, 12(3):035202, 2010.

[148] V. S. Ilchenko, A. A. Savchenkov, A. B. Matsko, and L. Maleki. Nonlinear optics and crystalline whispering gallery mode cavities. *Phys. Rev. Lett.*, 92:043903, 2004.

[149] Y.-P. Huang and P. Kumar. Interaction-free quantum optical Fredkin gates in $\chi^{(2)}$ microdisks. *Selected Topics in Quantum Electronics, IEEE Journal of*, 18(2):600–611, 2012.

[150] A.B. Matsko and V.S. Ilchenko. Optical resonators with whispering-gallery modes-part i: basics. *Selected Topics in Quantum Electronics, IEEE Journal of*, 12(1):3–14, 2006.

[151] J.-T. Shen and S. Fan. Theory of single-photon transport in a single-mode waveguide. ii. coupling to a whispering-gallery resonator containing a two-level atom. *Phys. Rev. A*, 79:023838, 2009.

[152] Y.-P. Huang and P. Kumar. Interaction-free all-optical switching in $\chi(2)$microdisks for quantum applications. *Opt. Lett.*, 35(14):2376–2378, 2010.

[153] D. E. Zelmon, D. L. Small, and D. Jundt. Infrared corrected Sellmeier coefficients for congruently grown lithium niobate and 5 mol.% magnesium oxide –doped lithium niobate. *J. Opt. Soc. Am. B*, 14(12):3319–3322, 1997.

[154] J. E. Heebner, T. C. Bond, and J. S. Kallman. Generalized formulation for performance degradations due to bending and edge scattering loss in microdisk resonators. *Opt. Express*, 15(8):4452–4473, 2007.

[155] G. Nunzi Conti, S. Berneschi, F. Cosi, S. Pelli, S. Soria, G. C. Righini, M. Dispenza, and A. Secchi. Planar coupling to high-Q lithium niobate disk resonators. *Opt. Express*, 19(4):3651–3656, 2011.

[156] R. Johne and A. Fiore. Single-photon absorption and dynamic control of the exciton energy in a coupled quantum-dot–cavity system. *Phys. Rev. A*, 84:053850, 2011.

[157] E. E. Hach, A. W. Elshaari, and S. F. Preble. Fully quantum-mechanical dynamic analysis of single-photon transport in a single-mode waveguide coupled to a traveling-wave resonator. *Phys. Rev. A*, 82:063839, 2010.

[158] J. Lin, Y. Xu, Z. Fang, M. Wang, J. Song, N. Wang, L. Qiao, W. Fang, and Y. Cheng. Fabrication of high-Q lithium niobate microresonators using femtosecond laser micromachining. *Sci. Rep.*, 5(8072), 2015.

[159] J. P. Reithmaier, G. Sek, A. Löffler, C. Hofmann, S. Kuhn, S. Reitzenstein, L. V. Keldysh, V. D. Kulakovskii, T. L. Reinecke, and A. Forchel. Strong coupling in a single quantum dot-semiconductor microcavity system. *Nature*, 432(7014):197–200, 2004.

[160] J. M. Gérard, D. Barrier, J. Y. Marzin, R. Kuszelewicz, L. Manin, E. Costard, V. Thierry-Mieg, and T. Rivera. Quantum boxes as active probes for photonic microstructures: The pillar microcavity case. *Applied Physics Letters*, 69(4):449–451, 1996.

[161] M. Lermer, N. Gregersen, F. Dunzer, S. Reitzenstein, S. Höfling, J. Mørk, L. Worschech, M. Kamp, and A. Forchel. Bloch-wave engineering of quantum dot micropillars for cavity quantum electrodynamics experiments. *Phys. Rev. Lett.*, 108:057402, 2012.

[162] T. Yoshie, A. Scherer, J. Hendrickson, G. Khitrova, H. M. Gibbs, G. Rupper, C. Ell, O. B. Shchekin, and D. G. Deppe. Vacuum Rabi splitting with a single quantum dot in a photonic crystal nanocavity. *Nature*, 432(7014):200–203, 2004.

[163] J. Vučković and Y. Yamamoto. Photonic crystal microcavities for cavity quantum electrodynamics with a single quantum dot. *Applied Physics Letters*, 82(15):2374–2376, 2003.

[164] S. Hughes, P. Yao, F. Milde, A. Knorr, D. Dalacu, K. Mnaymneh, V. Sazonova, P. J. Poole, G. C. Aers, J. Lapointe, R. Cheriton, and R. L. Williams. Influence of electron-acoustic phonon scattering on off-resonant cavity feeding within a strongly coupled quantum-dot cavity system. *Phys. Rev. B*, 83:165313, 2011.

[165] A. Majumdar, E. D. Kim, Y. Gong, M. Bajcsy, and J. Včković. Phonon mediated off-resonant quantum dot-cavity coupling under resonant excitation of the quantum dot. *Phys. Rev. B*, 84:085309, 2011.

[166] I. Wilson-Rae and A. Imamoğlu. Quantum dot cavity-QED in the presence of strong electron-phonon interactions. *Phys. Rev. B*, 65:235311, 2002.

[167] E. A. Muljarov and R. Zimmermann. Dephasing in quantum dots: Quadratic coupling to acoustic phonons. *Phys. Rev. Lett.*, 93:237401, 2004.

[168] E. M. Gauger, S. C. Benjamin, A. Nazir, and B. W. Lovett. High-fidelity all-optical control of quantum dot spins: Detailed study of the adiabatic approach. *Phys. Rev. B*, 77:115322, 2008.

[169] T. B. Norris, J.-K. Rhee, C.-Y. Sung, Y. Arakawa, M. Nishioka, and C. Weisbuch. Time-resolved vacuum rabi oscillations in a semiconductor quantum microcavity. *Phys. Rev. B*, 50:14663–14666, 1994.

[170] A. Kiraz, M. Atatüre, and A. Imamoğlu. Quantum-dot single-photon sources: Prospects for applications in linear optics quantum-information processing. *Phys. Rev. A*, 69:032305, 2004.

[171] J. Bylander, I. Robert-Philip, and I. Abram. Interference and correlation of two independent photons. *The European Physical Journal D - Atomic, Molecular, Optical and Plasma Physics*, 22(2):295–301, 2003.

[172] K. H. Madsen, P. Kaer, A. Kreiner-Møller, S. Stobbe, A. Nysteen, J. Mørk, and P. Lodahl. Measuring the effective phonon density of states of a quantum dot in cavity quantum electrodynamics. *Phys. Rev. B*, 88:045316, 2013.

[173] P. Kaer, T. R. Nielsen, P. Lodahl, A.-P. Jauho, and J. Mørk. Microscopic theory of phonon-induced effects on semiconductor quantum dot decay dynamics in cavity QED. *Phys. Rev. B*, 86:085302, 2012.

[174] H.-P. Breuer and F. Petruccione. *The Theory of Open Quantum Systems*. Oxford University Press, 2002.

[175] H. J. Carmichael. *An Open Systems Approach to Quantum Optics*. Springer-Verlag, 1993.

[176] H.-P. Breuer, B. Kappler, and F. Petruccione. Stochastic wave-function method for non-Markovian quantum master equations. *Phys. Rev. A*, 59:1633–1643, 1999.

[177] A. Smirne and B. Vacchini. Nakajima-zwanzig versus time-convolutionless master equation for the non-Markovian dynamics of a two-level system. *Phys. Rev. A*, 82:022110, 2010.

[178] S. Chaturvedi and F. Shibata. Time-convolutionless projection operator formalism for elimination of fast variables. Applications to Brownian motion. *Zeitschrift für Physik B Condensed Matter*, 35(3):297–308, 1979.

[179] G. Lindblad. On the generators of quantum dynamical semigroups. *Communications in Mathematical Physics*, 48(2):119–130, 1976.

[180] L. Jacak, P. Machnikowski, J. Krasnyj, and P. Zoller. Coherent and incoherent phonon processes in artificial atoms. *Eur. Phys. J. D*, 22(3):319–331, 2003.

[181] J. Bardeen and W. Shockley. Deformation potentials and mobilities in non-polar crystals. *Phys. Rev.*, 80:72–80, 1950.

[182] B. Krummheuer, V. M. Axt, and T. Kuhn. Theory of pure dephasing and the resulting absorption line shape in semiconductor quantum dots. *Phys. Rev. B*, 65:195313, 2002.

[183] B. Krummheuer, V. M. Axt, T. Kuhn, I. D'Amico, and F. Rossi. Pure dephasing and phonon dynamics in GaAs- and GaN-based quantum dot structures: Interplay between material parameters and geometry. *Phys. Rev. B*, 71:235329, 2005.

[184] C. Patel, T. J. Parker, J. Jamshidi, and W. F. Sherman. Phonon frequencies in GaAs. *Phys. Stat. Sol. (b)*, 122:461, 1984.

[185] G. Whitfield and P. B. Shaw. Interaction of electrons with acoustic phonons via the deformation potential in one dimension. *Phys. Rev. B*, 14:3346–3355, 1976.

[186] P. Y. Yu and M. Cardona. *Fundamentals of Semiconductors.* Springer, third edition, 2005.

[187] A. Grodecka, L. Jacak, P. Machnikowski, and K. Roszak. Phonon impact on the coherent control of quantum states in semiconductor quantum dots. *arXiv:cond-mat/0404364*, 2004.

[188] N. W. Ashcroft and N. D. Mermin. *Acoustic Fields and Waves in Solids, Vol II.* Krieger, 1989.

[189] M. Esposito and P. Gaspard. Quantum master equation for a system influencing its environment. *Phys. Rev. E*, 68:066112, 2003.

[190] A. Auffèves, D. Gerace, J.-M. Gérard, M. Fran ça Santos, L. C. Andreani, and J.-P. Poizat. Controlling the dynamics of a coupled atom-cavity system by pure dephasing. *Phys. Rev. B*, 81:245419, 2010.

[191] A. Naesby, T. Suhr, P. T. Kristensen, and J. Mørk. Influence of pure dephasing on emission spectra from single photon sources. *Phys. Rev. A*, 78:045802, 2008.

[192] M. S. Kushwaha, P. Halevi, L. Dobrzynski, and B. Djafari-Rouhani. Acoustic band structure of periodic elastic composites. *Phys. Rev. Lett.*, 71:2022–2025, 1993.

[193] B. Krummheuer, V. M. Axt, and T. Kuhn. Coupled polarization and acoustic-phonon dynamics after optical excitation of quantum dots near surfaces. *Phys. Rev. B*, 72:245336, 2005.

[194] M. Maldovan and E. L. Thomas. Simultaneous localization of photons and phonons in two-dimensional periodic structures. *Applied Physics Letters*, 88:251907, 2006.

[195] A. H. Safavi-Naeini and O. Painter. Design of optomechanical cavities and waveguides on a simultaneous bandgap phononic-photonic crystal slab. *Opt. Express*, 18(14):14926–14943, 2010.

[196] E. Gavartin, R. Braive, I. Sagnes, O. Arcizet, A. Beveratos, T. J. Kippenberg, and I. Robert-Philip. Optomechanical coupling in a two-dimensional photonic crystal defect cavity. *Phys. Rev. Lett.*, 106:203902, 2011.

[197] A. Vagov, M. D. Croitoru, V. M. Axt, T. Kuhn, and F. M. Peeters. Nonmonotonic field dependence of damping and reappearance of Rabi oscillations in quantum dots. *Phys. Rev. Lett.*, 98:227403, 2007.

[198] S. Weiler, A. Ulhaq, S. M. Ulrich, D. Richter, M. Jetter, P. Michler, C. Roy, and S. Hughes. Phonon-assisted incoherent excitation of a quantum dot and its emission properties. *Phys. Rev. B*, 86:241304, 2012.

[199] A. Wojs, P. Hawrylak, S. Fafard, and L. Jacak. Electronic structure and magneto-optics of self-assembled quantum dots. *Phys. Rev. B*, 54:5604–5608, 1996.

[200] S. Stobbe, J. Johansen, P. T. Kristensen, J. M. Hvam, and P. Lodahl. Frequency dependence of the radiative decay rate of excitons in self-assembled quantum dots: Experiment and theory. *Phys. Rev. B*, 80:155307, 2009.

[201] R. V. N. Melnik and M. Willatzen. Bandstructures of conical quantum dots with wetting layers. *Nanotechnology*, 15(1):1, 2004.

[202] I. Vurgaftman, J. R. Meyer, and L. R. Ram-Mohan. Band parameters for III-V compound semiconductors and their alloys. *Journal of Applied Physics*, 89(11):5815–5875, 2001.

[203] E. T. Jaynes and F. W. Cummings. Comparison of quantum and semiclassical radiation theories with application to the beam maser. *Proceedings of the IEEE*, 51(1):89–109, 1963.

[204] H. Ezawa. Phonons in a half space. *Annals of Physics*, 67(2):438 – 460, 1971.

[205] M. C. Oliveros and D. R. Tilley. Quantization procedure for phonons in an isotropic elastic half-space. *physica status solidi (b)*, 119(2):675–683, 1983.

[206] N. Bannov, V. Mitin, and M. Stroscio. Confined acoustic phonons in a free-standing quantum well and their interaction with electrons. *Physica Status Solidi (b)*, 183(1):131–142, 1994.

[207] N. Bannov, V. Aristov, V. Mitin, and M. A. Stroscio. Electron relaxation times due to the deformation-potential interaction of electrons with confined acoustic phonons in a free-standing quantum well. *Phys. Rev. B*, 51:9930–9942, 1995.

[208] Y. Y. Liao, Y. N. Chen, W. C. Chou, and D. S. Chuu. Decoherence of a charge qubit embedded inside a suspended phonon cavity. *Phys. Rev. B*, 77:033303, 2008.

[209] W.-M. Ju, K.-D. Zhu, P.-H. Huang, and H. Zheng. The dynamics of a double-dot charge qubit embedded in a suspended phonon cavity. *The European Physical Journal B*, 72(3):417–422, 2009.

[210] Y. Y. Liao and Y. N. Chen. Pure dephasing of double-quantum-dot charge qubits in freestanding slabs. *Phys. Rev. B*, 81:153301, 2010.

[211] K. J. Xu and C. Piermarocchi. Dynamics of elastic and inelastic energy transfer between quantum dots in a microcavity. *Phys. Rev. B*, 84:115316, 2011.

[212] A. Nysteen. Cavity QED - engineering the phonon interactions. Master's thesis, DTU Fotonik, 2011.

[213] Y. Y. Liao, D. S. Chuu, and S. R. Jian. Electric-field-controlled electron relaxation in lateral double quantum dots embedded in a suspended slab. *Journal of Applied Physics*, 104:104315, 2008.

[214] P. Borri, W. Langbein, S. Schneider, U. Woggon, R. L. Sellin, D. Ouyang, and D. Bimberg. Ultralong dephasing time in InGaAs quantum dots. *Phys. Rev. Lett.*, 87:157401, 2001.

[215] Charles Santori, David Fattal, Jelena Vuckovic, Glenn S. Solomon, and Yoshihisa Yamamoto. Indistinguishable photons from a single-photon device. *Nature*, 419(6907):594–597, 2002.

[216] M. Gullans, D. E. Chang, F. H. L. Koppens, F. J. García de Abajo, and M. D. Lukin. Single-photon nonlinear optics with graphene plasmons. *Phys. Rev. Lett.*, 111:247401, 2013.

[217] Y. Yu, M. Heuck, H. Hu, W. Xue, C. Peucheret, Y. Chen, L. K. Oxenløwe, K. Yvind, and J. Mørk. Fano resonance control in a photonic crystal structure and its application to ultrafast switching. *Applied Physics Letters*, 105:061117, 2014.

[218] T. P. M. Alegre, A. Safavi-Naeini, M. Winger, and O. Painter. Quasi-two-dimensional optomechanical crystals with a complete phononicbandgap. *Opt. Express*, 19(6):5658–5669, 2011.

[219] D. Press, S. Götzinger, S. Reitzenstein, C. Hofmann, A. Löffler, M. Kamp, A. Forchel, and Y. Yamamoto. Photon antibunching from a single quantum-dot-microcavity system in the strong coupling regime. *Phys. Rev. Lett.*, 98:117402, 2007.

[220] J. S. Blakemore. *Gallium Arsenide*. American Institute of Physics, 1993.

[221] K. Gawarecki, M. Pochwała, A. Grodecka–Grad, and P. Machnikowski. Phonon-assisted relaxation and tunneling in self-assembled quantum dot molecules. *Phys. Rev. B*, 81:245312, 2010.

[222] M. Bagheri Harouni, R. Roknizadeh, and M. H. Naderi. Influence of phonons on exciton-photon interaction and photon statistics of a quantum dot. *Phys. Rev. B*, 79:165304, 2009.

[223] H. Bruus, K. Flensberg, and H. Smith. Magnetoconductivity of quantum wires with elastic and inelastic scattering. *Phys. Rev. B*, 48:11144–11155, 1993.

[224] E. Peter, P. Senellart, D. Martrou, A. Lemaître, J. Hours, J. M. Gérard, and J. Bloch. Exciton-photon strong-coupling regime for a single quantum dot embedded in a microcavity. *Phys. Rev. Lett.*, 95:067401, 2005.